

Habilitation Thesis

**Czech
Technical
University
in Prague**

F6 Faculty of Transportation Sciences
Department of Mechanics and Materials

Advanced Dynamic Testing of Auxetic Metamaterials

**Utilisation of SHPB/OHPB Apparatus for Dynamic
Testing of Auxetic Metamaterials**

Ing. Petr Zlámal, Ph.D.

**Field of study: Transportation Systems and Technology
December 2021**

Acknowledgements

The research has been supported by the Czech Science Foundation (grant no. 19-23675S and grant no. 15-15480S) and the Ministry of Education Youth and Sports (grant no. OPVVV CZ.02.1.010.00.016_0190000766). All the support is gratefully acknowledged.

Also I would like to thank all my colleagues at the Department of Mechanics and Materials, CTU FTS for the excellent teamwork during the solution of the presented research topic.

Declaration

I hereby submit the habilitation thesis elaborated upon at the CTU in Prague, Faculty of Transportation Sciences for the evaluation and defence.

I have no relevant reason against using this work in the sense of §60 of Act No. 121/2000 Coll. on the Copyright and Rights Related to Copyright and on Amendment to Certain Acts (the Copyright Act)

This work is a compilation of papers published during my research work. Some of the articles included in this habilitation thesis are protected by the copyright of Elsevier B, WILEY-VCH Verlag GmbH and MDPI AG. They are presented and reprinted in accordance with the copyright agreements with the respective publishers. Further copying or reprinting can be undertaken exclusively with the permission of the respective publishers.

in Prague, December 2021

Abstract

The habilitation thesis is focused on a demonstration of advanced experimental methods for the investigation of the auxetic metamaterial response on high-strain rate loading. Several types of auxetic structures manufactured using an additive manufacturing technique are introduced. These structures are tested using a Split Hopkinson Pressure Bar (SHPB) technique and its modifications at different strain-rates. The design and properties of the SHPB apparatus and an Open Hopkinson Pressure Bar (OHPB) as well as the proper instrumentation are described in the thesis. Moreover, the supplementary experimental campaigns, such as testing at elevated and reduced temperatures or penetration testing, are mentioned. The final passage of the habilitation thesis is an introduction of the very unique and advanced facilities for the high-speed X-ray imaging of the high-strain rate or intermediate strain-rate testing that are currently implemented at the Department of Mechanics and Materials.

Keywords: auxetic structures, metamaterials, additive manufacturing, SHPB, OHPB, instrumentation, high-speed X-ray imaging

Abstrakt

Habilitační práce je zaměřena na demonstraci pokročilých experimentálních metod pro zkoumání odezvy auxetických metamateriálů při dynamickém rázu za vysokých rychlostí deformace. V práci je představeno několik typů auxetických struktur, které jsou vyráběny technologií 3D tisku. Tyto struktury jsou testovány pomocí sestavy Dělené Hopkinsonovi tyče (SHPB) a její modifikacích při různých rychlostech zatěžování. V práci je taktéž uveden popis sestavy SHPB tak jako sestavy OHPB (Open Hopkinson Pressure Bar) a příslušné instrumentace. Navíc, jsou zde uvedeny i doplňující experimentální kampaně, např. experimenty při zvýšené a snížené teplotě nebo penetrační experimenty. Závěrečné pasáže práce popisují unikátní a pokročilá zařízení, v současné době vznikající na Ústavu mechaniky a materiálů, pro vysokorychlostní rentgenové zobrazování se současným rázovým zatěžováním za vysokých a středních rychlostí deformace.

Klíčová slova: auxetické struktury, metamateriály, 3D tisk, SHPB, OHPB, instrumentace, vysokorychlostní rentgenové zobrazování

Contents

1 Introduction	1
2 Materials and Methods	6
2.1 Samples	6
2.1.1 Auxetic lattices	6
2.1.2 Hybrid auxetic structures	7
2.1.3 Advanced Pore Morphology (APM) foam	8
2.2 Principle of Split Hopkinson Pressure Bar	9
2.2.1 introduction to the theory	9
2.2.2 Selected approach for the testing using SHPB at the Department of Mechanics and Materials	10
2.3 SHPB at the Department of Mechanics and Materials	11
2.3.1 Design	11
2.3.2 Instrumentation	13
2.4 OHPB at the Department of Mechanics and Materials	26
2.4.1 Basic principle	28
2.4.2 Design of OHPB	29
2.4.3 Penetration test	33
3 Future work	36
3.0.1 High-speed X-ray imaging of the high-strain rate testing setup	36
3.0.2 High-speed X-ray imaging of the intermediate strain-rate testing setup	38
Bibliography	41
A Selected Papers	46

Figures

<p>1.1 The principle of auxetic materials 2</p> <p>2.1 Types of the auxetic lattices 7</p> <p>2.2 The printed and coated hybrid auxetic constructs 8</p> <p>2.3 The investigated specimens 8</p> <p>2.4 Principle of SHPB: principle and scheme of the SHPB apparatus 10</p> <p>2.5 The overview of the SHPB setup 13</p> <p>2.6 The overview of the SHPB setup instrumentation with the main sub-systems 14</p> <p>2.7 Initial instrumentation of the SHPB setup 17</p> <p>2.8 The variants of the strain-gauge arrangement used during the experimental campaigns 18</p> <p>2.9 The scheme of the experimental triggering and impact velocity measurement sub-system 20</p> <p>2.10 The scheme of the high-speed imaging sub-system 22</p> <p>2.11 Details of the heating/cooling stage and the overall experimental setup used to test auxetic structures at elevated and reduced temperatures 24</p> <p>2.12 Image sequence of deforming 2D re-entrant honeycomb auxetic lattice during impact 25</p> <p>2.13 2D re-entrant honeycomb structure: mean correlation coefficient and correlation grid 26</p>	<p>2.14 Principle of the forward DIHB, reverse DIHB and OHPB 28</p> <p>2.15 Diagram showing the strain wave propagation in the OHPB setup 29</p> <p>2.16 The arrangement of the OHPB experimental setup: uni-axial compression with the aluminium alloy/PMMA bars 30</p> <p>2.17 The experimental setup with the aluminium alloy bars and the important parts of the OHPB arrangement 32</p> <p>2.18 The experimental setup with the PMMA bars during the experimental campaign. 32</p> <p>2.19 The scheme of the OHPB modification for the penetration testing. 34</p> <p>2.20 The OHPB experimental setup for the penetration testing 35</p> <p>3.1 Scheme of the experimental facility for the high-speed X-ray imaging. 37</p> <p>3.2 Series of four images acquired using the Flash X-ray system 38</p> <p>3.3 Experimental facility for the high-speed X-ray imaging. 39</p> <p>3.4 Frame of the assembled loading device 39</p>
---	--

Tables

2.1 The main parameters of both types of high-speed cameras.	21
---	----



Chapter 1

Introduction

Nowadays, investigations into metamaterials and the further application of metamaterials are very popular tasks in research. The term metamaterial is a combination of the Greek word "meta" (meaning "beyond") and the Latin word "materia" (meaning "matter" or "material"). Metamaterials can be characterised by specific properties that are not found (or they occur very rarely) in naturally occurring materials. Metamaterials are often engineered with tailored properties for a given type of application and for a specific purpose (electrical, electromagnetics, optic, mechanical, etc.) [1]. Mechanical metamaterials are types of metamaterials where the mechanical properties obtained by arranging the internal structure to prevail over the mechanical properties of the base material [2].

An auxetic metamaterial is a type of mechanical metamaterial which is characterised by a negative Poisson's ratio. The term "auxetic" comes from the Greek word "auxetikos" which means "that which tends to increase". When an auxetic material is compressed, its structure shrinks in a perpendicular direction to the applied force. In the case of tension, the auxetic structure expands in the transverse direction (see Fig. 1.1).

This behaviour results from the structural geometry of the cells, which are specially designed for this purpose. Depending on the deformation direction and design, the man-made auxetic structure (two-dimensional and three-dimensional) can be generally subdivided into eight groups: (a) rigid node rotation, (b) chiral, (c) re-entrant lattice, (d) elastic instability, (e) kirigami fractal cut, (f) origami, (g) star shape connected, and (h) missing-rib [3, 4]. Auxetic structures are not just man-made arrangements, they can also rarely exist in nature in two forms: biological and minerals [5]. Examples of naturally occurring mineral auxetic materials are iron pyrites, arsenic monocrystals [6], while the representative of the biological form is the trabecular bone of a human

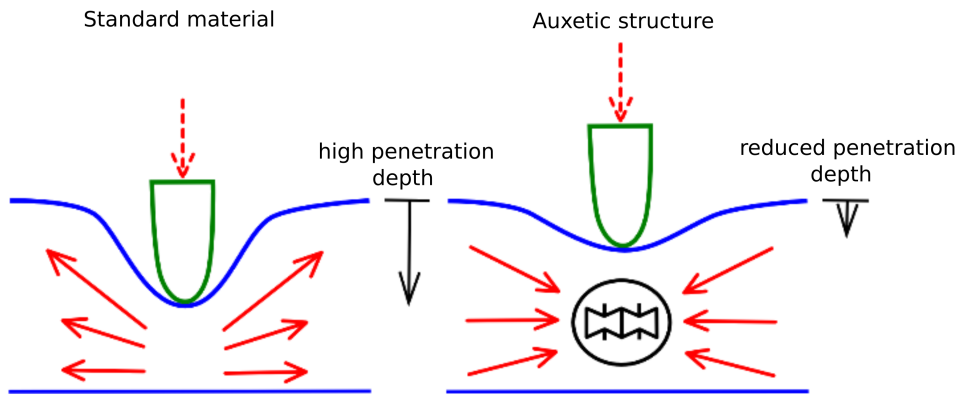


Figure 1.1: The principle of auxetic materials

tibia [7].

Kolpakov [8], in 1985, mathematically described an example of the structure which exhibits a negative Poisson's ratio. In 1987, Lakes et al. [9] firstly designed and manufactured auxetic cellular materials from conventional low-density open-cell polymer foams by causing the ribs of each cell to permanently protrude inward. The resulting scheme is known as the re-entrant topology.

The rapid development in production technologies opened the door to the wider use of auxetic structures in fields of engineering and technology. Because auxetic metamaterials are usually arranged in repeating patterns, manufacturing them using 3D printing/additive manufacturing techniques is a very promising way how to produce different type of structures with optimised parameters for the target application. Due to their unique mechanical properties, they have a high utility potential in a wide range of important applications across a broad range of engineering areas. These application areas can range from the medical (artificial skin, stents) [10], sports engineering (impact protector equipment, such as gloves and helmets) [11], sound and vibration reduction for automotive [12], blast protection structures (e.g., sandwich panels) [13, 14], aerospace or the space industries.

High attention has been paid to auxetic structures as lightweight structures suitable for absorbing a large deformation energy. This property is highly valued in applications where collisions with fast-moving objects occur (crashes, blasts, etc.). Auxetic topology enables one to increase the energy absorption capability through the possibility of using lighter and smaller components. To investigate the energy absorption capability, it is

essential to accurately describe the deformation behaviour of the structure under large deformations. In the case of experimental testing, it is necessary to reliably determine strain with respect to the appropriate loading mode. Moreover, several parameters need to be taken into account (e.g. large displacements and rotation, contact between struts, boundary conditions, etc.). The correct evaluation of the experimental data is a crucial task for the validation of numerical models [13].

With regard to the possible application areas of auxetic structures (crashes, high velocity impacts, blasts), it is necessary to take strain-rates and the velocity of the impact into account during the experiments. Various values of these loading parameters can lead to a different deformation process of the structure. It is well known that the deformation behaviour of many homogeneous materials (aluminium, copper, etc.) is strain-rate dependent and their response differs significantly during quasi-static and dynamic testing (and also between low and high velocity impacts) [15]. In the case of auxetic structures, the strain-rate effect of the basic material is amplified by the internal structural arrangement. The resulting strain-rate response of the auxetic structure is then a combination of the strain-rate dependency of the base material and the effects of the micro-inertia, localised heating, pore pressure, and others which are related to the specially designed topology [16].

The correct understanding of these phenomena and disclosure of the extent of their influence on the effective properties of the auxetics can be reliably determined only on the basis of experiments that ensure sufficient strain-rates in the tested sample. In addition to the drop-tower experiment (typically low or medium strain-rates $\approx 10 \text{ s}^{-1}$ to 10^3 s^{-1}), a Split Hopkinson Pressure Bar (SHPB) and its modifications (DIHB - Direct Impact Hopkinson Bar, OHPB - Open Hopkinson Pressure Bar, etc.) have been successfully used for the assessment of the mechanical properties of auxetic structures [17]. The typical achieved strain-rates using the SHPB experimental apparatus are in the range of 10^3 s^{-1} - 10^4 s^{-1} , which makes this technique a suitable one for investigation into dynamic response of auxetic structures under impact loading at various strain-rates. The SHPB technique is based on the elastic strain wave propagation in slender bars. Nowadays, the SHPB apparatus is a well-established method for the dynamic testing of a wide range of materials and can be successfully used for the evaluation of stress-strain dependency at high strain-rates in a compression mode. The main application of the SHPB technique is the measurement of ductile, high-strength materials, such as solid

metals, where the results are reliable and the technique is relatively easy to use. For materials with low mechanical impedance and a geometrically complex inner structure, its use is problematic and may lead to unreliable results [18]. To test these types of materials, it is most appropriate to use a modification of the setup or only some parts (e.g. incident and transmission bar made from a low mechanical impedance material). Moreover, advanced data correction techniques have to be applied during the evaluation process of the measured data [19].

The core of the thesis is a compilation of papers published during my research work at the Department of Mechanics and Materials in the Faculty of Transportation Sciences (FTS) over the last six years. At the beginning of this period, a working group aimed at the dynamic testing of cellular solid/auxetic materials was established. The main focus of this group was the design and implementation of a custom SHPB/OHPB apparatus in configurations suitable for the measurement of 3D printed auxetic structures or cellular solids produced by the foaming process. In addition to the construction of the SHPB apparatus itself, it was necessary to carry out proper instrumentation and evaluation procedures along with their modifications, which were based on the needs of the individual types of experiments. The experimental work during the mentioned period was focused on the characterisation of the deformation response of specimens with different types of materials:

- closed-cell aluminum alloy foam; Advanced pore morphology (APM) foam - aluminium spheres are coated by polyamide; hybrid APM foam (hAPM) - aluminium spheres are embedded in an epoxy [20].
- Ni/Polyurethane hybrid metal foams - polyurethane open-cell foam template and nickel coating [21]
- auxetic structure of various topologies fabricated by the laser powder bed fusion technique (LPBF) from SS316L powdered austenitic steel [22]
- hybrid 2D re-entrant auxetic lattices - polyurethane auxetic structure template and nickel coating [23]
- filling materials for inter-penetrating phase composites [24]
- polymer-filled auxetic structures [25]

- bulk samples fabricated by the LPBF technique from SS316L powdered austenitic steel with different printing orientations [26]

with different types of auxetic topologies:

- 2D re-entrant honeycomb [27, 22], 3D re-entrant honeycomb [22]
- 2D missing-rib [22]
- hexa-chiral 2D [28], tetra-chiral 2D [28], tetra-chiral 3D [28]
- re-entrant tetrakaidecahedral [29]

and with different types of ambient or loading mode conditions:

- penetration testing [20]
- testing using the OHPB apparatus [23]
- at elevated and reduced temperatures [27]

In addition to the experimental campaigns, the experimental setup was gradually improved and modified over time. For each setup modification or improvement of the instrumentation (e.g., custom strain-gauge measurement unit [30]), it is necessary to perform a calibration to verify the correct functionality to ensure that the reliability of the measured data is not affected. Thus, the strain assessment evaluated using Digital Image Correlation (DIC) and the force measured using a piezo-electric quartz impact force transducer were compared with the strain and force derived from strain-gauges [23, 31, 32]

This thesis is mainly a compilation of the selected papers (the articles are available as attachments, see Appendix A) covering the most important findings in the presented research topic. This compilation is supplemented by supporting parts: Introduction, Materials and Methods and Future work. The introduction briefly describes the motivation of the research and solved topic. The main methods and techniques relate to the research activity of this thesis are introduced in the section called Materials and Method. Finally, the last section outlines how the experimental work will be developed in the near future.

Chapter 2

Materials and Methods

This chapter summarises and briefly describes the materials, methods and techniques used, adopted or developed during the research work performed in the compilation of the selected papers. Mainly, the focus is placed upon the design and instrumentation of the SHPB setup and its modification, strain assessment (conventionally using strain-gauges and more advanced using DIC) and image post-processing, sample preparation, thermal imaging, etc.

2.1 Samples

2.1.1 Auxetic lattices

The production of different types of auxetic structures were performed using a laser powder bed fusion technique (LPBF) in an AM 250 device (Renishaw, UK). As a material for the additive manufacturing printing process, a powdered 316L-0407 austenitic stainless steel alloy was used. This alloy is an extra-low carbon variation on the standard 316L alloy with a density of 7990 kgm^{-3} (for wrought materials) and a melting point in a range of $1371 - 1399 \text{ }^\circ\text{C}$. The compressive strength, yield strength and modulus of elasticity of the sintered bulk material in a horizontal direction are 676 MPa, 547 MPa, 197 GPa, respectively. For the vertical direction, the compressive strength, yield strength and modulus of elasticity of the sintered bulk material are 624 MPa, 494 MPa, 190 GPa, respectively. These mechanical values are specified in a datasheet provided by the manufacturer. Some examples of the auxetic samples (2D re-entrant honeycomb, 3D re-entrant honeycomb and 2D missing-rib) produced using the LPBF technique are depicted in Fig. 2.1.

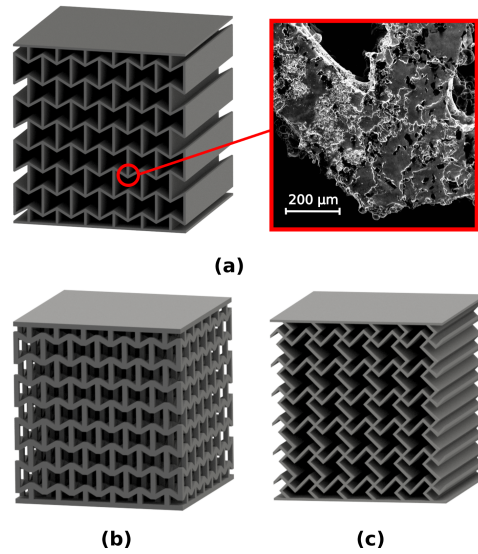


Figure 2.1: Auxetic lattices: a) 2D re-entrant honeycomb with SEM image detail of the strut joint, b) 3D re-entrant honeycomb, and c) 2D missing-rib (image taken from **paper 2** in Appendix A).

These samples were optimised versions with a nominal thickness of the individual struts of 0.3 mm, while the initial samples had a thickness of 0.6 mm. The optimisation of the production process enabled a significant reduction in the unit-cell size which led one to obtain at least 6 unit-cells in both directions of the specimen cross-section. This number of cells satisfied the general requirements on the representative volume element (RVE) as defined by Gibson and Ashby et al. [33]. The outer dimensions of the samples were $12.2 \times 12.2 \times 12.6$ mm. The overall cross-section dimensions of the samples were limited by diameter of the bars of the SHPB.

■ 2.1.2 Hybrid auxetic structures

A unit cell of the 3D re-entrant honeycomb auxetic was used as a template for the geometry of the hybrid auxetic samples. The specimens were printed using a Pro Jet HD3000 3D printer (3D Systems, Rock Hill, USA) from a UV-curable polymer VisiJet. The outer dimensions of the printed specimens were approximately $12.5 \times 12.5 \times 18.4$ mm. The printed polymeric samples were electro-chemically coated with a layer of a $60 \mu\text{m}$ or $120 \mu\text{m}$ in thickness (two types of hybrid auxetic samples) of nickel. The detailed description of the coating process can be found in Jung et al. [16]. After the coating

procedure, the samples were pyrolytically treated (approx. 1000 °C) and the polymer template was removed. In Fig. 2.2, the printed polymeric template as well as the final hybrid auxetic structures are shown.

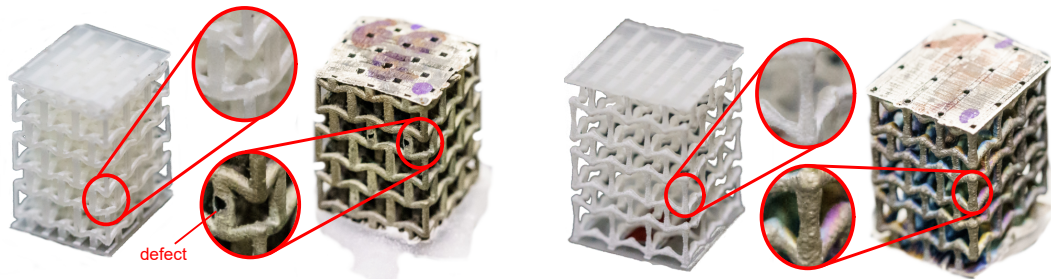


Figure 2.2: The printed and coated hybrid auxetic constructs (image taken from **paper 4** in Appendix A).

2.1.3 Advanced Pore Morphology (APM) foam

The fabrication process of the APM aluminium foam ($AlSi_{10}$) samples consists of two steps: the foaming and shaping step [34, 35]. The fabrication and coating of the basic APM spheres were performed by Fraunhofer IFAM Bremen (Germany). In the second step, Teflon (PTFE) moulds with a diameter of 60 mm and thickness of 30 mm were used to manufacture the APM specimens. The filled moulds with polyamide coated APM elements were placed into a 190 °C heated furnace for two hours to melt the adhesive. Thus after the cooling, the neighbouring APM elements were bonded together. The same manufacturing process was employed for the fabrication of the hAPM foam, unlike the APM foam, the heating was performed at 160 °C for three hours. The specimens of the APM and hAPM foam are shown in Fig. 2.3

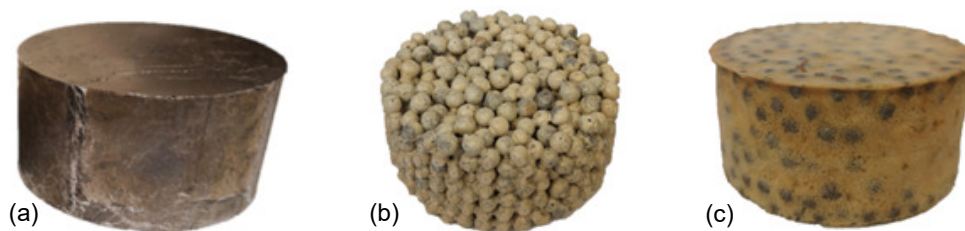


Figure 2.3: The investigated specimens: (a) the closed-cell aluminium foam, (b) APM, (c) hAPM (image taken from **paper 5** in Appendix A).

2.2 Principle of Split Hopkinson Pressure Bar

2.2.1 introduction to the theory

The split Hopkinson Pressure Bar (SHPB) is a promising technique used to investigate the mechanical properties of a wide range of materials at high strain-rates. The nominal achieved strain-rates of the experimental apparatus are in a range of 10^3 s^{-1} - 10^4 s^{-1} , which makes this technique suitable for the investigation of the dynamic response of auxetic structures under impact loading. The main principle of the SHPB method is based on an elastic strain wave propagation in a set of co-axial slender bars. A commonly used SHPB setup consists of three co-axial bars. The striker bar is usually significantly shorter than the other two bars called the incident and transmission bars. Between the incident and the transmission bar, the tested specimen is mounted. The striker bar is an impactor which is accelerated by the excitation system (e.g., a gas-gun, pre-tension). The accelerated striker bar impacts the incident bar and excites an elastic strain-wave. The elastic strain wave propagates through the incident bar to its end before reaching the interface with the mounted sample. On the interface with the specimen, a part of the incident wave is reflected back into the incident bar while a part of the incident wave passes through the specimen and gradually compresses it. On the opposite side of the sample (interface sample - transmission bar), the wave passes into the transmission bar. The transmission bar then hits a momentum trap where the residual energy of the experiment is absorbed. The SHPB experiment usually generates three waves (incident, reflected, transmission) which are propagated in the bars. These waves are most often measured using foil strain-gauges bonded onto the surface of the bars. The post-processing of the measured strain waves allows one to determine the stress-strain diagrams as well as the strain-rate diagrams of the tested material. The fundamental principle of the SHPB and the scheme of the SHPB apparatus with the initial instrumentation (year 2017) are shown in Fig. 2.4.

The simplest method used to evaluate of the SHPB experiment is the one-dimensional wave propagation theory. This theory is based on the assumption that the elastic strain waves in the bars propagate at a constant velocity without any damping and with non-dispersive behaviour. The theory also neglects the effects related to inertia and friction. Moreover, the theory is valid only if the dynamic force equilibrium (see Fig.

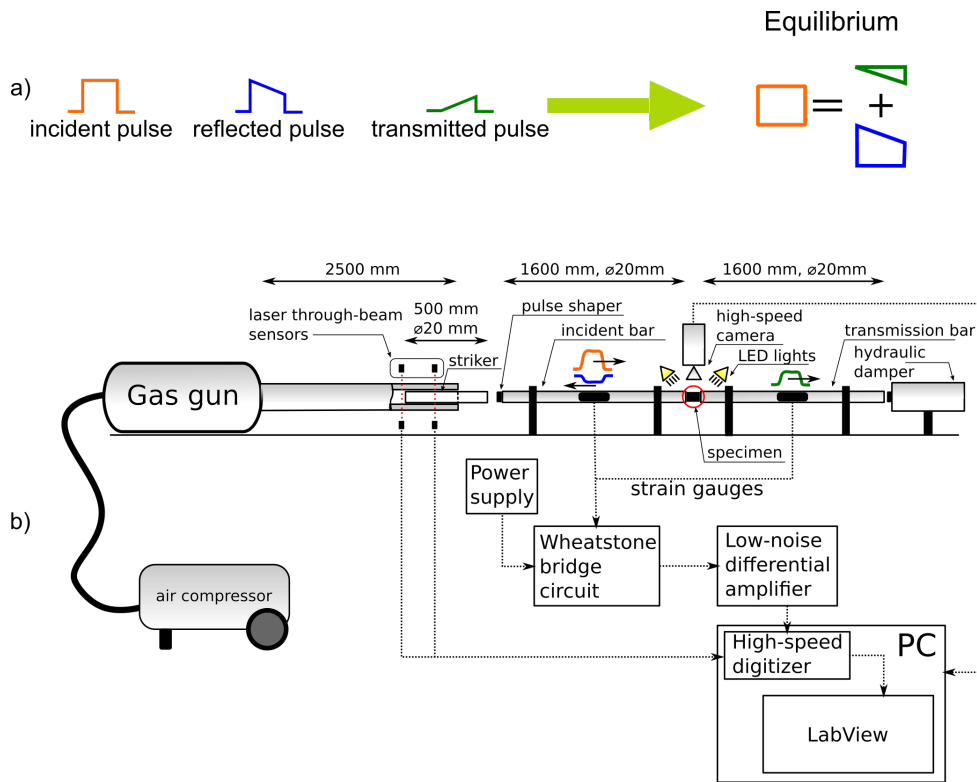


Figure 2.4: Principle of SHPB: a) fundamental principle and b) scheme of SHPB apparatus with initial instrumentation (year 2017) (image taken from **paper 1** in Appendix A).

2.4-a) has been achieved. The dynamic force equilibrium is a state when the forces in the specimen are equal to the forces on the both faces of the bars (at the place of contact with the sample). This method, the differences resulting from the real behaviour of the propagated wave, issues with the measurement of low impedance materials and cellural materials and recommendations for overcoming them are summarised by Fila [36].

2.2.2 Selected approach for the testing using SHPB at the Department of Mechanics and Materials

The following approach was chosen and applied to the SHPB apparatus at the Department of Mechanics and Materials to overcome the problems with the cellular and low impedance nature of the tested specimens [36]:

- A high-strength aluminium alloy was used as the material of the bars to get higher strain signals in comparison to steel.

- For testing specimens of the low impedance material, the bars of a visco-elastic polymethyl metacrylate (PMMA) material were used.
- Multiple strikers of different lengths were used to achieve the requested strain at a given strain-rate.
- A gas-gun with a long barrel and a high pressure capacity was used for the acceleration of the long striker for the high impact velocities.
- Optimisation of a specimen's design led to suitable stiffness to achieve an acceptable ratio between the maximum strain, strain-rate, strain wave amplitudes, inertia, friction effects and producibility.
- Using the pulse-shaping technique for the optimisation of an incident pulse.
- Application of noise reduction techniques to reduce the electromagnetic signal interference of the measured strain-gauges signals.
- Development and use of advanced calibration methods
- Redundancy of measuring points and multi-point measurements of the strain waves to the increase a precision and relevancy of the results.
- An optical inspection of the experiments using high-speed camera imaging.
- Digital image correlation technique for verification of the measured signals and advanced analysis of the deformation behaviour of the tested specimens

2.3 SHPB at the Department of Mechanics and Materials

2.3.1 Design

The SHPB apparatus in its initial version, developed and located at the Department of Mechanics and Materials, was based on the classical design introduced by [37] in 1949. The typical arrangement with three bars (striker bar, incident bar, transmission bar) and a momentum trap for the absorption of the residual energy. In our setup, the striker bar is accelerated using a gas-gun and the whole setup had already been

optimised at the design stage for testing cellular metamaterials. The setup was designed to allow the acceleration of a striker with a length of 500 mm up to the maximal impact velocity of around 50 ms^{-1} . Then, based on the calculations, the required length of the incident and transmission bar was approx. 1500 mm and the residual kinetic energy could be as high as approx. 2000 J.

The basis of our SHPB apparatus is a stiff modular frame consisting of an aluminium alloy profile (cross-sectional dimension of $180 \text{ mm} \times 90 \text{ mm}$) that is supported by the adjustable steel supports. The aluminium profile provides a mounting platform for all other parts of the setup, e.g., the gas-gun barrel, bars bearing the supports, damping elements, etc. The initial arrangement consists of two aluminium profiles (length of 2800 mm and 3500 mm) screwed together to form one long beam. The overall length (including the air reservoir, momentum trap) is approx. 8000 mm, however, due to its modular design, it can be easily extended up to the required length.

The gas-gun system consists of a steel barrel with an internal diameter 20 mm and a length of 2500 mm, a compressed air reservoir with a volume of 20 l, an electromagnetic fast-release solenoid valve (366531, Parker, USA) and safety elements and accessories. The valve is directly and coaxially connected to the barrel to maximise the performance. All the parts of the gas-gun system are designed for the maximum pressure of 16 bar. The incident and transmission bars are mounted co-axially to the frame using universal bearing supports. These supports enable the easy and fast adjustment of the bars and their replacement without damage to the strain-gauges. In the initial arrangement, the overall length of both bars was approx. 3500 mm (commonly $2 \times 1600 \text{ mm}$) with diameter of 20 mm. The 20 mm diameter was chosen as a reasonable compromise between the size of the specimen, the achievable strain and the strain-rate performance, the complexity of the setup and the manufacturing cost of the specimens. A high performance aluminium alloy (EN-AW-7075-T6) was selected as the material for the bars because it has relatively low mechanical impedance in comparison with other materials such as steel or titanium alloys. In the case of the measurements of materials with significantly lower impedance, bars made of polymethyl-metacrylate (PMMA) materials are used.

Absorption of the residual energy is provided using the momentum trap. Due to the absorption of a large amount of energy (typically hundreds of joules), the momentum trap was designed as a cascade consisting of several acting elements: short aluminium

bar clamped in the holders, an expendable wooden block and an industrial hydro-pneumatic damper. At first, the energy is dissipated during the friction contact of the clamped bar, then in the crushing or destruction of the wooden block and finally in the hydro-pneumatic damper.

In addition to the parts already described, the SHPB apparatus is equipped with a number of supporting or safety accessories and peripherals (an air compressor, polycarbonate safety shields, control electronics etc.). The overview of the SHPB setup with the marked main function parts is shown in Fig 2.5.

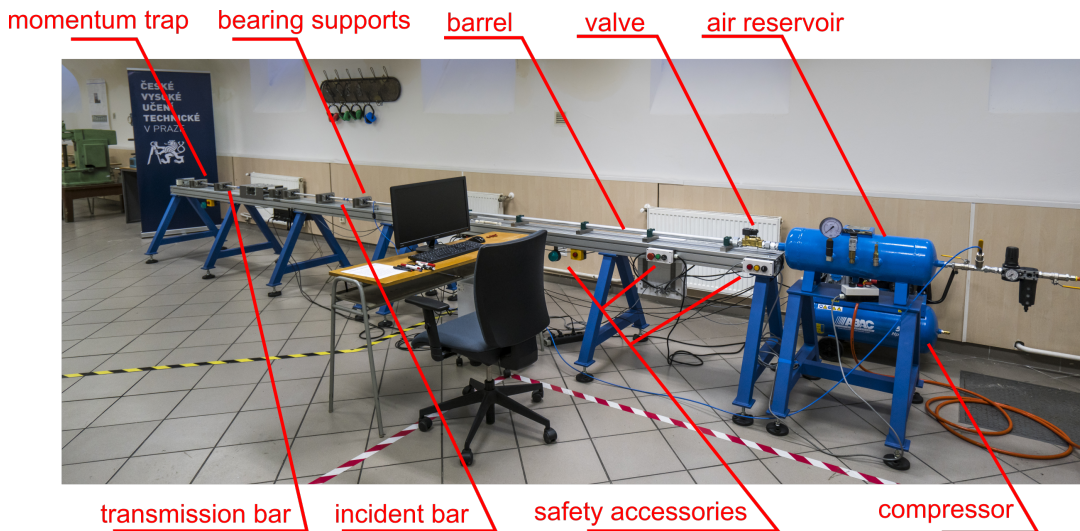


Figure 2.5: The overview of the SHPB setup located at the Department of Mechanics and Materials.

2.3.2 Instrumentation

The instrumentation of the setup is crucial for the data acquisition during the experiment. The precise and reliable evaluation of the mechanical properties and other quantities is dependent on the proper instrumentation. Instrumentation of the setup consists of several apparently independent sub-systems that work together to obtain comprehensive data from the performed experiment. Thus, the individual sub-systems are used depending on the type of the experimental test. The main parts of the instrumentation of the SHPB apparatus and its modification (located at the Department of Mechanics and Materials) are depicted in Fig. 2.6 and described in the following sections.

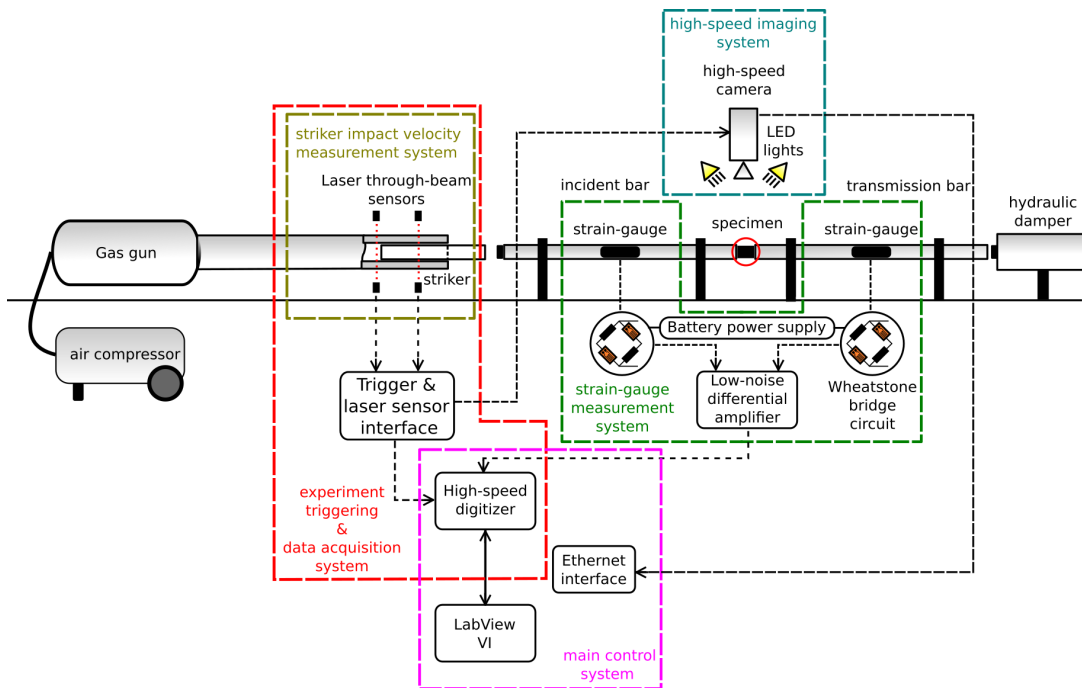


Figure 2.6: The overview of the SHPB setup instrumentation with the main sub-systems (image was originally created for [36])

■ Strain-gauges

Strain-gauges are devices used to measure the strain on an object. They are a fundamental part of the instrumentation. The vast majority of SHPB setups use strain-gauges for the direct measurement of the strain. The strain-gauges are bonded directly onto the surface of the measurement bars and measure the strain of the bars caused by the passage of an elastic wave.

The principle of the strain-gauge is based on the change of its electrical resistance due to its own deformation (deformation transferred from the measured object to the active part of the strain-gauge). However, the change in the resistance is very small and cannot be reliably detected directly. For this reason, the strain-gauges are arranged to a special electrical circuit called a Wheatstone bridge. Although other similar circuits exist, the Wheatstone bridge is the most frequently used one.

The Wheatstone bridge is an electrical circuit used to measure changes in the electrical resistance of a strain-gauge using its voltage output. From the rate of unbalance of the voltage output, it is easy to determine the change in the electrical resistance of

the strain-gauge. The bridge circuit is a very precise tool for the detection of very small changes in the electrical resistance. There are several possible arrangements of a Wheatstone bridge circuit depending on the number of active strain-gauges and measured loading mode [38]. These arrangements are: a full-bridge (four active strain-gauges), half-bridge (two active strain-gauges) and quarter bridge (one active strain-gauge).

Strain-gauges are attached to the substrate with a special glue. Two types of adhesives are used according to the application. Cyanoacrylate glue is appropriate for short time measurements while epoxy glue is used for long lasting installations. A complication of the epoxy adhesive that precludes its use in some applications is the need for high temperature curing (at about $80 - 100^\circ\text{C}$). In the case of the strain-gauge bonding on bars which are already adjusted in the SHPB setup, the use of an epoxy adhesive is excluded.

Historically, two types of strain-gauges were tested in our setup: (i) foil strain-gauges and (ii) semiconductor strain-gauges. The foil strain-gauge consists of a thin flexible insulating backing on which the strain sensitive pattern (conductive metallic wire) is applied. The main advantages of foil strain-gauges are the almost ideal linearity, the high strain capacity, ability to measure higher strain values (approx. $50,000 \mu\varepsilon$), mechanical durability and relatively simple manipulation and bonding with regard to the damage. The main disadvantage is the low sensitivity called gauge factor which requires the use of a low noise amplifier and additional steps to reduce noise in the measuring chain.

The semiconductor strain-gauge is based on the piezoresistive effect. The piezoresistive effect is the change in the electrical resistivity of a semiconductor material when a mechanical strain is applied. The change only concerns the electrical resistance, not on the electric potential (in contrast to the piezoelectric effect). The main advantage of the semiconductor strain-gauge is the higher gauge factor (more than 100 times larger than in the case of the foil strain-gauge). Due to higher output signal and higher signal-to-noise ratio, it is possible not to use the signal amplifier in the measuring chain. The crucial disadvantages are the significant non-linearity behaviour and the asymmetric response of the sensor in tension and compression. The other main disadvantages are the very limited strain capacity (approx. $2,000 \mu\varepsilon$) and more complicated manipulation and bonding due to the fragility of the sensor itself.

Although we tested two types of semiconductor strain-gauges in our SHPB setup: AP170-3-100/BP/CuSn N-sort (VTS Zlin, Czech Republic) and AFP-500-090 (Kulite, Japan), only the foil strain-gauges were used for experimental campaigns. Significantly, the non-linearity behaviour together with the asymmetric response of the sensor and limited strain capacity were key limitations of their application in the Hopkinson bar setup, particularly for testing cellular metamaterials. In our setup, foil strain-gauges in the half-bridge arrangement were commonly used at the individual measurement points. In the half-bridge arrangement, a pair of strain-gauges of the same type is bonded at the same distance from the face of the bar with a half-revolution angular offset. This arrangement is capable of reducing the eventual minor bending of the bar during the experiments and, in the case of the pure tensile or compression loading mode, amplifying the output signal twice. During all our experimental campaigns, the incident and the transmission bar of the SHPB setup were equipped with foil strain gauges (3/120 LY61, HBM, Germany) with a strain sensitive pattern length of 3 mm. The relatively small length of the selected strain gauges enabled high precision strain measurements (integration of the strain wave along the length of the strain gauge) with respect to the wavelength of the strain wave. The strain-gauges were bonded to the surface of the bars by special cyanoacrylate bonding (Z70, HBM, Germany) and cured for at least 24 hours. To maximise the signal-to-noise ratio, each strain-gauge circuit was independently powered using a battery pack (with an excitation voltage of 3 V), which is part of a custom strain-gauge control unit [30], to decrease the noise of strain-gauge signal to a minimum. Due to the small sensitivity of the foil strain gauges, it was necessary to use an active differential low noise amplifier (EL-LNA-2, Elsys AG, Switzerland) with a gain 100. The strain-gauge measurement unit was connected to the amplifier using specially designed twisted-pair cables to protect the raw strain-gauge signal from noise. The bonding process, circuitry and noise reduction techniques are described in more detail in [39]. The amplified strain-gauge signal was sampled and recorded using a pair of a high speed 16-bit digitisers (PCI-9826H, ADLINK Technology, Inc., Taiwan) with maximal 20 MHz sample rate. The SHPB apparatus with the above-mentioned instrumentation is shown in Fig. 2.7.

The position of the strain-gauges on the measurement bars may vary for different applications and setups. A basic arrangement is a single measurement point (a pair of strain-gauges connected in a half-bridge configuration) in the middle of each bar.

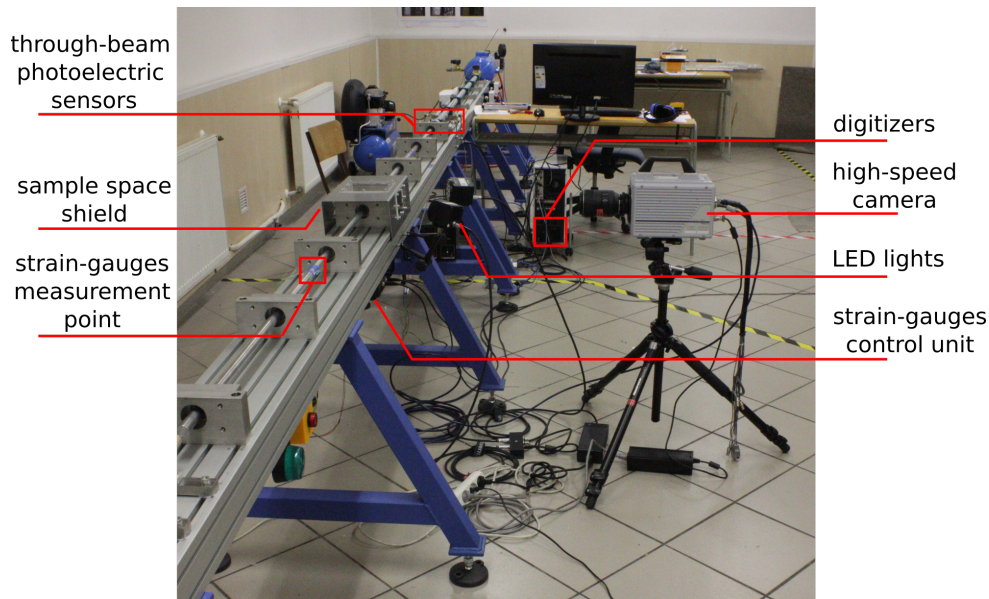


Figure 2.7: Initial instrumentation of the SHPB setup (image taken from **paper 2** in Appendix A).

The location of the strain-gauges is the optimal trade-off between the complexity of the system (the number of strain-gauges - cost and mounting time), the prevention of the wave superposition at the measurement point and the quality of the signal. We used this arrangement in several experimental campaigns. In the case of more complex experiments (more complex samples, high impact velocities, bars of PMMA material, using a pulse-shaping technique to prolong the wavelength of the pulse, etc.), the arrangement of the strain-gauges was adapted. The number of the measuring points and their positions on the bars were modified. The proper modification of the measurement points leads to higher reliability, data redundancy (backup signals), application of advanced methods of the setup calibration and wave decomposition techniques. Detailed information can be found in [36]. In Fila [36], several rules for the position of the strain-gauges were drawn:

- The strain-gauges have to be placed at a distance of at least $10 \times$ the diameter from the bar's face.
- The first transmission strain-gauge should be placed as close to the specimen as possible to obtain the most reliable record of its deformation behaviour and to eliminate or reduce the wave superposition with the backward propagating wave.

- As the attenuation and wave dispersion are negligible when the aluminum alloy bars with an optimal pulse-shaper are used, the travel distance of the pulses can be relatively long (units of meters).
- The travel distance of the pulses when using of visco-elastic PMMA bars has to be as short as possible (< 1000 mm) due to the strong dispersion behaviour of wave.

The scheme of variants of the strain-gauge arrangement used during the experimental campaigns over time are shown in Fig. 2.8.

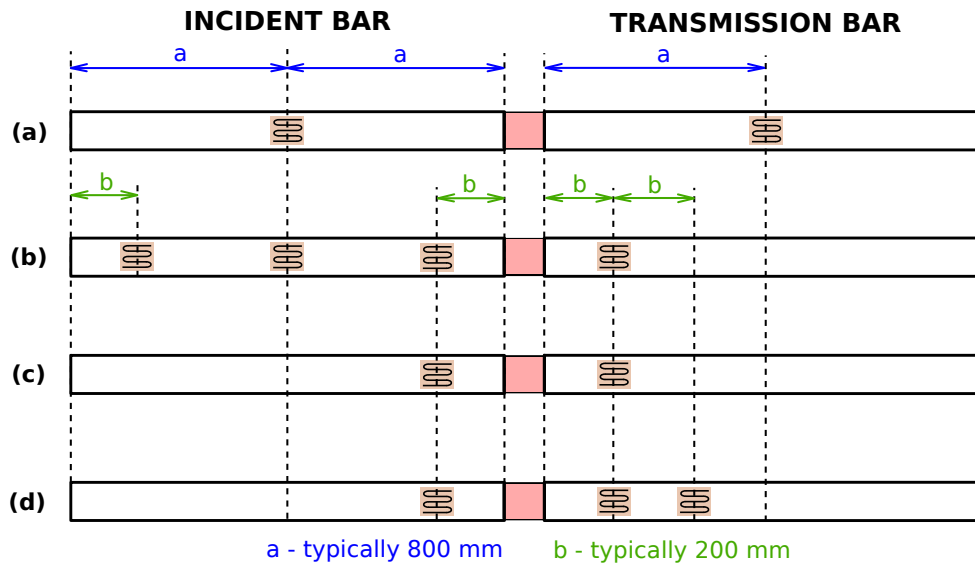


Figure 2.8: The variants of the strain-gauge arrangement used during the experimental campaigns: (a) standard Kolsky bar with strain-gauges in the middle of the bars, (b) multi-point measurement with the SHPB, (c) direct impact OHPB bar, (d) direct impact OHPB with visco-elastic bars (image taken from [36]).

After each strain-gauge arrangement modification or before the experimental campaign, it is highly appropriate to perform the quasi-static force calibration of the strain-gauges to evaluate the setup precision. A quasi-static force calibration is performed as the uni-axial compression of the bars. A piston mounted on the end of the experimental setup loads both bars (arranged in line) and the reaction force is measured using a standard load-cell (U9C, HBM, Germany) which is mounted co-axially between the bars. The measured force of the load-cell is compared with the force calculated base of the strain-gauge signal and its precision is evaluated. A common error of the individual pair of foil strain-gauges is up to 2 – 4% of the measured value.

■ Impact velocity measurement and triggering of acquisition

The measurement of the impact velocity of the striker bar is important for the estimation of the strain wave amplitude because it is directly proportional to the impact velocity. Based on the known value of the impact velocity, an initial estimation of the experimental validity can be made. Moreover, in the case of negligible attenuation over a short travel distance (aluminium alloy elastic bars), the maximum strain calculated from the impact velocity value is comparable with the signal from the strain-gauges (the error is in the range of a few percent). In the case of the OHPB modification, the knowledge of the value of the impact velocity is crucial to evaluate of the test.

Two pairs of laser through-beam photoelectric sensors (FS/FE 10-RL-PS-E4, Sensopart, Germany) are installed on the barrel of the SHPB at a fixed distance from each other. Each assembly includes a laser beam transmitter and its receiver, creates an optical gate together. When the laser beam is interrupted by a foreign object (in our case by the striker) in its path (oriented perpendicularly to the barrel), the voltage output suddenly changes and generates a pulse. This pulse is detected using same the digitiser as in the case of the strain-gauge signal. Thus, it is possible to calculate the striker velocity from measured time (and known distance between the optical gate) of the falling edge of the pulses of the first and second optical gates. Because the striker bar is accelerated through the whole length of the gas-gun barrel, for the higher precision of measured impact velocity (higher precision of estimation of strain amplitude), we deduced a simple constant acceleration analytical model based on the measurement using three optical gates.

The second usage of the optical gate is triggering of the data acquisition. As the output from the optical gates is digitised by the same digitiser device (different channel) as the signal from the strain-gauges, there is a fixed time stamp in the record. The pulse generated by the optical gates is also used to trigger other devices, e.g., high-speed cameras, a high-speed thermal imaging camera, etc. Then, the synchronisation of the signal from these relatively independent devices can be performed on the basis of the fixed time stamp in all the records. The scheme of the experimental triggering and the impact velocity measurement sub-system is shown in Fig. 2.9.

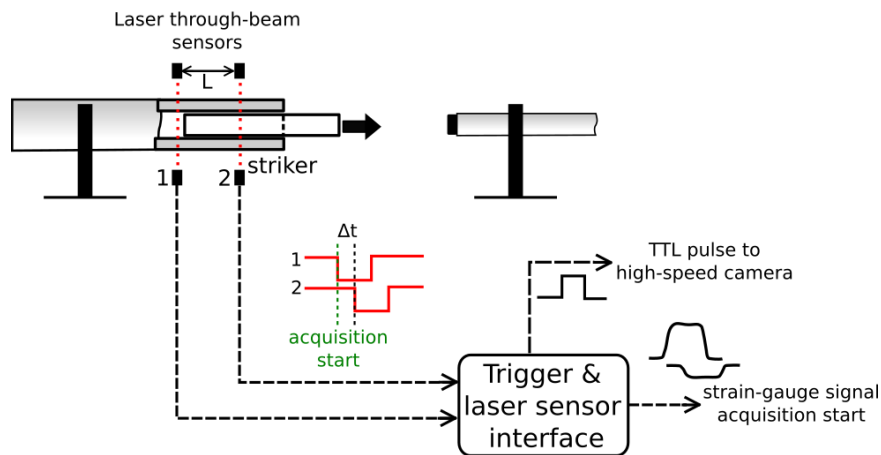


Figure 2.9: The scheme of the experimental triggering and impact velocity measurement sub-system (image was originally created for [36])

High-speed imaging

During the experimental campaigns in our laboratory, the high-speed imaging has become an integral part of all the performed experiments. The high-speed imaging in our setup has two main functions: i.) inspection technique to confirm the correct process of the experiment, ii.) advanced analysis of the experiments using the digital image correlation (DIC) technique. The high-speed imaging sub-system consists of a high-speed camera, a high performance lighting system, a camera positioning stage and a control PC.

A high-speed camera is a device capable of capturing images with exposures of less than $1/1000$ s or frame rates in excess of 250 fps. The images are captured using a CMOS image sensor and they are usually stored in the internal memory. In the first years of the SHPB testing in our laboratory, a Fastcam SA-5 (Photron, Japan) high-speed camera was used to observe the experiment. Currently, the laboratory is equipped by a pair of high-end Fastcam SA-Z 2100K (Photron, Japan) high-speed cameras. The pair of cameras has significantly expanded the possibilities of the performed experiments. The first camera can capture sample details for further strain evaluations using the DIC technique, while the second camera can capture the entire scene for the inspection of the experiment or can record the details of another side of the sample for the strain evaluation on two faces. Both types of cameras are capable of capturing the SHPB experiment with sufficient resolution and frame-rate in the range of 50 – 300 kfps and

both cameras have a TTL trigger capability to start the acquisition using our triggering sub-system. The main parameters of both types of cameras are summarised in Tab. 2.1.

Parameter	Fastcam SA-5	Fastcam SA-Z
Max. frame rate	$1 \cdot 10^6$	$2.1 \cdot 10^6$
Max. resolution [px]	1024×1024	1024×1024
Max. full-frame speed [fps]	7000	20000
Light sensitivity [–]	10000	50000
Dynamic Range	12-bit	12-bit
Sensor size [mm]	20.48×20.48	20.48×20.48
Pixel size [μm]	20×20	20×20
Min. shutter speed [ns]	1000	159
Internal storage [GB]	16	32
TTL triggering	yes	yes

Table 2.1: The main parameters of both types of high-speed cameras.

Because the high-speed imaging is very sensitive to the proper illumination of the scene, suitable illumination has to be used. In our laboratory for the SHPB testing, two high performance LED illumination systems are available: i.) a pair of high intensity Constellation 60 (Veritas, USA) LED lights, ii.) a pair of high intensity Multiled QT (GS Vitec, Germany) LED lights. Both illumination systems are able to properly illuminate the scene during the high-speed imaging.

The positioning and holding of the high-speed camera in a fixed position is performed by a standard tripod or the in-house motorised remote-controlled hybrid optics positioning system (HOPS) [40]. The high-speed imaging sub-system also includes transparent shields made of a high performance non-shattering polycarbonate with a thickness of 5 mm to protect the operators and equipment. The scheme of the high-speed imaging sub-system is depicted in Fig. 2.10. The high-speed imaging sub-system is also shown in Fig. 2.11 and partially in Fig. 2.8.

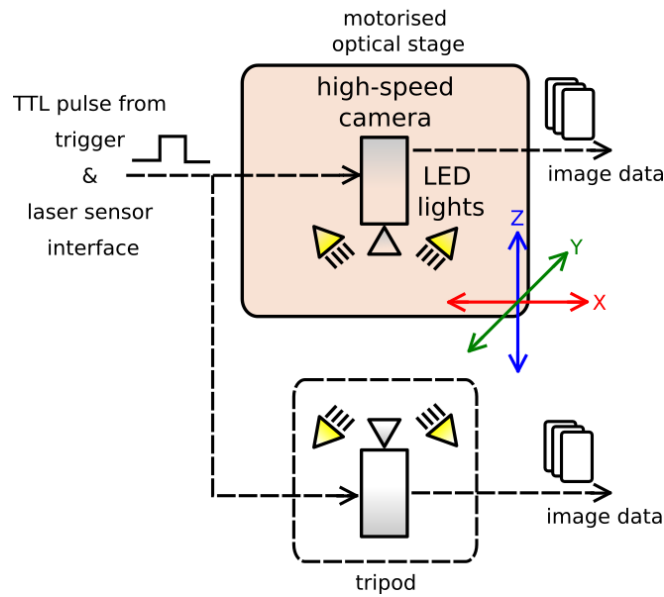


Figure 2.10: The scheme of the high-speed imaging sub-system (image was originally created for [36])

■ High-speed thermography

Outside the mainstream of the experiments with auxetic metamaterials, supplementary methods were used to obtain additional data about the deformation behaviour of the structures. The most important supplementary method employed during the experimental campaigns was the testing of auxetic structures at elevated and reduced temperatures. For this experimental campaign ¹, the usual instrumentation of the SHPB was extended by a high-speed thermal imaging camera and an in-house developed a cooling and a heating stage.

A high-speed thermal imaging camera SC7600 (FLIR, USA) equipped with an actively cooled focal plane array (FPA) InSb photon-counting detector and a 50 mm f/2 silicon-based lens with an antireflection coating were used for the thermal imaging during the impact test. The camera detector operates in the spectral range of $1.5\text{--}5.0\ \mu\text{m}$ (short-to-medium wavelength infrared band—SWIR to MWIR) with 640×515 px full frame resolution. Thermal imaging was used for the inspection of the specimen's temperature before the experiment and to estimate the temperature increase and heat distribution during the impact.

¹this experimental campaign relates **paper 3** in Appendix A

The high-speed thermal imaging system was calibrated for a temperature range of -5 to 300 °C. To maximise the frame rate of the camera, the image resolution was down-scaled and set to 96×44 px by sensor image windowing. In this configuration, the maximum frame rate of approx. 2 kfps was achieved. The safety shatterproof polycarbonate specimen shield was modified (window mounting hole was made) and attached by a MgF_2 protective window to make the infrared imaging possible and safe for the high-speed thermal imaging system.

The heating stage includes ceramic heating elements (output power of 40 W) that are commonly used for the construction of hotends (printing heads of thermal 3D printers). The heating elements were attached to movable aluminium clamps to provide close contact with the specimen to ensure the best possible heat transfer. The clamps were operated using a servo-based actuator that allows the quick remote control removal of the heating elements just before the impact. The servo system was controlled by in-house developed electronics and the temperature was regulated using open-loop control circuitry with pulse width modulation (PWM). The heating stage was able to heat the sample to approximately 200 °C.

The cooling setup was designed as a gas cooling system using carbon dioxide (CO_2) as an active cooling medium. The cooling stage consisted of a pressure vessel with a volume of 6.7 L containing 5 kg of liquid CO_2 , a thermally isolated box containing dry ice with a temperature of -78 °C and a piping system. Inside the thermally isolated box, a low temperature compatible piping coil was submerged in a mixture of dry ice and 1 L of pure ethanol. The cooling process began with the release of the valve, the gas from the reservoir was released at a pressure of 1.5 MPa and was rapidly cooled down by contact with the ethanol and dry ice mixture. The super-cooled gas was then led directly to the specimen area using hoses and nozzles. The cooling stage reached a sample temperature of -27 °C before the start of the experimental procedure. A temperature change to approx. -5 °C of the specimen at the time of the impact was given by the thermal conductivity of the samples leading to a rapid rise in the temperature in the time delay between the cooling process and the moment when the impact could be performed.

Details of both stages and the overall experimental setup used to test auxetic structures at elevated and reduced temperatures are shown in Fig. 2.11.

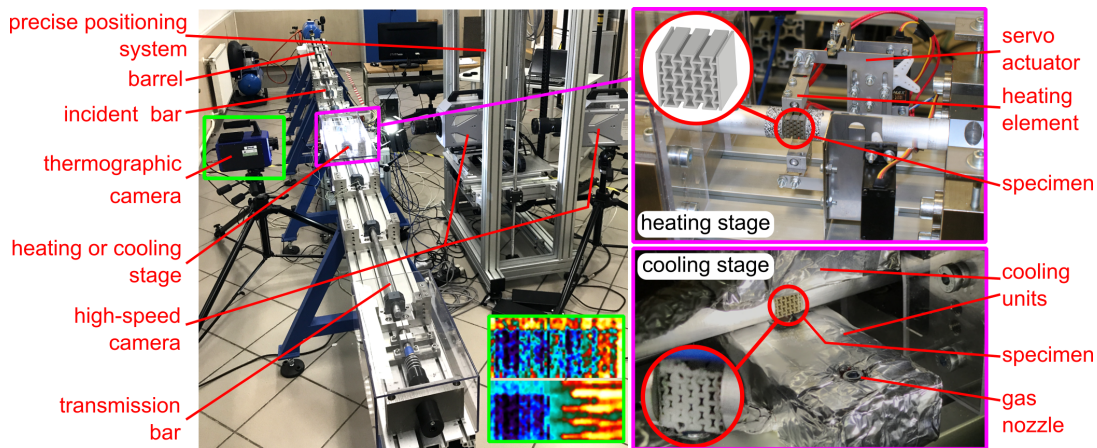


Figure 2.11: Details of the heating/cooling stage and the overall experimental setup used to test auxetic structures at elevated and reduced temperatures (image taken from **paper 3** in Appendix A).

Digital Image Correlation

The digital Image Correlation (DIC) is an optical method for tracking changes in digital images. In our application, the DIC technique is used for the evaluation of changes in the images acquired using the high-speed imaging. As the high-speed camera observes the sample area, the displacements of the bar's ends or the displacement of the individual cells in the specimens can be evaluated. Based on the evaluated displacement, the impact velocity or strain field on the sample surface can be determined. From the obtained displacement/strain field, it is possible to investigate, e.g., the auxetic behaviour of the sample. In addition to quantities relating to the sample, DIC can also be used to create "virtual strain gauges" to determine the strain (direct comparison with the strain measured using strain-gauges) and particle velocity during the experiment [36].

The basic principle of DIC is as follows: The DIC procedure begins by overlying the region of interest with a virtual correlation pattern that forms a set of points. To calculate the displacement, the location of every pixel is then tracked between each pair of images (high-speed images in case of the SHPB) in the series of images capturing the deforming/moving object. To find the exact solution of the problem, subsets of pixels are used. The subset is defined as a square shaped area with dimensions $(2M + 1) \times (2M + 1)$ pixels formed around a centroid, which is the location of the

individual tracked point $P(x_0, y_0)$ in the correlation pattern. The size of the subset (value of parameter M) influences the analysis in two contradictory ways. The subset has to have sufficient dimensions to contain a unique pattern of image (this is the reason why the bars or sample surface is covered by a random speckle pattern). It can be assumed that the probability of the uniqueness increases with the size of the subset, but with an increasing size, the computational costs of the correlation procedure also increases.

To find the deformed subset, the location of the pattern from the reference subset in the deformed image is established from the extremum of the correlation coefficient calculated using the selected criterion. In our custom DIC tool, the correlation coefficients were estimated using a two-step procedure in a pixel level and consequently in a sub-pixel level to determine the displacement vectors more accurately. On the pixel level, the sum-squared difference (SSD) criterion was used. On the sub-pixel level, the Lucas-Kanade algorithm based on the zero-normalised SSD (ZNSSD) criterion was used [41]. For more details about used the custom DIC algorithm see [31, 42, 43]. An example of using DIC for the estimation of longitudinal strain and Poisson's ratio of 2D re-entrant honeycomb auxetic lattice in the SHPB experiment is illustrated in Fig. 2.12.

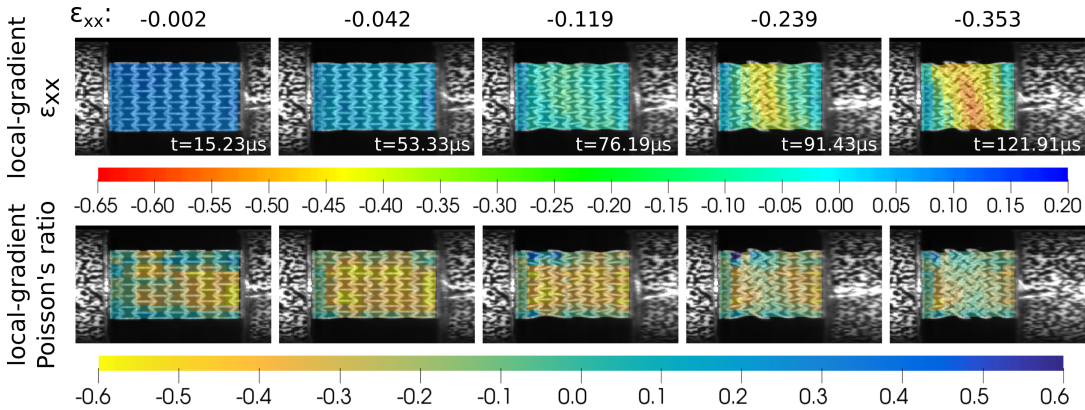


Figure 2.12: Image sequence showing the deforming 2D re-entrant honeycomb auxetic lattice during impact with the mapped local-gradient results of the longitudinal strain and Poisson's ratio. (image taken from **paper 2** in Appendix A).

An example of the typical value of the mean correlation coefficient throughout the grid plotted against the strain, and an example of the correlation grid in the representative states of deformation (no deformation, auxetic behaviour, and densification) of the 2D

re-entrant honeycomb structure are shown in Fig. 2.13.

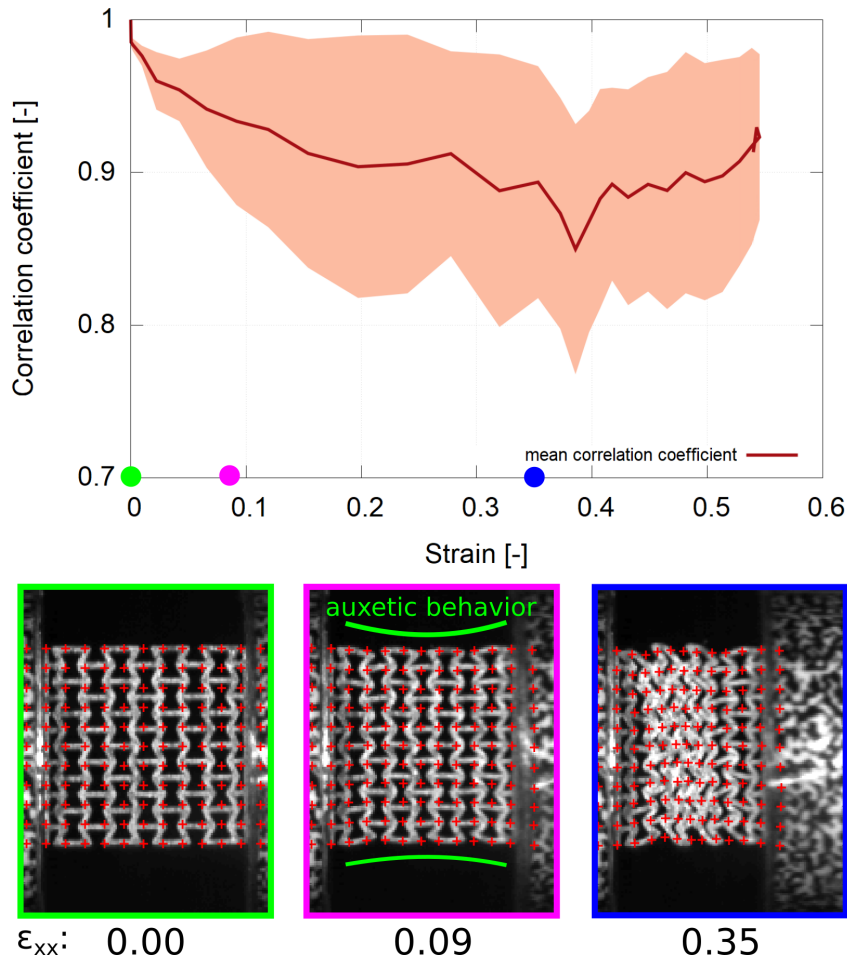


Figure 2.13: Mean correlation coefficient throughout the grid plotted against the strain with the highlighted representative states of deformation (no deformation, auxetic behaviour, and densification) of the 2D re-entrant honeycomb structure. (image taken from **paper 2** in Appendix A).

2.4 OHPB at the Department of Mechanics and Materials

Open Hopkinson Pressure Bar (OHPB) is a advanced and novel method for the high strain-rate testing of materials which was firstly introduced by Govender [44] in 2016.

The OHPB technique is a derivative of a direct impact Hopkinson bar technique. The development of the OHPB method has been one of the main task of our laboratory work in recent years. **Paper 4** in Appendix A describes the developed OHPB apparatus in our laboratory and the initial experimental campaign with metal foam samples and auxetic structure samples (hybrid and conventional)

The motivation for the design and commissioning of the OHPB apparatus was to overcome the problems and limitations of the SHPB setup, especially with regard to the testing of soft cellular materials. The OHPB method also has its disadvantages and is definitely not a complete replacement of the SHPB setup, but rather an alternative for testing a specific type of material. The main reasons for the design of the OHPB apparatus were to overcome the main limitations summarised in [36] and described below:

- The strain in the specimen is directly proportional to the length of the striker and its impact velocity. Therefore, a higher sample deformation can be obtained with a higher impact velocity (higher strain-rate) or a longer striker or both. The striker is a moving object and its length is limited by friction, the housing and performance of the gas-gun. For these reasons, the SHPB has its minimum strain-rate limit.
- The duration of the experiment is limited by the wavelength of the strain wave pulse and the wave propagation velocity. Thus, the deformation of the sample must occur in a short time window.
- The amplitudes of the incident, reflected and transmission pulse are disproportionate in the case of testing the cellular materials. The transmission pulse commonly has a very low amplitude in comparison to the incident pulse. This disparity in the amplitude can lead to noisy oscillations hiding the true state of the force equilibrium.
- Oppositely propagating strain waves cause a wave superposition that makes the evaluation from the strain-gauges mounted close to the specimen difficult.
- The validity of the SHPB experiment is strongly dependent on the state of the force equilibrium. Equations for the evaluation of the results, respecting the standard theory, are valid only during the time period when the force equilibrium occurs.

- The necessary application of correction methods of the wave dispersion effects in use of low-impedance visco-elastic bars (e.g. PMMA). These corrections are not generally valid, they are valid only under certain conditions.

■ 2.4.1 Basic principle

The principle of the OHPB method (described in detail in **paper 4** in Appendix A.) is directly derived from the Direct Impact Hopkinson Bar (DIHB) methods. The schemes of both the forward and reverse DIHB method and the OHPB are shown in Figure 2.14.

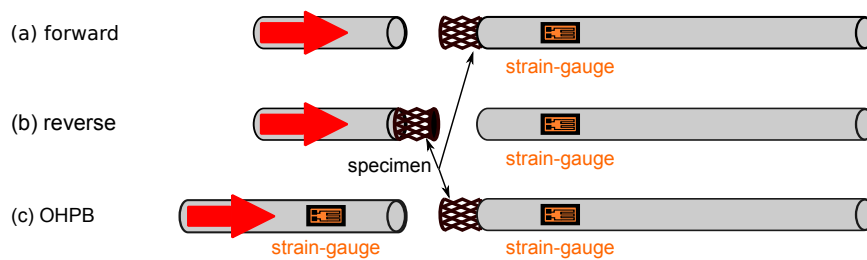


Figure 2.14: Principle of the forward DIHB (a), reverse DIHB (b), and OHPB (c). (image taken from **paper 4** in Appendix A).

From these schemes, it is obvious that, in the case of the forward and reverse DIHB, only the transmission bar is instrumented with a strain-gauge. The OHPB consists of two measurement bars (incident and transmission), unlike the DIHB, both of which are instrumented with strain-gauges. The incident bar is directly inserted into the barrel of the gas-gun and simultaneously serves as the striker bar. The tested specimen is mounted on the impact face of the transmission bar. During the experiment, the incident bar is accelerated using the gas-gun and directly impacts the specimen. The impact generates the strain waves in both bars. The pulses propagate from the specimen to the free ends of the bars. Then, the pulses are reflected and travel back to the specimen. The end of the experiment occurs when the backward-propagating waves reach the strain-gauges. At this point, the strain-gauges produce superposed signals. As the waves propagate from the specimen, they have an approximately identical shape. The beginning of the transmission pulse is delayed in comparison with the incident pulse. This delay is caused by the longer path as the strain wave has to pass through the specimen (similarly to the SHPB). The diagram showing the strain wave

propagation in the OHPB setup is shown in Fig. 2.15.

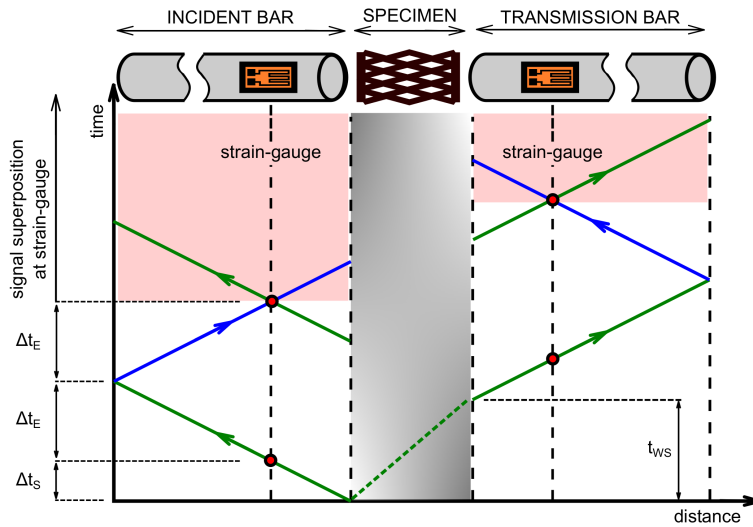


Figure 2.15: Diagram showing the strain wave propagation in the OHPB setup (image taken from **paper 4** in Appendix A).

The forces and displacements on the respected faces of the bars can be calculated using the strain-gauge signals [44]. For the detailed calculation procedure see **paper 4** in Appendix A. From the derived equations, it is obvious that the evaluation of the actual length of the specimen (strain) is strongly dependent on the initial impact velocity v_0 . This fact highlights the key importance of the accurate measurement of the initial impact velocity with high precision (by, e.g., the DIC) unlike in the SHPB method, where the impact velocity serves as a secondary parameter useful for the verification of the results.

2.4.2 Design of OHPB

Our SHPB experimental setup has been adapted for the OHPB apparatus and all the major parts of the SHPB setup were used in this OHPB modification. Due to sharing the major parts, SHPB setup can be modified to the OHPB setup relatively quickly, and vice versa. This modularity allows one to choose the optimal apparatus and method for a given type of sample.

In our design (unlike [44]), the incident bar is not fully loaded in the barrel of the gas-gun system, but its frontal part always protrudes from the barrel. The reason for this approach is that the strain-gauges are mounted on the protruding part of the

incident bar. Unlike other concepts, the guiding of the incident bar is not provided only by the barrel, but by a linear guidance system. This concept allows one to maximise the stroke of the gas-gun and increase the performance of the apparatus. The scheme of the OHPB apparatus according to our concept is depicted in Fig. 2.16.

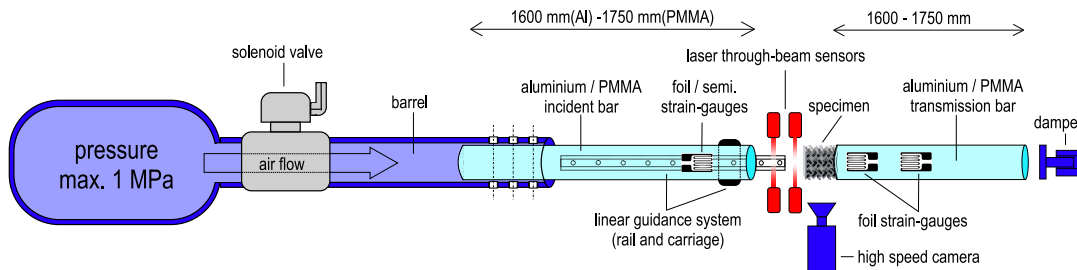


Figure 2.16: The arrangement of the OHPB experimental setup: uni-axial compression with the aluminium alloy/PMMA bars (image taken from **paper 4** in Appendix A).

Linear guidance system of the incident bar

The guiding of the incident bar during the acceleration is provided by a low mass/low friction linear guidance system. The linear guidance system consisted of a linear motion guide with a high performance polymeric slider bearing (drylinT, IGUS, USA) and a rail with a length of 1200 mm. The incident bar front-end was attached by a friction contact clamp to link the incident bar to the carriage, while the back-end of the incident bar is loaded in the gas-gun barrel. During the calibration testing, it was found that if the friction clamp is adjusted properly, it did not bring any distortion to the incident wave. The frontal part of the incident bar, which protrudes from the barrel, is used for the strain-gauge mounting at a typical distance of 200 mm from the impact face.

Gas-gun system

For the acceleration of the incident bar, the identical gas-gun system as in the case of the SHPB apparatus (see section 2.3.1) was used. The only change is the absence of the system used for the loading of the striker bar (reverse air pressure supplied by a separate hose), which is not needed in the case of the OHPB. The incident bar is loaded manually into the barrel.

■ Instrumentation

As the OHPB apparatus is a modification of the SHPB setup, the whole instrumentation can be identical. All the equipment and sensors have been used in the same way as described in 2.3.2. Small changes, especially in the placement of equipment and sensors, were performed. Due to the longer deformation process the optical gates are as close to the specimen as possible to tighten the triggering of the experiment. As mentioned above, the proper evaluation of the OHPB experiment is strongly dependent on the accuracy of the impact velocity determination. To reduce the acceleration effect between the pair of optical gates, they are mounted as close to each other as possible. Moreover, the position and the trigger of the high-speed camera are adjusted in order that the camera also records the movement of the incident bar in the pre-impact phase. Thus, the DIC technique can be used for the precise evaluation of the initial impact velocity. The adjusted positions of the high-speed camera and the optical gates allow for the determination of the impact velocity by two independent systems which is advantageous in the case of the OHPB. A modification was also performed in the case of the momentum trap because the moving mass impacting the specimen (long incident bar instead of a relatively short striker) is usually higher and the momentum trap is more stressed than in the SHPB apparatus. The experimental setup with the aluminum alloy bars/PMMA bars and the important parts of the OHPB arrangement and instrumentation is shown in Fig. 2.17 and Fig. 2.18

■ Performance

The compressor dedicated to the gas-gun system has a maximal pressure of 10 bar (all components of the gas-gun system are designed at 16 bar). At this pressure level the gas-gun system is capable to accelerate the incident bar:

- material: aluminum alloy, length: 1600 mm → max. impact velocity approx. $18 - 20 \text{ m} \cdot \text{s}^{-1}$
- material: PMMA, length: 1750 mm → max. impact velocity approx. $25 - 30 \text{ m} \cdot \text{s}^{-1}$

The strain-rate achieved at this maximum pressure level is at the bottom range of the strain-rates achievable by the SHPB. This fact confirms that the OHPB technique is

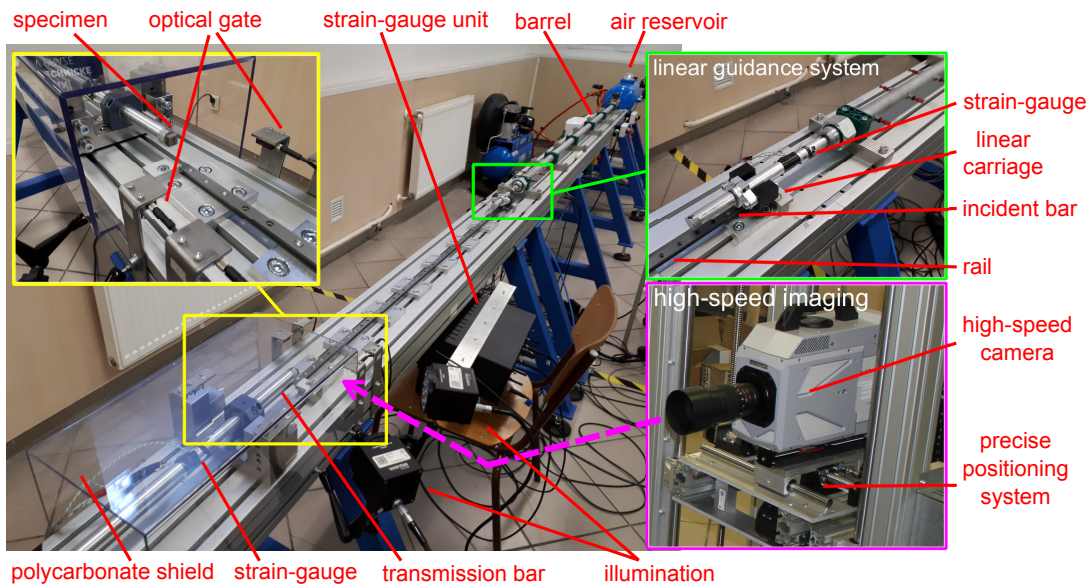


Figure 2.17: The experimental setup with the aluminium alloy bars and the important parts of the OHPB arrangement (image taken from **paper 4** in Appendix A).

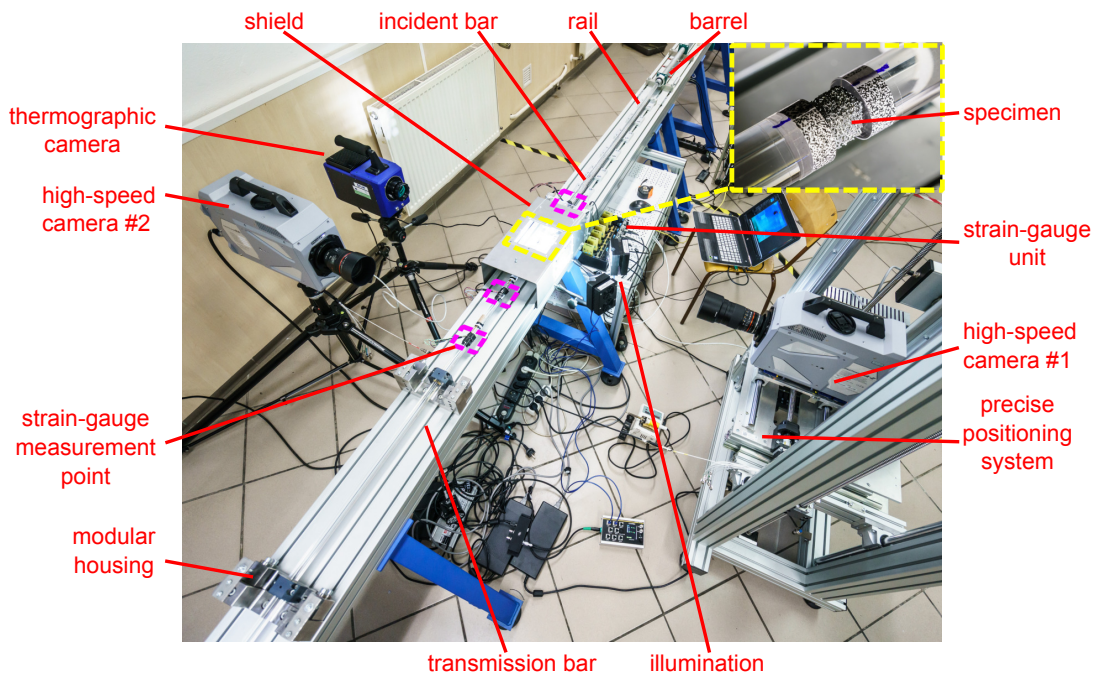


Figure 2.18: The experimental setup with the PMMA bars during the experimental campaign.(image taken from **paper 4** in Appendix A).

not a better successor to the SHPB technique, but rather an additional experimental

technique for testing at strain-rates between the drop-weight test and the SHPB. The lower strain-rate, in the case of the OHPB, is mainly caused by the mass of the impactor (incident bar). The impact energy depends directly on the mass and the square of the impact velocity. As the impact velocity decreases, the impact energy decreases dramatically. Due to the lower impact energy margin in the experiment, the strain-rate dramatically drops.

■ Comparison with SHPB

The OHPB method has several advantages in comparison to the SHPB and the direct impact Hopkinson bar methods. On the other hand, it also has several disadvantages. The main advantages are: the higher achievable strain of the specimen, the long time period without the superposition, the strain wave measurement from both sides of the specimen, approx. the same level of the measured signals in both bars, the dynamic equilibrium in good quality. The main disadvantages are: more complex assembly, high sensitivity of determining the correct value of the impact velocity to the accuracy of the results, the possibility of an unstable strain-rate during the experiment due to a significant decrease in the impact velocity (and the impact energy).

■ 2.4.3 Penetration test

Penetration or dynamic indentation is one of the important dynamic loading modes. During the penetration test the specimen is impacted with an object with a cross-section smaller than the cross-section of the specimen. As the penetrating object passed through the specimen, its kinetic energy is dissipated in the material. This loading mode is crucial for the description of the crushing behaviour of the investigated material under the impacting object. **Paper 5** in Appendix A describes the developed setup for the penetration testing in our laboratory and the initial experimental campaign with three types of samples: i.) closed-cell aluminum alloy foam, ii.) an APM foam, where aluminium spheres are coated by polyamide, and iii.) an hAPM foam, where aluminium spheres are embedded in an epoxy.

Based on our experience from previous studies investigating the strain-rate sensitivity of cellular materials using the Hopkinson bar a DIHB experimental setup with advanced instrumentation for the low to medium velocity penetration of cellular materials has been developed in our laboratory. For purposes of penetration testing, the OHPB

experimental setup introduced in Section 2.4 was modified. The penetration setup used aluminium bars made of a high-strength aluminium alloy (EN-AW-7075-T6) with a diameter of 20 mm. The gas-gun system is capable of accelerating the incident bar (length of 1600 mm) to an impact velocity of approx. 20 ms^{-1} corresponding to an impact energy of approximately 300 J. The front face of the transmission bar (length of 1600 mm) was attached to the specimen's supporting plate with a diameter of 60 mm and thickness of 40 mm using a bolted joint. The diameter of the supporting plate corresponded to the diameter of the samples. A pair of strain-gauges in a half-bridge arrangement were bonded at a distance of 200 mm from the specimen on both adjacent bars. Amplifying, sampling and recording the strain-gauges signals were performed using the same instrumentation as in case of SHPB/OHPB (see Section 2.3.2). The

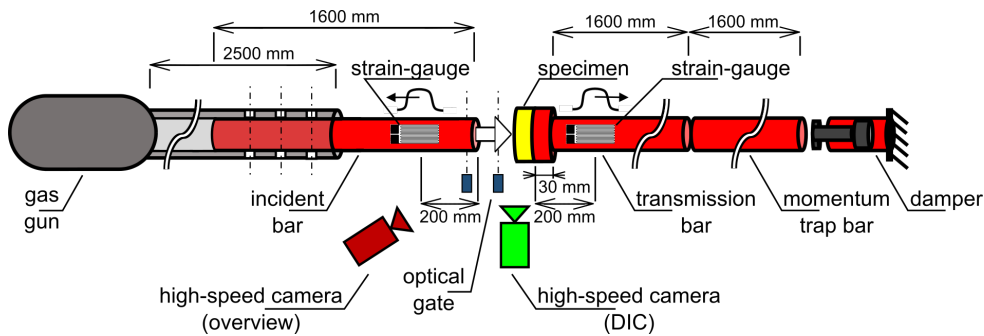


Figure 2.19: The scheme of the OHPB modification for the penetration testing.

optical gates were placed in front of the tested sample and a signal interruption of the first gate was used for the triggering and time synchronisation of the experiment. Observation of the penetration test was performed using a pair of high-speed cameras (Fastcam SA-Z, Photron, Japan). The first "overview" camera (recording speed of 20 kfps, resolution of 1024×1024 pixels) served as an inspection of the specimen's front face during the impact. The second "DIC" camera (recording speed of 180 kfps, resolution of 768×112 pixels) was oriented perpendicularly to the setup's longitudinal axis and observed the ends of both bars. The images from the "DIC" camera were post-processed using a custom DIC tool for the evaluation of the displacements of both bars, the initial impact velocity and the longitudinal strain on the surface of the penetrated specimens. The proper illumination of the scene was performed using a high-performance LED illumination system (Multiled QT, GS Vitec, Germany). The scheme and assembly of the fully instrumented setup for the penetration testing

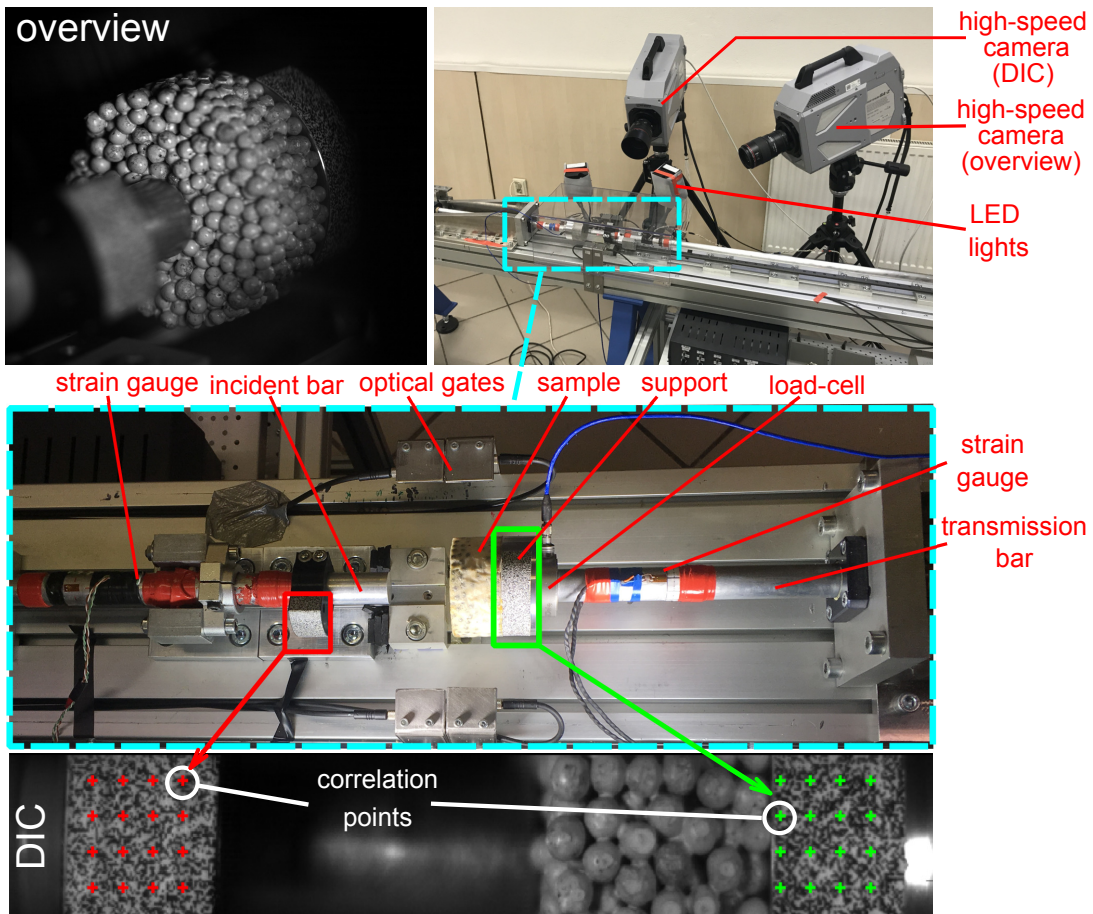


Figure 2.20: The OHPB experimental setup: High-speed cameras, their field of view and an example of the grid of correlation points established in the incident and transmission bar. (image taken from **paper 5** in Appendix A).

are shown in Fig. 2.19 and Fig. 2.20, respectively. For a detailed description of the performed penetration experimental campaign, see **paper 5** in Appendix A.

Chapter 3

Future work

The previous chapters and the collection of the selected papers attached in Appendix A demonstrate the experimental work in the area of testing of cellular metamaterials over the last few years. In this time period, all aspects of the experimental work (experimental devices, instrumentation, evaluation of the results, etc.) were improved. The initial SHPB apparatus was gradually improved and other in-house developed equipment (heating/cooling stage, strain-gates control unit, etc.) were developed. The experience gained over the years has enabled the design of more advanced and sophisticated experimental techniques (OHPB, penetration testing) that push the possibilities of the materials research even further. Currently, two very unique and advanced experimental facilities are being prepared in the laboratory: i.) a modular high-strain rate testing setup with high-speed X-ray radiography imaging and ii.) an intermediate strain-rate testing setup with a high power X-ray source for high speed X-ray radiography and tomography imaging. Both of the setups have a high potential to expand the knowledge about the materials at several areas, i.e., behaviour of the structures during penetration, the fracture mechanics, constitutive modelling, fatigue, etc.

3.0.1 High-speed X-ray imaging of the high-strain rate testing setup

In the previous year, the laboratory at the Department of Mechanics and Materials was significantly expanded with a new type of equipment enabling the very fast X-ray radiography called Flash X-ray. Typical applications of the Flash X-ray device are found in ballistics, detonics and simulations of space debris impacts [45]. The Flash X-ray system Model 300 (Scandiflash, Sweden) at our laboratory is equipped with 4

anodes (X-ray sources) with a small focal spot size of 1 mm and are built into the same vacuum chamber in a circle arrangement. Each source is connected to a pulser with a high voltage coaxial cable and can be individually pulsed. The system can generate X-rays with a voltage in a range of 100 – 300 kV and with a current of 10 kA. Before the

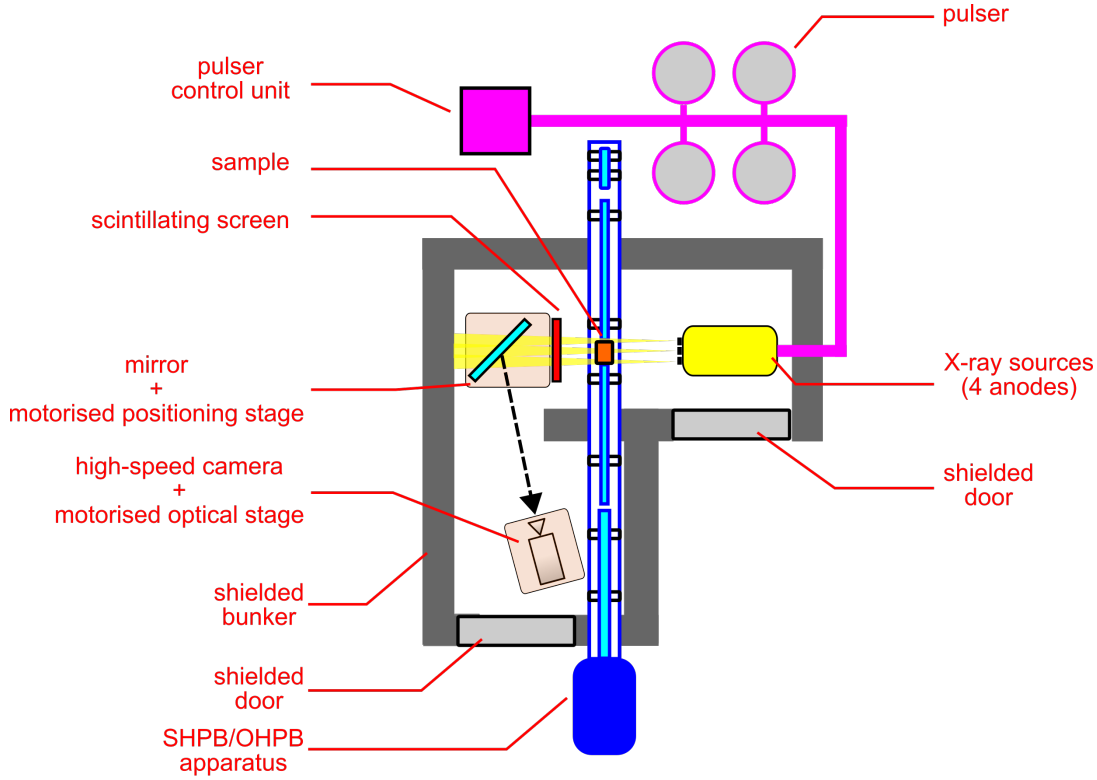


Figure 3.1: Scheme of the experimental facility for the high-speed X-ray imaging during the high-strain rate testing.

image acquisition, the pulser is charged up and waits on a trigger in the standby mode. Thus, the image is taken after the trigger pulse is received. Images are recorded using a high-speed camera. Between the irradiated object and the camera, a scintillating screen is placed. The scintillating screen converts the X-ray image (front side of the screen) into a visible image (rear side of the screen). A large area (468×468 mm) CsI(Tl) scintillating screen (Hamamatsu, Japan) with a high transformation efficiency (X-ray to visible spectrum), a short reaction period and fast decay time of a few μs is used in our setup. The fast decay time of the scintillating screen is a very important parameter because the maximum frame rate is not limited by the X-ray system, but only by the decay time. The time between the pulses is optional, it has no lower limit.

The exposure time for each individual image is determined by the X-ray system pulser and the duration of the X-ray burst is normally 20 ns. Between the scintillating screen and the high-speed camera, the mirror, mounted on an in-house developed positioning stage [40], is placed to reduce the potentially harmful effect of the irradiation on the high-speed camera electronics. The initial setup arrangement was tested in a pilot experiment and the first series of images were acquired (see Fig. 3.2). The pilot

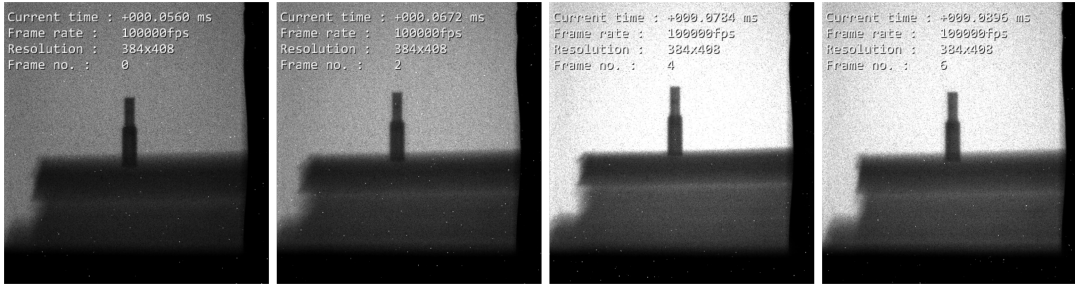


Figure 3.2: Series of four images (≈ 4 anodes) of a small object from chromium-vanadium steel acquired using the Flash X-ray system (240 kV), scintillating screen and high-speed camera (100 kfps). The increasing brightness of the images is caused by the gradual saturation of the scintillation layer.

experiment proved that the concept is applicable for high speed X-ray imaging and is able to capture four images during a single experiment. Thus, a combination of the X-ray flash system, high-speed camera, scintillating screen and mirror assembly is potentially ready to reliably capture impacts and processes as short as a few dozen microseconds. Currently, the SHPB/OHPB apparatus is being integrated into the high-speed X-ray imaging system and the pilot impact test is being prepared. The scheme and assembly of the experimental facility for the high-speed X-ray imaging during high-strain rate testing are depicted in Fig. 3.1 and Fig. 3.3, respectively.

■ 3.0.2 High-speed X-ray imaging of the intermediate strain-rate testing setup

Currently, the novel loading device capable of performing dynamic experiments at low impact velocities (up to 6 ms^{-1}) and intermediate strain rates with well defined boundary conditions is assembled in the laboratory. The designed loading performance is aimed at filling the gap between the quasi-static and high strain rate testing. The frame (see Fig. 3.4) of the loading device consists of aluminium profiles. Two main



Figure 3.3: Experimental facility for the high-speed X-ray imaging during the high-strain rate testing.



Figure 3.4: Frame of the assembled loading device

profiles placed horizontally across the frame form the support for the rails of the sledges propelled by linear motors. A set of linear motors is used for the loading and its motion can be controlled very precisely (modify the experiment parameters within dozens of microseconds) and, therefore, the optimal load function (displacement, velocity, force)

of the tested specimens can be prescribed. This feature will allow the testing of the samples' deformation response to a specific type of prescribed load or can be used to investigate the specific material properties. The two types of load-cells were selected for the initial instrumentation because the loading device is able to load the samples dynamically and quasi-statically. For the dynamic testing, impact piezoelectric load-cells can be used. In the case of the quasi-static, conventional strain-gauge load-cells can be mounted on the loading sledges. Other equipment, such as a polycarbonate safety shields, limit and safety switches, etc., are also important parts of the device and will be integrated simultaneously with the main parts.

This stand-alone loading device will be further extended by a high power X-ray source and the same acquisition sub-system (scintillating screen, mirror, high-speed camera) as in the case of the Flash X-ray system. By combining both systems, it will be possible to perform high speed X-ray imaging of the dynamic experiments conducted at low and intermediate strain rates. A suitable X-ray tube has already been tested in a voltage range of 160 – 225 kV and maximum power of 900 W and the results confirmed that imaging at frame rates of at least 14 kfps is possible with the current acquisition sub-system. For imaging of impacts at low and intermediate strain-rates, the achieved frame rate is sufficient.



Bibliography

- [1] Rakesh Kumar, Manoj Kumar, Jasgurpreet Singh Chohan, and Santosh Kumar. Overview on metamaterial: History, types and applications. *Materials Today: Proceedings*, 2021.
- [2] James Utama Surjadi, Libo Gao, Huifeng Du, Xiang Li, Xiang Xiong, Nicholas Xuanlai Fang, and Yang Lu. Mechanical metamaterials and their engineering applications. *Advanced Engineering Materials*, 21(3):1800864, 2019.
- [3] Wenwang Wu, Yong Tao, Yong Xia, Chen Jikun, Hongshuai Lei, Lijuan Sun, and Daining Fang. Mechanical properties of hierarchical anti-tetrachiral metastructures. *Extreme Mechanics Letters*, 16, 09 2017.
- [4] Wenwang Wu, Xiaoke Song, Jun Liang, Re Xia, Guian Qian, and Daining Fang. Mechanical properties of anti-tetrachiral auxetic stents. *Composite Structures*, 185:381–392, 2018.
- [5] Alexey Mazaev, Oleg Ajenezza, and Marina Shitikova. Auxetics materials: classification, mechanical properties and applications. *IOP Conference Series: Materials Science and Engineering*, 747:012008, 03 2020.
- [6] D. J. Gunton and G. A. Saunders. The young's modulus and poisson's ratio of arsenic, antimony and bismuth. *Journal of Materials Science*, 7:1573–4803, 09 1972.
- [7] John Williams and J Lewis. Properties and an anisotropic model of cancellous bone from the proximal tibial epiphysis. *Journal of biomechanical engineering*, 104:50–6, 03 1982.

- [8] A.G. Kolpakov. Determination of the average characteristics of elastic frameworks. *Journal of Applied Mathematics and Mechanics*, 49(6):739–745, 1985.
- [9] Roderic S. Lakes. Foam structures with a negative poisson’s ratio. *Science*, 235:1038 – 1040, 1987.
- [10] Jianxing Liu and Yihui Zhang. Soft network materials with isotropic negative poisson’s ratios over large strains. *Soft Matter*, 14:693–703, 2018.
- [11] Mohammad Sanami, Naveen Ravirala, Kim Alderson, and Andrew Alderson. Auxetic materials for sports applications. *Procedia Engineering*, 72:453–458, 2014. The Engineering of Sport 10.
- [12] Nguyen Dinh Duc, Kim Seung-Eock, Pham Hong Cong, Nguyen Tuan Anh, and Nguyen Dinh Khoa. Dynamic response and vibration of composite double curved shallow shells with negative poisson’s ratio in auxetic honeycombs core layer on elastic foundations subjected to blast and damping loads. *International Journal of Mechanical Sciences*, 133:504–512, 2017.
- [13] Gabriele Imbalzano, Phuong Tran, Tuan D. Ngo, and Peter V.S. Lee. A numerical study of auxetic composite panels under blast loadings. *Composite Structures*, 135:339–352, 2016.
- [14] Gabriele Imbalzano, Phuong Tran, Tuan D Ngo, and Peter VS Lee. Three-dimensional modelling of auxetic sandwich panels for localised impact resistance. *Journal of Sandwich Structures & Materials*, 19(3):291–316, 2017.
- [15] Shaoyu Hou, Tiantian Li, Zian Jia, and Lifeng Wang. Mechanical properties of sandwich composites with 3d-printed auxetic and non-auxetic lattice cores under low velocity impact. *Materials and Design*, 160:1305–1321, 2018.
- [16] A. Jung, A.D. Pullen, and W.G. Proud. Strain-rate effects in ni/al composite metal foams from quasi-static to low-velocity impact behaviour. *Composites Part A: Applied Science and Manufacturing*, 85:1–11, 2016.
- [17] Nejc Novak, Kazuyuki Hokamoto, Matej Vesenjsek, and Zoran Ren. Mechanical behaviour of auxetic cellular structures built from inverted tetrapods at high strain rates. *International Journal of Impact Engineering*, 122:83–90, 2018.

- [18] Timothy Johnson, S. Sarva, and Simona Socrate. Comparison of low impedance split-hopkinson pressure bar techniques in the characterization of polyurea. *Experimental Mechanics*, 50:931–940, 09 2010.
- [19] M. Peroni, George Solomos, and Norbert Babcsán. Development of a hopkinson bar apparatus for testing soft materials: Application to a closed-cell aluminum foam. *Materials*, 9:27, 01 2016.
- [20] J. Šleichrt, T. Fíla, P. Koudelka, M. Adorna, J. Falta, P. Zlámál, J. Glinz, M. Neuhäuserová, T. Doktor, A. Mauko, D. Kytýř, M. Vesenjāk, I. Duarte, Z. Ren, and O. Jiroušek. Dynamic penetration of cellular solids: Experimental investigation using hopkinson bar and computed tomography. *Materials Science and Engineering A*, 800, 2021.
- [21] M. Felten, M. Fries, T. Fíla, P. Zlámál, J. Falta, O. Jiroušek, and A. Jung. High strain-rate compression experiments on ni/polyurethane hybrid metal foams using the split-hopkinson pressure bar technique. *Advanced Engineering Materials*, 2021.
- [22] T. Fíla, P. Koudelka, P. Zlámál, J. Falta, M. Adorna, M. Neuhäuserová, J. Luksch, and O. Jiroušek. Strain dependency of poisson’s ratio of sls printed auxetic lattices subjected to quasi-static and dynamic compressive loading. *Advanced Engineering Materials*, 21(8), 2019.
- [23] T. Fíla, P. Koudelka, J. Falta, P. Zlámál, V. Rada, M. Adorna, S. Bronder, and O. Jiroušek. Dynamic impact testing of cellular solids and lattice structures: Application of two-sided direct impact hopkinson bar. *International Journal of Impact Engineering*, 148, 2021.
- [24] T. Doktor, T. Fíla, P. Zlámál, D. Kytýř, and O. Jiroušek. High strain-rate compressive testing of filling materials for inter-penetrating phase composites. pages 21–24, 2019.
- [25] T. Fíla, P. Zlámál, O. Jiroušek, J. Falta, P. Koudelka, D. Kytýř, T. Doktor, and J. Valach. Impact testing of polymer-filled auxetics using split hopkinson pressure bar. *Advanced Engineering Materials*, 19(10), 2017.

- [26] M. Neuhäuserová, P. Koudelka, J. Falta, M. Adorna, T. Fíla, and P. Zlámal. Strain-rate and printing direction dependency of compressive behaviour of 3d printed stainless steel 316l. pages 68–72, 2019.
- [27] T. Fíla, P. Koudelka, J. Falta, J. Šleichrt, M. Adorna, P. Zlámal, M. Neuhäuserová, A. Mauko, J. Valach, and O. Jiroušek. Impact behavior of additively manufactured stainless steel auxetic structures at elevated and reduced temperatures. *Advanced Engineering Materials*, 23(1), 2021.
- [28] A. Mauko, T. Fíla, J. Falta, P. Koudelka, V. Rada, M. Neuhäuserová, P. Zlámal, M. Vesenjajak, O. Jiroušek, and Z. Ren. Dynamic deformation behaviour of chiral auxetic lattices at low and high strain-rates. *Metals*, 11(1):1–15, 2021.
- [29] M. Neuhäuserová, T. Fíla, P. Koudelka, J. Falta, V. Rada, J. Šleichrt, P. Zlámal, and O. Jiroušek. Compressive behaviour of additively manufactured periodical re-entrant tetrakaidecahedral lattices at low and high strain-rates. *Metals*, 11(8), 2021.
- [30] J. Falta, T. Fíla, P. Zlámal, and M. Adorna. Instrumentation of split hopkinson pressure bar for testing of cellular metallic materials. *16th Youth Symposium on Experimental Solid Mechanics, YSESM 2018*, pages 10–14, 2018.
- [31] M. Adorna, S. Bronder, J. Falta, P. Zlámal, and T. Fíla. Evaluation of hopkinson bar experiments using multiple digital image correlation software tools. pages 1–5, 2019.
- [32] J. Falta, M. Adorna, T. Fíla, and P. Zlámal. Direct measurement of reaction forces during fast dynamic loading. pages 32–35, 2019.
- [33] Lorna J. Gibson and Michael F. Ashby. *Cellular Solids: Structure and Properties*. Cambridge Solid State Science Series. Cambridge University Press, 2 edition, 1997.
- [34] Joachim Baumeister, Jorg Weise, Eva Hirtz, Klaus Hohne, and Jorg Hohe. Applications of aluminum hybrid foam sandwiches in battery housings for electric vehicles. *Procedia Materials Science*, 4:317 – 321, 2014. 8th International Conference on Porous Metals and Metallic Foams.

- [35] Karsten Stobener and Gerald Rausch. Aluminium foam-polymer composites: Processing and characteristics. *Journal of Materials Science*, 44:1506 – 1511, 2009.
- [36] T. Fíla. Mechanical behavior of materials under high strain-rates investigated by shpb. *PhD thesis*, 2020.
- [37] H Kolsky. An investigation of the mechanical properties of materials at very high rates of loading. *Proceedings of the Physical Society. Section B*, 62(11):676–700, nov 1949.
- [38] Karl Hoffmann. Applying the wheatstone bridge circuit. *Hottinger Baldwin Messtechnik*.
- [39] Jan Falta, Tomáš Fíla, Marcel Adorna, and Petr Zlámal. Optimization of hopkinson bar instrumentation for testing of cellular and low impedance materials. pages 97–100, 05 2019.
- [40] M. Hudak. *Upgrade of SHPB for Advanced Measurements in transportation - master thesis*. Czech Technical University, Prague, 2018.
- [41] Bruce D Lucas, Takeo Kanade, et al. An iterative image registration technique with an application to stereo vision. 1981.
- [42] D. Kytýř, P. Zlámal, P. Koudelka, T. Fíla, N. Krčmářová, I. Kumpová, D. Vavřík, A. Gantar, and S. Novak. Deformation analysis of gellan-gum based bone scaffold using on-the-fly tomography. *Materials and Design*, 134:400–417, 2017.
- [43] I. Jandejsek, J. Valach, and D. Vavřík. Optimization and calibration of digital image correlation method. In *EAN 2010: 48th International Scientific Conference on Experimental Stress Analysis*, pages 131–136, 2010.
- [44] R. A. Govender and R. J. Curry. The “open” hopkinson pressure bar: Towards addressing force equilibrium in specimens with non-uniform deformation. *Journal of Dynamic Behavior of Materials*, 2(1):43–49, 2016.
- [45] Arne Mattsson. New developments in flash radiography - art. no. 62790z. 01 2007.



Appendix A

Selected Papers

- **Paper 1** - Impact Testing of Polymer-filled Auxetics Using Split Hopkinson Pressure Bar [25]
- **Paper 2** - Strain Dependency of Poisson's Ratio of SLS Printed Auxetic Lattices Subjected to Quasi-Static and Dynamic Compressive Loading [22]
- **Paper3** - Impact Behavior of Additively Manufactured Stainless Steel Auxetic Structures at Elevated and Reduced Temperatures [27]
- **Paper 4** - Dynamic impact testing of cellular solids and lattice structures: Application of two-sided direct impact Hopkinson bar [23]
- **Paper 5** - Dynamic penetration of cellular solids: Experimental investigation using Hopkinson bar and computed tomography [20]

DOI: 10.1002/adem.201700076

Impact Testing of Polymer-filled Auxetics Using Split Hopkinson Pressure Bar**

By Tomáš Fíla,* Petr Zlámal, Ondřej Jiroušek, Jan Falta, Petr Koudelka, Daniel Kytýř, Tomáš Doktor and Jaroslav Valach

In this paper, impact testing of auxetic structures filled with strain rate sensitive material is presented. Two dimensional missing rib, 2D re-entrant honeycomb, and 3D re-entrant honeycomb lattices are investigated. Structures are divided into three groups according to type of filling: no filling, low expansion polyurethane foam, and ordnance gelatine. Samples from each group are tested under quasi-static loading and dynamic compression using Split Hopkinson Pressure Bar. Digital image correlation is used for assessment of in-plane displacement and strain fields. Ratios between quasi-static and dynamic results for plateau stresses and specific energy absorption in the plateau are calculated. It is found out that not only the manufactured structures, but also the wrought material exhibit strain rate dependent properties. Evaluation of influence of filling on mechanical properties shows that polyurethane increases specific absorbed energy by a factor of 1.05–1.4, whereas the effect of gelatine leads to increase of only 5–10%. Analysis of the Poisson's function reveals influence of filling on achievable (negative) values of Poisson's ratio, when compared to unfilled specimens. The results for the Poisson's function yielded apparently different values as the assessed minima of quasi-static Poisson's ratio in small deformations are constrained by a factor of 15.

1. Introduction

Materials with negative Poisson's ratio, so called auxetic materials, is a group of advanced materials with mechanical properties promising for energy absorption applications.^[1–5] Auxetic materials exhibit high specific energy absorption as they can have significant plateau region where a large amount of impact energy is dissipated. Moreover, the auxetic materials show increased resistance against penetration as

they increase density under the impacting object.^[1] The auxetic behavior is important in a plateau region and in the early part of a densification, where most of the energy is mitigated.

Auxetic structures can be manufactured using volumetric compression of conventional foams.^[6,7] Other options are additive manufacturing and rapid prototyping that can produce periodic lattice structures with controlled geometry.^[8–10] Moreover, additive manufacturing can be used to build periodic auxetic lattices from metal alloys that exhibit high ductility and extended plateau region. Such a structure can be used, after careful optimization of the design, as a functionally graded material with tailored properties (e.g., optimized for high energy absorption).^[11–13]

The design optimization requires an in-depth investigation of deformation behavior for given specific loading conditions. Analytical, numerical, and experimental studies investigating re-entrant, chiral, cross-chiral, and other auxetic lattices under quasi-static loading have already been carried out.^[4,14–18] Energy absorption and deformation behavior of tubes filled with auxetics has been studied by, e.g., Mohsenizadeh.^[19] Papers dealing with characteristics of auxetic materials subjected to dynamic loading are also available. Dynamic crushing of open-cell polyurethane auxetic foam using impact

[*] T. Fíla, Dr. P. Zlámal, Prof. O. Jiroušek, J. Falta, P. Koudelka, Dr. D. Kytýř, T. Doktor

Department of Mechanics and Materials, Faculty of Transportation Sciences, Czech Technical University in Prague, Na Florenci 25, 110 00, Prague, Czech Republic
E-mail: fila@fd.cvut.cz

Dr. J. Valach

The Czech Academy of Sciences, Institute of Theoretical and Applied Mechanics, Centre of Excellence Telč, Batelovská 485, 486, Telč, 588 56, Czech Republic

[**] The research has been supported by the Czech Science Foundation (project no. 15-15480S). Authors thank Centre of Excellence Telč for providing a high-speed camera that was an essential experimental device in this study.

test was investigated by Scarpa and Lim.^[20–22] Yang investigated auxetic sandwich panels using quasi-static three-point bending test and dynamic drop-weight impact test.^[23] Auxetic materials for sport safety application were investigated by Duncan using a drop hammer impact test.^[5] Both Scarpa and Duncan showed that auxetic foams can exhibit performance superior to conventional foams, e.g., in terms of damping properties, acoustic properties, and dynamic crushing.^[5,20]

Generally, a key factor influencing deformation behavior under dynamic loading is strain rate of the impact. For many materials, mechanical behavior at various strain rates can be significantly different. Mechanical properties based on quasi-static testing can produce misleading results and can significantly underestimate or overestimate the properties valid for the dynamic impact conditions.^[24] Dynamic impact testing at high strain rates is performed using specialized experimental apparatuses, particularly Split Hopkinson Pressure Bar (SHPB).

SHPB is a well-established method for dynamic testing of materials and can be used for evaluation of stress–strain curves at high strain rates. While SHPB can be easily used for measurements of ductile, high-strength materials such as solid metals, its application to materials with low mechanical impedance and geometrically complex inner structure is complicated and may lead to unreliable conclusions.^[25] Such a measurement requires a modification of the experimental setup and advanced data correction techniques have to be applied for proper evaluation of mechanical properties.^[25,26] Recently, a number of studies analyzing lattices,^[27] foams, and honeycomb structures subjected to impact loading in SHPB were published.^[28–30] Strain rate sensitivity, inertia effects, and deformation behavior at high strain rates were investigated. A novel approach utilizing digital image correlation (DIC) techniques in SHPB experiments was also introduced.^[31]

In this study, we investigate deformation behavior of additively manufactured metal auxetic lattices under impact loading in SHPB. SHPB was employed as an approach for characterization of metallic auxetic lattices under dynamic compression at strain rates significantly higher than typical rates of drop weight impact tests ($1\text{--}200\text{ s}^{-1}$). Re-entrant and missing rib (cross-chiral) auxetic structures were used in the experiments.^[2,16,18,32] Voids in the selected specimens were filled using strain rate sensitive material. The filling was employed to investigate a possible synergistic effect during impact energy absorption of a ductile auxetic lattice with a soft strain rate sensitive filling. Three types of auxetic structures were prepared using selective laser sintering (SLS) and filled with two types of strain rate sensitive material. Quasi-static experiments were performed and mechanical behavior of the filled structures and the structures without filling was evaluated. Then, a series of SHPB experiments was carried out to evaluate mechanical behavior of the structures at high strain rate. Striker impact velocity and corresponding strain rate were selected to analyze the influence of strain-rate

sensitivity effect at rates corresponding to a very high velocity impact of vehicles, blast loading, and particle penetration. In this field, a sandwich panels filled with additively manufactured auxetic structures can potentially exhibit beneficial performance. Deformation behavior and selected mechanical properties derived from quasi-static tests and from SHPB experiments were analyzed and compared. The SHPB experiments were observed using a high-speed camera and the recorded image data were used to analyze the displacement and strain fields using DIC. As a result, deformation behavior of the studied samples at quasi-static conditions and at high strain rate was evaluated, compared and summarized in the paper together with the effect of the two considered strain rate sensitive fillings.

2. Materials and Methods

2.1. Samples

Three different types of auxetic structures exhibiting in-plane and volumetric negative strain-dependent Poisson's ratio were printed using SLS method. Material used for printing the auxetic structures using additive manufacturing technology was 316L–0407 austenitic stainless steel alloy, which comprises iron alloyed with chromium of mass fraction up to 18%, nickel up to 14%, and molybdenum up to 3%, along with other minor elements. The alloy is an extra-low carbon variation on the standard 316L alloy.

The density of the wrought material is 7990 kg m^{-3} and melting is in the range $1371\text{--}1399\text{ }^{\circ}\text{C}$. Mechanical properties of the sintered bulk material are: compressive strength in horizontal direction $662 \pm 2\text{ MPa}$, in vertical direction $574 \pm 10\text{ MPa}$; yield strength in horizontal direction $518 \pm 5\text{ MPa}$, in vertical direction $440 \pm 10\text{ MPa}$, modulus of elasticity in horizontal direction $167 \pm 8\text{ GPa}$, in vertical direction $134 \pm 17\text{ GPa}$.

The following auxetic structures were used in the study: two dimensional missing rib, two dimensional re-entrant honeycomb and three-dimensional re-entrant honeycomb. The structures are shown in Figure 1. The aforementioned types of structures were selected as they can be produced using SLS with satisfactory quality and reasonable ratio between overall dimensions (limited by employed SHPB setup) and the number of unit cells in the structure. Moreover, they exhibit a significant development potential as their properties can be tuned by optimization of the cell geometry.

The missing rib specimen had dimensions of $11.7 \times 12.0 \times 13.0\text{ mm}$ ($w \times d \times h$) and nominal porosity 53.1%. The 2D re-entrant had dimensions of $12.0 \times 12.0 \times 13.0\text{ mm}$ and nominal porosity 52.3%. The 3D inverted re-entrant had dimensions of $12.1 \times 12.0 \times 13.0\text{ mm}$ and nominal porosity 74.0%. All structures had nominal strut thickness 0.6 mm. The overall dimensions of the samples were chosen to fit in the SHPB setup and, based on the SHPB performance, to reach densification region in the impact experiment. The cross-section to specimen height ratio was approx. 1 and was

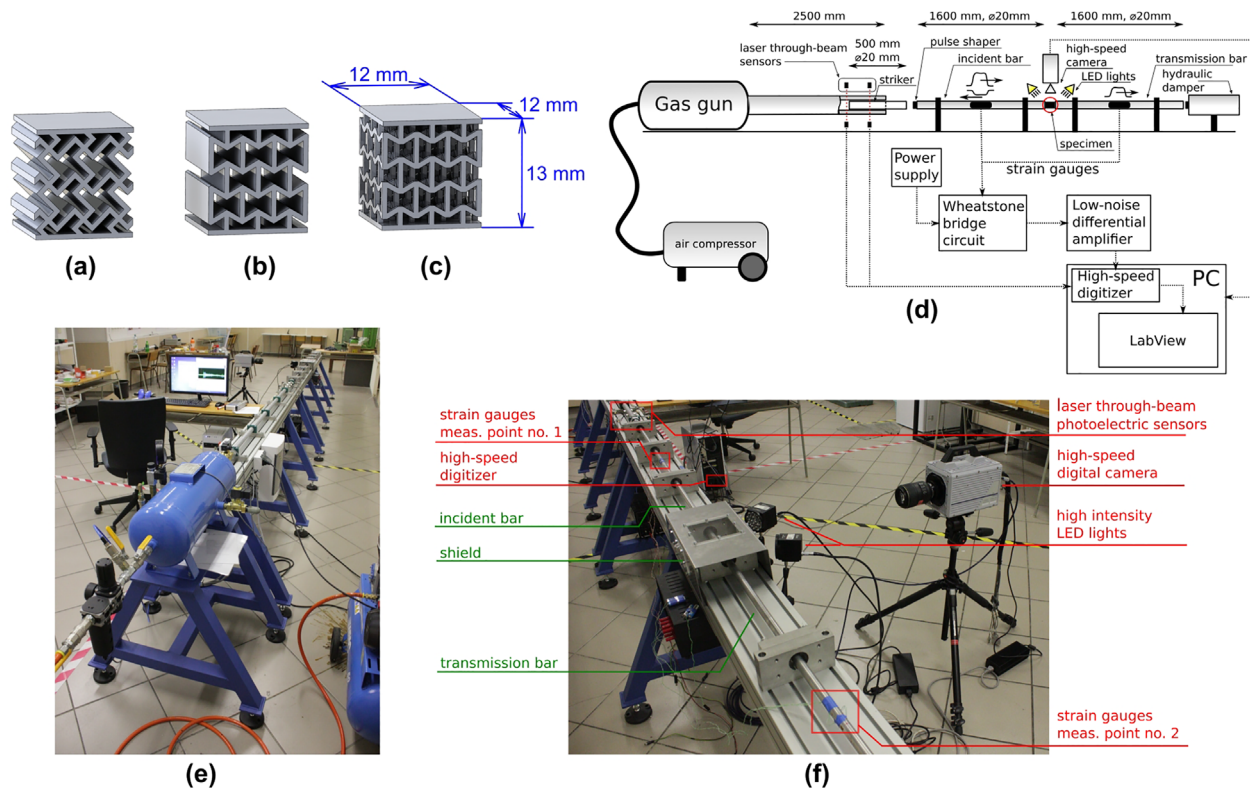


Fig. 1. (a) 2D missing rib, (b) 2D re-entrant, (c) 3D re-entrant, (d) experimental setup scheme, (e) overall experimental setup, (f) part of the experimental setup with specimen location, high-speed camera, and instrumentation.

selected to minimize frictional and inertia effects in the SHPB experiment.

The samples were divided into three groups for subsequent filling with strain rate sensitive material. The samples from the first group were filled using ordnance gelatine. This type of filling was selected due to its low viscosity during preparation, which provided a highly homogeneous distribution of the filling in the open cellular structure. The mixture was prepared as 20% 260 Bloom beef powder gelatine (Remi MB, Ltd., Czech Republic). The powder was poured into tap water with temperature 45 °C and stirred for 10 min to remove the air bubbles. Then, the auxetic structure specimens were immersed into the mold and cured for 24 h at room temperature and subsequently 24 h in the refrigerator. Then, the gelatine block was cut to separate the samples and to reveal their surface. Nominal density of the gelatine after curing was 1 084 kg m⁻³. Plateau stress of gelatine was reported at both low (0.0013 s⁻¹) and high strain rates (3 200 s⁻¹) to be 3 kPa and 6 MPa,^[33] respectively.

Samples of the second group were filled with porous low expansion polyurethane foam (Soudal, N.V., Belgium). This type of filling was selected due to its low specific weight and closed pore nature after curing, which contributes to strain rate sensitivity of this filling. As this foam cures at room temperature and in ambient air conditions, the liquid mixture was sprayed at the samples' surface and pressed carefully into the entire cellular structure. Then, the liquid mixture was removed from the faces to ensure proper curing of the mixture

filled within the porous structure of the auxetic constructs. A sufficient level of bonding between struts and filling was achieved due to good adhesive properties of the used mixture. The adhesive capabilities between the PU foam and metallic struts were justified by a pull-off adhesion test prior to the samples' preparation. After 12 h of curing at room temperature, the foam was removed from the samples' surface with a scalpel. Finally, the faces were ground and polished to restore their plan parallelism and suitable optical surface properties of the solid phase. Nominal properties of the PU foam after curing were: nominal density 26 kg m⁻³, compressive strength 30 kPa, and shear strength 170 kPa.

Samples of the third group were kept unfilled for comparison of influence of the considered filling materials and assessment of the deformation behavior of the auxetic structure themselves.

After the filling process density of the specimens was evaluated. 2D re-entrant with no filling had average density 4 381 kg m⁻³, with polyurethane filling 4 456 kg m⁻³, and with gelatine filling 4 976 kg m⁻³. 3D re-entrant with no filling had average density 2 944 kg m⁻³, with polyurethane filling 3 041 kg m⁻³, and with gelatine filling 3 686 kg m⁻³. 2D missing rib with no filling had average density 4 266 kg m⁻³, with polyurethane filling 4 415 kg m⁻³, and with gelatine filling 4 845 kg m⁻³.

Following sample combinations were tested: (i) quasi-static, all structures, 1 + 1 + 1 (unfilled + polyurethane filling + gelatine filling); (ii) SHPB, 2D re-entrant, 3 + 2 + 2;

(iii) SHPB, 3D re-entrant, 2 + 2 + 2; (iv) SHPB, 2D missing rib, 3 + 2 + 2.

2.2. Quasi-static Testing

Quasi-static compression tests were carried out for each type of auxetic structure and filling using a uniaxial testing machine (Instron 3382, Instron, USA). All samples were loaded at the speed of 0.5 mm min^{-1} (strain rate 0.001 s^{-1}) up to their 50% overall deformation (defined by cross-head displacement) and the applied force was measured. During the experiments, the deforming samples were observed using a digital camera (Manta G-504B, AVT, Germany) with 2452×2056 px resolution equipped with a telecentric lens (TCZR072, Opto Engineering, Italy). Captured images were evaluated using DIC technique to obtain in-plane displacement and strain fields. For each sample, stress-strain diagrams valid for quasi-static loading were determined and compared with deformation behavior measured at high strain rates. The data were also used to estimate the expected measured values during the SHPB experiment.

2.3. SHPB Setup

A modified Kolsky SHPB setup was used in the study. The incident, transmission, and striker bars had the same nominal diameter 20 mm with solid cross-section and were made of high-strength aluminum alloy (EN-AW-7075) to match the mechanical impedance of the specimens as close as possible. A gas-gun system with 16 bar maximum pressure was used to accelerate the striker bar. The gas-gun system consisted of a 20 l air reservoir, a pressure gauge, high-flow fast release solenoid valve (366531, Parker, USA), a steel barrel with the maximal stroke 2500 mm, and other peripherals (compressor unit, safety elements, piping etc.). The incident bar and the transmission bar had the same length 1600 mm and were supported by eight low-friction polymer-liner slide bearings with aluminum housing (Drylin FJUM housing, IGUS, Germany). The striker bar with length 500 mm was used for generation of the incident wave. A fixed aluminum rod and a hydraulic damper were used as the absorbers of the residual kinetic energy of the experiment. The experiments were carried out without momentum trap as the damping elements were not in initial contact with the transmission bar.

The experimental setup was carefully adjusted to reduce negative effects of improper geometrical alignment. Selected high precision extruded rods with tight diameter tolerance were used for the experiments. Surfaces of the bars were ground and polished. Position of the bars was adjusted in the bearing housings to achieve system axis straightness better than 1 mm m^{-1} and friction effects of the slider bearings were minimized. The impact faces of the bars were finished using high-precision grinding and polishing and were adjusted to be in full contact at interfaces (striker to incident bar interface and bars to specimen interface). The precision of the contact was measured by feeler gauge and maximal distortion of in-plane contact was in order of tens of micrometers.

As the experiments with auxetic structures required a high impact velocity, it was necessary to use a pulse shaper at the striker to incident bar interface. Paper pulse-shaper (thickness $= 2 \times 0.25 \text{ mm}$) was selected on the basis of results from calibration experiments that were carried out prior to the experiments with auxetics. Paper pulse-shaper satisfactorily reduced the spurious effects of wave dispersion, while the wave shape was not significantly influenced. This allowed for constant strain rates in the plateau region with no wave interference in the bars.

2.4. Instrumentation

The incident and transmission bar of the SHPB setup were equipped with foil strain gauges (3/120 LY61, HBM, Germany) for the strain wave measurement during the test. Foil strain gauges were selected despite their low sensitivity in comparison to semiconductor strain gauges (approximately hundred times lower), because of their linearity and ability to measure higher strain values (50 000 micro strains compared to 2500 micro strains in case of semiconductor gauges) expected during the experiments. A relatively small length of selected strain gauges (3 mm) enabled high precision strain measurement (integration of the strain wave along the length of the strain gauge) with respect to the wavelength of the strain wave. Two strain gauges were applied on each measurement point using a single component low-viscosity cyanoacrylate adhesive (Cyberbond 2003, Cyberbond Europe GmbH, Germany) in half-bridge arrangement to eliminate a potential influence of bending, and cured for at least 24 h. One measurement point in the middle of both the incident and transmission bars was selected. To maximize the signal-to-noise ratio each strain gauge circuit was powered using a battery pack (with excitation voltage 3 V) to decrease the noise of strain gauge signal to a minimum. Due to small sensitivity of the foil strain gauges, it was necessary to use the active differential low noise amplifier (EL-LNA-2, Elsys AG, Switzerland) with gain 10 (bandwidth: 20 MHz) or 100 (bandwidth: 15 MHz). Amplified strain gauge signal was sampled and recorded using high speed 16-bit digitizer (PCI-9826H, ADLINK Technology, Inc., Taiwan) with maximal 20 MHz sample rate. Because the internal memory of the digitizer is limited, triggering of the measurement is very important as the maximal length of the record is only 65 536 samples per channel, which corresponds to 3.2 ms at 20 MHz sample rate. Thus, a laser through-beam photoelectric sensor (FS/FE 10-RL-PS-E4, Sensopart, Germany) was employed for measurement triggering. Two pairs of these sensors were installed on the barrel of the SHPB at a fixed distance from each other. The laser beam interruption of the first pair (closer to the air tank) starts data acquisition (signal from strain gauges, image data from high-speed camera, etc.), while the interrupt signals from both sensors enable to assess the speed of the projectile. The process of the deformation of the sample was observed using a high-speed digital camera (FASTCAM SA5, Photron, Japan) with $20 \mu\text{m}$ square CMOS

sensor with maximal 1 000 000 fps at a 64×16 image pixel resolution. Due to hardware configuration of the camera, the value of maximal frame rate depends on the image resolution and vice versa. As a compromise between the frame rate and the image resolution with respect to the DIC analysis 100 000 fps and 320×192 px image resolution were chosen. Because high-speed imaging is very sensitive to proper illumination of the scene, a pair of high intensity LED lights (Constellation 60, Veritas, USA) was used for illumination of the sample during the deformation process. Custom virtual instrument was designed in LabView (National Instruments, USA) and used for controlling instruments, data acquisition and source synchronization during the SHPB test. Scheme of the experimental setup and instrumentation is shown in Figure 1d. The experimental setup is shown in Figure 1e and f.

2.5. SHPB Experiments

A prepared sample was placed into the SHPB setup between the incident bar and the transmission bar. Faces of the bars were carefully aligned on the faces of the sample to eliminate the distortion of the strain pulse. The ends of both bars (adjacent to the sample) were covered by random artificial black and white texture to increase the contrast for image tracking algorithm. The gas-gun release pressure of 5 bars was used in the experiments. Resulting impact velocity of the striker bar was 33 m s^{-1} (one experiment was carried out with 8 bar pressure with impact velocity 43 m s^{-1} , see Results section). The impact velocity was tuned to achieve maximal deformation in the specimen and constant strain rate during most of the time of the experiment (duration). A thick paper ($2 \times 0.25 \text{ mm}$) was placed on the impact face of the incident bar and used to reduce the Pochhammer–Chree oscillations and dispersion effects of the elastic wave propagating in the incident bar and to reduce the ramp-in effect at the specimen boundary.

2.6. SHPB Data Processing

As the mechanical impedances of the bars and specimen were significantly different a number of calibration and correction methods was utilized to evaluate the results. Series of calibration experiments and void tests were carried out at different impact velocities to obtain correction data. Data from void tests were used to evaluate the actual mechanical properties of the aluminum bars and to correct the signals from strain-gauges. Two types of void tests were performed: “incident bar apart” void test and “bars together” void test. The “incident bar apart” void test was carried out to analyze the impact velocity, elastic properties of the bar, wave propagation velocity, damping characteristics, wave shape, strain-gage position error, and linearity of the incident bar. The “bars together” void test was carried out to analyze the same properties valid for the transmission bar, the quality of the contact between the bars, wave transfer parameters, strain-gauge signals equilibrium, and friction losses of the system. All the evaluated parameters were consistent and the

experimental setup was evaluated as suitable for the measurements of auxetic structures with adequate precision.

Void tests with 50 mm short striker bar and no pulse shaper were performed to record wave dispersion effects in the bars. The data were used to calculate the experimentally determined wave transfer function and wave propagation coefficient in frequency domain, according to Bacon’s method and its modification.^[34,35] Wave propagation coefficient was calculated separately for incident and transmission bars using “bars together” and “incident bar apart” void tests. Fourier transforms of the first measured pulse in the bar $\tilde{e}_1(\omega)$ and its reflection $\tilde{e}_2(\omega)$ on the free end of the bar were used to calculate wave transfer function $H^*(\omega)$ of the system in frequency domain. The propagation coefficient was obtained using equation

$$H^*(\omega) = -\frac{\tilde{e}_2(\omega)}{\tilde{e}_1(\omega)} = e^{-\gamma(\omega)2d},$$

where $\gamma(\omega)$ is the propagation coefficient and d is the distance between the strain-gauge and the free end of the bar.^[13]

Recorded incident, transmission, and reflected strain-gauge signals measured in the center of the bars were shifted to specimen boundary using the propagation coefficient. The aforementioned geometrical calibration, pulse-shaping technique, and correction methods ensured that the dynamic equilibrium was achieved in the specimen and the SHPB experiments were valid. Thus, the sample was undergoing homogeneous deformation after initial ramp-in effect of the incident pulse. Examples of force equilibrium recorded without aforementioned techniques and equilibrium after the calibration of the setup are shown in Figure 2a and b. The experiments with auxetic materials produced consistent data, which is demonstrated in Figure 2c, where all the measured curves of one selected auxetic structure are shown.

2.7. Digital Image Correlation of SHPB Results

Deformation of the samples was recorded using a high-speed camera. The camera was triggered by interruption of a laser beam of a photoelectric sensor installed on the barrel. Images were taken at frame rate 100 000 fps with recorded image size 320×292 pixels. Total number of the recorded frames per experiment was approximately 2000. This enabled to capture the whole deformation process of the sample. Raw data from the high-speed camera were exported to TIFF image format without compression. For the DIC procedure, the TIFF images were converted to PNG image file format with lossless compression using the command-line convert tool from ImageMagick package and identical region of interest was cropped from the images.^[36] To verify that the compression level is only a trade-off between the resulting file size and the encoding/decoding speed and does not affect the image data quality, converted images were subtracted from the original images and zero matrices were obtained. From the captured image sequence, 10 frames that captured the first part of the

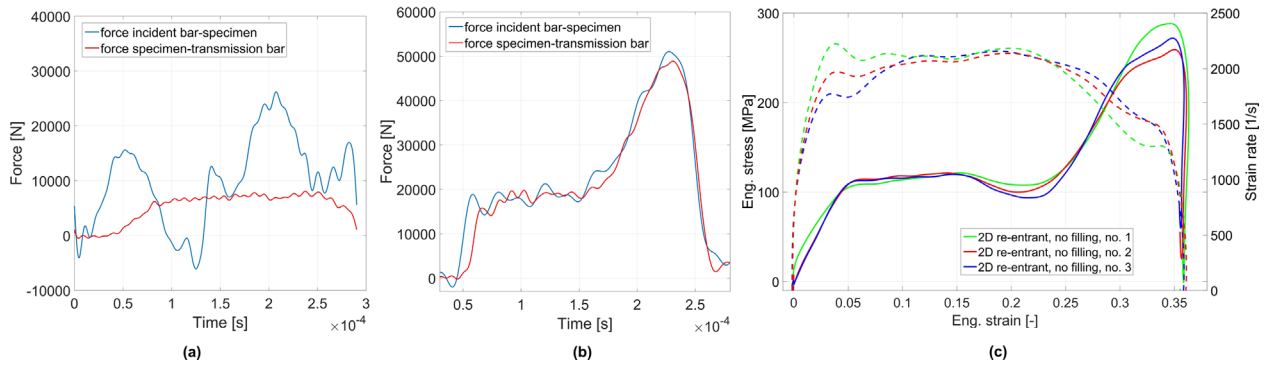


Fig. 2. (a) recorded forces at sample boundary – dynamic equilibrium not achieved, (b) recorded forces at sample boundary – valid experiment, (c) results consistency for 2D re-entrant specimens with no filling.

deformation process (the first image represented the undeformed state and the next nine images captured the deformation process up to approximately 20% deformation) were selected. These images were used in the DIC analysis using Ncorr open source 2D-DIC tool for Matlab (MathWorks, USA). To ensure the same image processing procedure was applied to all measurements, no histogram equalization was performed, and raw data were used in the correlation procedure. For all measurements, every parameter set in the DIC scheme, such as correlation criteria, sub-pixel registration algorithm, interpolation scheme, initial guess, and convergence conditions (number of iterations and PCG error criterion) was kept identical.

Because the basic principles of DIC algorithm have been fully described in literature, the algorithm is described here only briefly for clarity.^[37–39] DIC generally employs a zero-mean normalized sum-of-square difference (ZNSSD) criterion to compute the similarity in pixel intensity between reference and deformed image subsets.^[40] In this manner, displacements with pixel accuracy are obtained. Then, to obtain deformation with sub-pixel accuracy, the above mentioned ZNSSD criterion is iteratively optimized using the classic Newton–Raphson iterative algorithm.

From the displacement fields, full-field strains were calculated as Green-Lagrange strain tensors. This involves differentiation of the displacements fields, which is sensitive to noise and one must be careful that the displacement fields contain no noise prior differentiation. Attention was paid to keep the smoothing window as low as possible not to over-smooth the resulting strain fields. In all the experiments, the smoothing window was 15 pixels.

Set of parameters used for calculation of the results (displacements, strains, Poisson's ratios) were kept constant for all the experiments performed. The only smoothing procedure used in the DIC was the initial displacement smoothing using 2 × 2 pixel Gaussian kernel. Since the position and settings for the camera used in the experiments did not change, all the experiments were processed using the same Matlab scripts. This enabled an easy and reliable result evaluation and comparison.

3. Results and Discussion

3.1. Quasi-Static Poisson's Function from DIC

The Poisson's ratio ν_{12} was calculated using quasi-static strain fields evaluated by the DIC method according to

$$\nu_{12} = -\frac{\varepsilon_2}{\varepsilon_1},$$

where ε_2 is lateral strain in direction perpendicular to the direction of loading and ε_1 is a strain in the direction of loading. In every case, the deformation perpendicular to the direction of loading was evaluated from the middle parts of specimens' microstructure, where the concentration of the lateral strain occurred.

The Poisson's ratio of an unfilled missing rib structure gradually decreased to its minimum value of -0.25 at 2.5% strain and remained constant at this level up to 8% strain. Then, the Poisson's ratio linearly increased and reached zero at 35% strain. The Poisson's function of the 2D re-entrant honeycomb specimens reached its minimum of -1.4 at 2% deformation. From this point, it gradually increased and reached its asymptotic value in the observed range of deformation yielding Poisson's ratio -0.05 at 30% strain. Minimum value -1.2 of the Poisson's function of the 3D re-entrant honeycomb structure has been measured at 1% strain. After that, the Poisson's ratio increased to 0.2–4.5% strain and remained positive until the end of the experiment.

The gelatine-filled cut missing rib structure reached Poisson's ratio -0.145 at very small strains up to 0.5% that progressively increased to zero at 0.5% strain and remained approximately constant. The polyurethane-filled cut missing rib structure reached similar value of the Poisson's ratio at small strains, but the polyurethane filling significantly altered behavior of this microarchitecture at higher strains. The Poisson's ratio remained, in this case, lower than -0.125 up to 3.5% strain, and then linearly decreased to -0.62 at 6.2% strain. From this point, gradual increase of the Poisson's ratio to zero at 22% strain was observed.

The gelatine-filled 2D re-entrant honeycomb structure exhibited negative Poisson's ratio during the whole

investigated deformation process. At the initial stage of loading, the Poisson's reached -0.1 at 0.3% strain and decreased from this point to -0.23 at 0.7% strain. After that, the Poisson's ratio gradually increased to -0.04 at 27% strain followed by decrease to constant level of -0.14 . By contrast, Poisson's function of the polyurethane-filled re-entrant honeycomb structure is quasi-cyclic. In the first cycle, the Poisson's ratio decreases to -0.18 at 4.2% strain, and then increases to 0.05 at 12% of strain. From this point, the Poisson's ratio decreased again to -0.12 at 19% strain and then gradually reached zero at 36% strain.

The Poisson's ratio of the gelatine-filled 3D re-entrant honeycomb structure decreased to -0.075 at 1.9% strain and then increased to zero at 20% strain. As in the experiments of polyurethane-filled 2D re-entrant honeycomb structure, Poisson's function of the polyurethane-filled 3D re-entrant honeycomb structure exhibited cyclic changes in the values of Poisson's ratio. In small deformations up to 0.07% of strain, the Poisson's ratio reached the minimum value of -0.2 that was followed by its three cyclic changes. The respective minima and maxima of Poisson's ratio occurred in the following scheme:

- 1) Minima-Poisson's ratios -0.175 , -0.09 , -0.02 at strains 8% , 21.25% , 31%
- 2) Maxima-Poisson's ratios -0.09 , -0.07 , -0.002 at strains 5% , 17% , 26%

3.2. Specific Energy Analysis

Stress-strain diagrams from the quasi static experiments were used for evaluation of specific energy analysis (SEA) of the structures. As the plateau region is the most important part of the stress-strain diagram for effective energy absorption, the plateau was identified for all structures and a plateau energy analysis was carried out.

For the 2D re-entrant structures, a plateau region was identified in the range $5-25\%$ of engineering strain for the structure with the gelatine filling and without filling, and in the range $5-15\%$ for the specimen with the polyurethane filling. Plateau specific energy density for the 2D re-entrant with gelatine filling was 15.779 MJ m^{-3} comparing to 15.748 MJ m^{-3} of the specimen with no filling in the same plateau region. Plateau specific energy of the specimen with gelatine filling was 3.182 KJ kg^{-1} comparing to 3.602 KJ kg^{-1} of the specimen with no filling. Plateau specific energy density for the 2D re-entrant with polyurethane filling was 12.801 MJ m^{-3} comparing to 11.677 MJ m^{-3} of the specimen with no filling in the same plateau region. Plateau specific energy of the specimen with polyurethane filling was 2.883 KJ kg^{-1} comparing to 2.662 KJ kg^{-1} of the specimen with no filling.

For the 3D re-entrant structures plateau region was identified in the range $7-27\%$ of engineering strain for all the structures. Plateau specific energy density for the 3D re-entrant with no filling was 6.647 MJ m^{-3} , for gelatine filling 6.337 MJ m^{-3} and for polyurethane filling 8.409 MJ m^{-3} .

Plateau specific energy of the specimen without filling was 2.308 KJ kg^{-1} , for the specimen with gelatine filling 1.800 KJ kg^{-1} and for the specimen with polyurethane filling 2.766 KJ kg^{-1} .

For the 2D missing rib structures plateau region was identified in the range $5-12\%$ of engineering strain for all the structures. Plateau specific energy density for the 2D missing rib with no filling was 1.476 MJ m^{-3} , for gelatine filling 1.333 MJ m^{-3} and for polyurethane filling 1.696 MJ m^{-3} . Plateau specific energy of the specimen without filling was 0.349 KJ kg^{-1} , 0.274 KJ kg^{-1} for the specimen with gelatine filling, and 0.386 KJ kg^{-1} for the specimen with polyurethane filling.

3.3. SHPB Results

Employed SHPB setup was suitable to measure the dynamic response of auxetic structures. Foil strain gauges were successfully employed instead of semiconductor strain gauges. Increased noise and lower sensitivity were compensated by linearity of the foil gauge and its extensive working range. Values of measured strain in the incident bar were significantly above the measurable limit of a semiconductor gauge type. Digitizer sample rate 20 MHz and high-speed camera sample rate 100 kHz were sufficient to capture the deformation of specimen.

Stress-strain curves, strain rate curves, and specific material parameters of three types of auxetic structures without filling, and with two different strain rate sensitive fillings were evaluated. Average plateau stress and specific energy absorption in the plateau region were calculated from the stress-strain curves and compared with the quasi-static data. In the following sections, the specific energy absorption is represented using the parameters "specific energy absorption ratio" and "filling/no filling energy ratio". The specific energy absorption ratio was evaluated as a ratio of an area under the plateau region in the dynamic stress-strain curve to the quasi-static stress-strain curve. Moreover, it represents a comparison of energy mitigated in the plateau region in quasi-static and dynamic compression. The filling/no filling energy ratio was evaluated as a ratio of area under the plateau region in the stress-strain curve for a structure with filling to a structure without filling. It was evaluated separately for the quasi-static tests and for the dynamic tests and it represents a contribution of the filling to overall energy absorption. Comparison of this parameter evaluated for quasi-static and dynamic curves was also used to investigate the strain rate sensitivity of the filling materials. The averaged stress-strain and strain rate curves of the auxetic structures are shown in the Figure 3. Results of the quasi-static and SHPB experiments are summarized in Table 1.

3.3.1. 2D Re-Entrant

The 2D re-entrant structures were compressed at constant strain rate approx. 2000 s^{-1} , adequate dynamic equilibrium was achieved in all experiments, and all the measured curves were consistent. Plateau region was identified in the range

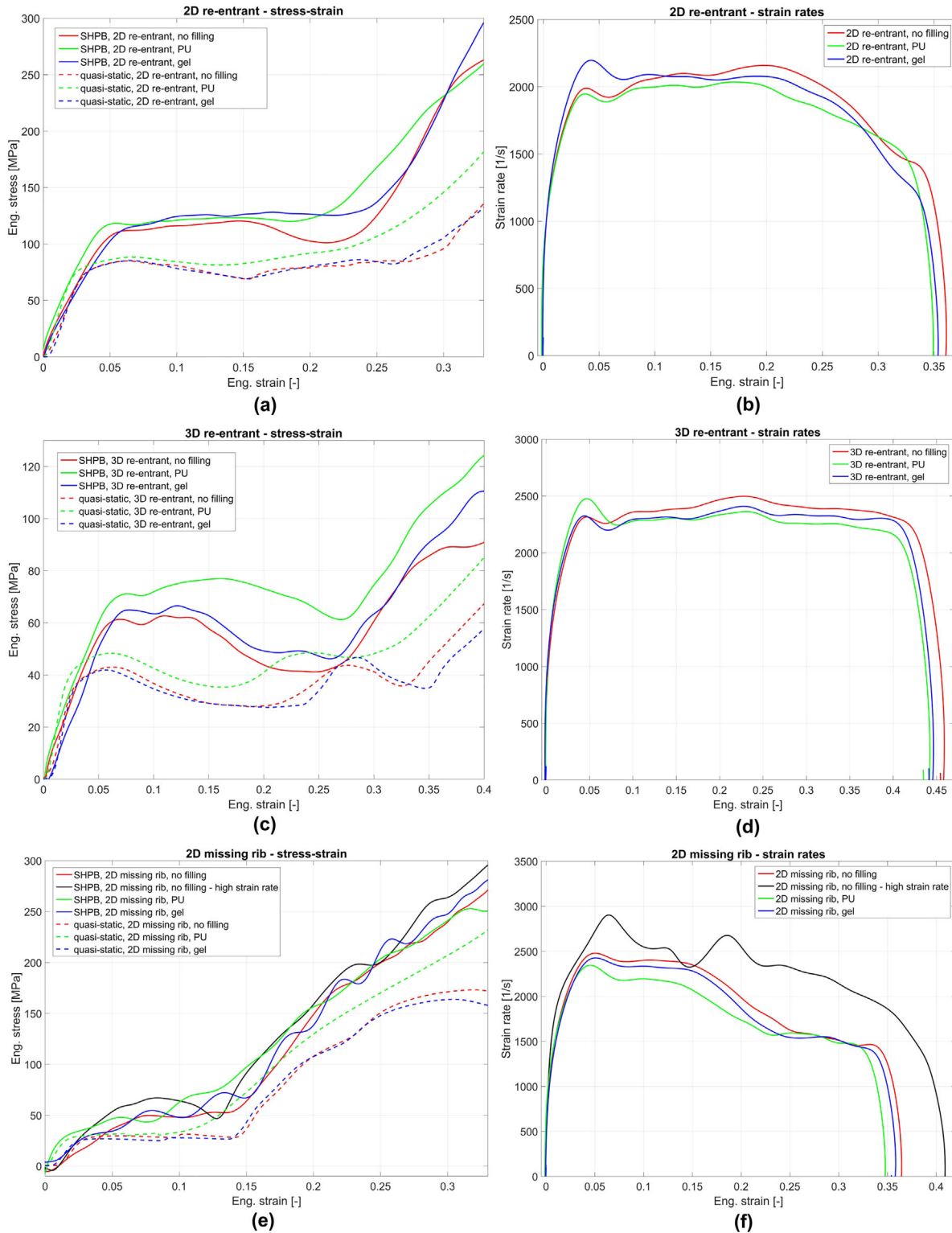


Fig. 3. Averaged stress–strain curves and strain rate–strain curves: (a) 2D re-entrant stress–strain, (b) 2D re-entrant strain rate–strain, (c) 3D re-entrant stress–strain, (d) 3D re-entrant strain rate–strain, (e) 2D missing rib stress–strain, (f) 2D missing rib strain rate–strain.

5–25% of engineering strain for the structure with the gelatine filling and without filling, and in the range 5–15% for the specimen with the polyurethane filling. Strain rate sensitive behavior of the sintered auxetic structure and both fillings was

identified. Average plateau stress and specific energy absorption were significantly higher in the dynamic tests. Moreover, different deformation behavior of the structure was observed as densification of the structure occurred at lower

Table 1. Specific energy absorption

	Average plateau stress			Specific energy absorption ratio		Filling/No filling plateau energy ratio	
	Static	Dynamic	Ratio	Dynamic/Static		Static	Dynamic
2D re-entrant							
No filling	80 MPa	113 MPa	1.41	1.43		–	–
PU	85 MPa	121 MPa	1.42	1.42		1.09	1.06
Gelatine	79 MPa	123 MPa	1.53	1.58		1.00	1.11
3D re-entrant							
No filling	33 MPa	51 MPa	1.56	1.55		–	–
PU	40 MPa	72 MPa	1.73	1.71		1.27	1.39
Gelatine	31 MPa	56 MPa	1.70	1.78		0.96	1.09
2D missing rib							
No filling	30 MPa	49 MPa	1.66	1.66		–	–
PU	34 MPa	57 MPa	1.69	1.70		1.15	1.18
Gelatine	28 MPa	52 MPa	1.76	1.95		0.90	1.06

strains in the SHPB experiments in comparison to quasi-static experiments. The effect of filling can be observed in stress-strain curves in specific energy absorption ratios. Polyurethane filling has approximately the same effect on the plateau stress in quasi-static and dynamic compression. Gelatine filling has negligible effect in quasi-static compression and recognisable effect in SHPB compression. Both fillings eliminated the plateau stress drop observed in dynamic compression of the structures without filling.

3.3.2. 3D Re-Entrant

The 3D re-entrant structures were compressed at constant strain rate approx. 2300 s^{-1} , adequate dynamic equilibrium was achieved in all experiments, and all the measured curves were consistent. Plateau region was identified in the range 7–27% of engineering strain for all the structures. Strain rate sensitive behavior of the sintered auxetic structure and both fillings was also identified, as in the case of 2D variant of the microstructure. Average plateau stress and specific energy absorption were significantly higher in the dynamic tests. Moreover, different deformation behavior of the structure was observed as densification of the structure occurred at lower strains in the SHPB experiments, in comparison to the quasi-static experiments. The effect of filling can be observed in stress-strain curves as well as in specific energy absorption ratios. Polyurethane filling has significantly higher effect on the plateau stress in dynamic compression. Gelatine filling has negligible effect in quasi-static compression and recognizable effect in SHPB compression. The value lower than one in the case of the “filling/no filling plateau energy ratio” is caused by measurement errors during the quasi-static experiments. It can be seen, that filling is the most effective in case of the 3D re-entrant structure as this structure has the highest porosity and the lowest strength from all the structures tested.

3.3.3. 2D Missing Rib

The 2D missing rib structures were compressed at constant strain rate approx. 2300 s^{-1} and adequate dynamic equilibrium was achieved in all experiments. The measured curves were consistent, but showed lower quality than the two aforementioned structures. A plateau-like region was identified in the range 5–12% of engineering strain for all structures. One experiment with this type of structure was intentionally conducted at higher strain rate of approx. 2800 s^{-1} . The experiment at higher strain rate was performed to investigate the effect of strain rate sensitivity of the sintered structure without filling. Strain rate sensitive behavior of the sintered auxetic structure without filling at both strain rates was identified. The effect of polyurethane filling and gelatine filling can be only identified with difficulties. The low significance of filling effect is connected with a high relative density together with small fragmented pores of the structure and, therefore low amount of the effective filling material within the auxetic structure.

The values in Table 1 should be interpreted as only approximate and are of a lower relevance than the results for other two structures. However, using the image sequence recorded by the high-speed camera, it was possible to evaluate deformation behavior properly.

As it can be seen from Table 1, the “filling/no filling plateau energy ratio” was approx. 10% lower for the structure with gelatine filling than for the specimen with no filling in quasi-static compression. This can be observed also in case of the 3D re-entrant with gelatine filling but the difference was very low (4%). As the effect of the gelatine filling is very low in quasi-static test, this can be interpreted as a proportional error of the measurement. In case of the 2D missing rib, this behavior was caused also by virtually no effect of the gelatine filling in the structure together with higher dispersion of the measured curves. The deformation behavior of the structure under

quasi-static and dynamic conditions was significantly different. Shear deformation and considerable lateral deformation of the specimen was observed in quasi-static compression. Such a complex deformation mechanism together with no effect of the filling caused higher distortion of the measured data. In the SHPB experiments, the failure of the structure was homogenous and was not distorted laterally, however the measured data was of lower quality than in case of other structures. Although the dynamic equilibrium in the sample was achieved in all experiments, there was a higher level of error of the measured signals. The oscillations were caused by the complex deformation of the sample and its low mechanical impedance. An optimized pulse-shaping of incident pulse would be necessary for further reduction in these effects. The comparison of the deformation mechanisms for all the investigated structures during the quasi-static compression and the SHPB compression is shown in Figure 4.

3.4. DIC Results

The example of displacement and strain fields in horizontal and vertical direction is presented in Figure 5. This example shows resulting displacement and strain fields in 2D re-entrant auxetic structure. From the vertical displacements and vertical strains, the auxetic behavior of the sample is clearly evident. For all the samples (with/without the filling material), it was possible to calculate the displacements and strains up to 20% deformation. This enables to compare the results to geometrically nonlinear finite element models. These models describe the auxetic structures using beam elements and the auxetic behavior of the structures was studied in interrelations to several design parameters.^[41,42] In these FE simulations, the auxetic structures were developed using 3D beam element formulation (Timoshenko beam theory) directly from the CAD models. These FE models were loaded according to the experimental loading conditions (the lower part of the model restrained in vertical direction and the

upper part loaded by prescribed displacement) and stress-strain relations, the Poisson's ratio dependency on strain value were calculated. The comparison between the experimental and numerical results shows that the nonlinear FEA predicted lower values for the Poisson's ratio, however the trends are identical. Both the FEA and experiments showed the highest auxetic behavior (the highest absolute value of the Poisson's ratio) for the 2D missing rib and the lowest for the 2D re-entrant.

In the first frame capturing, the horizontal deformation (ϵ_1) (see Figure 5b), the non-homogeneous strain field, is visible, which indicates that the initial ramp-in part of the incident pulse impacts the specimen. From the following frames, it is evident that the ϵ_1 is quite homogeneous and, thus the experiment was successfully performed. The strain fields in the vertical direction show a very good symmetry and clearly indicate the auxetic behavior of the sample. The strains and Poisson's ratios calculated from the DIC for selected experiments are shown in Table 2.

The effect of filling on the Poisson's ratio for each type of the studied material has been established. For each filling, the Poisson's ratio has been calculated using DIC as described above in 3.1. Since the fillings are all low-stiffness materials, the effect was expected to be very low. This was proven for the missing rib structure where the Poisson's ratio effect was decreased from -0.25 to -0.145 for both gelatine and polyurethane fillings. For higher strain values, the Poisson's ratio gradually increases almost to zero (this was proved for gelatine filling). On the other hand, for the 2D re-entrant and 3D re-entrant honeycomb structures, the constrain effect for the Poisson's ratio was found regardless to the very low stiffness of fillers. For both filling materials the Poisson's ratio effect was constrained by the factor of 15 for small deformations. For higher deformations, the change of the Poisson's ratio has a cyclic feature, however, the values remain small compared to unfilled structures.

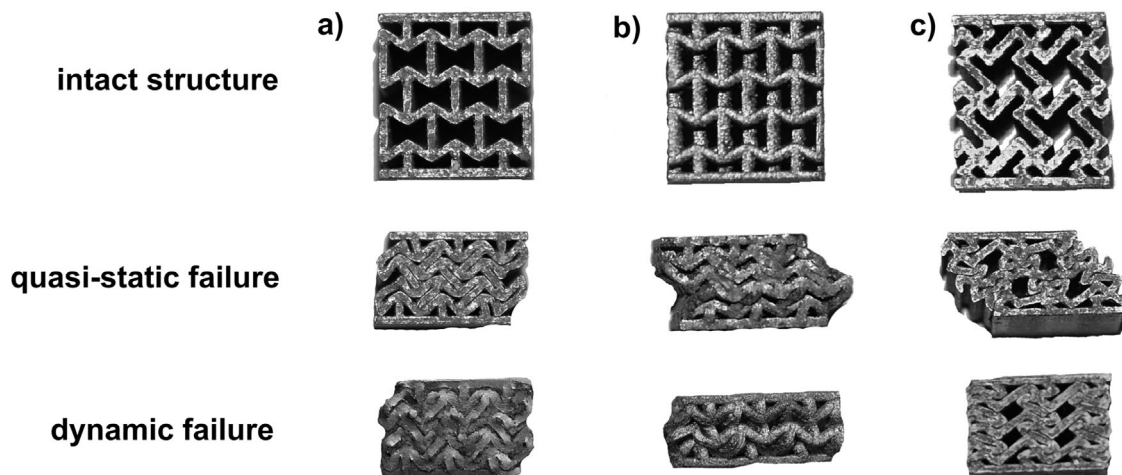


Fig. 4. Comparison of intact structures, structures collapsed in quasi-static experiment, and structures collapsed in SHPB experiments, (a) 2D re-entrant, (b) 3D re-entrant, (c) 2D missing rib.

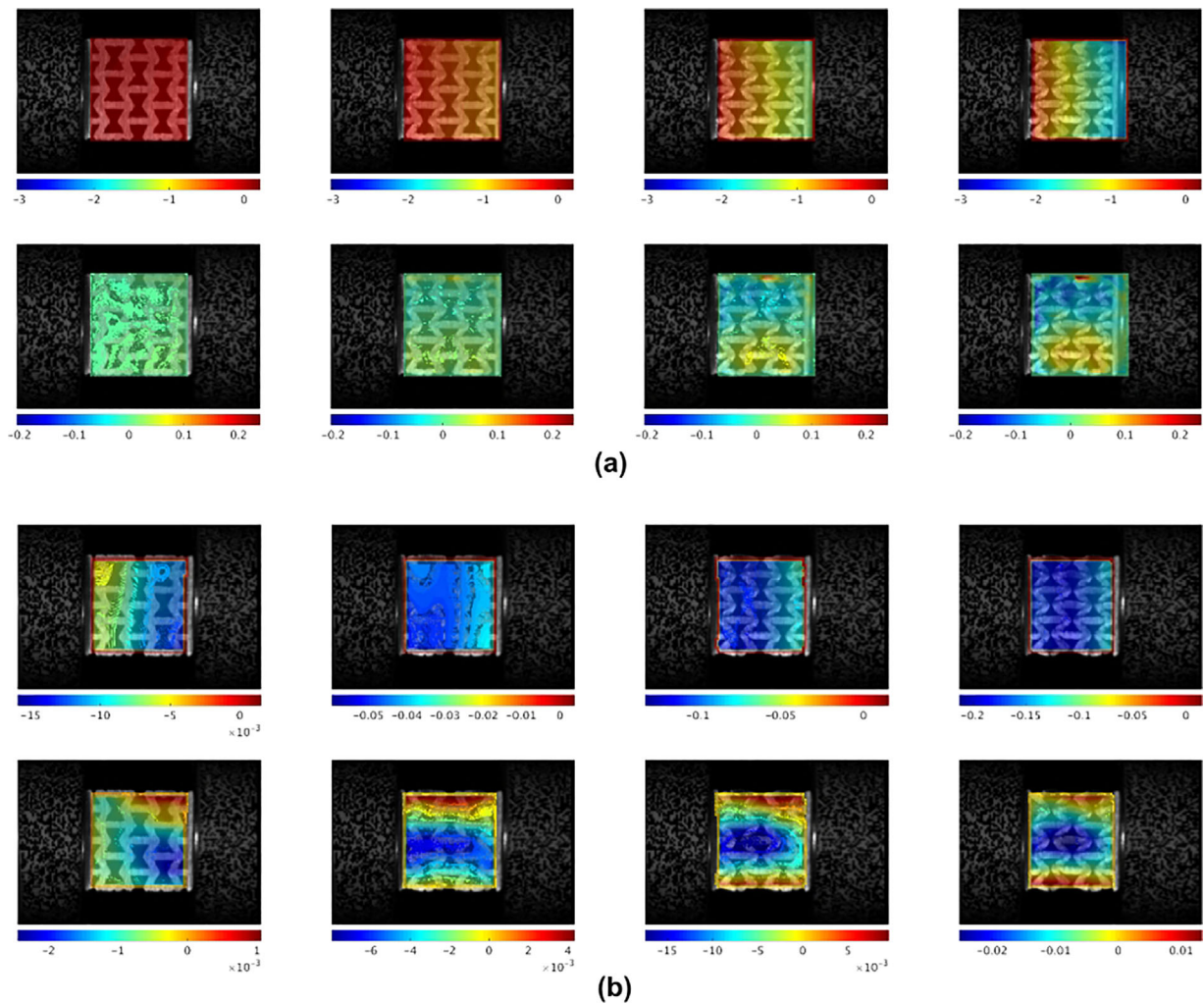


Fig. 5. (a) Full-field displacements in the 2D re-entrant sample during compression in selected time instants. Horizontal displacements (first row) and vertical displacements (second row). From the vertical displacement field, the auxetic behavior is clearly visible. (b) Full-field strains in the 2D re-entrant sample during compression in selected time instants. The ϵ_1 (first row) field shows homogeneous deformation in the sample during the whole process, while from the vertical strains (second row) the auxetic behavior can be assessed.

4. Discussion

The employed SHPB experimental setup and instrumentation was suitable for measurement of the auxetic structures under high strain rates. The setup calibration, pulse shaping techniques, and data correction methods were used for evaluation of dynamic material characteristics. The dynamic equilibrium was achieved in a short space of time after the impact of an incident wave on the specimen. The evaluated stress-strain curves were valid and were successfully used for the analysis of the effect of filling.

By the comparison of the ability of individual samples to absorb deformation energy, the following conclusions were drawn: gelatine filling has virtually no effect under quasi-static conditions, whereas its effect under dynamic loading is substantial. This was observed for all the studied auxetic structures. The effect of polyurethane filling on the plateau stress value was similar for quasi-static and dynamic compression.

The strain rate sensitivity of both the additively manufactured auxetic lattices and the filling was observed. The strain

Table 2. Results obtained for selected tests: Maximum values of strains in vertical (first row) and horizontal direction (second row) and calculated Poisson's ratio (third row).

	2D re-ent (Sample 1)	2D re-ent (Sample 2)	3D re-ent (Sample 1)	3D re-ent (Sample 2)	mRib (Sample 1)	mRib (Sample 2)
Max. ϵ_1	-0.129	-0.102	-0.112	-0.107	-0.121	-0.139
Max. ϵ_2	-0.017	-0.021	-0.018	-0.018	-0.038	-0.040
ν_{12}	-0.131	-0.197	-0.157	-0.171	-0.295	-0.286

rate sensitivity of the sintered structure is comparable with the results summarized in literature, where additively manufactured bulk specimens from sintered material were studied when SHPB was used.^[43,44]

The quasi-static compression tests showed similar deformation behavior of the auxetic lattices, as can be seen in quasi-static compression study concerning sintered metallic re-entrant lattices of similar geometry.^[41] A significant buckling effect and loss of stability of single layers in quasi-static compression were observed. All investigated structures exhibited lateral distortion, particularly the 2D missing rib structure. This effect was reduced significantly in dynamic compression in SHPB, where the lateral distortion was minimum and the structures underwent homogeneous deformation. The structure densification occurred at lower strains in dynamic compression as well.

As expected, the most distinct effect on energy absorption capacity was found for the 3D re-entrant. For this structure, not only the ratio between dynamic and static plateau stress was the highest, but also the effect of strain rate sensitive filling was the most significant among all studied structures. This was especially apparent for the polyurethane filling. The effect of the gelatine filling on average plateau energy for the same structure was less than 10% for the dynamic experiments.

The DIC was used to compute the displacement and strain fields during the dynamic and quasi-static compression of the samples. The DIC was used primarily to compute the Poisson's ratio of the structures and compare the values for static and dynamic loading. The important finding is that the auxetic behavior of the structures under quasi-static loading is not very strong, but it is very profound under dynamic loading. The calculated values of the Poisson's ratio for all studied auxetic structures was close to the values predicted by the referenced FE simulations.^[41,42] However, the experimentally obtained values were approximately 20% higher than those predicted by the simulations. This is mainly caused by the localized necking in the middle of the samples, which is not captured in the simulations. From the DIC, it was found that nearly homogeneous compression in the loading direction was maintained for all samples. For all experiments, we were successful in computation of the strain fields from the recorded images for compression up to 20%.

We have shown that the dynamic compression of additively manufactured auxetic lattices can be investigated by SHPB and that the effect of the strain rate sensitive filling can be experimentally evaluated at high strain rates. Thus, the obtained results can be used in conjunction with methods of numerical modeling, namely the explicit dynamic simulations, to propose auxetic lattice filled with strain rate sensitive material. However, these structures have to be numerically optimized for a given application. The application potential of 3D printed auxetic materials ranges from structural components to reduce the vibration or car crash absorber elements to wearable impact protection.^[45]

Additive manufacturing technologies (3D printing, powder metallurgy/sintering, krigami, laser writing, SLS, etc.) produce complex parts without the design constraints of traditional manufacturing technologies. The traditional manufacturing, like machining and casting, produces parts with higher accuracy and better quality of surface finish and, more importantly, with better mechanical properties. This has to be taken into account since in the presented application the impact properties of the printed structures can differ significantly.

5. Conclusion

Three types of auxetic structures were prepared using SLS from stainless steel powder. Two types of strain rate sensitive fillings were used in these structures to study their influence on energy absorption capacity at wide range of strain rates. The samples were subjected to quasi-static and dynamic compressive loading using SHPB. Stress strain diagrams were obtained for each sample at a given strain rate. The mechanical properties of the structures were compared in terms of an average plateau stress and specific energy absorption in the plateau region. Auxetic behavior of the samples was assessed using the DIC – the Poisson's ratio was calculated from the recorded images of the deforming samples. Based on the evaluated results, the following conclusions can be drawn:

- 1) SHPB is a suitable method for investigation of deformation behavior of the laser-sintered auxetic structures. Dynamic equilibrium was achieved in the experiments and the specimens were crushed at constant strain rate.
- 2) Material used for sintering was identified as strain rate sensitive. All structures exhibited approximately 40–70% higher plateau stress in dynamic compression.
- 3) The effect of the strain rate sensitive filling on mechanical properties was evaluated. Gelatine filling had negligible effect on the plateau stress and absorbed energy in quasi-static compression. The polyurethane filling specimens exhibited specific plateau energy 10–25% higher than that of specimens without filling in quasi-static compression. Specific absorbed energy of the specimens with gelatine filling was approx. 5–10% higher than of the specimens without filling in dynamic compression. Specific absorbed energy of the specimens with polyurethane filling was approx. 5–40% higher than of the specimens without filling in dynamic compression.
- 4) Different deformation behavior of the specimens was observed during the quasi-static and dynamic experiments. Structures in quasi-static compression exhibited lateral deformation during compression, in particular the 2D missing rib. The dynamically compressed specimens exhibited homogeneous deformation without lateral distortion. Densification of the structures occurred at lower strain in dynamic compression compared to quasi-static tests.
- 5) The Poisson's ratio was evaluated in both quasi-static and dynamic experiments using the DIC. Deformation with negative Poisson's ratio was identified in all structures in quasi-static and dynamic compression. Although the

stiffness of the filling materials was very low, negative Poisson's ratio of all filled auxetic structures was significantly reduced. This effect was particularly strong in the 3D re-entrant structure.

Article first published online: May 8, 2017

Manuscript Revised: April 12, 2017

Manuscript Received: January 31, 2017

-
- [1] K. E. Evans, A. Alderson, *Adv. Mater.* **2000**, *12*, 9, 617
- [2] K. K. Saxena, R. Das, E. P. Calius, *Adv. Eng. Mater.* **2016**, *18*, 1847.
- [3] H. M. A. Kolken, A. A. Zadpoor, *RSC Adv.* **2017**, *7*, 5111.
- [4] L. Yang, O. Harrysson, H. West II, D. Cormier, *22nd Annual Int. Solid Freeform Fabrication Symposium – An Additive Manufacturing Conf.*, SFF, The University of Texas at Austin, USA **2011**, p. 464.
- [5] O. Duncan, L. Foster, T. Senior, A. Alderson, T. Allen, *Smart Mater. Struct.* **2016**, *25*, 5.
- [6] E. A. Friis, R. S. Lakes, J. B. Park, *J. Mater. Sci.* **1988**, *23*, 4406.
- [7] N. Chan, K. E. Evans, *J. Mater. Sci.*, **1997**, *32*, 5945.
- [8] J. Schwardtfefer, P. Heinel, R. F. Singer, C. Körner, *Phys. Status Solidi B* **2010**, *247*, 267.
- [9] A. Alderson, K. L. Alderson, D. Attard, K. E. Evans, R. Gatt, J. N. Grima, W. Miller, N. Ravirala, C. W. Smith, K. Zied, *Compos. Sci. Technol.* **2010**, *70*, 1042.
- [10] A. Lorato, P. Innocenti, F. Scarpa, A. Alderson, K. L. Alderson, K. M. Zied, N. Ravirala, W. Miller, C. W. Smith, K. E. Evans, *Compos. Sci. Technol.* **2010**, *70*, 1057.
- [11] S. Li, H. Hassanin, M. M. Attallah, N. J. E. Adkins, K. Essa, *Acta Mater.* **2016**, *105*, 75.
- [12] K. Wang, Y.-H. Chang, Y. Chen, C. Zhang, B. Wang, *Mater. Des.* **2015**, *67*, 159.
- [13] J. Schwardtfefer, F. Schury, M. Stingl, F. Wein, R. F. Singer, C. Körner, *Phys. Status Solidi B* **2012**, *249*, 1347.
- [14] F. Warmuth, F. Osmanlic, L. Adler, M. A. Lodes, C. Körner, *Smart Mater. Struct.* **2017**, *26*, article code 025013.
- [15] L. Yang, O. Harrysson, H. West, D. Cormier, *Int. J. Solids Struct.* **2015**, *69–70*, 475.
- [16] R. Magalhaes, P. Subramani, T. Lisner, S. Rana, B. Ghiassi, R. Figueiro, D. V. Oliveira, P. B. Lourenco, *Compos. Part A Appl. Sci. Manuf.* **2016**, *87*, 86.
- [17] T.-C. Lim, *Micromechanical Models for Auxetic Materials, Engineering Materials*, Springer, Science+Business Media, Singapore **2014**.
- [18] L. Yang, D. Cormier, O. Harrysson, H. West, In *Proc. of the Solid Freeform Fabrication Symp.* The University of Texas at Austin, USA **2015**, p. 1394.
- [19] S. Mohsenizadeh, R. Alipour, A. Farokhi Nejad, M. Shokri Rad, Z. Ahmad, *Procedia Manuf.* **2015**, *2*, 331.
- [20] F. Scarpa, J. R. Yates, L. G. Ciffo, S. Patsias, *Proc. Inst. Mech. Eng. Part C: J. Mech. Eng. Sci.* **2002**, *216*, 1153.
- [21] F. Scarpa, L. G. Ciffo, J. R. Yates, *Smart Mater. Struct.* **2004**, *13*, 49.
- [22] T. C. Lim, A. Alderson, K. L. Alderson, *Phys. Status Solidi B*, **2014**, *251*, 307.
- [23] L. Yang, O. Harrysson, D. Cormier, H. West, C. Park, K. Peters, In *Proc. 24th Int. SFF Symp. – Add. Manuf. Conf.*, SFF, The University of Texas at Austin, USA **2013**, p. 929.
- [24] R. E. Raj, V. Parameswaran, B. S. S. Daniel, *Mater. Sci. Eng. A* **2009**, *526*, 11.
- [25] T. P. M. Johnson, S. S. Sarva, S. Socrate, *Exp. Mech.* **2010**, *50*, 931.
- [26] M. Peroni, G. Solomos, N. Babcsan, *Materials* **2016**, *9*, 27.
- [27] T. Tancogne-Dejean, A. B. Spierings, D. Mohr, *Acta Mater.* **2016**, *116*, 14.
- [28] P. Wang, S. Xu, Z. Li, J. Yang, C. Zhang, H. Zheng, S. Hu, *Mater. Sci. Eng. A* **2015**, *620*, 253.
- [29] B. Yang, L. Tang, Y. Liu, Z. Liu, Z. Jiang, D. Fang, *Mater. Sci. Eng. A* **2013**, *560*, 734.
- [30] B. Hou, H. Zhao, S. Patoffatto, J. G. Liu, Y. L. Li, *Int. J. Solids Struct.* **2012**, *49*, 2754.
- [31] J. Liu, D. Saletti, S. Patoffatto, H. Zhao, *Polym. Test.* **2014**, *36*, 101.
- [32] C. W. Smith, J. N. Grima, K. E. Evans, *Acta Mater.* **2000**, *48*, 4349.
- [33] J. Kwon, G. Subhash, *J. Biomech.* **2010**, *43*, 420.
- [34] C. Bacon, *Exp. Mech.* **1998**, *38*, 242.
- [35] J. Janiszewski, W. Buzantowicz, P. Baranowski, *Prob. Mechatron. – Armament, Aviat. Saf. Eng.* **2016**, *7*, 17.
- [36] S. Montabone, *Beginning Digital Image Processing: Using Free Tools for Photographers*, Apress, New York, USA **2010**, 312, ISBN 978-1-4302-2841-7. <https://doi.org/10.1007/978-1-4302-2842-4>
- [37] H. A. Bruck, S. R. McNeill, M. A. Sutton, W. H. Peters III, *Exp. Mech.* **1989**, *29*, 1.
- [38] G. Vendroux, W. G. Knauss, *Exp. Mech.* **1998**, *38*, 1.
- [39] P. Zhou, K. E. Goodson, *Opt. Eng.* **2001**, *40*, 1.
- [40] W. Tong, *Strain* **2005**, *41*, 1.
- [41] T. Doktor, P. Koudelka, T. Fila, O. Jirousek, In *Proc. of the Fifteenth Int. Conf. on Civil, Structural and Environmental Engineering Computing Paper 153*, Civil-Comp Press, Stirlingshire, United Kingdom **2015**.
- [42] P. Koudelka, O. Jirousek, T. Fila, T. Doktor, *Mater. Technol.* **2016**, *50*, 3.
- [43] R. Fadida, D. Rittel, A. Shirizly, *J. Appl. Mech.* **2015**, *82*, 4.
- [44] W.-S. Lee, J.-K. Chou, *Mater. Trans.* **2005**, *46*, 805.
- [45] K. K. Saxena, E. P. Calius, R. Das, *ASME Int. Mechanical Engineering Congress and Exposition*, Vol. 9, Mechanics of Solids, Structures and Fluids; NDE, Diagnosis, and Prognosis, ASME, Phoenix, Arizona, USA **2016**.
-

Strain Dependency of Poisson's Ratio of SLS Printed Auxetic Lattices Subjected to Quasi-Static and Dynamic Compressive Loading

Tomáš Fíla,* Petr Koudelka, Petr Zlámal, Jan Falta, Marcel Adorna, Michaela Neuhäuserová, Jutta Luksch, and Ondřej Jiroušek

This paper deals with experimental investigation into a strain-rate dependent function of Poisson's ratio of three auxetic structures subjected to compressive loading. The missing rib, the 2D re-entrant honeycomb, and the 3D re-entrant honeycomb lattices printed using selective laser sintering from powdered SS316L austenitic steel are investigated. The samples are subjected to uni-axial compression under quasi-static conditions and dynamic conditions using the Split Hopkinson Pressure Bar (SHPB). The deforming specimens are optically observed in order to apply a digital image correlation for evaluation of the in-plane displacement and strain fields. From the calculated strain fields, the function of Poisson's ratio is calculated for each experiment using different methods taking specific regions of interest of the specimen microstructures into account. The obtained functions of Poisson's ratio are plotted for each microstructure and strain-rate. The analysis of the results shows that the strain-rate has a significant influence on the deformation characteristics of all the investigated microstructures yielding differences in the magnitude of the minima of Poisson's ratio and the differences in the maximum overall compressive strain, where the lattices are still auxetic.

special design of the internal structuring, but examples of naturally occurring materials with the same property also exist, such as mineral rods, zeolites, silicates, and a few biological tissues.^[1]

The example of a material with a negative Poisson's ratio was described by Kolpakov^[2] in 1985. The first cellular materials with a negative Poisson's ratio were designed and synthesized in 1987 by Lakes et al.^[3] from conventional low-density open-cell polymer foams by tri-axial compression and the subsequent placing in a mold causing the ribs of each cell to protrude inward permanently. The word "auxetic" referring to material with negative Poisson's ratio was used by Evans^[4] in 1991. With the advancement of material science and especially with the emergence of computer-aided design together with additive manufacturing technologies, different structures with 2D and 3D auxetic behavior have been designed, produced, and tested.^[4–8] Currently, there are generally eight types of common auxetic structures that can be classified


1. Introduction

Auxetic structures are metamaterials that possess a negative Poisson's ratio due to the deformation response of their internal structure to the applied loading. As a result, they expand in a transverse direction when loaded in tension and shrink when compressed. This behavior can be achieved artificially due to the

as: (a) rigid node rotation, (b) chiral, (c) re-entrant lattice, (d) elastic instability, (e) kirigami fractal cut, (f) origami, (g) star shape connected, and (h) missing-rib.^[9,10] Design optimization and improvements of the deformation characteristics have been also investigated^[11–13] including out-of-plane deformation characteristics and bending behavior.^[14,15] Owing to their specific properties, many interesting applications of auxetic materials have been described as potentially rendering use in different application areas, ranging from the medical (foldable devices, angioplasty, or esophageal stents)^[16,17] to the automotive, aerospace, sport, or defense industry. Due to the possible increase in strain energy absorption, special attention has been paid to the application of auxetic materials for the energy absorption purposes during crash, blast, and other impact loading.^[18–20] Advancement in additive manufacturing and particularly the introduction of selective laser sintering/melting (SLS/SLM), powder metallurgy (P/M) sintering, and pulsed electric current sintering (PECS) enabled one to use metals as the base material for the production of the structures.^[21] This has broadened the application area of auxetic materials in impact

T. Fíla, P. Koudelka, Dr. P. Zlámal, J. Falta, M. Adorna, M. Neuhäuserová, Prof. O. Jiroušek
Department of Mechanics and Materials
Faculty of Transportation Sciences
Czech Technical University in Prague
Na Florenci 25, 110 00 Prague 1, Czech Republic
E-mail: fila@fd.cvut.cz

J. Luksch
Saarland University
Applied Mechanics
Campus A4.2, 661 23 Saarbruecken, Germany

 The ORCID identification number(s) for the author(s) of this article can be found under <https://doi.org/10.1002/adem.201900204>.

DOI: 10.1002/adem.201900204

protector devices,^[22] and increased the energy absorption capability through the possibility of using lighter and thinner components. These new technologies are still rather expensive, but with their increasing accessibility and the potential of their utilization in mass production leading to reduction in the final price, the application of 3D printing in this area is expanding.

Regarding the issue of energy absorption, it is crucial to describe the deformation behavior of the structure under large deformation (i.e., large overall compressive strain) properly. In the experimental investigation, it is necessary to reliably evaluate the strains during the experiment and assess the deformation modes taking the large displacements, large rotations, and contacts between the struts into account. This is crucial for the calibration or verification of the numerical models against the experimentally obtained data.^[23]

For the proper description of the deformation behavior, it is necessary to evaluate Poisson's ratio of the structure and more importantly, the dependency of Poisson's ratio on the compressive strain (the so-called function of Poisson's ratio). The design parameters, especially the re-entrant angles, influencing Poisson's ratio and its strain dependency, can be predicted using analytical or numerical (FE – finite elements) models. Nevertheless, outside the small-strain linear region, these characteristics must be evaluated experimentally due to their strong non-linearity.^[24]

Furthermore, the strain-rates and the velocities of the specific deformation processes have to be taken into account considering the expected applications of the auxetics, particularly the energy absorption of the rapidly moving objects or blasts. The deformation response of many homogeneous materials (i.e., ferrous alloys, copper, aluminum, etc.) is strain-rate dependent and significant variations between the quasi-static and the dynamic characteristics can be observed, including differences in low and high velocity impacts.^[25] The difference of the dynamic behavior is further amplified in the case of auxetics due to the cellular nature of the constructs. The strain-rate dependency of the base material is then combined with the effects of the micro-inertia, localized heating, pore pressure, and others.^[26,27] Understanding these phenomena and the assessment of their influence on the effective properties of the auxetics can only be revealed by experimental methods providing sufficient strain-rates in the sample. Among the available methods, particularly the Split Hopkinson Pressure Bar (SHPB) and the single-stage powder gun have been successfully used for the evaluation of the mechanical characteristics of auxetics.^[28–30] Other experimental studies investigating the mechanical behavior of the auxetic structures under dynamic loading conditions, e.g., the crash behavior of a cylindrical tube with auxetic structures,^[31] the drop-weight impact characteristics,^[32] and the impact properties of an auxetic textile^[33] were also published. Studies analyzing auxetic structures under dynamic conditions using numerical simulations are also available.^[34–37]

In our previous studies, we have already shown that experimentally verified numerical modeling can be used for the prediction of the mechanical properties of the auxetics as a basis for optimization procedures.^[38] In the field of dynamic testing, we have shown that the SHPB technique can be successfully used to evaluate the deformation characteristics of

structures based on different auxetic unit cells and to assess the influence of the strain-rate dependent filling on their overall properties.^[28] This paper is aimed at addressing the issue of the experimental investigation of the deformation behavior of additively manufactured auxetic structures under high strain-rates using SHPB with a focus on the evaluation of the function of Poisson's ratio (strain dependent Poisson's ratio) using an in-house developed digital image correlation (DIC) procedure applied on sets of images of the deforming samples captured using a high-speed camera.^[39,40] The samples were designed as structures with both in-plane and volumetric auxetic behavior and 3D printed from powdered SS316L stainless steel using the SLS method. The manufactured specimens were experimentally studied under quasi-static and dynamic loading and the strains during the compression were evaluated using DIC with sub-pixel precision to calculate the highly detailed function of Poisson's ratio of the micro-geometries up to the densification region of their deformation response.

2. Experimental Section

2.1. Specimens

Three different types of auxetic microarchitectures exhibiting either in-plane and volumetric negative Poisson's ratio were investigated. The specimens were printed in an AM 250 device (Renishaw, UK) using the SLS method by sintering powdered SS316L-0407 austenitic stainless steel composed of iron alloyed by 16–18 wt% of chromium, 10–14 wt% of nickel, and 2–3 wt% of molybdenum. The maximum permissible content of carbon is up to 0.03 wt% making this material an extra-low carbon modification of a standard SS316L alloy. The melting range of the material is 1371–1399 °C and the density of the wrought solid is 7990 kg m⁻³. The mechanical properties of the additively manufactured components (according to the manufacturer of the sintering device) are summarized in **Table 1**.

The SLS based additive manufacturing method was used to produce samples composed of the periodic assembly of three different unit cell geometries: the missing-rib structure, the two dimensional, and the three-dimensional re-entrant honeycomb structures. Both the missing rib and the two dimensional re-entrant honeycomb structures exhibit the in-plane negative Poisson's ratio, whereas the three-dimensional re-entrant honeycomb exhibits a volumetric negative Poisson's ratio during deformation. The printed samples of the structures are shown in **Figure 1**. In contrast with our previous study,^[28] we designed the geometry of the samples with a higher number of

Table 1. Direction dependent mechanical properties of the wrought SS316L-0407 steel.

Parameter	Horizontal direction	Vertical direction	Unit
Compressive strength	662 ± 2	574 ± 10	MPa
Yield strength	518 ± 5	440 ± 10	MPa
Modulus of elasticity	167 ± 8	134 ± 17	GPa
Elongation at break	43 ± 2	35 ± 8	%

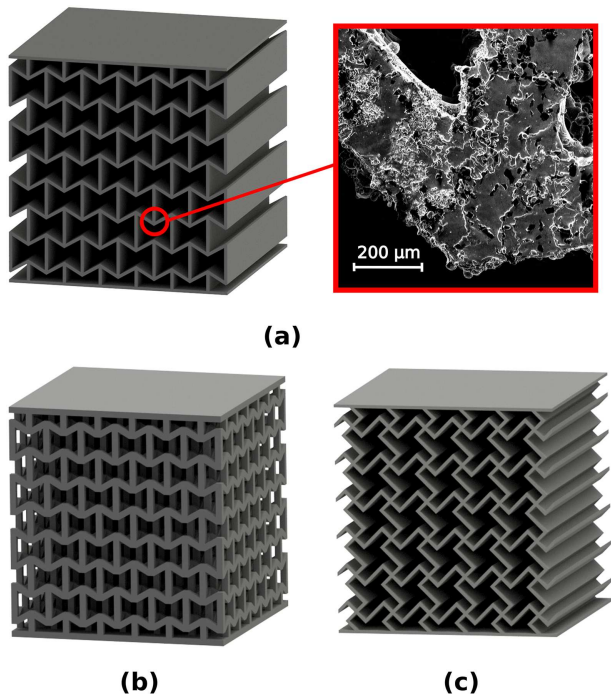


Figure 1. Tested auxetic lattices: a) 2D re-entrant honeycomb with SEM image detail of the strut joint, b) 3D re-entrant honeycomb, and c) 2D missing-rib.

unit-cells in the cross-section of the produced samples. This was achieved by changing the ratio of the characteristic unit-cell dimension to the overall specimen dimensions (constrained by the diameter of the bars used in the SHPB setup), i.e., the dimensions of the unit-cells were reduced to obtain at least 6 unit-cells in both directions of the specimen cross-section. This number was selected according to the general requirements on the RVE as defined by Gibson and Ashby et al.^[41] In relation to the decrease of the unit-cell dimensions, the nominal thickness of the individual struts within the microstructure was also reduced down to approximately 0.3 mm. The overall dimensions of the samples were $12.15 \times 12.15 \times 12.58$ mm ($w \times d \times h$) according to the dimensions and performance of the SHPB setup, which ensured reaching the densification region of the materials response during the impact experiments. The ratio of approximately 1 between the specimen height and cross-section dimensions was selected to minimize the frictional and inertia effects in the SHPB experiment. The missing-rib specimens were composed of 36 unit-cells in a 6×6 arrangement at a nominal porosity of 74.37%, the two-dimensional re-entrant honeycomb specimens were composed of 42 unit-cells in a 6×7 arrangement at a nominal porosity of 73.43%, and the three-dimensional re-entrant honeycomb specimens were composed of 252 unit-cells in $6 \times 6 \times 7$ arrangement at a nominal porosity of 72.36%. The production of such samples was at the resolution limit of the used SLS device as the treatment of the heat dissipation brought serious challenges to tuning the manufacturing procedure in order to avoid the collapse of the specimens during printing. For every type of the micro-architecture, three specimens were used during the quasi-static

experiments and five specimens for each strain-rate during the SHPB dynamic testing. Hence, 13 samples of every microstructure were tested and evaluated yielding 39 tested samples in total. SEM inspection of the printed lattices was performed showing that imperfections occur primarily on the surface of the specimen with the magnitude of twice the size of powder particles of the printing material. This is in this case approximately $2 \times 50 \mu\text{m}$. The resulting surface quality affects the ability of the SLS printing to reproduce the sharp edges and corners designed in the microstructure, where particularly the sharp corners are printed as filleted connections with the radius equivalent to the surface roughness.

2.2. Quasi-Static Testing

To obtain the quasi-static response of the auxetic micro-architectures, the SLS printed samples were subjected to uniaxial compression tests performed using the electromechanical loading device (Instron 3382, Instron, USA). The crosshead speed was set to 0.5 mm min^{-1} (strain-rate 0.006 1/s) up to 50% of the overall deformation defined by the crosshead displacement. The deforming microstructure of the samples was observed by a CCD digital camera to enable the optical evaluation of the displacement and strain fields of the investigated microstructures, which was necessary for the evaluation of the stress-strain diagrams and the functions of Poisson's ratio. The optical part of the experimental setup was composed of a monochromatic camera (Manta G-504B, AVT, Germany) with resolution of 2452×2056 px operated at 3 fps and attached to a bi-telecentric zoom revolver (TCZR072, OptoEngineering, Italy). The specimens were illuminated using a high-power cold-light LED source (KL2500, Schott, Germany). The acquisition of the projections was controlled with custom-developed software based on the OpenCV library and Python programming language. The observed faces of the specimens were sprayed using a granite paint to generate a random pattern to enable reliable optical deformation tracking. The quasi-static loading setup is shown in **Figure 2**.

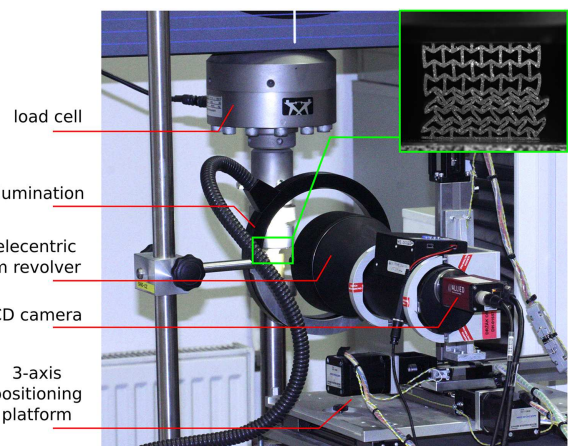


Figure 2. Experimental setup used for uni-axial quasi-static compression.

2.3. Digital Image Correlation of the Quasi-Static Experiments

The acquired series of images were exported to a PNG format using a lossless compression algorithm and subjected to a custom DIC procedure implemented in Matlab (Mathworks, USA). The procedure based on the Lucas–Kanade tracking algorithm^[42] uses a zero-mean normalized sum-of-square differences (ZNSSD) criterion to compute the similarity in pixel intensity between the reference and the deformed image subsets,^[43] which is then followed by the optimization of the received displacement by the Newton–Raphson iterative algorithm to achieve the sub-pixel accuracy of the results. Thus, a periodical grid of correlation points was generated for every investigated sample, where the location and distance between the individual correlation points was selected in order to track the deformation of the joints between the individual struts to enable the reliable evaluation of the function of Poisson’s ratio. Each marker was then tracked throughout the acquired series of projections by searching for the highest correlation coefficient between two consequent projections. As a result, the in-plane displacement and strain fields of the deforming microstructures were obtained and averaged over all the measurements comprising the respective auxetic microarchitecture. Because the derivation of the strains from the displacements is based on the calculation of a Green–Lagrange strain tensor, which involves the differentiation of the strain fields, particular attention has to be paid to the treatment of noise in the data. For this reason, a correlation window was set to 25 px and its neighborhood, where the correlation was sought around a centroid of the correlation window in the two consequent projections, was set to 30 px and kept constant in all the evaluated quasi-static experiments. To evaluate the influence of the boundary effects in the periodical assembly of the different unit-cells, the DIC procedure was performed on different regions within the specimens’ microstructure as depicted by the red and green colors in **Figure 3** on an example of the 2D re-entrant honeycomb structure. The correlation points were generated in the selected joints of the individual struts; in total, 48 points were tracked on the re-entrant honeycomb structures and 36 points on the missing-rib structures.

2.4. Dynamic Testing

To evaluate the response of the auxetic structures under dynamic conditions, the specimens were subjected to dynamic impacts using the SHPB apparatus at two different strain-rates to reveal the possible strain-rate sensitivity of the samples and the changes in the deformation behavior of the structures. The standard arrangement of the experimental setup with the striker, incident, and transmission bars was used for the testing. All the bars had a nominal diameter of 20 mm and were made of a high-strength aluminum alloy (EN-AW-7075). A striker bar with a length of 500 mm was accelerated using a gas-gun system with a barrel length of 2500 mm. The incident bar and the transmission bar had an identical length of 1600 mm. The incident bar was instrumented by establishing three individual measurement points, each equipped by foil strain-gauges (3/120 LY61, HBM,

Germany) with an active length of 3 mm. The foil strain-gauges were selected instead of semiconductor strain-gauges because of their linearity up to high strains and higher service-life which were key factors in the testing at high impact velocities. On the incident bar, one measurement point was located in the middle of the bar and the other two measurement points were located 200 mm from each of the faces of the bar, while the transmission bar was equipped with one measurement point located 200 mm from the impact face of the bar. At each measurement point, a pair of strain-gauges wired in the Wheatstone half-bridge arrangement was used. This solution enabled one to compensate for the possible minor bending of the bars during the impact test and to amplify the output signal two times in comparison with a quarter-bridge arrangement. The strain-gauge signals were amplified using a differential low noise amplifier (EL-LNA-2, Elsys AG, Switzerland) with a gain of 100. The amplified strain-gauge signals were digitized and recorded using a pair of synchronized high-speed 16-bit digitizers (PCI-9826H, ADLINK Technology, Taiwan) at a sampling rate of 20 MHz. Data acquisition and control of the experiment was performed using a custom LabView (National Instruments, USA) interface. The striker impact velocity measurement and the triggering of the data acquisition system were performed by a pair of a short-reaction time through-beam photoelectric sensors (FS/FE 10-RL-PS-E4, Sensopart, Germany). The experiments were observed by a high-speed camera (Fastcam SA-5, Photron, Japan) with a CMOS sensor having a pixel size of 20 μm and full-frame resolution of 1024 \times 1024 pixels. In the experiments, the region of interest was set to 256 \times 168 pixels. The reduced resolution of the camera allowed for observation of the specimen during the impact with approximately 130 kfps. The triggering of the camera was performed using the same photoelectric sensor used for the triggering of the data acquisition system. Thus, the image sequence captured with the high-speed camera was

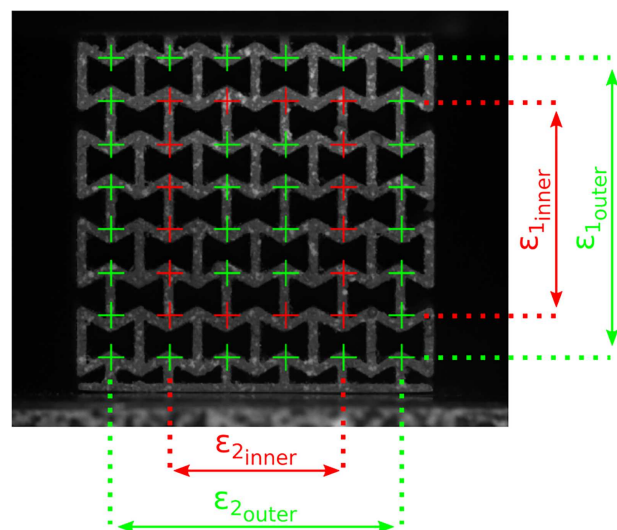


Figure 3. Example of the correlation pattern (green color) generated on the 2D re-entrant honeycomb specimen showing the inner (red) and outer part used for the DIC evaluation of the results.

synchronized with the strain-gauge signals. The overall view of the SHPB experimental setup is shown in **Figure 4**.

To reach two different strain-rates in the specimens, two impact velocities of the striker bar were used. A lower striker impact velocity of approx. 21 m s^{-1} was used to compress the specimens at a strain-rate of approximately 1500 $1/\text{s}$ (referred to as low-rate in the following text). A higher striker impact velocity of approximately 43 m s^{-1} was used to compress the specimens at a strain-rate of approximately 3000 $1/\text{s}$ (referred to as high-rate in the following text). The maximum reachable strain in the SHPB method is dependent on the striker impact velocity and the striker length. However, a longer striker bar could not be used in the low-rate experiments due to the superposition of the forward-propagating and backward-propagating waves in the strain-gauge signals. Depending on the type of the auxetic structure, the specimens in the low-rate experiments were compressed to a maximum overall strain of approximately 25–30%. The specimens in the experiments conducted at the high-rate reached a significantly higher overall strain of approximately 40–50%. For the minimization of the wave dispersion effects, cylindrical soft copper pulse-shapers were placed on the incident bar impact face. Depending on the type of the auxetic structure and strain-rate, the diameter and the thickness of the pulse-shapers varied between 7–8 mm and 0.5–1 mm, respectively. The pulse-shapers were very effective in filtering out the high frequencies causing Pochhammer–Chree oscillations and in the reduction of the ramp-in effect during the initial phase of the wave impact on the specimen. Sufficient quality dynamic equilibrium was reached in all the experiments at both strain-rates. Using the pulse-shaping technique, it was possible to maintain a constant strain-rate during the impact up to the densification of the auxetic structure. The typical measured response of the lattice during the impact is shown in **Figure 5**. The plot represents the stress–strain diagrams of the 3D re-entrant honeycomb evaluated using different methods (1 wave, 2 waves, 3 waves) and the strain-rate-strain diagram for the same experiment. All the methods used for the evaluation of the stress–strain curves exhibit good convergence after the initial phase of the impact, representing good quality dynamic equilibrium during the experiment. The strain-rate-strain curve shows constant values of the strain-rate up to the densification of

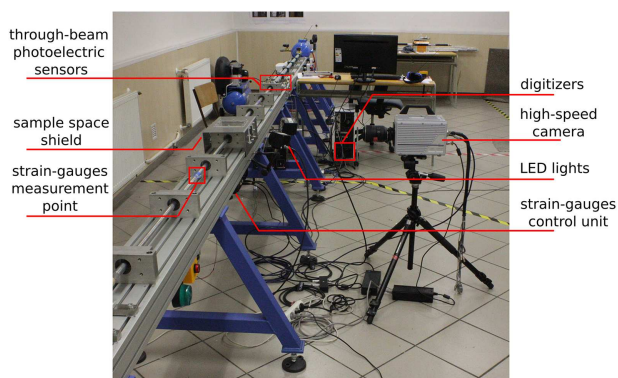


Figure 4. Hopkinson bar experimental setup used for dynamic compression of the specimens.

the structure. Approximately 35 images of the deforming specimen during the first deformation pulse were captured using the high-speed camera and processed using the DIC technique.

2.5. Digital Image Correlation of the SHPB Experiments

From the recorded image sequences, only the initial part of the recordings capturing the first deformation pulse was used for the further DIC analysis and evaluation of Poisson's ratio, while the consequent images in the sequence were used for the inspection of the experiment validity. For the DIC procedure, the native raw files were converted to a PNG image file format with lossless compression and the identical region of interest (ROI) was cropped from the images. The DIC procedure was then performed using the same tracking algorithm as in the case of the quasi-static experiments. The output from the algorithm was a matrix of current coordinates of the markers for each loading state in the image sequence that was used for further evaluation of the strain dependent Poisson's ratio using Matlab.

2.6. Function of Poisson's Ratio – Evaluation

From the strain fields assessed by DIC, Poisson's ratio ν_{12} was calculated using the formula

$$\nu_{12} = \frac{-\varepsilon_2}{\varepsilon_1}$$

where ε_2 is the lateral strain in the direction perpendicular to the direction of loading and ε_1 is the strain in the direction of loading.

Different methods were used for determining the function of Poisson's ratio for both the quasi-static and dynamic experiments. The outputs of the different methods were analyzed and

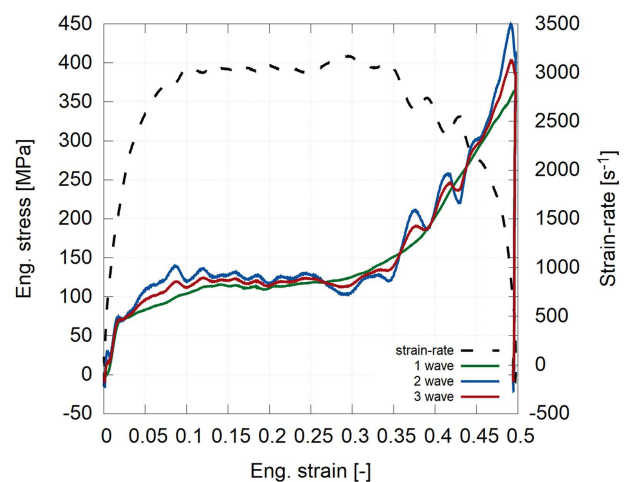


Figure 5. Typical measured stress–strain and strain-rate-strain diagram (3D re-entrant honeycomb).

compared to evaluate their reliability. As three specimens of each microarchitecture were tested in the quasi-static experiments and five specimens were tested at each strain-rate during the SHPB experiments, the mean curves and standard deviation envelopes of the functions of Poisson's ratio for each type of experiment were calculated.

The methods for calculating Poisson's ratio were based on different sets of correlation markers selected for the calculation. In the first method, both the deformation parallel and perpendicular to the direction of loading were evaluated from the inner part of the specimens' microstructure, where the concentration of the lateral strain occurred (see the red markers of the correlation points in Figure 3). In the following text, the function of Poisson's ratio calculated from this region of interest will be designated as the "inner-inner" function. In the second method, the deformation in the same direction was calculated from the outer part of the specimens' microstructure (see the outer green markers of the correlation points in Figure 3). The corresponding function of Poisson's ratio will be designated as the "outer-outer" function. The difference in the functions of Poisson's ratio using both methods enables one to characterize the influence of boundary effects emerging from the cellular nature of the specimens. In the dynamic experiments, another method based on the local Poisson's ratio was also employed to study its variations in different parts of the crushed microstructures. Here, Poisson's ratio was derived as a mean of the ratio between the lateral and longitudinal strains in the localized regions around every correlation point within the outer-outer region. Since Poisson's ratio calculated at every time step for a given correlation point is based on a local gradient of the lateral and longitudinal deformation, the corresponding function of Poisson's ratio will be designated as the "local-gradient" function. The inner-inner and outer-outer methods were based on a correlation grid composed of markers generated over the joints of the individual struts forming the auxetic microstructure. Due to the lower resolution of the high-speed images and rapid changes in the microstructure, the local-gradient method was based on a grid with higher density composed of 11×11 points covering the whole observed face of the specimen. Apart from the possibility to plot maps of the strains and Poisson's ratio over the entire investigated structure, the average over the region corresponding to the inner-inner method of evaluation was calculated to obtain the comparative Poisson's ratio-strain curves.

3. Results

In the following paragraphs, we firstly concentrate on the functions of Poisson's ratio calculated using the inner-inner evaluation method described in the previous section. The motivation for this is that the results calculated according to the inner-inner approach can be considered the most representative by taking the region of the cellular microstructure into account, where the boundary effects arising from the free outer faces of the specimens are neglected. We also provide a comparison of the results based on all the evaluation methods in the last paragraphs of the results section.

3.1. Function of Poisson's Ratio from the DIC – Quasi-Static Loading

As can be seen in Figure 6a, the 2D re-entrant honeycomb structure exhibited auxetic behavior during the quasi-static tests over the whole range of applied compressive strain and the calculated Poisson's ratio remained negative up to a 28% strain. The maximum absolute value of Poisson's ratio identified for this type of microarchitecture was approximately -0.9 at 1% of strain. From this strain, Poisson's ratio then gradually increased to zero at the maximum compressive strain achieved in the experiments.

On the contrary, the calculated function of Poisson's ratio of the 3D re-entrant honeycomb specimens showed a significantly different quasi-static response of such a similar type of unit-cell geometry (see Figure 6b). Here, the extreme value of Poisson's ratio reached the value of only -0.1 at the same 1% of compressive strain. Poisson's ratio then gradually increased, reaching a value of -0.05 at 5% strain and formed a plateau-like region of approximately constant Poisson's ratio up to the compressive strain over 30%.

Figure 6c depicts the function of Poisson's ratio of the missing rib structure. It can be seen that, in this case, the identified compressive response is, in terms of the function of Poisson's ratio, very similar to the 3D re-entrant honeycomb. However, the difference between these two microarchitectures consists in the value of Poisson's ratio at the plateau-like region, where the missing rib structure reaches $\nu_{12} = 0$ at a 10% strain. Furthermore, from the 25% point of the compressive strain, Poisson's ratio increases to positive values. This effect was investigated by the visual inspection of the images captured during the late stages of the experiment and such behavior can be accounted for the overall loss of stability of the specimens due to excessive rotations of the individual strut joints.

3.2. Function of Poisson's Ratio from the DIC – Dynamic Loading

For every investigated microarchitecture, the DIC-based evaluation of the function of Poisson's ratio was performed for both strain-rates and the resulting curves were compared to reveal the strain dependent characteristics of the structures.

From the comparison of the strain dependent function of Poisson's ratio of the 2D re-entrant honeycomb structure depicted in Figure 6a, it can be seen that the overall shape of the curve is very similar for both the considered strain-rates. Poisson's ratio reaches its global minimum in the initial stages of deformation and then gradually increases up to positive values. The difference between the high and the low strain-rate is the magnitude of the auxetic effect. The extremum of Poisson's ratio in the case of the lower strain-rate was also reached at the lower compressive strain (5% compared to 8%).

Similar to the quasi-static results, the 3D re-entrant honeycomb structures exhibited a significantly different response than the periodical assembly of the two-dimensional re-entrant honeycombs. As can be seen in Figure 6b, the results from the dynamic testing at both strain-rates are very similar to each other and the results of the quasi-static test. During the

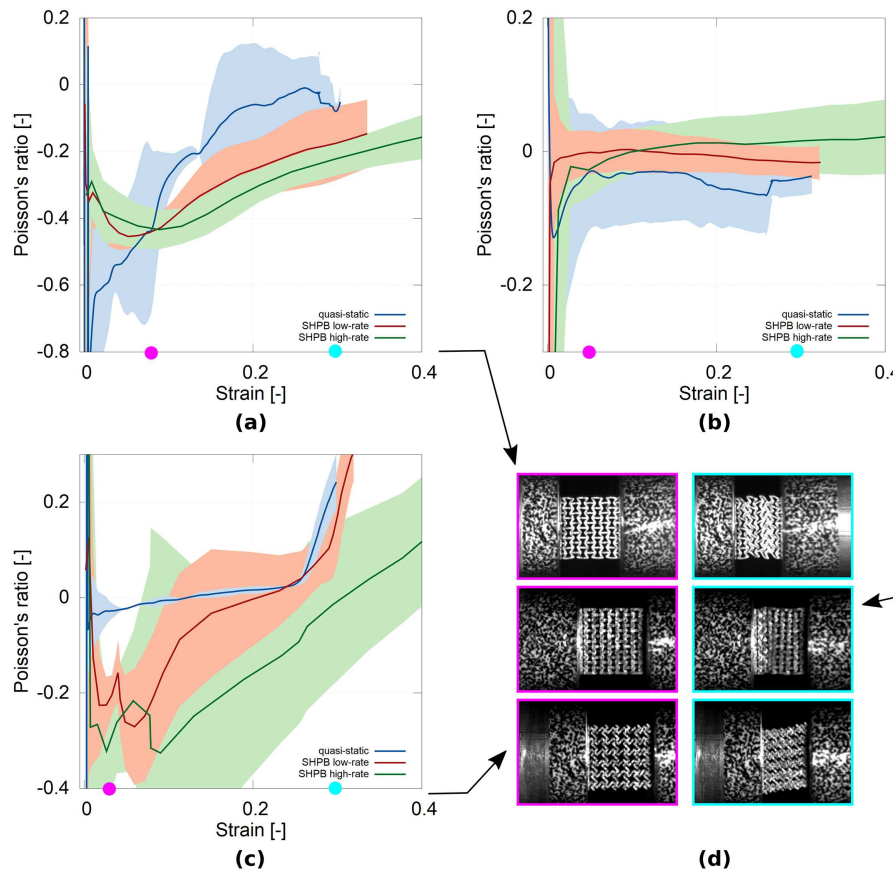


Figure 6. DIC evaluated Poisson's ratio curves, inner-inner method: a) 2D re-entrant honeycomb, b) 3D re-entrant honeycomb, c) missing-rib, d) structures in two representative deformation states marked by the dots on the strain axis.

dynamic experiments, Poisson's ratio increased from the values of approximately -0.1 at the very small strains and then formed the plateau-like region similar to the specimens subjected to the quasi-static loading. Comparison of the low and the high strain-rate experiments shows that the values of Poisson's ratio at the plateau region increase with a higher strain-rate. At the lower strain-rate, Poisson's ratio remains constantly negative (approx. -0.02) beyond the 30% compressive strain. However, with the increase of the applied strain-rate, the plateau region reaches positive values at 10% of the compressive strain and further increases at 40% strain.

The most profound difference between the quasi-static and the dynamic response (i.e., the strain-rate dependence) was revealed in the case of the missing-rib structure (see Figure 6c). At both considered strain-rates, Poisson's ratio decreased to one local and a global minimum located between 2 and 10% of the compressive strain. The global minimum was, in both cases, followed by a gradual increase to positive values while a zero Poisson's ratio was reached at 20% of the compressive strain in the case of the low strain-rate and 30% in the case of the high strain-rate. Both strain-rates produced insignificantly different values of the lowest achieved Poisson's ratio of -0.28 during the low strain-rate and -0.33 during the high strain-rate experiments. Interestingly, this trend is inverse to the other dynamic experiments. A visual inspection of the deforming structures

also showed that the two observable local extrema of the function of Poisson's ratio can be accounted for the initial collapse of the layers of the microstructure. All structures in two representative deformation states during the dynamic experiment are shown in Figure 6d.

3.3. Local-Gradient Results of Poisson's Ratio in the Dynamic Compression

The local-gradient method was used for the strain evaluation of the dynamic experiments in parallel to the calculations based on the displacements and strains calculated for each pair of correlation points in the respective direction. Due to the significantly lower resolution and number of images in the captured sequence during the dynamic tests, the higher-density correlation grid used in the local-gradient evaluation methods enabled one to support conclusions based on the results from the other methods. A set of images showing the deforming auxetic structure during impact with the local-gradient results in the form of a map of strain and Poisson's ratio is shown in Figure 7.

The results of the local-gradient analysis of the 2D re-entrant honeycomb lattice are shown in Figure 8a. The functions of Poisson's ratio for both strain-rates are represented by solid lines showing the mean values with standard deviations obtained

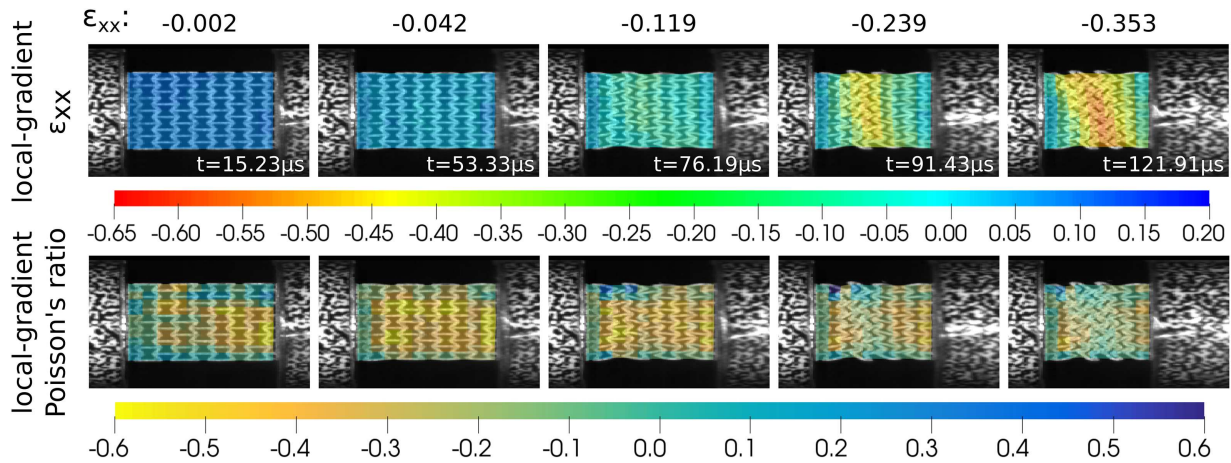


Figure 7. Image sequence showing the deforming 2D re-entrant honeycomb auxetic lattice during impact with the mapped local-gradient results of longitudinal strain and Poisson's ratio.

from the region equivalent to the inner-inner method. For comparison, the dashed lines in this figure represent similar curves of the mean Poisson's ratio calculated according to the inner-inner method from the quasi-static and dynamic

experiments. It can be seen that the strain-rate dependence of Poisson's ratio was captured by both methods. The results from the inner-inner method are within the standard deviation envelopes from approximately 10% strain up to densification.

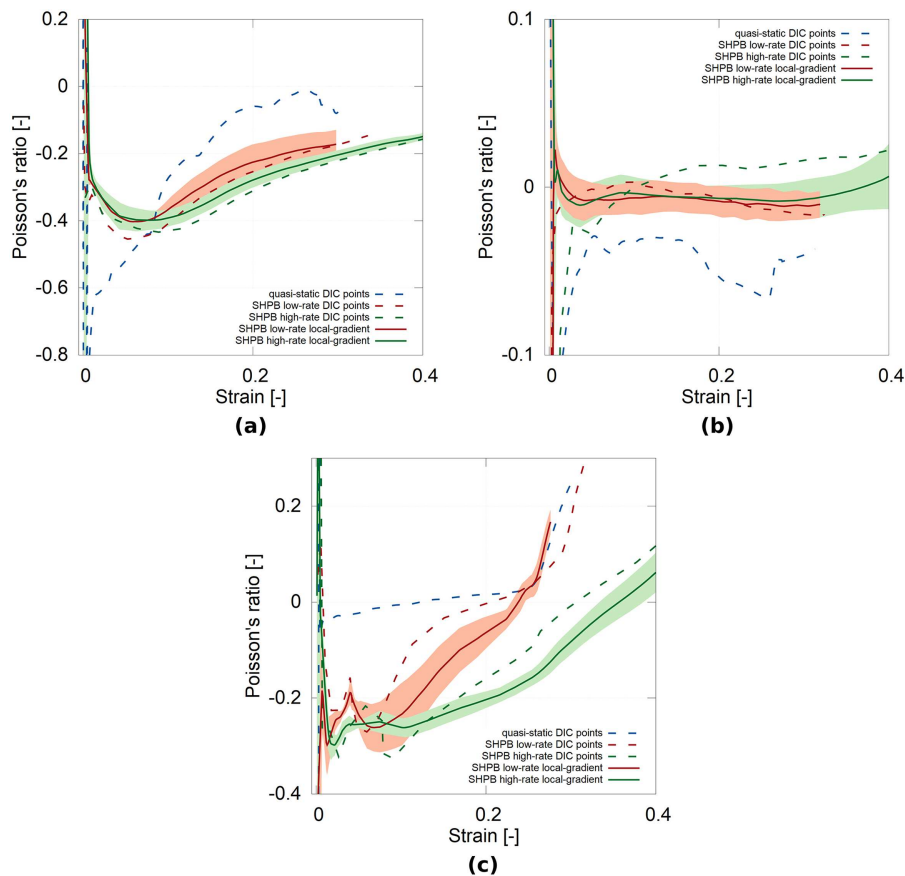


Figure 8. DIC evaluated Poisson's ratio functions, solid lines – local-gradient method, dashed lines – inner-inner method: a) 2D re-entrant honeycomb, b) 3D re-entrant honeycomb, c) missing-rib.

Nevertheless, the results from both methods are in very good agreement. The local-gradient functions of Poisson's ratio exhibit slightly lower values than the inner-inner results.

The results of the local-gradient analysis of the 3D re-entrant honeycomb lattice are shown in Figure 8b. It can be seen that apart from the high strain-rate measurements, the results from both evaluation methods are also in good agreement. Only Poisson's ratio evaluated using the inner-inner method reaches positive values at approximately a 10% strain, while the local-gradient method indicates an auxetic behavior up to the densification region. From the comparison with the quasi-static results, it can be seen that the deformation behavior of this microstructure is similar to the behavior of the metal foams and the difference in Poisson's ratio decreases with the higher strain-rates.

The results of the full-field analysis of the 2D missing-rib structure are shown in Figure 8c. The difference of the inner-inner and local-gradient results is higher than in the case of the 2D re-entrant honeycomb, particularly between 10 and 30% of the compressive strain. The local-gradient method also gives lower values of Poisson's ratio. However, the results of both methods are very close to the standard deviation envelopes of the local-gradient approach and can be considered very similar. The plot also shows the diametrically different behavior of this

structure in comparison with the 3D re-entrant honeycomb. Here, the magnitude of the negative Poisson's ratio of the missing-rib structure increases with the higher strain-rates showing that the dynamic effects induce a significant auxetic response resulting in approximately 5 times a lower Poisson's ratio up to 10% of the compressive strain.

3.4. Comparison of All the Methods

Comparison of the results calculated by all three methods is shown in Figure 9a (the 2D re-entrant honeycomb), Figure 9b (the 3D re-entrant honeycomb), and Figure 9c (the missing-rib structure). The solid lines represent the curves estimated by the inner-inner method, the dashed lines represent the curves estimated by the outer-outer method and the dotted lines represent the curves estimated by the local-gradient method. As can be seen in all the figures, the results of all three methods are in good agreement and exhibit very similar trends. The only significant difference can be found in the quasi-static curves of the 3D re-entrant lattice. Here, Poisson's ratio evaluated by the outer-outer method is considerably higher than the estimation of the inner-inner method and is close to zero in the whole range of deformation.

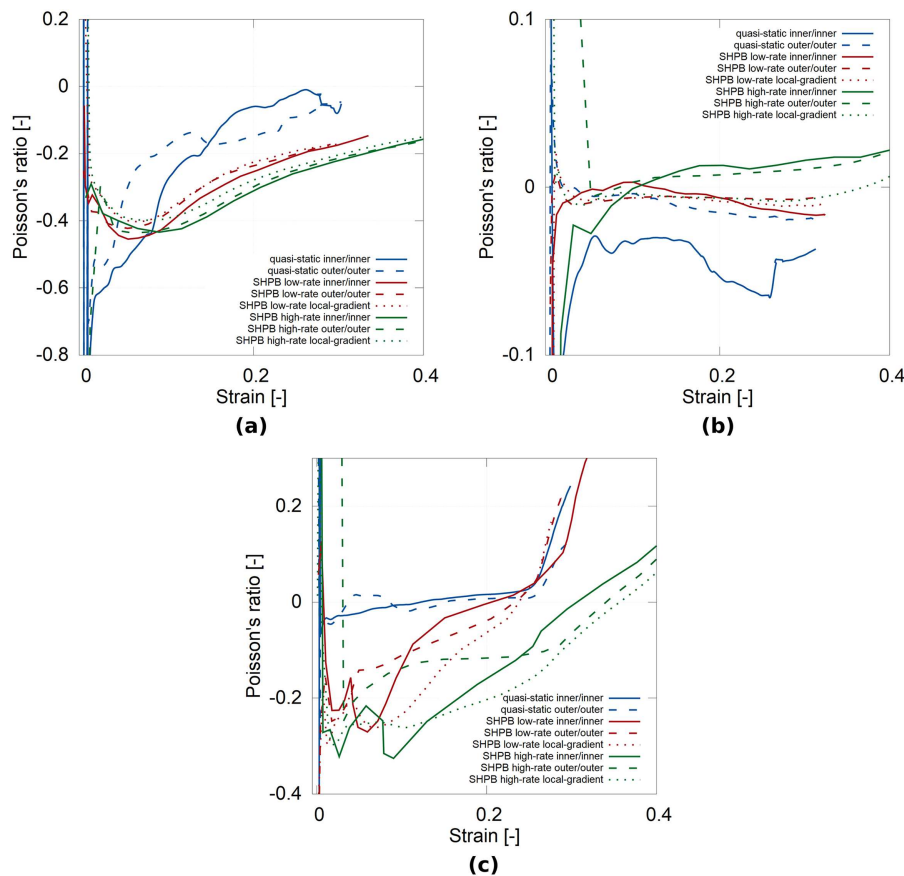


Figure 9. Comparison of the functions of Poisson's ratio calculated by all methods, solid line – inner-inner, dashed line – outer-outer, dotted line – local-gradient: a) 2D re-entrant honeycomb, b) 3D re-entrant honeycomb, c) missing-rib.

3.5. DIC Reliability

A high degree of reliability of the digital image correlation results was achieved in all the quasi-static and dynamic experiments. The overall mean correlation coefficient of all the measurements was higher than 90% representing the reliable tracking of the correlation points. Moreover, the displacement paths of the individual tracked points were optically inspected to reveal a possible loss of correlation or a sudden change of the point's position. In all the cases, the majority of the grid exhibits continuous displacement paths up to the densification of the structure. A loss in the correlation occurred in a limited extent and only for individual correlation points particularly located on the edges of the specimen. The typical values of the mean correlation coefficient throughout the grid plotted against the strain, and the example of the correlation grid in the representative states of deformation (no deformation, auxetic behavior, and densification) of the 2D re-entrant honeycomb are shown in **Figure 10**. The tracking results started to be unreliable during the initial phase of the densification of the structure. Note, that the mean correlation coefficient in Figure 10 reached its minimum at the strain of approximately 38%. From this point it seemingly increased and reached values above 0.9 again. However, this effect was identified not as the restoration of the tracking precision, but as the misidentification of the correlation points in the densified structure. The incorrectly identified positions of a limited number of points can be found even in the blue image corresponding to the strain of approximately 35% (see Figure 10). In some experiments,

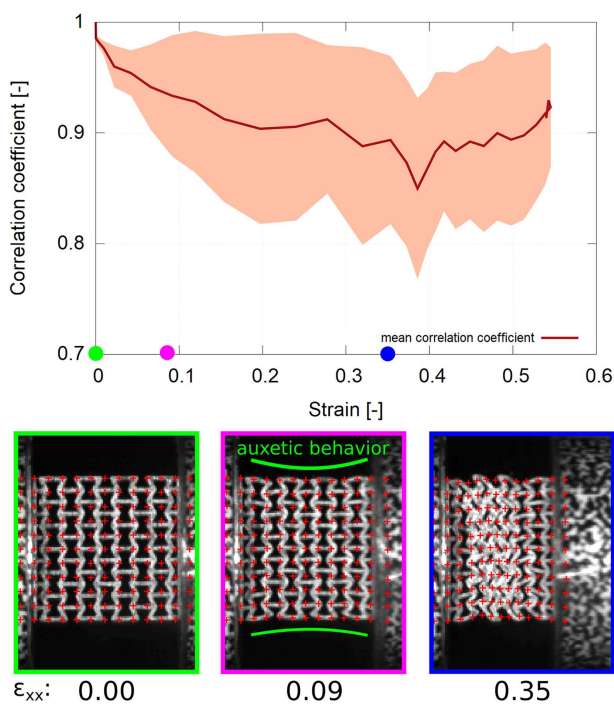


Figure 10. Mean correlation coefficient throughout the grid plotted against the strain with the highlighted representative states of deformation (no deformation, auxetic behavior, and densification) of the 2D re-entrant honeycomb structure.

the mean correlation coefficient exhibited a different behavior and tended to oscillate after reaching the densification phase revealing the loss of the correlation in the crushed structure. This behavior was similar to the analysis performed on hybrid nickel-polyurethane foams.^[39] Thus, the DIC results presented in this paper can be considered reliable up to the strain of ca. 30%. Also, the values of Poisson's ratio in the very low strains (up to ca. 3%) exhibit large numerical errors as the low values of the lateral strain are divided by the low values of the longitudinal strain. Moreover, in the dynamic experiments, the values are also affected by the ramp-in effects of the strain wave and by its propagation through the sample in the initial phase of impact. Thus, dramatic changes in Poisson's ratio at the low strain apparent in the graphs are caused by the abovementioned errors and are not connected with the deformation behavior.

4. Discussion

In this work, DIC was successfully used for the evaluation of the displacement and strain fields and used as a basis for the calculation of the function of Poisson's ratios. The precision and reliability of the methods (inner-inner, outer-outer, and local-gradient) enabled one to reveal differences in the quasi-static and dynamic deformation responses of all the studied microstructures. As a result, it was possible to assess the strain-rate dependency characteristics of the individual auxetic microarchitectures additively manufactured from powdered stainless steel by the SLS method. Every method has its advantages and disadvantages and it is hard to evaluate the most reliable method in general. The local-gradient method provides the most consistent results with the lowest standard deviation as it is calculated as an average through a certain area of the specimen. As such, it is not over-sensitive to the loss of correlation in a limited number of the correlation points. On the other hand, it requires a high density grid of the correlation points and cannot be evaluated only in the certain points of interest. The other two methods can be used for the points-of-interest based analysis of Poisson's ratio, however, they are very susceptible to the loss of correlation or to the big displacements of the individual points. The inner-inner method is good for the analysis of the internal part of the structure itself whereas the outer-outer method is valuable for the analysis of the given complex specimen. Improvement of the evaluation of the displacement and strain fields of such experiments using DIC would require taking the incremental strain theory into account. It would be necessary to account for the additional effects, e.g., out-of-plane deformation, Lagrangian mesh tracking to follow the strain localization and checking for the distorted mesh occurrence. However, for the comparison purposes between the studied lattices, we chose, at this stage, to use a simplified procedure based on the described two-stage DIC algorithm with sub-pixel precision for the displacements evaluation and 2D full-affine transformation for the strain field evaluation. Since the strain values in longitudinal and lateral directions are used to mutually compare the behavior of the structures and compare Poisson's ratio of the studied lattices, the simplified procedure enables one for an easy comparison. To take the aforementioned effects into account, it

would be necessary to use two camera system, higher frame-rate and/or higher resolution.

The 2D re-entrant honeycomb auxetic structure exhibited a negative Poisson's ratio under all three loading conditions. The results of all three evaluation methods for each strain-rate were in very good agreement. The structure exhibited a strain-rate sensitivity of Poisson's ratio. In the dynamic compression, the global minimum Poisson's ratio did not reach the magnitude observed in the quasi-static compression, but the microstructure remained auxetic up to significantly higher compressive strains.

The 3D re-entrant honeycomb auxetic structure exhibited a negative Poisson's ratio in the central part of the lattice during the quasi-static loading evaluated using the inner-inner approach. From all the other methods, and particularly during the dynamic loading scenarios, the structure exhibited a Poisson's ratio close to zero. It was not possible to clearly identify the strain-rate sensitivity of the structure due to the high standard deviations of the evaluated Poisson's ratio curves in all the loading cases. The results correspond to the behavior observed during the visual inspection of the experiments. Such an architecture exhibits not only the highest porosity, but the assembly is based on slender individual struts prone to the loss of stability and with significantly lower loading capacity than in the case of structural the elements of the other analyzed microarchitectures. As a result, the compressive response of such a structure is very similar to the compression of an open-cell or a closed-cell metal foam.

In contrast, the missing-rib microstructure exhibited a negative Poisson's ratio in all three loading cases. The results of all three evaluation methods for each strain-rate were in good agreement and exhibited identical trends. Due to the chiral nature of the unit-cells and the lateral movements of all the layers during the compression, the standard deviations of Poisson's ratio curves in the dynamic compression were higher than in the experiments of the other structures. Nevertheless, the missing-rib structure exhibited a strain-rate sensitivity of the function of Poisson's ratio, where the global minimum of Poisson's ratio decreased with the increasing strain-rate. With the increasing strain-rate, the structure also exhibited an auxetic behavior up to higher compressive strains.

The discussed effects of the strain-rate on the observed deformation properties are caused by non-linearity at several levels of the hierarchical structure of the material, i.e., from strain-rate dependence of the printed steel at the microscale to micro-inertia effects and shock-wave propagation at the macroscale. As a result, the mode of deformation of the individual struts and their joints varies in quasi-statics and dynamics. For example, it can be seen in the quasi-static experiments that every layer of the unit cells moves laterally after its collapse leading to a very high lateral difference in the final position of the lowest and the highest layers. In the dynamic experiments, however, the mentioned effects are not so significant and exhibit more uniaxial response of the microstructure, where the pronounced Poisson's ratio effects cause the more uniform compression.

As the boundary conditions during the quasi-static experiments and dynamic compression using Hopkinson bar can be different and can affect the measured data, all the contact faces of the specimens as well as the faces of the loading devices in the contact with the specimens were precisely polished and

lubricated with a small amount of grease. Thus, the boundary conditions of the experiments were very similar. Moreover, the bending of the incident and transmission bars (the off axis-movement that can negatively affect the results) was investigated by a high-speed camera. No significant bending of the bars was observed during the impact up to the densification of all types of structures. Considering this analysis, it can be concluded that any changes in the deformation behavior can be addressed solely with the strain-rate. Friction and shock effects on the specimen's boundaries during the dynamic experiments can be considered consistent and are therefore a part of the specimen's response to the impact loading.

The design of the specimen is a trade-off between the specimen's suitability for the high strain-rate dynamic measurements, actual limits of the manufacturing technology (resolution, printing technique, mechanical properties of the printed specimen) and representative volume element of the cellular structure. Moreover, a valid SHPB experiment has to be conducted in the dynamic equilibrium and attention has to be paid to the friction and inertia effects. Mechanical impedance of the specimen and the wave propagation phenomena are key factors for the relevant results of the test. Thus, the dimensions of the specimens were selected to minimize the friction and inertia effects. Also, the specimen was equipped with the necessary supporting platens on the contact faces to provide good contact with the propagating stress wave on the contact faces. Otherwise, the ramp-in effect of the propagating stress-wave would cause the non-ideal contact of the bar with the specimen's struts resulting in the limited wave transfer, long times for reaching the dynamic equilibrium, very non-uniform wave propagation through the specimen, or even sudden collapse of the struts during the initial ramp-in phase. On the other hand, the supporting platens change boundary conditions of the neighboring cells.^[44] Using the selected geometry of the specimens it was possible to have at least 3×3 cells in the auxetic core completely surrounded by the other cells. The core of the specimen was of main interest as the behavior in this region should be the most representative for the investigated structures. It can be concluded, that the specimens exhibit stress concentrations in the central part (core of the specimen) and the resulting properties of the auxetic structure itself would be dependent on the array configuration.

5. Conclusions

Three types of additively manufactured auxetic lattices were subjected to uni-axial quasi-static and compressive impact loading in Hopkinson bar at two different strain-rates. The 2D re-entrant honeycomb, the 3D re-entrant honeycomb, and the 2D missing-rib structures were sintered from powdered austenitic steel. Quasi-static compression was observed using the CCD camera, whereas the dynamic experiments were recorded using a high-speed camera. The recorded images of the experiments were processed using the DIC technique. The longitudinal and lateral strain fields were calculated and the strain dependent Poisson's ratio was evaluated for all types of structures and loading scenarios using three different methods. The derived functions of Poisson's ratio were analyzed and the

changes in the deformation behavior induced by the different compressive strain-rates were identified. The 2D re-entrant honeycomb and the 2D missing-rib structures exhibited a significant strain-rate dependency of an auxetic behavior. The 3D re-entrant structure exhibited an auxetic behavior only on a limited number of the unit-cells close to its centroid and only during the quasi-static compression. Other evaluation methods and loading scenarios yielded Poisson's ratio close to zero over the whole range of the deformation and the deformation response of this microarchitecture was very similar to metal foams. To conclude, DIC was successfully and reliably used as an advanced tool for the evaluation of the functions of the strain dependent Poisson's ratio during both the quasi-static and dynamic loading conditions.

Acknowledgements

The research has been supported by Operational Programme Research, Development and Education in the project INAFYM (CZ.02.1.01/0.0/0.0/16_019/0000766). All the financial support is gratefully acknowledged.

Conflict of Interest

The authors declare no conflict of interest.

Keywords

auxetic materials, digital image correlation, Hopkinson bar, impact testing, Poisson's ratio

Received: February 22, 2019

Revised: April 30, 2019

Published online:

- [1] K. E. Evans, M. A. Nkansah, I. J. Hutchinson, S. C. Rogers, *Nature* **1991**, 353, 124.
- [2] A. G. Kolpakov, *J. Appl. Math. Mech.* **1985**, 49, 739.
- [3] R. Lakes, *Science* **1987**, 235, 1038.
- [4] K. E. Evans, *Endeavour* **1991**, 15, 170.
- [5] R. F. Almgren, *J. Elast.* **1985**, 15, 427.
- [6] P. S. Theocaris, G. E. Stavroulakis, P. D. Panagiotopoulos, *Arch. Appl. Mech.* **1997**, 67, 274.
- [7] K. K. Saxena, R. Das, E. P. Calius, *Adv. Eng. Mater.* **2016**, 18, 1847.
- [8] H. M. A. Kolken, A. A. Zadpoor, *RSC Adv.* **2017**, 7, 5111.
- [9] W. Wu, Y. Tao, Y. Xia, J. Chen, H. Lei, L. Sun, D. Fang, *Extreme Mech. Lett.* **2017**, 16, 18.
- [10] W. Wu, X. Song, J. Liang, R. Xia, G. Qian, D. Fang, *Compos. Struct.* **2018**, 185, 381.
- [11] Y. Jiang, Y. Li, *Adv. Eng. Mater.* **2017**, 19, 1600609.
- [12] Y. Jiang, Y. Li, *Adv. Eng. Mater.* **2018**, 20, 1700744.
- [13] T. Li, Y. Chen, X. Hu, Y. Li, L. Wang, *Mater. Des.* **2018**, 142, 247.
- [14] T. Li, X. Hu, Y. Chen, L. Wang, *Sci. Rep.* **2017**, 7, 8949.
- [15] T. Li, L. Wang, *Compos. Struct.* **2017**, 175, 46.
- [16] K. Kuribayashi, K. Tsuchiya, Z. You, D. Tomus, M. Umemoto, T. Ito, M. Sasaki, *Mater. Sci. Eng. A* **2006**, 419, 7.
- [17] M. N. Ali, I. U. Rehman, *J. Mater. Sci. Mater. Med.* **2011**, 22, 2573.
- [18] L. Jiang, H. Hu, *Compos. Struct.* **2017**, 169, 8.
- [19] G. Imbalzano, P. Tran, T. D. Ngo, P. V. S. Lee, *J. Sandwich Struct. Mater.* **2017**, 19, 291.
- [20] M. Liaquat, H. A. Samad, S. T. A. Hamdani, Y. Nawab, *J. Textile Inst.* **2016**, 108, 1264.
- [21] I. Gibson, D. W. Rosen, B. Stucker, *Additive Manufacturing Technologies: Rapid Prototyping to Direct Digital Manufacturing*, Springer, New York, USA **2010**.
- [22] L. Foster, P. Peketi, T. Allen, T. Senior, O. Duncan, A. Alderson, *Appl. Sci.* **2018**, 8, 354.
- [23] G. Imbalzano, P. Tran, T. D. Ngo, P. V. S. Lee, *Compos. Struct.* **2016**, 135, 339.
- [24] M. Fu, Y. Chen, W. Zhang, B. Zheng, *Phys. Status Solidi B* **2016**, 253, 1565.
- [25] S. Hou, T. Li, Z. Jia, L. Wang, *Mater. Des.* **2018**, 160, 1305.
- [26] A. Jung, S. Bronder, S. Diebels, M. Schmidt, S. Seelecke, *Mater. Des.* **2018**, 160, 363.
- [27] A. Jung, A. D. Pullen, W. G. Proud, *Compos. Part A Appl. Sci. Manuf.* **2016**, 85, 1.
- [28] T. Fila, P. Zlamal, O. Jirousek, J. Falta, P. Koudelka, D. Kytyr, T. Doktor, J. Valach, *Adv. Eng. Mater.* **2017**, 19, 1700076.
- [29] M. F. Rabbi, V. Chalivendra, Y. Kim, *Compos. Struct.* **2018**, 195, 1.
- [30] N. Novak, K. Hokamoto, M. Vesenjajk, Z. Ren, *Int. J. Impact. Eng.* **2018**, 122, 83.
- [31] W. Lee, Y. Jeong, J. Yoo, H. Huh, S. Park, S. H. Park, J. Yoon, *Compos. Struct.* **2019**, 208, 836.
- [32] A. Beharic, R. R. Egui, L. Yang, *Mater. Des.* **2018**, 145, 122.
- [33] L. Zhou, J. Zeng, L. Jiang, H. Hu, *J. Mater. Sci.* **2018**, 53, 3899.
- [34] H. Wang, Z. Lu, Z. Yang, X. Li, *Compos. Struct.* **2019**, 208, 758.
- [35] L.L. Hu, M. Zh. Zhou, H. Deng, *Thin. Wall. Struct.* **2018**, 131, 373.
- [36] H. Wang, Z. Lu, Z. Yang, X. Li, *Int. J. Mech. Sci.* **2019**, 151, 746.
- [37] N. Novak, L. Starcevic, M. Vesenjajk, Z. Ren, *Compos. Struct.* **2019**, 210, 167.
- [38] P. Koudelka, O. Jirousek, T. Fila, T. Doktor, *Mater. Tehnol.* **2016**, 50, 311.
- [39] M. Adorna, P. Zlamal, T. Fila, J. Falta, M. Felten, M. Friez, A. Jung, *Acta Polytechnica CTU Proceedings* **2018**, 18, 72.
- [40] T. Fila, P. Zlamal, J. Falta, T. Doktor, P. Koudelka, D. Kytyr, M. Adorna, J. Luksch, M. Neuhauserova, J. Valach, O. Jirousek, *EPJ Web Conf.* **2018**, 183, 02045.
- [41] L. J. Gibson, M. F. Ashby, *Cellular Solids: Structure and Properties*, Cambridge University Press, Cambridge, UK **1997**.
- [42] B. D. Lucas, T. Kanade, *Proc. of Imaging Understanding Workshop* **1981**, pp. 121–130.
- [43] W. Tong, *Strain*, **2005**, 41, 1.
- [44] Y. Liu, Z. Dong, J. Liang, J. Ge, *Int. J. Mech. Sci.* **2019**, 152, 568.

Impact Behavior of Additively Manufactured Stainless Steel Auxetic Structures at Elevated and Reduced Temperatures

Tomáš Fíla,* Petr Koudelka, Jan Falta, Jan Šleichrt, Marcel Adorna, Petr Zlámal, Michaela Neuhäuserová, Anja Mauko, Jaroslav Valach, and Ondřej Jiroušek

Metamaterials produced using additive manufacturing represent advanced structures with tunable properties and deformation characteristics. However, the manufacturing process, imperfections in geometry, properties of the base material as well as the ambient and operating conditions often result in complex multiparametric dependence of the mechanical response. As the lattice structures are metamaterials that can be tailored for energy absorption applications and impact protection, the investigation of the coupled thermomechanical response and ambient temperature-dependent properties is particularly important. Herein, the 2D re-entrant honeycomb auxetic lattice structures additively manufactured from powdered stainless steel are subjected to high strain rate uniaxial compression using split Hopkinson pressure bar (SHPB) at two different strain rates and three different temperatures. An in-house developed cooling and heating stages are used to control the temperature of the specimen subjected to high strain rate impact loading. Thermal imaging and high-speed cameras are used to inspect the specimens during the impact. It is shown that the stress-strain response as well as the crushing behavior of the investigated lattice structures are strongly dependent on both initial temperature and strain rate.

broad range of possible applications ranging from deformation energy mitigation^[1,2] to biomaterials.^[3] Herein, a deep understanding and knowledge of the coupled thermomechanical behavior, strain rate sensitivity,^[4] and temperature-dependent mechanical properties are crucial since such phenomena seriously affect the response and performance of the lattices at high strain rates. However, in the case of coupled thermomechanical behavior of additively manufactured (AM) materials, particularly during dynamic impact conditions, this topic is still not fully explored and only a few research studies are available. Commonly, only wrought metallic materials have been investigated. In the case of the austenitic stainless steel, strain rate sensitivity and coupled thermomechanical behavior of the bulk specimens have been investigated in research studies covering topics like microstructure characterization,^[5] adiabatic heating,^[6] or constitutive modelling.^[7–9] Kluczyński et al. dealt

Additively manufactured auxetic metamaterials represent lattice structures that are being intensively investigated thanks to their


with the influence of additive manufacturing production parameters on the resulting mechanical parameters.^[10] In their study, the specimens produced with different settings of laser power, exposure velocity, hatching distance, and layer thickness were subjected to microstructural analysis, hardness measurement, and a combination of quasistatic and dynamic compression. The authors concluded that the observed mechanism of material cracking during dynamic loading is affected by the energy dissipation capacity of the resulting structures. The effects of laser energy density in terms of point distance and exposure time on the resulting porosity, surface finish, microstructure, density, and hardness of the samples were studied by Cherry et al.^[11] It was shown that surface roughness was primarily affected by point distance with increased point distance resulting in increased surface roughness, whereas laser energy density was shown to affect total porosity. Relationships between porosity, microstructure, and mechanical properties of additively manufactured stainless steel were investigated by Ronneberg et al. through heat treatment.^[12] Heat treatment of the additively manufactured austenitic steel is considered as a suitable approach to modify and improve the mechanical properties of the as-built material.

Strain rate- and temperature-dependent properties of the additively manufactured materials have been investigated in papers focused mainly on strain rate dependency of polymers,^[13–15]

Dr. T. Fíla, P. Koudelka, J. Falta, J. Šleichrt, M. Adorna, Dr. P. Zlámal, M. Neuhäuserová, Prof. O. Jiroušek
Faculty of Transportation Sciences
Czech Technical University in Prague
Konviktská 20, 110 00 Prague, Czech Republic
E-mail: fila@fd.cvut.cz

A. Mauko
Faculty of Mechanical Engineering
University of Maribor
Smetanova ul. 17, 2000 Maribor, Slovenia

Dr. J. Valach
Institute of Theoretical and Applied Mechanics
Czech Academy of Sciences
Prosecká 76, 190 00 Prague, Czech Republic

 The ORCID identification number(s) for the author(s) of this article can be found under <https://doi.org/10.1002/adem.202000669>.

© 2020 The Authors. Published by Wiley-VCH GmbH. This is an open access article under the terms of the Creative Commons Attribution-NonCommercial License, which permits use, distribution and reproduction in any medium, provided the original work is properly cited and is not used for commercial purposes.

DOI: 10.1002/adem.202000669

mechanical characterization of the Inconel superalloy,^[16] the thermomechanical model of a titanium alloy,^[17] and strain rate dependency of the printed bulk stainless steel.^[18] In the case of similar materials, temperature-dependent penetration resistance of the aluminum foam sandwich panels has been investigated numerically.^[19] Lattice structures and auxetic metamaterials have been studied at both quasistatic^[20] and dynamic loading conditions.^[21–29] However, coupled thermomechanical effects related to changes of strain rate and temperature are scarce. For polymers, the performance of additively manufactured Nylon 12 lattice structures at different temperatures has been investigated using the drop-weight dynamic loading conditions.^[30] To our knowledge, there is no publication dedicated to thermomechanical effects of strain rate dependency of additively manufactured metallic auxetic lattices.

In this article, a split Hopkinson pressure bar (SHPB) apparatus was used together with in-house developed heating and cooling stages to investigate the coupled thermomechanical effects of 2D re-entrant auxetic lattices having in-plane negative Poisson's ratio (NPR) at high strain rates. The lattices were additively manufactured from the powdered stainless steel using laser powder bed fusion (LPBF) and subjected to dynamic uniaxial compression at two different strain rates and three different temperatures. Temperature- and strain rate-dependent changes in deformation behavior were investigated and the important trends related to changes in temperature and impact velocity were identified and described. It was found out that the stress–strain response of the auxetic lattices as well as their crushing behavior were strongly dependent on both initial temperature and strain rate. With an increasing strain rate, lateral motion of the individual lattice layers during their collapse was suppressed. Therefore, the densification of the structure occurred at lower strain with elevated stresses. Moreover, the initial temperature strongly affected the stress–strain response of the structure as the measured stresses exhibited lower values with increasing temperature and temperature-related softening of the lattice could be identified.

Experimental Section

Specimens: Re-entrant honeycomb auxetic lattice having in-plane NPR was selected for the study as the mechanical response of this microarchitecture has already been described in previous studies conducted at room temperature.^[24,25] The designed dimensions of the structure and its unit cell are shown in **Figure 1a**. The re-entrant angle of 70° was selected to maximize the auxetic effect in the lattice structure over the whole range of deformation. The thickness of the cell walls of 0.6 mm was selected to elevate the thermomechanical effects induced by stress concentration in individual struts and joints during crushing of the lattice. The other specific dimensions of the unit cell were derived from the cell-wall thickness and re-entrant angle to achieve overall dimensions of the structure with respect to the specifics of the SHPB measurement (specimen cross-sectional dimensions to height ratio and diameter of the bars).

The specimens were additively manufactured from the powdered SS316–0407 austenitic stainless steel using the LPBF technique in AM250 device (Renishaw, UK). During the AM process the structures were oriented perpendicularly to the powder bed plane and thus the particular layers of the fused base material were parallel to the direction of loading (see scheme in **Figure 1a**). The metal powder granularity was 15–45 μm, the layer thickness was 50 μm, and the maximal laser power was 200 W. The chessboard scanning strategy was used and the specimens were

produced in Argon 5.0 protective atmosphere. No heat treatment of the specimens was carried out. The size of the AM produced specimens was 14.0 × 14.0 × 15.2 mm³. Each specimen was composed of 5 × 4 planar re-entrant auxetic cells with a nominal strut thickness of 0.6 mm. In total, 35 specimens were produced and tested. **Figure 1b** shows scanning electron microscopy (SEM) of the investigated lattices. Both the surface roughness on the as-built sample as well as the porosity in the microstructure of the polished surface were captured. Furthermore, the micrographs with the higher resolution show the resulting microstructure in the area of the strut joint as a result of the printing strategy.

Experimental Setup: To obtain reference data, the specimens were tested in quasistatic conditions at room temperature. The quasistatic tests were carried out using 3382 testing system (Instron, USA) equipped with 100 kN load cell and an optical setup for noncontact strain measurement. The imaging was carried out using bi-telecentric zoom revolver TCZR072 (OptoEngineering, Italy) attached to a monochromatic CMOS camera Manta G504B (AVT, Germany) at full-frame resolution of 5 Mpx (2452 × 2056 px) and 1 fps readout rate. The uniaxial loading of the samples was carried out with the cross-head speed of 0.03 mm s^{−1} (strain rate 0.002 s^{−1}) and readout rate of displacement and force data of 10 Hz.

The SHPB equipped with the heating and cooling stages was used to subject the specimens to impacts in six scenarios combining two impact velocities and three temperatures. In the setup, incident and transmission bars with a diameter of 20 mm and with an identical length of 1600 mm were used. The bars were manufactured from a high-strength aluminum alloy (EN-AW-7075-T6). The strain waves in the Hopkinson bar were induced by an impact of a striker bar with the same diameter of 20 mm, accelerated using a single-stage gas-gun, onto the impact face of the incident bar. The striker bar was manufactured from the identical aluminum alloy as the other bars. While the compressive strain of the specimen is proportional to the striker bar length and its impact velocity, two striker bars with various lengths were used to compress the specimens to a nominal engineering strain of at least 0.25: 1) 750 mm for the lower impact velocity of 30 ms^{−1} and 2) 500 mm for the higher impact velocity of 45 ms^{−1}. The SHPB bars were instrumented using the foil strain-gauges (3/120 LY61, HBM, Germany) with an active length of 3 mm connected in a Wheatstone half-bridge arrangement (measurement point) for compensation of a possible (very small) bending of the bars during the experiment. Conventional arrangement with a single strain-gauge measurement point located in the middle of each bar was selected for its simplicity and straightforward calibration. Each bar was supported by four high-performance polymeric slide bearings (drylin TJUM, IGUS, USA) mounted in the adjustable stainless steel housings. Soft copper pulse-shapers with a diameter in the range of 5–7 mm and thickness of 0.5–1 mm were mounted at the incident bar impact face to produce smooth incident strain pulse, to reduce the wave dispersion effects in the bars, and to stabilize the resulting strain rate. More information and technical details about the used SHPB apparatus (e.g., data acquisition system, experiment triggering, etc.) can be found in our previous study.^[25] The SHPB experimental apparatus is shown in **Figure 1c**.

The experiments were observed using a pair of high-speed cameras (Fastcam SA-Z, Photron, Japan). The first camera was used for the high-speed optical inspection of the specimen at the highest achievable frame rate. In this case, the frame rate of the camera was set to 252 kfps and image resolution was 256 × 168 px with spatial resolution of ≈100 μm. The specimen before the impact was projected to an area of ≈153 × 138 px. The images acquired by this camera were further processed using an in-house digital image correlation (DIC) algorithm to obtain displacement and strain fields of the specimen and to evaluate the deformation response of the lattice at different strain rates and temperatures. The second camera was used for the optical inspection of the experiment and provided a general overview of the experimental setup at the moment of the impact. This camera was operated at 80 kfps with image resolution of 512 × 424 px. Illumination of the scene was performed using a pair of high-intensity light emitting diode light sources (Multiled QT, GS Vitec, Germany).

A high-speed thermal imaging camera (SC7600, FLIR, USA) equipped with an actively cooled focal plane array (FPA) InSb photon-counting

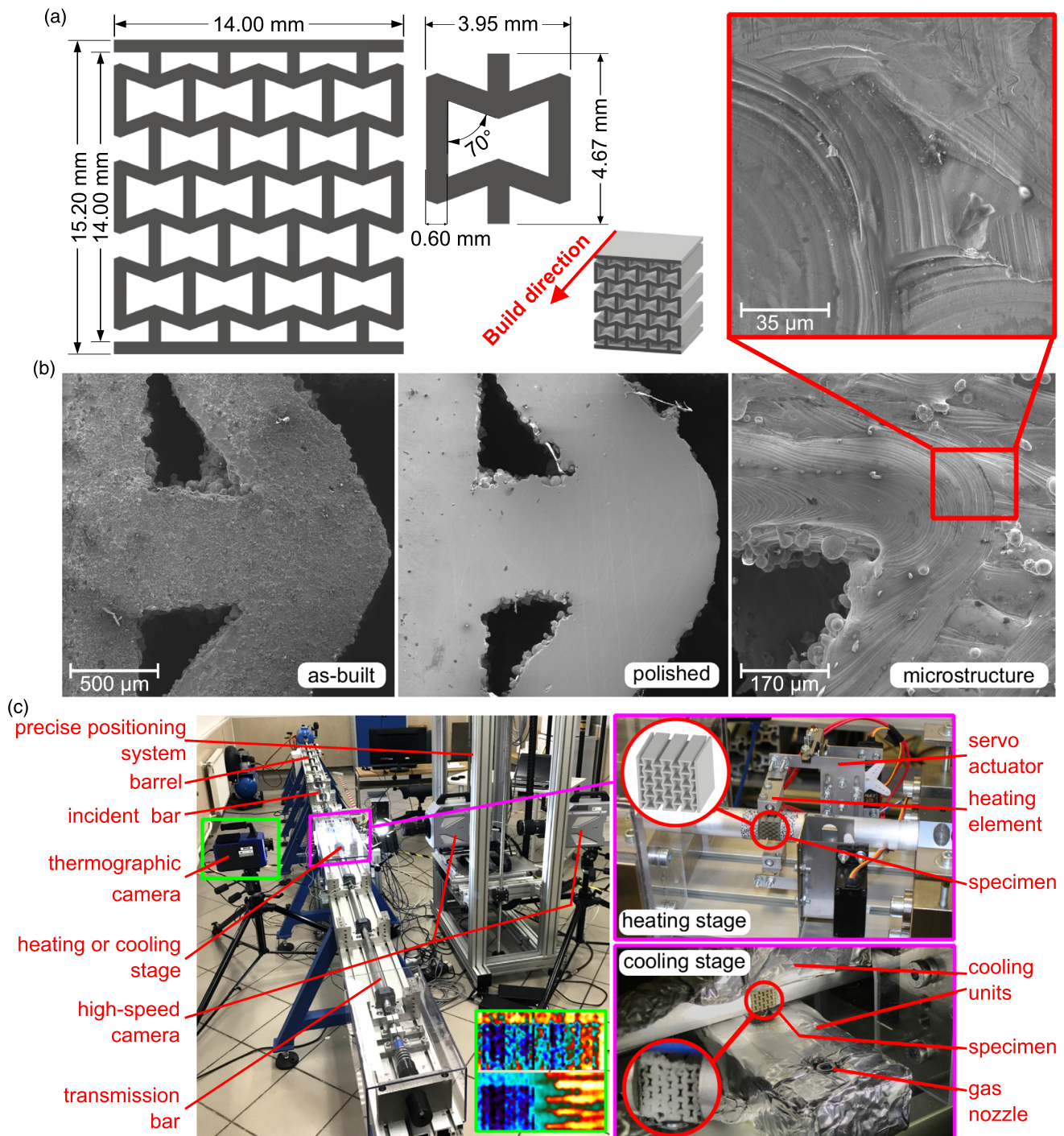


Figure 1. a) Geometry of the auxetic lattice; b) SEM micrographs of the printed specimen; and c) SHPB experimental setup with the high-speed camera, thermal imaging camera and the heating/cooling stages.

detector and 50 mm $f/2$ silicon-based lens with an antireflection coating were used for thermal imaging. Full frame resolution of the camera was 640×512 px and the detector operates in the spectral range of 1.5–5.0 μm (short-to-medium wavelength infrared band—SWIR to MWIR). Thermal imaging was used for the inspection of the specimen's temperature before the experiment and for estimation of the temperature increase and heat distribution during the impact. The camera-lens

assembly system was calibrated for a temperature range of -5 to 300 $^{\circ}\text{C}$. To maximize the frame rate of the camera for the dynamic experiments, the image resolution was downscaled to 96×44 px by sensor image windowing. In this configuration, the maximum frame rate was ≈ 2 kfps. A MgF_2 protective window was mounted in the shatterproof polycarbonate specimen shield to make the infrared imaging possible, while guaranteeing the safety of the thermal imaging optics.

The specimens were tested at three different temperatures to reveal the possible strain rate and temperature-dependent behavior. Based on the performance of the used heating/cooling stages, the thermal conductivity of the specimen and its surrounding components, the following temperatures were selected for the experiments: 1) lowered temperature of $\approx -5^\circ\text{C}$, 2) room temperature of $\approx 20^\circ\text{C}$, and 3) elevated temperature of $\approx 120^\circ\text{C}$. The in-house developed cooling/heating stages were used to control the temperature of the specimen before the impact.

The heating stage consisted of ceramic heating elements with a rated output power of 40 W that are commonly used for the construction of hot-ends (printing heads of the thermal 3D printers). The heating elements were connected to the aluminum clamps that were in contact with the specimen. The clamps with the heating elements were mounted in the servo-based actuator that was used for a quick remote control removal of the heating elements just before the impact. The servo system was controlled by a custom electronics. The output temperature was regulated using an open-loop control circuitry with pulse width modulation (PWM). The heating stage was capable to raise the temperature of the specimen to $\approx 220^\circ\text{C}$.

The cooling stage consisted of a pressure vessel with a volume of 6.7 L containing 5 kg of liquid CO_2 , a thermally isolated box containing dry ice

(CO_2 in a solid state) with a temperature of -78°C and a piping system. Inside the thermally isolated box, the low-temperature compatible piping coil was submerged in a mixture of dry ice and 1 L pure ethanol. During the cooling process, the gas from the reservoir was released at a pressure of 1.5 MPa and was rapidly cooled further down by contact with the mixture of ethanol and dry ice. Then, the supercooled gas was led directly to the specimen using the low-temperature compatible hoses and nozzles. Using this system, it was possible to cool the specimen to $\approx -27^\circ\text{C}$.

Experimental procedure: In total, 35 specimens were tested at three different temperatures. Five specimens were tested using the standard electromechanical testing rig under quasistatic conditions and room temperature to obtain the reference data for comparison with the dynamic experiments at different temperatures. The experimental campaign was carried out according to the following scheme: 1) quasistatics, room temperature ($\approx 20^\circ\text{C}$): five specimens. 2) SHPB, room temperature ($\approx 20^\circ\text{C}$), strain rate $\approx 1150\text{ s}^{-1}$: five specimens. 3) SHPB, low temperature ($\approx -5^\circ\text{C}$), strain rate $\approx 1150\text{ s}^{-1}$: five specimens. 4) SHPB, high temperature ($\approx 120^\circ\text{C}$), strain rate $\approx 1150\text{ s}^{-1}$: five specimens. 5) SHPB, room temperature ($\approx 20^\circ\text{C}$), strain rate $\approx 2300\text{ s}^{-1}$: five specimens. 6) SHPB, low temperature ($\approx -5^\circ\text{C}$), strain rate $\approx 2300\text{ s}^{-1}$: five specimens. 7) SHPB, high temperature ($\approx 120^\circ\text{C}$), strain rate $\approx 2300\text{ s}^{-1}$: five specimens.

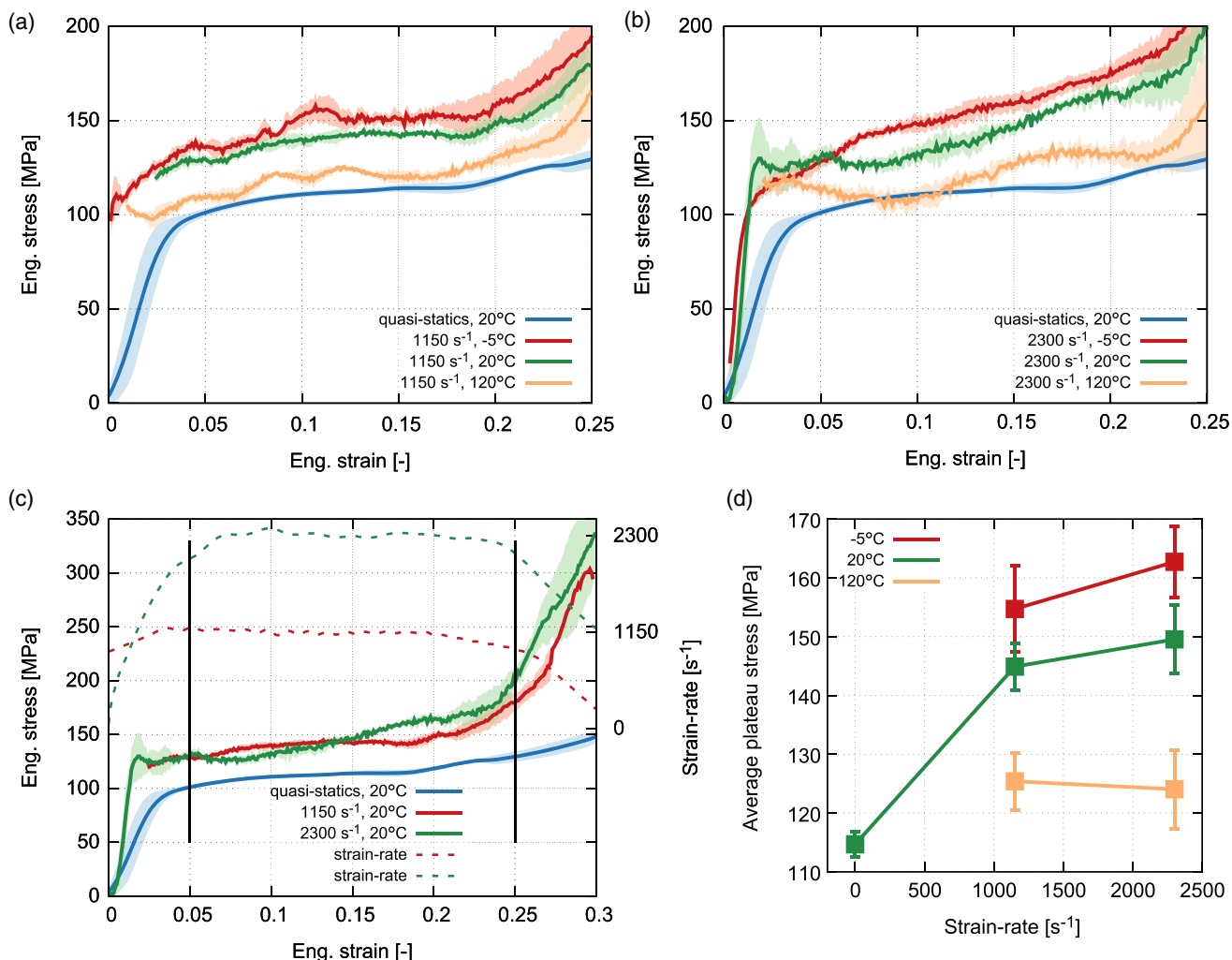


Figure 2. Thermomechanical response of the 2D re-entrant auxetic lattice: a) stress–strain curves for three different temperatures at strain rate of $\approx 1150\text{ s}^{-1}$; b) stress–strain curves for three different temperatures at strain rate of $\approx 2300\text{ s}^{-1}$; c) stress–strain and strain rate curves for temperature of 20°C at two different strain rates—vertical bars represent the interval of the approximately constant strain rate where the average plateau stress was calculated. d) Average plateau stress for different temperatures and strain rates.

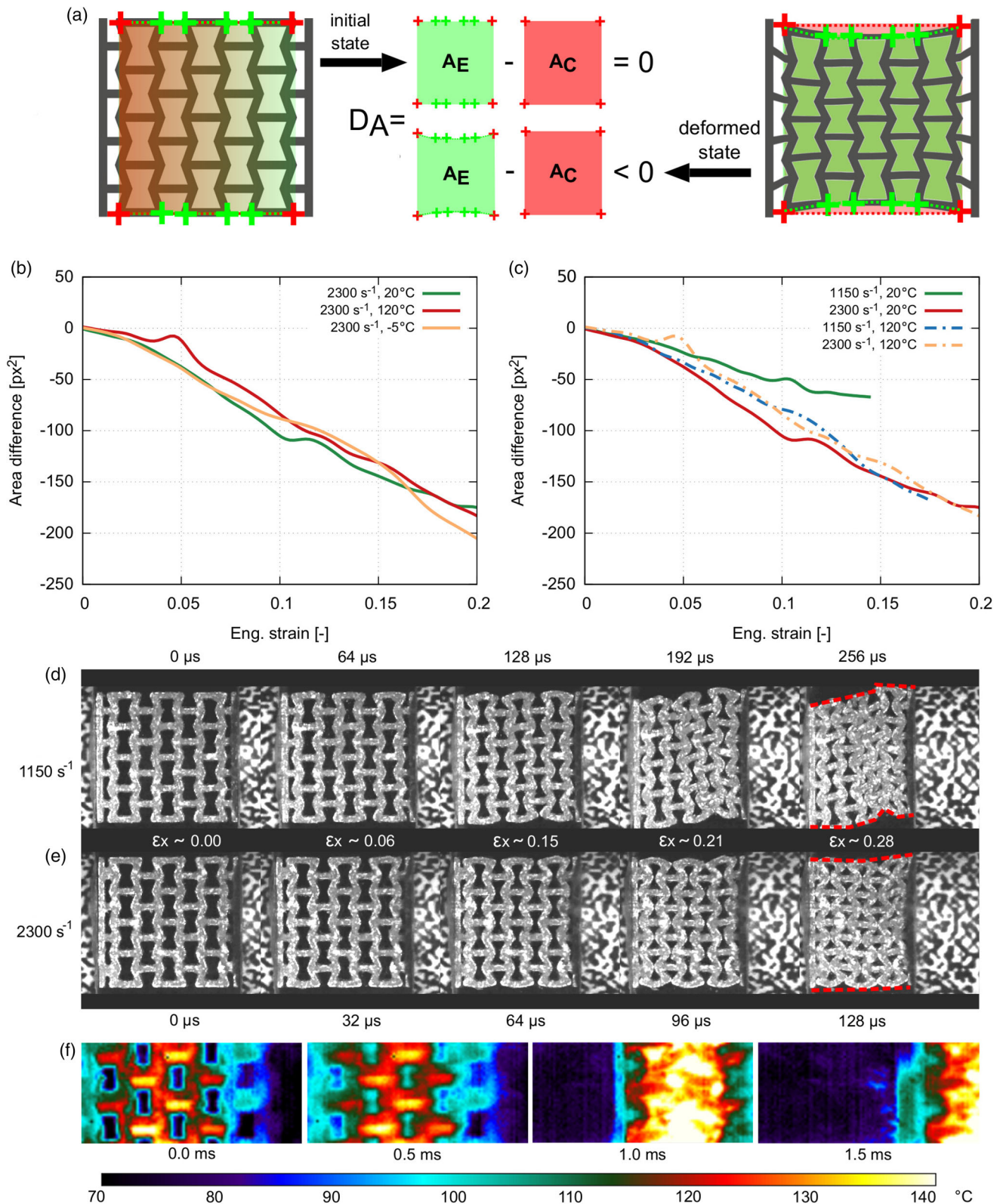


Figure 3. a) Scheme explaining calculation of the area difference. b) Area difference for 2D re-entrant lattice at three different temperatures at strain rate of ≈ 2300 s⁻¹. c) Area difference for temperatures of 20 °C and 120 °C at two different strain rates. Crushing behavior of the auxetic lattice at temperature of 20 °C and strain rate of d) ≈ 1150 s⁻¹ and e) ≈ 2300 s⁻¹. f) Series of thermograms—the heated specimen subjected to strain rate of ≈ 1150 s⁻¹ loading showing concentration of deformation in the first two layers of cells near the impact face of the specimen.

Coupled temperature- and strain rate-dependent properties: Stress–strain curves for the individual temperatures and strain rates were evaluated from the strain-gauge signals according to the standard 1D wave propagation theory valid for SHPB. The average dynamic stress–strain diagrams for all the tested temperatures at a strain rate of $\approx 1150 \text{ s}^{-1}$ are compared with the average quasistatic curve in Figure 2a. For all the temperatures, the stresses in dynamic compression were considerably higher than in the case of the quasistatic loading conditions ($\approx 30\%$ higher at the room temperature). The stresses in the experiments with the low temperature were higher than the stresses during the experiments conducted at room temperature. The same trend was observed in the experiments at the elevated temperature, where the stresses were significantly lower than during the room temperature testing and even approached the values of the quasistatic room temperature curve. The average dynamic stress–strain diagrams for all tested temperatures at a strain rate of $\approx 2300 \text{ s}^{-1}$ are compared with the average quasistatic curve in Figure 2b. Note that the trends are identical to the previous case. Average stress–strain diagrams and strain rate histories for room temperature and three different velocities (quasistatic, strain rate 1150 s^{-1} and 2300 s^{-1}) are compared in Figure 2c. Note that the difference between the two strain rates is particularly distinct at a nominal strain higher than 0.15, where a different densification behavior can be identified. With the increasing strain rate, the densification of the structure occurred at the lower strain. To quantify the strain rate and temperature-related sensitivity of the lattice structure, the average plateau stress was calculated from the stress–strain diagram in a strain range of 0.05–0.25 (see black vertical lines in Figure 2c). This range was selected as the strain rate in this interval remained approximately constant and was not affected by the initial ramp-in phase of the strain pulse or rapid strain rate decrease during the densification. The average plateau stress values for all the temperatures and strain rates are shown in Figure 2d. Here, the coupled thermomechanical behavior of the lattice structure was very profound as the average plateau stress was increasing with the strain rate at low and room temperature. The rate of its increase was marginally higher for the low temperature. Different behavior was observed in the experiments conducted at the high temperature, where the average plateau stress was decreasing with the strain rate, revealing the thermal-related softening of the lattice structures. The revealed coupled thermomechanical behavior was similar to the trends observed during heat treatment of the additively manufactured stainless steel specimens that, in horizontal orientation of the printed structure, exhibited a decrease in yield stress and increase in elongation at break with the increasing heat treatment temperature.^[12]

The changes in the crushing behavior of the auxetic cells were investigated using the DIC to reveal possible changes of the crushing mechanism of the lattices and to compare the results with the stress–strain response shown in Figure 2. DIC was used to track the positions of correlation points created at the nodes of the lattice structures. The difference between the area defined by the actual edges of the deformed specimen and the area defined by the points in the four corners of the specimen was used to characterize the change in the crushing behavior. The area difference D_A was calculated according to

$$D_A = A_E - A_C \quad (1)$$

where A_E represents the area of a polygon with its vertices defined by the nodes at the edges of the auxetic structure tracked by the DIC and A_C represents the area of the trapezoid defined by the four corner nodes of the auxetic structure tracked by the DIC. According to this relation, the auxetic behavior of the structure results in the negative area difference. The scheme explaining calculation of the area difference is shown in Figure 3a. Area difference of the auxetic lattice for all the temperatures and strain rate of $\approx 2300 \text{ s}^{-1}$ is plotted against nominal engineering strain in Figure 3b. Note that at all the temperatures, the structures exhibited NPR with no significant difference in the crushing behavior. The area difference of the lattice for the room temperature and both strain rates is compared with the area difference for the high temperature at both strain rates in Figure 3c. Note that at the room temperature and the lower strain rate, the crushing behavior of the lattice was different as the area difference

was considerably less compared with the high strain rate. Interestingly, this trend was not observed at the high temperature, where the area difference was approximately identical for both strain rates and corresponded in both cases approximately to the area difference at room temperature and higher strain rate. Unfortunately, this trend could not be investigated at the low temperature as the frozen specimens were covered by frost that made the tracking of the lattice by DIC in most cases impossible. Nevertheless, the lattice response was strongly affected by both strain rate and temperature. Crushing behavior of the re-entrant lattice at lower and higher strain rates at room temperature is compared in Figure 3d,e. Here, the changes in deformation behavior at a nominal strain higher than 0.15 are clearly apparent. At a strain rate of $\approx 1150 \text{ s}^{-1}$, the structure exhibited extensive lateral movements, whereas at a strain rate of $\approx 2300 \text{ s}^{-1}$, the lateral movements were prevented by the velocity of the impact and inertia effects. Therefore, the principal mode of deformation of the lattice changed with the increasing strain rate. During the quasistatic and dynamic tests at the lower strain rate, the structure exhibited a slow rotation of the strut joints followed by self-contact induced densification of individual unit cells. During the dynamic tests at the higher strain rate, the structure exhibited longitudinal displacement of strut joints and bending of outer struts in the cell layers.

Qualitative analysis of the deformation processes was carried out by studying the heat distribution in the acquired thermograms. The data showed that the initial temperature of the sample not only trivially influenced the highest observable temperature of the deforming microstructure, but also more importantly affected the difference between the initial and the highest measured temperature during the given experiment. As such, the highest temperature difference ($101 \text{ }^\circ\text{C}$) was calculated for the room temperature samples at high strain rate loading, whereas the lowest difference ($30 \text{ }^\circ\text{C}$) was assessed for the elevated-temperature samples loaded at a lower strain rate. In terms of relative temperature difference in dependence on strain rate, i.e., the ratio of temperature increase between the low and the high strain rate loading, the lowest value of 23% was calculated for the low-temperature experiments, whereas the highest value of 113% was assessed for the high-temperature experiments. Furthermore, the thermograms can be used as a mean for inspection of concentration of deformation within the specimen microstructure, as shown in Figure 3f. Here, it is possible to reveal, e.g., localized heating in the joints of struts and overall distribution of deformation over the microstructure including possible localization of deformation to certain cell layers.

The additively manufactured 2D re-entrant auxetic lattices produced from the powdered austenitic steel were subjected to high strain rate uniaxial compressive loading in SHPB at three different temperatures and two different rates of deformation. It was found out that both the studied auxetic lattice constructs and the base material exhibited considerable strain rate and temperature sensitivity. Coupled thermomechanical behavior of the lattice structures was investigated. The structure exhibited a strain rate-related hardening with thermal softening effects. It was identified that the crushing behavior of the construct was strain rate dependent as the lateral movements of the structure were effectively prevented with the increasing strain rate by the inertia effects and short time duration of the impact.

Acknowledgements

The authors acknowledge the financial support from the Operational Programme Research, Development and Education in the project INAFYM (CZ.02.1.01/0.0/0.0/16_019/0000766) and the Czech Science Foundation (project no. 19-23675S).

Conflict of Interest

The authors declare no conflict of interest.

Keywords

additive manufacturing, auxetic metamaterials, split Hopkinson pressure bar, strain rate sensitivity, thermomechanical behavior

Received: June 4, 2020

Revised: August 13, 2020

Published online: October 1, 2020

-
- [1] T. Tancogne-Dejean, A. B. Spierings, D. Mohr, *Acta Mater.* **2016**, 116, 14.
- [2] T. Li, Y. Chen, X. Hu, Y. Li, L. Wang, *Mater. Des.* **2018**, 142, 247.
- [3] H. Kolken, K. Lietaert, T. van der Sloten, B. Pouran, A. Meynen, G. Van Loock, H. Weinans, L. Scheys, A. Zadpoor, *J. Mech. Behav. Biomed. Mater.* **2020**, 104, 103658.
- [4] M. Vesenjak, C. Veyhl, T. Fiedler, *Mater. Sci. Eng. A* **2012**, 541, 105.
- [5] J. Talonen, H. Hänninen, *Acta Mater.* **2007**, 55, 6108.
- [6] N. I. Vazquez-Fernandez, G. C. Soares, J. L. Smith, J. D. Seidt, M. Isakov, A. Gilat, V. T. Kuokkala, M. Hokka, *J. Dyn. Behav. Mater.* **2019**, 5, 221.
- [7] Y. Takahashi, *Int. J. Pressure Vessels Piping* **2019**, 172, 166.
- [8] G. Z. Voyiadjis, F. H. Abed, *Mech. Mater.* **2005**, 37, 355.
- [9] E. Puchi-Cabrera, J. Guérin, M. Dubar, L. Dubar, A. Dubois, *Mater. Sci. Eng. A* **2016**, 673, 660.
- [10] J. Kluczyński, L. Sniezek, K. Grzelak, J. Janiszewski, P. Płatek, J. Torzewski, I. Szacholuchowicz, K. Gocman, *Materials* **2020**, 13, 1449.
- [11] J. Cherry, H. Davies, S. Mehmood, N. Lavery, S. Brown, J. Siens, *Int. J. Adv. Manuf. Technol.* **2014**, 76, 869.
- [12] T. Ronneberg, C. M. Davies, P. A. Hooper, *Mater. Des.* **2020**, 189, 108481.
- [13] W. M. H. Verbeeten, M. Lorenzo-Bañuelos, P. J. Arribas-Subiñas, *Addit. Manuf.* **2020**, 31, 100968.
- [14] J. Cook, R. D. Goodridge, C. R. Siviour, *EPJ Web Conf.* **2015**, 94, 02019.
- [15] M. Robinson, S. Soe, R. Johnston, R. Adams, B. Hanna, R. Burek, G. McShane, R. Celeghini, M. Alves, P. Theobald, *Addit. Manuf.* **2019**, 27, 398.
- [16] O. G. Rivera, P. G. Allison, J. B. Jordon, O. L. Rodriguez, L. N. Brewer, Z. McClelland, W. R. Whittington, D. Francis, J. Su, R. L. Martens, N. Hardwick, *Mater. Sci. Eng. A* **2017**, 694, 1.
- [17] R. Ganeriwala, M. Strantza, W. King, B. Clausen, T. Phan, L. Levine, D. Brown, N. Hodge, *Additive Manufacturing* **2019**, 27 489.
- [18] M. Neuhäuserová, P. Koudelka, J. Falta, M. Adorna, T. Fila, P. Zlámal, *Acta Polytechnica CTU Proc.* **2019**, 25, 68.
- [19] H. Xi, L. Tang, S. Luo, Y. Liu, Z. Jiang, Z. Liu, *Compos. Part B Eng.* **2017**, 130, 217.
- [20] P. Koudelka, O. Jiroušek, T. Fla, T. Doktor, *Mater. Technol.* **2016**, 50, 311.
- [21] N. Novak, L. Krstulović-Opara, Z. Ren, M. Vesenjak, *Compos. Struct.* **2020**, 234, 111718.
- [22] N. Novak, L. Starčević, M. Vesenjak, Z. Ren, *Compos. Struct.* **2019**, 210, 167.
- [23] S. Hou, T. Li, Z. Jia, L. Wang, *Mater. Des.* **2018**, 160, 1305.
- [24] T. Fila, P. Zlámal, O. Jiroušek, J. Falta, P. Koudelka, D. Kytýř, T. Doktor, J. Valach, *Adv. Eng. Mater.* **2017**, 19, 10.
- [25] T. Fila, P. Koudelka, P. Zlámal, J. Falta, M. Adorna, M. Neuhäuserová, J. Luksch, O. Jiroušek, *Adv. Eng. Mater.* **2019**, 21, 8.
- [26] N. Novak, M. Vesenjak, S. Tanaka, K. Hokamoto, Z. Ren, *Int. J. Impact Eng.* **2020**, 141, 103566.
- [27] T. Fila, P. Zlámal, J. Falta, T. Doktor, P. Koudelka, D. Kytýř, M. Adorna, J. Luksch, M. Neuhäuserová, J. Valach, O. Jiroušek, *EPJ Web of Conf.* **2018**, 183, 02045.
- [28] Y. Duan, B. Du, X. Shi, B. Hou, Y. Li, *Int. J. Impact Eng.* **2019**, 132, 103303.
- [29] J. A. Harris, R. E. Winter, G. J. McShane, *Int. J. Impact Eng.* **2017**, 104, 177.
- [30] A. Beharic, R. Rodriguez Egui, L. Yang, *Mater. Des.* **2018**, 145, 122.



Dynamic impact testing of cellular solids and lattice structures: Application of two-sided direct impact Hopkinson bar

Tomáš Fíla^{*,a}, Petr Koudelka^a, Jan Falta^a, Petr Zlámal^a, Václav Rada^{a,b}, Marcel Adorna^a, Stefan Bronder^c, Ondřej Jiroušek^a

^a Czech Technical University in Prague, Faculty of Transportation Sciences, Konviktská 20, Prague 110 00, Czech Republic

^b Czech Academy of Sciences, Institute of Theoretical and Applied Mechanics, Prosecká 809/76, Prague 190 00, Czech Republic

^c Saarland University, Applied Mechanics, Campus A4.2, Saarbruecken 661 23, Germany

ARTICLE INFO

Keywords:

Direct impact Hopkinson bar
Cellular solids
Auxetic metamaterials
Digital image correlation
Wave separation

ABSTRACT

Direct impact testing with a Hopkinson bar is, nowadays, a very popular experimental technique for investigating the behavior of cellular materials, e.g., lattice metamaterials, at high strain-rates as it overcomes several limitations of the conventional Split Hopkinson Pressure Bar (SHPB). However, standard direct impact Hopkinson bars (DIHB) have only single-sided instrumentation complicating the analysis. In this paper, a DIHB apparatus instrumented with conventional strain-gauges on both bars (a so called Open Hopkinson Pressure Bar - OHPB) is used for dynamic impact experiments of cellular materials. Digital image correlation (DIC) is used as a tool for investigating the displacements and velocities at the faces of the bars. A straight-forward wave separation technique combining the data from the strain-gauges with the DIC is adopted to increase the experiment time window multiple times. The experimental method is successfully tested at impact velocities in a range of 5 – 30 m·s⁻¹ with both linear elastic and visco-elastic bars of a medium diameter. It is shown that, under certain circumstances, a simple linear elastic model is sufficient for the evaluation of the measurements with the visco-elastic bars, while no additional attenuation and phase-shift corrections are necessary. The applicability of the experimental method is demonstrated on various experiments with conventional metal foams, hybrid foams, and additively manufactured auxetic lattices subjected to dynamic compression.

1. Introduction

The dynamic testing of materials is an important task for describing the deformation behavior at high strain-rates and for understanding phenomena like wave propagation, inertia and friction effects, shock front formation, or coupled thermo-mechanical effects [1]. For such high strain-rate testing, Hopkinson bar experimental techniques have been found to be a vital method that produces reliable and consistent results. Nowadays, extensive research is performed in the field of cellular solids like metal foams [2,3], hybrid foams [4], additively manufactured materials [5], or lattice structures and metamaterials [6] including materials with a negative Poisson's ratio (auxetics) [7–12]. In this field, the behavior of cellular solids and metamaterials can be used for the development of, e.g., lightweight structures of complex shapes or shock absorbers [13]. However, as the internal structure of cellular solids and metamaterials is rather complex (often on all levels: micro, mezzo or macro), the description of their mechanical properties is

non-trivial, dependent on many factors, and their behavior often exhibits mechanisms that are still not well described and understood. This problem is particularly significant in dynamic loading, where a lot of effects influence the deformation behavior of the material. While the standard Kolsky bar arrangement [14] is a well-established technique for the high strain-rate testing of bulk materials in compression, it has a number of disadvantages limiting its application for cellular solids and additively manufactured lattices [15,16]. Nevertheless, the topic is very attractive and papers describing the experimental and/or numerical investigation of metal foams [17–21], metamaterials or additively manufactured materials and lattices [22] using the Hopkinson bar or gas-/powder-gun [23,24] are available. In some papers, digital image correlation (DIC) has been employed as a tool for the advanced analysis of the displacement and strain fields during the experiments [25–28]. The dynamic indentation of cellular materials subjected to dynamic loading has also been of interest [29–34].

In the conventional split Hopkinson pressure bar (SHPB), the

* Corresponding author.

E-mail addresses: fila@fd.cvut.cz, filatoma@fd.cvut.cz (T. Fíla).

<https://doi.org/10.1016/j.ijimpeng.2020.103767>

Received 20 May 2020; Received in revised form 14 September 2020; Accepted 1 November 2020

Available online 5 November 2020

0734-743X/© 2020 The Authors.

Published by Elsevier Ltd.

This is an open access article under the CC BY-NC-ND license

(<http://creativecommons.org/licenses/by-nc-nd/4.0/>).

maximum achievable strain in the specimen is proportional to the length of the striker bar and its impact velocity. Therefore, the maximum strain is significantly constrained by the geometry of the setup and performance of its mechanism accelerating the striker. Moreover, in classical theory, the time window of the experiment is limited to the short period of time before the wave superposition occurs at the location of the strain wave sensing instrument (typically a strain-gauge). As the cellular solids and lattices are materials with a relatively low mechanical impedance, another problem arises with the disproportion between the amplitudes of the reflected and transmitted signal that are additionally distorted by the wave dispersion. Typically, the transmitted signal is much lower in comparison with the amplitude of the incident and reflected pulse making the analysis of dynamic equilibrium difficult. Due to the complex nature of cellular solids and lattices, another problem is related to the specimen size. The testing of the representative volume element (RVE), as defined for cellular solids [35], usually requires large specimens that can barely be tested up to the densification region in the classical Kolsky bar. Here, larger strain of the specimen can be achieved by increase of the striker bar impact velocity or by increase of striker bar length. Both approaches have their physical limits. The maximum striker bar impact velocity in the SHPB is limited by the performance of the device for the acceleration of the striker (typically a gas-gun) and by the yield strength of the material of the bars. As the incident pulse is generated by the impact of the striker on the incident bar, the amplitude of the pulse is much higher than the pulse transmitted through the specimen. Therefore, an apparent velocity limit exists that would result in the plastic deformation of the bar (e.g., for aluminum alloys approximately $50 - 60 \text{ m}\cdot\text{s}^{-1}$). On the other hand, an increase in the striker bar length is limited by the geometrical tolerances of the gas-gun barrel. Generally, longer strikers have to be used for testing at lower strain-rates to achieve a similar strain as those by shorter strikers at higher velocities. Moreover, large specimens require a long time to achieve an equilibrium of the dynamic forces.

Many improvements in the standard Hopkinson bar experimental setup have been developed to overcome the aforementioned problems, to extend its application envelope and to reliably test cellular solids and low impedance materials in general. Pulse-shaping techniques [36–41] have been used to reduce the wave dispersion in the bars, to prolong the ramp-in period of the strain wave (so called “ringing effects”), to achieve a dynamic equilibrium in a shorter time and to optimize the strain-rate. Specialized sensors based on quartz technology have been employed for precise force measurements directly at the faces of the specimen [42]. Low impedance visco-elastic bars have been used for the better impedance matching of the bar with the specimen [43–45] and specific calibration and wave time-shifting methods have been developed to process the signals from the visco-elastic bars [46]. Various wave separation techniques have been introduced to extend the experiment duration [47–51].

Special attention has been paid to the development of the specialized Hopkinson bar experimental setups optimized for testing of low impedance and cellular materials [15]. The experimental techniques often combine the specialized apparatus together with the aforementioned approaches. A long pre-loaded bar has been used instead of the conventional striker to develop very long incident strain waves and to compress the specimens of metal foam up to densification [16,52]. Important improvements have been made related to the application of direct impact Hopkinson bar [53] (DIHB) for the testing of cellular materials. DIHB has been employed for the testing of metal foams at high impact velocities [17,54,55] and has overcome a number of limitations of the conventional experimental setups. In DIHB, the specimen can be easily deformed to large strains (up to densification in the case of cellular solids), while the strain waves propagating in the setup do not exhibit disproportional amplitudes and are similar to each other. Moreover, DIHB can be used for the testing of cellular solids at high impact velocities as plateau stresses of the specimens are much lower than that of the bars. Therefore, the strain wave generated at the

specimen-bar interface cannot induce plastic deformation in the bars. Both variants of the DIHB represented by the forward DIHB (FDIHB) and reverse DIHB (RDIHB) has been used for the testing of cellular materials [17,19,56], additively manufactured lattice structures [57,58] and to investigate shock effects in the material [54,59]. In FDIHB, the specimen is mounted on the instrumented transmission bar and is directly impacted by a projectile. The RDIHB is, in fact, a variant of the Taylor anvil test [60,61], where the specimen that is mounted on a projectile is launched against the instrumented transmission bar. However, as the DIHB is instrumented only on either side of the specimen, the equilibrium of the dynamic forces and strain of the specimen cannot be directly analyzed from the signals recorded at the transmission bar. This represents one of the limiting factors of the DIHB testing. The problem can be partially overcome by the combined testing using FDIHB and RDIHB [19], while the FDIHB is used to investigate the force histories on the back-side of the specimen and RDIHB is used for the same analysis on the impact-side of the specimen. This approach has two limitations: (i) it is considered that the wave propagation effects and dynamic forces are similar for all the tested specimens, (ii) the specimen has to fit into the barrel of the gas-gun. Therefore, this method cannot be employed for the testing of large specimens and/or specimens that are difficult to produce in large numbers like, e.g., additively manufactured panels. With the single-sided instrumentation, the strains are often evaluated using high-speed camera images.

A few research groups have investigated the methods for the two-sided instrumentation of the DIHB setup. A DIHB instrumented on both the incident bar (striker) and the transmission bar using a thin PVDF (polyvinyl fluoride) film gauges has been used for the testing of soft materials like rubber [62]. Another approach using photon Doppler velocimetry (PDV) has been tested in DIHB [63] to evaluate the velocity and force histories for both bars according to the PDV technique developed for SHPB [64]. The approach described in [62] has been tested at low velocities (up to approximately $10 \text{ m}\cdot\text{s}^{-1}$). Although the PVDF gauges have a low noise and can produce smooth clear signals, their mounting is demanding and requires careful calibration to prevent stress concentrations at the contact. The method described in [63] has been employed on the direct impact testing of metal foams [65]. While it was demonstrated that the PDV instrumentation can be used even at velocities of approximately $100 \text{ m}\cdot\text{s}^{-1}$ [63], some limitations arise from the demanding evaluation, flexural waves compensation and expensive instrumentation. Furthermore, problems with the laser beam positioning under the angle with the longitudinal axis of the striker bar, the weak reflected signal and mounting of the reflective pattern or coating on the striker bar complicate the application of the PDV method for measurements with large striker bar displacements. An advanced approach using the in-situ deceleration measurement has also been tested [66]. In this method, the striker bar instrumented with an accelerometer is employed to directly impact the specimen. As in the PDV based method, the technique can be used for the high velocity compression of the tested material. However, as the accelerometer is used as a sensor, extensive filtering of the measured signals has to be performed to estimate the forces and velocities during the impact. Another DIHB setup was proposed by Govender and Curry [67]. In the paper, the setup has been called the Open Hopkinson Pressure Bar (OHPB). The OHPB setup is, in principle, the DIHB instrumented by conventional strain-gauges on both bars. It was demonstrated that the technique is simple and with many benefits suitable for the testing of low impedance materials. The setup was tested via compression tests of a SAN (styrene acrylonitrile) foam using PMMA (poly-methyl methacrylate) bars with a diameter of 20 mm at impact velocities of up to $10 \text{ m}\cdot\text{s}^{-1}$. The conventional SHPB setups can be relatively easily adapted to the OHPB variant, while standard strain-gauges can still be used as the instrumentation. As the PDV based method requires complex instrumentation and data processing, the in-situ deceleration technique requires an extensive filtering of the input signal and the applicability of

the other methods has been demonstrated at low velocities only, thus, the further experimental investigation of the performance and application envelope of the OHPB method is desired. Moreover, testing at low impact velocities (i.e., a relatively long impact duration) up to high strains, particularly with linear elastic bars (e.g., aluminum alloy) is complicated by the fact that the wave superposition occurs early at the strain-gauge location. In this case, the situation is worse for the incident bar, where the mounting of the second strain-gauge at the end of the bar is problematic. The second strain-gauge is necessary for the standard wave separation according to, e.g., [51].

In this paper, we introduce a different version of the OHPB setup than presented in [67]. A linear guidance system is employed to guide the incident bar during its acceleration provided by a gas-gun. With this arrangement, it is possible to achieve higher impact velocities without any bar alignment problems, parasitic bending and damage to the strain-gauges or wiring. The system has been successfully tested at impact velocities of up to approximately $30 \text{ m}\cdot\text{s}^{-1}$. However, we are convinced that, with a higher performance of the gas-gun, this limit can be increased even further. DIC is used as a tool for the verification of the straight-forward wave separation technique requiring only a single strain-gauge at each bar allowing for the extension of the experimental time window several times. The experimental method has been tested with mid-sized linear elastic bars made of a high strength aluminum alloy and with visco-elastic bars made of PMMA. It is shown that, under certain circumstances, a simple linear elastic model is sufficient to perform measurements with the visco-elastic bars, while no additional attenuation and phase-shift corrections are necessary. The methods of the wave separation, the setup calibration and the DIC analysis are described in detail. The applicability of the experimental method is demonstrated on various experiments with conventional metal foams, hybrid foams, and additively manufactured auxetic lattices subjected to dynamic compression. Thus, the presented OHPB and methodology represent an interesting alternative to the testing of low impedance materials using the standard DIHB or SHPB that can be easily adapted, provides reliable results and uses standard instrumentation. The method is particularly beneficial for experiments, where instrumented striker bar is critically required together with the large strain in the specimen, i. e., the dynamic indentation of large specimens or panels that cannot be launched against an instrumented transmission bar in RDIHB.

2. Materials and methods

2.1. Open Hopkinson pressure bar

The principle of the OHPB method is directly derived from the DIHB methods. The schemes of both the forward and reverse DIHB method and the OHPB are shown in Fig. 1. Note that in the forward and reverse DIHB, only the transmission bar is instrumented with a strain-gauge. The OHPB consists of two measurement bars (incident and transmission) both of which are instrumented with strain-gauges. The incident bar is inserted into the barrel of the gas-gun and simultaneously serves as the striker bar. The specimen is mounted on the impact face of the transmission bar. During the experiment, the incident bar is accelerated using

the gas-gun and directly impacts the specimen (see Videos S1 and S2). At the impact, the strain waves are generated in both bars. The pulses propagate from the specimen to the free ends of the bars. Then, the pulses are reflected and travel back to the specimen. The experiment ends (in the classical representation [67]) when the backward-propagating waves reach the strain-gauges, thus, producing superposed signals. As the waves propagate from the specimen, they have an approximately identical shape. The beginning of the transmission pulse is delayed in comparison with the incident pulse as the strain wave has to pass through the specimen (similarly to the SHPB).

Using the strain-gauge signals, it is possible to calculate the forces and displacements on the respected faces of the bars [67]. The forces on the incident face $F_{in}(t)$ and on the transmission face $F_{out}(t)$ can be calculated according to the relations

$$F_{in}(t) = A_{in}E_{in}\epsilon_{in}(t), \quad (1)$$

$$F_{out}(t) = A_{out}E_{out}\epsilon_{out}(t), \quad (2)$$

where A_{in} , A_{out} represent the cross-sectional area of the (input and output) bars, E_{in} , E_{out} represent Young's modulus of the individual bars and $\epsilon_{in}(t)$, $\epsilon_{out}(t)$ are the measured strain-gauge signals. The particle velocities $v_{in}(t)$, $v_{out}(t)$ at the ends of the bars can be represented using the relations

$$v_{in}(t) = C_{0in}\epsilon_{in}(t), \quad (3)$$

$$v_{out}(t) = C_{0out}\epsilon_{out}(t), \quad (4)$$

where C_{0in} and C_{0out} are the wave propagation velocities in the bars. By adopting the aforementioned formulas, the actual impact velocity $v(t)$ and the distance between the bars (or actual specimen length) $l_s(t)$ are given by

$$v(t) = v_0 - C_{0in}\epsilon_{in}(t) - C_{0out}\epsilon_{out}(t), \quad (5)$$

$$l_s(t) = l_0 - \int_0^t v(t)dt = l_0 - \int_0^t (v_0 - C_{0in}\epsilon_{in}(t) - C_{0out}\epsilon_{out}(t))dt, \quad (6)$$

where l_0 is the initial length of the specimen and v_0 is the initial impact velocity. Note that the evaluation of the actual length of the specimen (strain) is strongly dependent on the initial impact velocity v_0 . Thus, in the OHPB, it is crucial to measure the velocity with high precision (by, e. g., DIC), unlike in the SHPB method, where the impact velocity serves as a secondary parameter useful for the verification of the results.

All the above described equations are valid for linear elastic bars. For experiments with visco-elastic bars, one of the well-known methods based on the propagation coefficient and the time-shifting in frequency domain [46,47,49,51] can be used. However, as it is demonstrated further in the text, under certain strict conditions, the linear elastic model can be adopted even for visco-elastic bars (see Section 2.4.4).

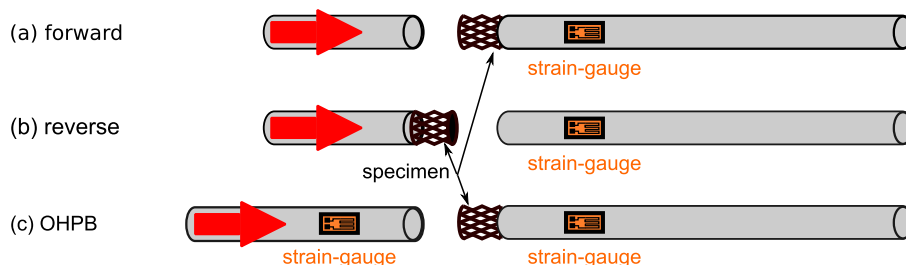


Fig. 1. Principle of the forward DIHB (a), reverse DIHB (b), and OHPB (c).

2.2. Digital image correlation

Digital Image Correlation (DIC) is an optical method employing tracking techniques for the measurements of the changes in the images. In this paper, an in-house developed software tool is employed for the tracking of the pseudo-random black-and-white speckles mounted on the bars and for the evaluation of the particle velocities at the faces of the bars. With the DIC tool, the tracking is achieved with a sub-pixel precision. First, the correlation is evaluated at the pixel level using template matching employing the Sum of Squared Differences (SSD) method. To obtain the sub-pixel precision, the pixel level difference is interpolated using a third order bivariate spline over the pixel grid. The best match is in the position of the minimum difference. The minimum of the difference (best match) is then found by minimizing the interpolated bivariate spline using the LM-BFGS algorithm.

2.3. Wave separation technique

The equations described in Section 2.1 are valid only until the strain wave is reflected at the free-end of the bar and it arrives back to the strain-gauge location producing the superposed signals. This situation is represented by the wave propagation diagram in Fig. 2(a). From this moment, the recorded signal is composed of a sum of forward- and backward-propagating strain waves. According to standard one-dimensional wave propagation theory, the actual particle velocity $v(t)$, and the actual force $F(t)$ at a certain cross-section of the bar are given by [51]

$$\varepsilon(t) = \varepsilon_F(t) + \varepsilon_B(t), \quad (7)$$

$$v(t) = c_0(\varepsilon_F(t) - \varepsilon_B(t)), \quad (8)$$

$$F(t) = EA(\varepsilon_F(t) + \varepsilon_B(t)), \quad (9)$$

where $\varepsilon_F(t)$ is the forward-propagating strain-wave and $\varepsilon_B(t)$ is the backward-propagating strain-wave. Wave separation methods for the decomposition of the forward- and backward-propagating waves in SHPB have been developed and are available [47,49,51]. The methods usually separate the waves using signals from at least two strain-gauges (or a strain-gauge and velocity sensor for a bar with a free-end) and are applicable even for visco-elastic bars. For the SHPB, a wave separation technique based on a single-point measurement and known boundary conditions was published in [50]. This method works without any redundant data source and does not account for the wave dispersion. In the case of the OHPB, the application of a second strain-gauge or direct velocity sensor would be complicated for the incident bar. Therefore, under certain circumstances, a simplified wave separation technique

requiring only a single strain-gauge on each bar can be employed, while, in our case, its output is verified using DIC.

The straight-forward wave separation technique can be used if the following assumptions are satisfied:

- The waves propagate from the specimen to the free-ends of the bars.
- The free-ends are not in contact with other parts of the setup.
- The waves are generated directly at the interface between the specimen and the bar.
- The specimen has the lowest mechanical impedance in the experimental setup and deforms plastically up to a large strain.
- High frequencies are not present in the strain pulse as they are attenuated by the plastic deformation of the specimen.
- The wavelengths present in the strain pulse are several times higher than the diameter of the bar. Thus, the wave attenuation and dispersion effects can be neglected.

Under the aforementioned circumstances, a boundary condition valid for the free-end of the bar can be used to separate the individual waves. According to this boundary condition, the force at the free-end of the bar has to be zero. Thus, the waves at the free-end of the bar have to satisfy the following relations (see Fig. 2(b))

$$\varepsilon_F(t) + \varepsilon_B(t) = 0, \quad (10)$$

$$\varepsilon_B(t) = -\varepsilon_F(t). \quad (11)$$

According to the diagram shown in Fig. 2(a) the experiment begins at time $t = -\Delta t_s$ and the strain wave arrives at the strain-gauge location at time $t = 0$. Then, the time required for the wave to travel through the bar to its free-end is equal to Δt_c . Thus, at time $t = 2\Delta t_c$ the superposed signal is recorded by the strain-gauge and the measured signal $\varepsilon(t)$ is composed of two waves $\varepsilon_F(t)$ and $\varepsilon_B(t)$. By adopting the equations from above, the forward- and backward-propagating waves can be separated and are given by

$$\varepsilon_B(t) = -\varepsilon_F(t - 2\Delta t_c), \quad (12)$$

$$\varepsilon_F(t) = \varepsilon(t) - \varepsilon_B(t) = \varepsilon(t) + \varepsilon_F(t - 2\Delta t_c). \quad (13)$$

Using the procedure shown in Fig. 2(b), the relevant forward- and backward-propagating waves can be time-shifted to the bar-specimen interface producing strain waves $\varepsilon_{FS}(t - \Delta t_s)$, $\varepsilon_{BS}(t - \Delta t_s)$ at the specimen's location and can be used to calculate the particle velocity $v(t - \Delta t_s)$ and the contact force $F(t - \Delta t_s)$ using the relations

$$\varepsilon_{FS}(t - \Delta t_s) = \varepsilon(t) + \varepsilon_F(t - 2\Delta t_c), \quad (14)$$

$$\varepsilon_{BS}(t - \Delta t_s) = -\varepsilon_F(t - 2\Delta t_c + \Delta t_s), \quad (15)$$

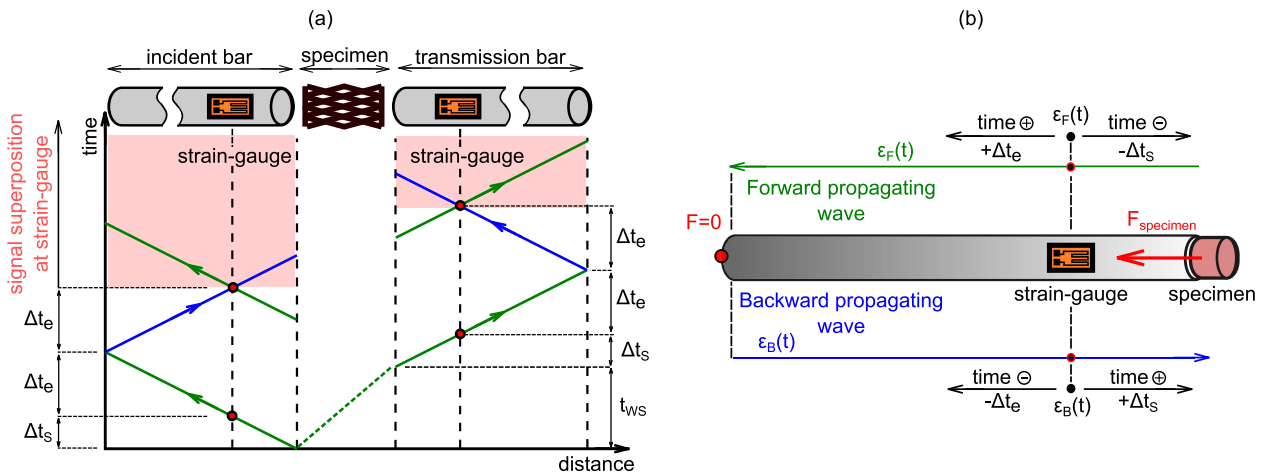


Fig. 2. Diagram showing the strain wave propagation in the OHPB setup (a). Principle of the wave separation and time-shifting (b).

$$v(t - \Delta t_s) = c_0(\varepsilon_{FS}(t - \Delta t_s) - \varepsilon_{BS}(t - \Delta t_s)), \quad (16)$$

$$F(t - \Delta t_s) = EA(\varepsilon_{FS}(t - \Delta t_s) + \varepsilon_{BS}(t - \Delta t_s)). \quad (17)$$

As the wave dispersion effects can be considered negligible, the waves can be separated using this procedure. Neither the shape nor amplitude of the waves needs to be updated. At the beginning of the experiment, the strain-gauge signal $\varepsilon(t)$ is not superposed between time $t = -\Delta t_s$ and $t = 2\Delta t_c$. Thus, this part of the pulse can be used for the iterative reconstruction of the signal.

In the real bars, the wave dispersion effects are always present and the strain wave is attenuated over time. Therefore, it is necessary to check whether the wave separation technique still produces reliable results. For this purpose, pseudo-random black-and-white speckle patterns are mounted on the bars as close to the specimen as possible. The high-speed camera is used to observe the specimen during the experiment, while the speckle patterns are observed together with the specimen. DIC is used to evaluate the displacements at the boundaries between the bars and the specimen. The displacements are calculated from the strain-gauge data by integration of the indicated velocities producing smooth curves (typically monotonous), where difference between the DIC and strain-gauges is represented by typically marginally different slopes of the curves. Conversely, the particle velocities of the bars' faces are calculated from the DIC displacements by differentiation. By its nature, differentiation brings more noise into the resulting velocity signal. Thus, a comparison of velocities is more difficult, but it is more useful to identify possible errors in the measurement and, if successful, produces more representative results. If the setup and DIC are properly calibrated, the particle velocities indicated by DIC have to be comparable with the velocities indicated by the separated strain-gauge signals time-shifted to the bar-specimen interface. The strain calculated without the wave separation plotted against time is compared with the strain calculated using the wave separation technique in Fig. 3(a). The velocities indicated by strain-gauges calculated without the wave separation and with the wave separation are compared with the velocity evaluated by the DIC in Fig. 3(b). Results of the wave separation technique in the incident bar of the OHPB are shown in Videos S3 and S4.

The wave separation technique, in this form, does not account for the wave dispersion effects including the attenuation and phase-shift. Therefore, it is not possible to use it for the visco-elastic bars. In the OHPB, the wave travel distance is usually long (typically close to 3 m for the experiments presented in this paper) because the strain wave has to propagate to the free end of the bar and then return back to the location of the strain-gauge. Thus, in the case of the visco-elastic bars, the backward propagating wave is significantly attenuated and phase-

shifted. As a result, the assumption that the forward-propagating wave can be directly used for the wave decomposition does not hold true. However, a simple analysis valid until the wave superposition (see Section 2.1) can be used even for visco-elastic bars. Comparing typical materials used for visco-elastic and linear elastic bars in the Hopkinson bar devices (with the same length and configuration of the bars), a longer time window prior to the wave superposition is available for the visco-elastic materials because of their lower wave propagation velocities. For instance, the wave propagation velocity in aluminum alloy bars is approximately $5100 \text{ m}\cdot\text{s}^{-1}$, while the wave propagation velocity for the PMMA is approximately $2100 \text{ m}\cdot\text{s}^{-1}$. Therefore, approximately $2.5\times$ longer time window is available for the PMMA compared to aluminum before the backward-propagating strain wave hits the strain-gauge producing superposed signals.

2.4. Setup calibration

The setup calibration is an important task that has to be carried out prior to every set of experiments. During the calibration procedure, the response of the strain-gauges is tested using a quasi-static force calibration. Furthermore, the behavior of the strain-gauges and DIC is compared in a series of dynamic void tests.

2.4.1. Quasi-static calibration

During the quasi-static calibration, the bars of the setup are subjected to an uni-axial compression using a piston mounted at the end of the experimental setup. A conventional membrane load-cell (U9B, HBM, Germany) is mounted co-axially between the bars (as the specimen). The values of the force calculated from the strain-gauges (and the known material properties of the bars) are compared with the force indicated by the load-cell. Using the quasi-static calibration, the proper functionality and precision of the strain-gauges are verified. Typically, the error of an individual pair of foil strain-gauges is up to 2 – 4% of the load-cell force.

2.4.2. Dynamic void tests

A void test is, in principle, an OHPB experiment without any specimen. The incident bar is accelerated using the gas-gun and directly impacts the transmission bar forming an elastic collision between two bars. Under such conditions, the kinetic energy of the incident bar is transferred to the transmission bar, while the duration of the collision corresponds to $2l/C_0$ in the case when both bars are made of the same material with the nominal wave propagation velocity C_0 and have the same length l . In such a theoretical case, the initial impact velocity v_0 of the incident bar decreases to $v_0/2$ during the collision. After the collision, the incident bar has zero velocity, while the transmission bar is

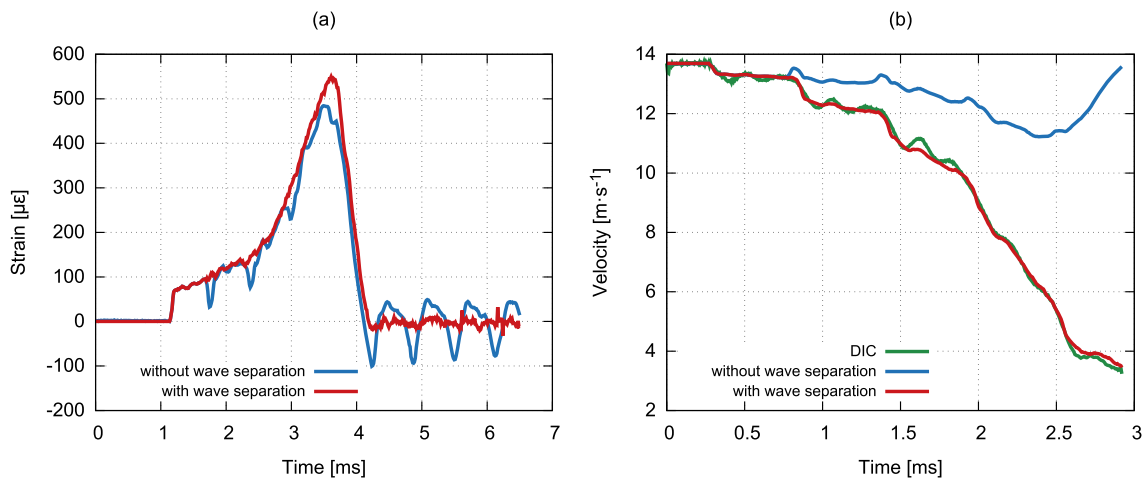


Fig. 3. Strain calculated without the wave separation plotted against time compared with the strain calculated using the wave separation (a). The velocities indicated by the strain-gauges calculated without the wave separation and with the wave separation compared with the DIC (b).

accelerated to v_0 . During the void test, the strain-gauge signals are compared with the velocity obtained from the DIC and with the theoretical velocity value estimated according to the elastic collision theory. In the case of linear elastic bars, the error has to be maximally in the order of a few percent (typically better than 1 – 3%). The situation is more complicated for visco-elastic bars, however, the strain-gauge signals still have to closely correspond to the values obtained from the DIC (where an average difference approaching 6 – 10% is considered to be an unacceptable error).

2.4.3. Linear elastic bars

The dynamic material properties, wave propagation velocity and dispersion of the bars are investigated according to method published by Bacon [46] using the "bars together" void test. The impact of the short striker colliding with the incident bar directly in the barrel of the gas-gun is used to evaluate the required parameters. For linear elastic bars, the results of the quasi-static calibration should closely match the outputs of the dynamic testing. Then, a set of dynamic void tests is performed, while the consistency of the strain-gauge signals is investigated. The velocities indicated by strain-gauges have to closely match the velocities evaluated using the DIC. Result of the quasi-static calibration of the high-strength aluminum alloy bars is shown in Fig. 4(a). The velocities indicated by the strain-gauges and DIC during the void test are compared in Fig. 4(b).

2.4.4. Visco-elastic bars

The situation is more complicated for visco-elastic bars. In this case, during the quasi-static calibration, the quasi-static material parameters have to be used to compare the strain-gauge signals with the load-cell. Then, the "bars together" void test is performed similarly as in the case of the linear elastic bars and the dynamic material properties of the visco-elastic model are evaluated according to [46]. Then, a set of dynamic void tests is used to compare the response of the strain-gauges with the DIC and with the theory of the elastic collision. The result of the quasi-static calibration of the PMMA bars is shown in Fig. 5(a). The velocities indicated by the strain-gauges and DIC during the void test are compared in Fig. 5(b).

Conventionally, the waves in the visco-elastic bars have to be time-shifted in the frequency domain using the visco-elastic material model and a function of the wave propagation coefficient [46]. However, in the case of the OHPB, simplifications can be adopted if the following testing conditions are satisfied:

- The strain-gauges are mounted as close as possible to the specimen. Proximity of the sensors to the location of the impact ensures that the

recorded signals are highly similar to the original signals generated by the impact.

- The amplitudes of the strain waves are low in comparison with the theoretical strain capacity of the bar at a given impact velocity. For the small strain amplitudes, non-linear effects in the polymeric bars are significantly suppressed, while the distortion becomes more severe with the increasing amplitudes.
- The wavelengths of the frequencies present in the recorded pulses are several times higher than the diameter of the bars. This assumption is essential for significant reduction of the wave dispersion effects during the experiment.
- The specimen deforms plastically and acts as an effective filter of the higher frequencies. Plastic collapse of the specimen prevents transfer of high frequencies that are significantly affected by the wave dispersion effects.
- No significant bending is present during the testing. If significant bending is observed during the experiment, the specimen does not follow the uni-axial loading leading to more complex modes of deformation. Moreover, the measurement technique cannot compensate for a minor bending of the bars and the measured signals are distorted.

When the above described conditions are fulfilled, the time-shifting procedure can be processed identically as in the case of the linear elastic bars. Because the dynamic properties of some visco-elastic materials are approximately constant at lower frequencies for long projectiles (as presented in Fig. 6(a,b) for a projectile with a length of 1750 mm and a diameter of 20 mm made of PMMA), the average value of the complex modulus and the phase velocity for that can be used for the calculation of the particle velocity and the force, while the frequency domain based time-shifting of the signal is not necessary. The signals recorded by the strain-gauges at distances of 200 mm and 400 mm from the impact face of the PMMA bar with a diameter of 20 mm are time-shifted by the frequency domain method and compared with the output of this simplified approach in Fig. 7(a). It can be seen that, using this simple approach, the error caused by the wave attenuation is more profound with the increasing amplitude of the recorded signal, while the frequency domain time-shifting procedure can better compensate for this error. No significant phase-shift effects are observable in the presented example. The method for the dispersion correction in the visco-elastic bar based on the frequency domain approach produces more precise results. However, as the recorded amplitudes of the tested cellular materials are usually low and the effects of the attenuation and dispersion are small or negligible for the short travelled distance, the simple method can be adopted. As can be seen in Fig. 7(a), its error over

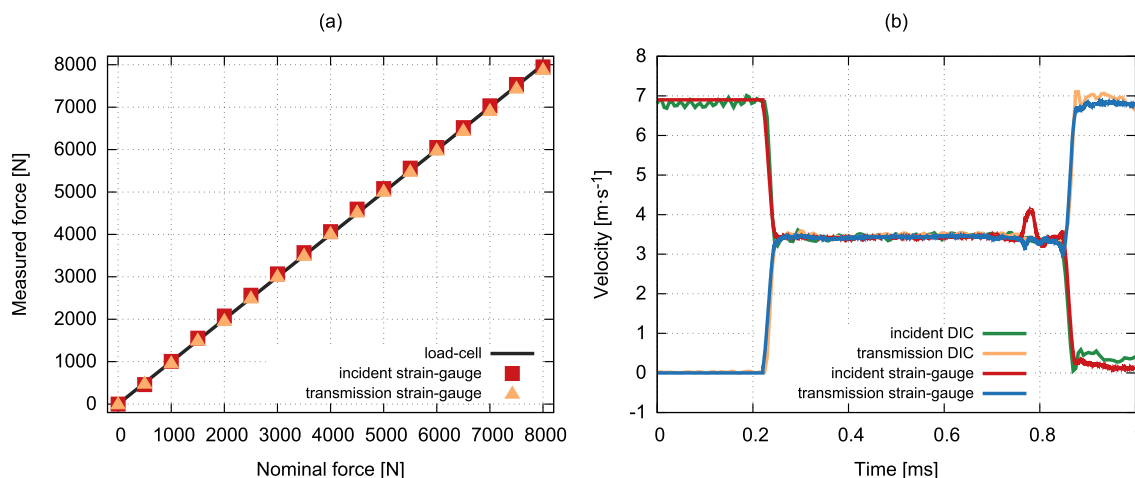


Fig. 4. Force indicated by the strain-gauges compared with the load-cell during the quasi-static calibration procedure, aluminum alloy bars (a). The velocities indicated by the strain-gauges during the void test compared with the DIC, aluminum alloy bars (b).

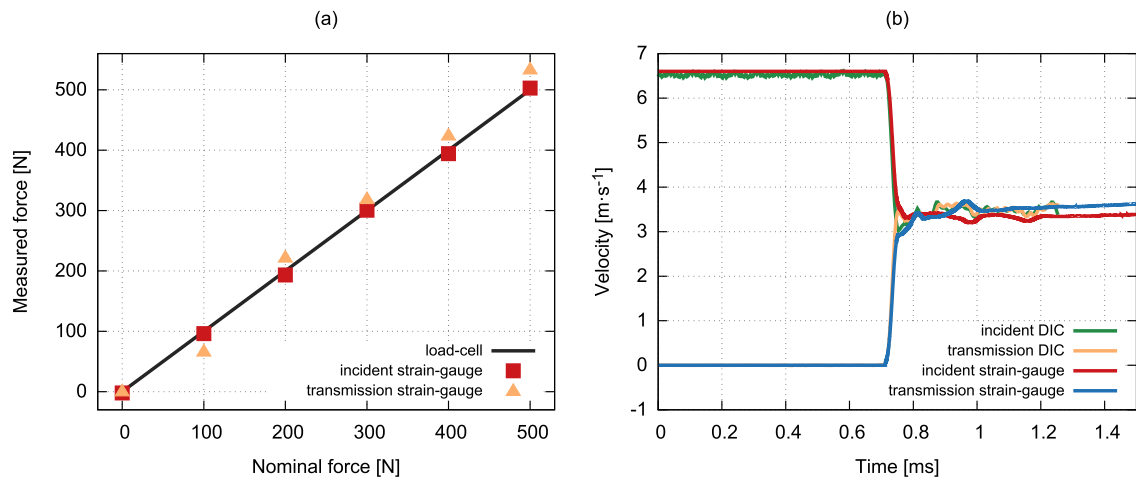


Fig. 5. Force calculated from the strain-gauge signals compared with the force value measured by the load-cell during the quasi-static calibration procedure, PMMA bars (a). The velocities calculated from the strain-gauge signals during the void test compared with values from the DIC, PMMA bars (b). Note that the DIC was not able to capture the separation of the bars as it happened out of the field of view due to the large displacements of the PMMA bars.

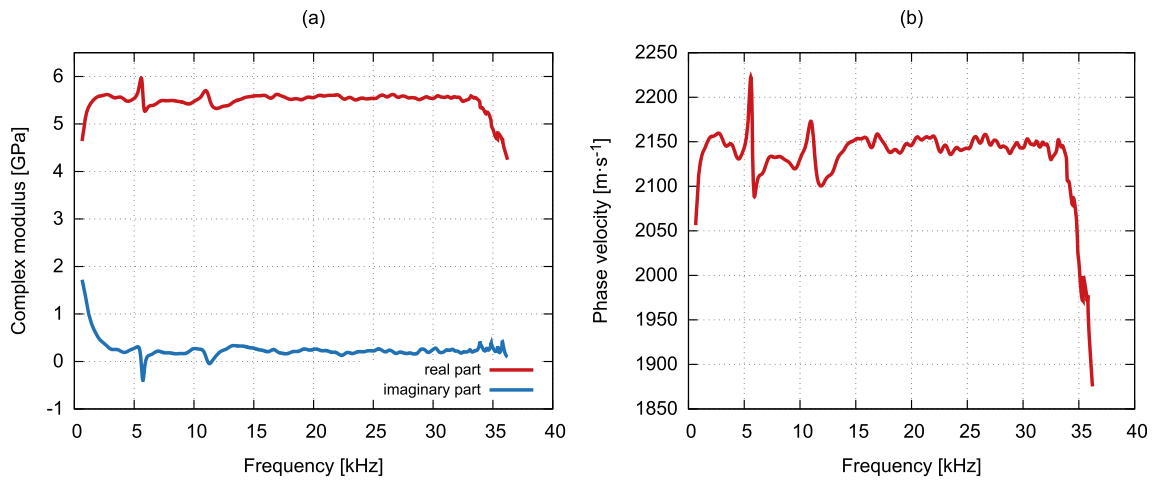


Fig. 6. Visco-elastic properties of the PMMA projectile with a length of 1750mm and a diameter of 20mm at an impact velocity of $7m \cdot s^{-1}$. Complex modulus (a). Note that the rapid changes in the low frequencies (approximately below 2kHz) are related to the conversion of the measured signal to frequency domain using Fast Fourier Transform and does not represent the actual material properties. The phase propagation velocity of the PMMA bars (b).

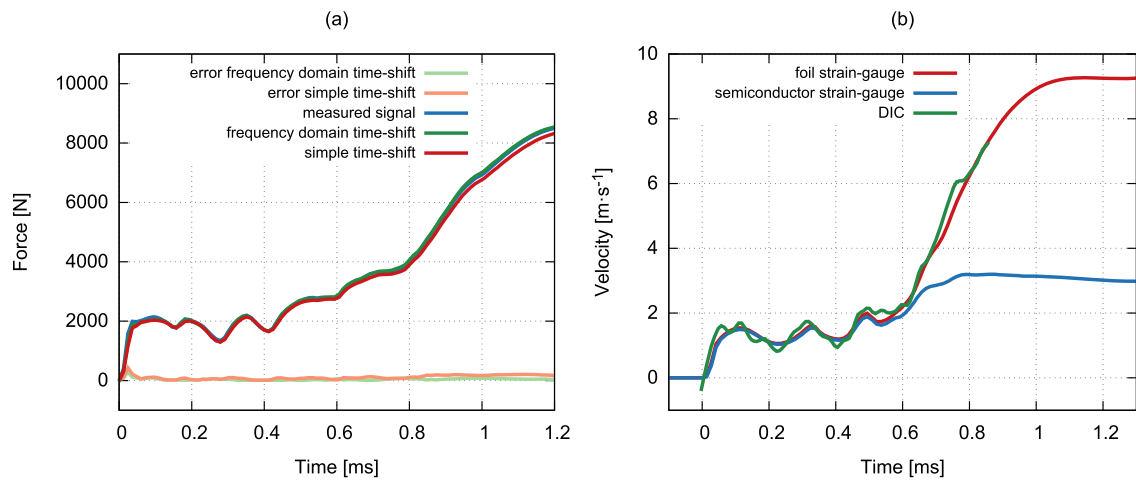


Fig. 7. Signals recorded by the strain-gauges at distances of 200mm and 400mm from the impact face of the PMMA bar with a diameter of 20mm time-shifted by the conventional frequency domain method compared with the output of the simplified approach (a). The velocity calculated using the data of the semiconductor (AFP-500-090, Kulite, USA) and foil (3/120, LY61, HBM, Germany) strain-gauge during the impact experiment compared with the DIC (b).

the 200 mm travel distance is negligible for forces of up to approximately 4000N and the error is around 2% at a force of approximately 8000N. Therefore, with care, this simple approach can be used to avoid problems caused by the inverse Fourier transform, where the errors or peaks in a function of the propagation coefficient can result in the reconstruction of distorted signals.

2.5. Experimental setup

In this paper, we present a set of representative results from the two-sided direct impact Hopkinson bar testing of conventional metal foams, additively manufactured auxetic lattices, and hybrid auxetic constructs. For the measurements, two variants of the OHPB experimental setup were used: (i) a setup with aluminum alloy bars of an identical diameter for the uni-axial compression testing, (ii) a setup with PMMA bars of an identical diameter for the uni-axial compression testing. Foil strain-gauges were used instead of the semiconductor strain-gauges due to their linearity, durability and longer service-life. The use of the semiconductor strain-gauges was rejected mainly because of their strongly non-linear response above approximately $500\mu\epsilon$ (see the velocity profiles evaluated from the semiconductor and foil strain-gauges compared with the DIC in Fig. 7(b)). Nevertheless, the semiconductor strain gauges were used as the auxiliary sensors with limited service-life in the selected experiments. The arrangement of the individual experimental setups is presented in Fig. 8.

2.5.1. Linear guidance system

In all the variants of the presented OHPB setup, a low mass/low friction linear guidance system was employed to guide the incident bar during the acceleration over a relatively long travel distance. The linear guidance system consisted of a linear motion guide with a high performance polymeric slider bearing (drylinT, IGUS, USA) and a rail with a length of 1200 mm. The incident bar was attached to the carriage via a friction contact clamp. The tightening moment of the clamp had to be kept constant for all the experiments and was re-adjusted after each impact. During the calibration testing, it was found out that the friction clamp did not bring any distortion to the incident wave if adjusted properly. As the design parameters of the used bearing type were partially outside the OHPB velocity envelope, the bearings had to be replaced after a certain number of measurements (usually after a few dozen impacts) due to wear and tear. The stiffness, performance and durability of the system could be probably further improved with the use of caged-ball linear motion guides optimized for high-speed applications.

2.5.2. Gas-gun system

An in-house gas-gun system was used for the acceleration of the incident bar. This system consists of a barrel with an inner diameter of 20 mm and a length of 2500 mm which is connected to a 20l air reservoir with a maximum operating pressure of 1.6 MPa. The compressed air is released by a solenoid valve (366531, Parker, USA).

2.5.3. High-speed imaging and data acquisition system

All the experiments were observed with high-speed camera(s). In the described experiments, two types of high-speed cameras were used: (i) Fastcam SA-5 (Photron, Japan), (ii) Fastcam SA-Z (Photron, Japan). A typical experiment was captured with the latter camera at 252kfps with an image resolution of $256 \times 168px$. The illumination of the scene was undertaken using a pair of high intensity LED lights systems: (i) Constellation 60 (Veritas, USA) and (ii) Multiled QT (GS Vitec, Germany). The strain-gauge signals were amplified by a pair of low-noise differential amplifiers (EL-LNA-2, Elsys AG, Switzerland) with a gain of 100 and recorded by high-speed digitizer cards (PCI-9826H, ADLINK Technology, Inc., Taiwan) operating at 20 MHz. The digitizer cards were synchronized with the high-speed camera(s) using a pair of short-reaction-time through-beam photoelectric sensors (FS/FE 10-RL-24 PS-E4, Sensopart, Germany) serving as a trigger and as a redundant method (together with DIC) for the estimation of the initial impact velocity. The data acquisition system was implemented in LabView software (National Instruments, USA).

2.5.4. Aluminum alloy bars

A high-strength aluminum alloy (EN-AW-7075-T6) was used as the material of the bars. Both bars had a length of 1600 mm. The bars were instrumented by a pair of foil strain-gauges (3/120, LY61, HBM, Germany) located at a distance of 200 mm from the impact faces arranged in a half-bridge circuit. The transmission bar was supported by low friction bearings (drylin TJUM series, IGUS, USA). Using this setup, the results summarized in Section 3.1 and 3.3 were acquired. The experimental setup with the aluminum alloy bars and the important parts of the OHPB arrangement are shown in Fig. 9.

2.5.5. PMMA bars

For the testing of the low impedance materials, the setup was fitted with PMMA bars with a diameter of 20 mm and a length of 1750 mm. The basic characteristics of the setup remained unchanged with only a few minor changes in the instrumentation. Semiconductor strain-gauges (AFP-500-090, Kulite, USA) with an active length of 2.29 mm were mounted together with the foil strain-gauges as redundant strain sensors. A single measurement point was mounted at the incident bar at a distance of 200 mm from the impact face. Two measurement points were mounted at the transmission bar at a distance of 200 mm and 400 mm from the impact face. Using this setup, the results summarized in Section 3.2 and 3.4 were measured. The OHPB setup with the PMMA bars during the experimental campaign is shown in Fig. 10.

3. Applications and results

The applications of the OHPB experimental setup and the representative results exploiting the important features of the direct impact Hopkinson bar with two-sided instrumentation are presented. The applicability and performance of the setup is demonstrated with the results of two different experimental campaigns: (i) the uni-axial high strain-rate compression of the additively manufactured auxetic lattices

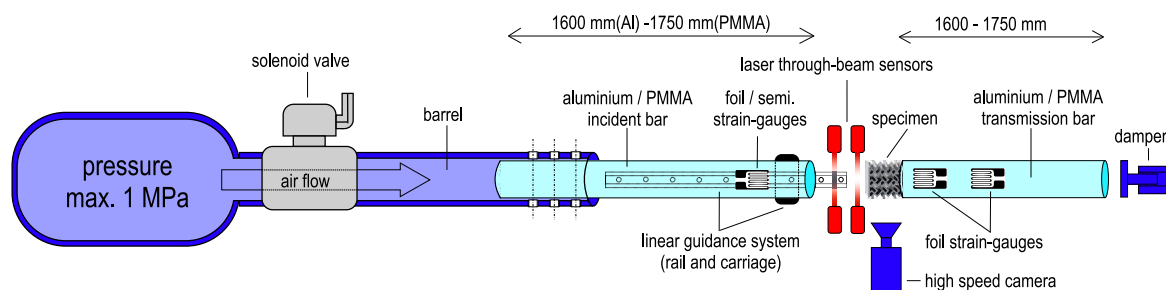


Fig. 8. The arrangement of the OHPB experimental setup: uni-axial compression with the aluminum alloy/PMMA bars.

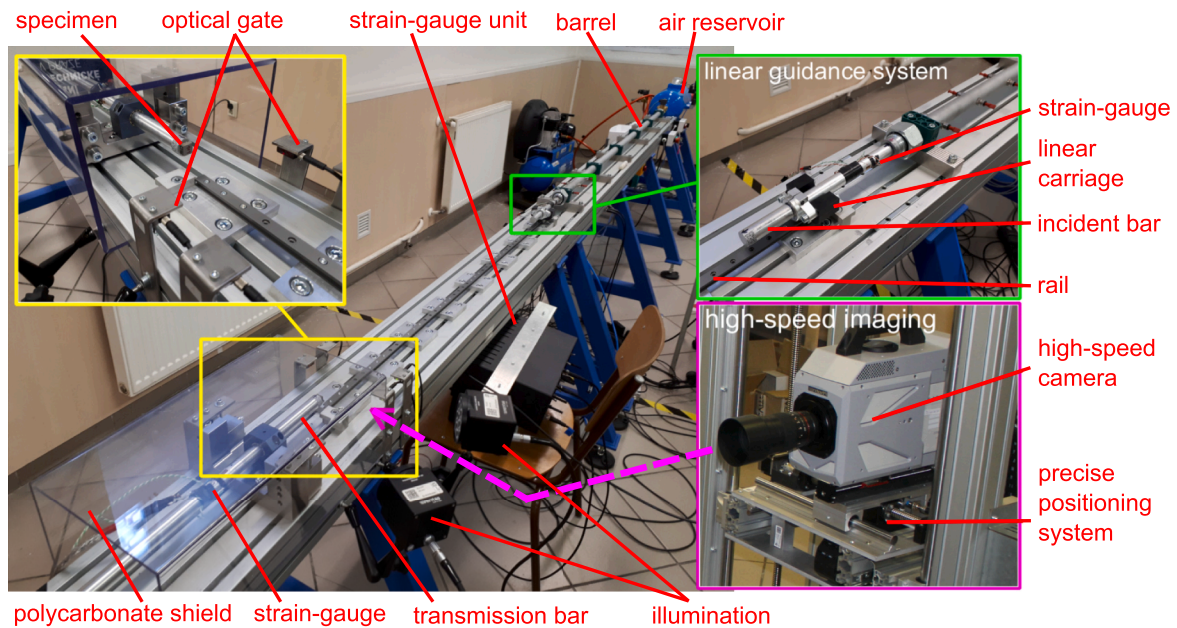


Fig. 9. The experimental setup with the aluminum alloy bars and the important parts of the OHPB arrangement.

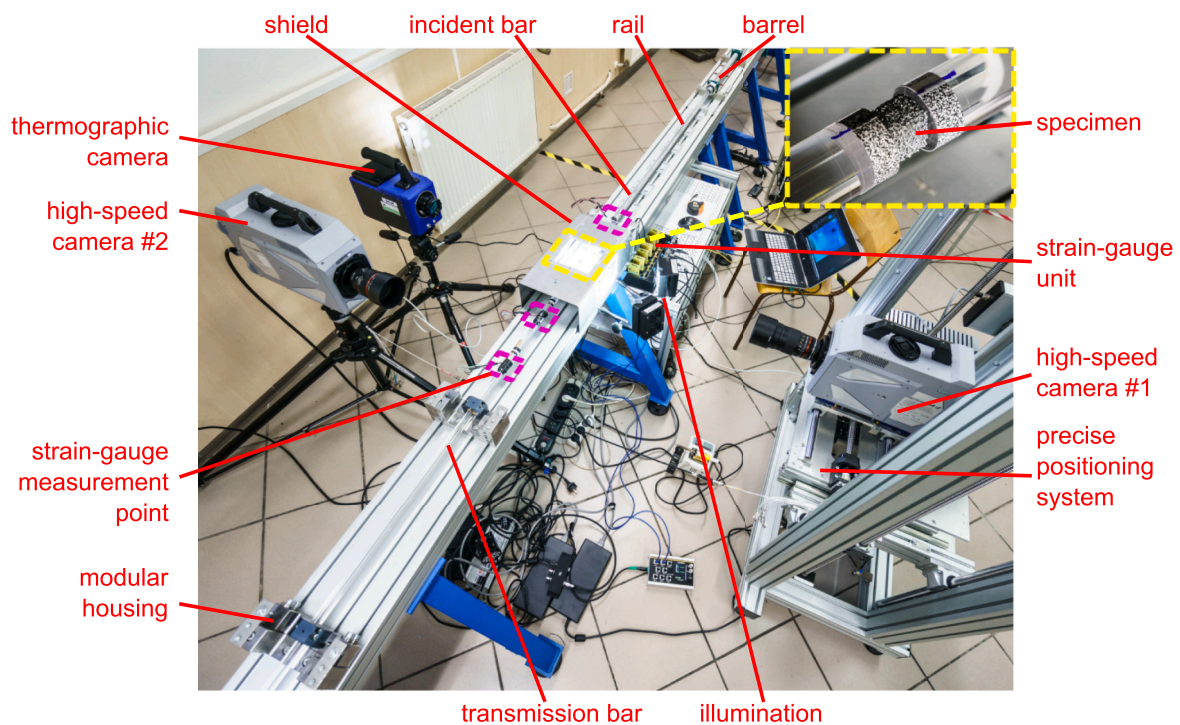


Fig. 10. The experimental setup with the PMMA bars during the experimental campaign.

and conventional metal foams, (ii) the uni-axial high strain-rate compression of the low impedance hybrid auxetic lattices. The range of impact velocities for every type of material was selected by taking multiple aspects into account. Besides the quasi-static response of the specimens, indicating on the stiffness, plateau stress, and densification strain, numerical simulations with the virtual OHPB apparatus developed in LS-DYNA were used to predict the deformation response of the specimens together with the performance of the setup including effective DIC measurement windows. The following sections show the representative results for different impact velocities selected according to the deformation characteristics of the particular tested material.

3.1. Closed-cell aluminum foam

Cubic specimens of the closed-cell aluminum foam with commercial name Alporas with a size of approximately $15 \times 15 \times 15$ mm, a density of $0.25\text{--}0.3 \text{ g} \cdot \text{cm}^{-3}$ and a porosity of 89% were tested with the aluminum bars. The material had a low mechanical impedance and exhibited localized strain bands in compression, where the majority of deformation was observed. A slideshow showing a specimen of Alporas foam during dynamic compression is presented in Fig. 11(a). The Alporas foam has already been tested by a number of research teams [68–71]. In this paper, we present the results showing the ability of the

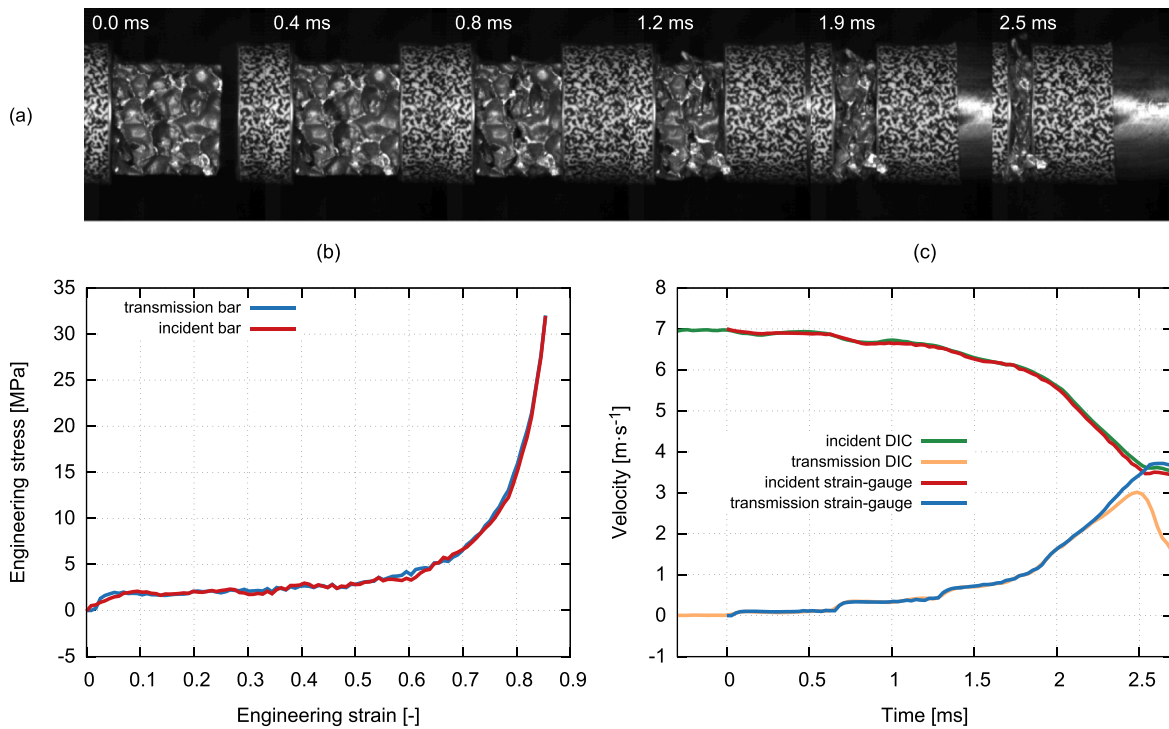


Fig. 11. Closed-cell Alporas foam, EN-AW-7075 bars. Slideshow showing a specimen of the Alporas foam in dynamic compression (a). Dynamic equilibrium and stress-strain diagram (b). Velocity profiles on both bars compared with the velocities from the DIC (c).

OHPB method to reliably capture the dynamic behavior of the foam with a very nice dynamic equilibrium. The dynamic equilibrium after wave separation is shown in Fig. 11(b). The wave separation technique produced precise results verified by the DIC. The velocity profiles on the both bars are compared with the DIC in Fig. 11(c). Impact into the Alporas foam recorded by the high-speed camera with mapped DIC results of the longitudinal displacement and incremental strain is shown in Videos S5 and S6.

3.2. Open-cell aluminum foam

Cubic specimens of an open-cell aluminum foam with a size of approximately $15 \times 15 \times 15$ mm, a density of $0.18 - 0.25 \text{ g} \cdot \text{cm}^{-3}$ and a porosity of 93% were tested in dynamic compression using the OHPB with PMMA bars. As this foam has significantly lower mechanical

impedance than the Alporas foam, the testing of such a material using the conventional setups is quite challenging. The force-displacement diagram recorded during the impact with an initial impact velocity of approximately $6.5 \text{ m} \cdot \text{s}^{-1}$ is shown in Fig. 12(a). Note that the stress level at the initial part of the plateau region was approximately 0.2MPa (corresponding to a force of approximately 100N in this case), while the dynamic behavior, oscillations of the incident stress, and its convergence with the transmission stress were clearly recorded. The velocity profiles on both bars compared with the DIC are shown in Fig. 12(b).

3.3. Additively manufactured auxetic lattices

Additively manufactured auxetic lattices (metamaterials with a negative Poisson's ratio) were manufactured using a selective laser sintering (SLS) method from SS316L powdered austenitic steel. Different

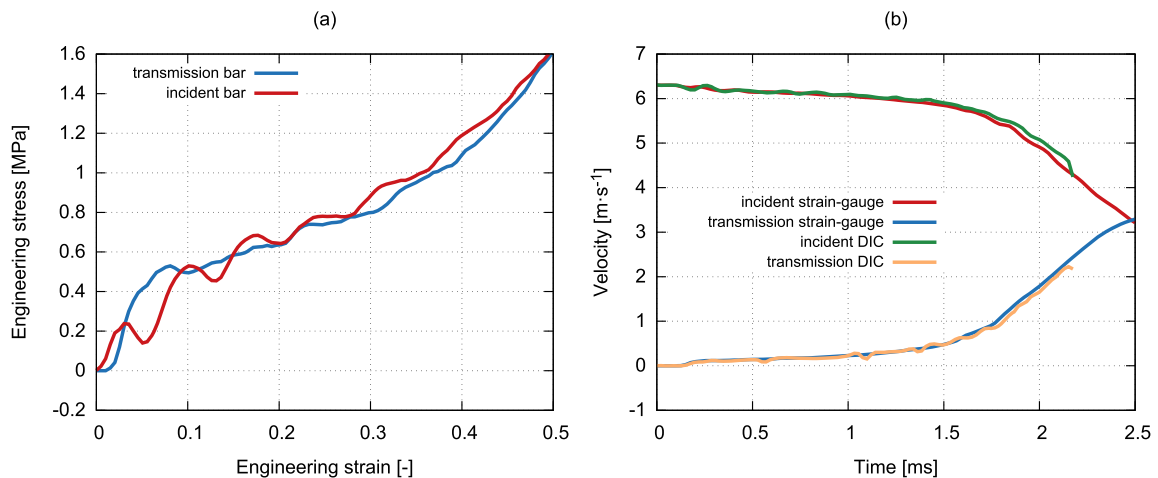
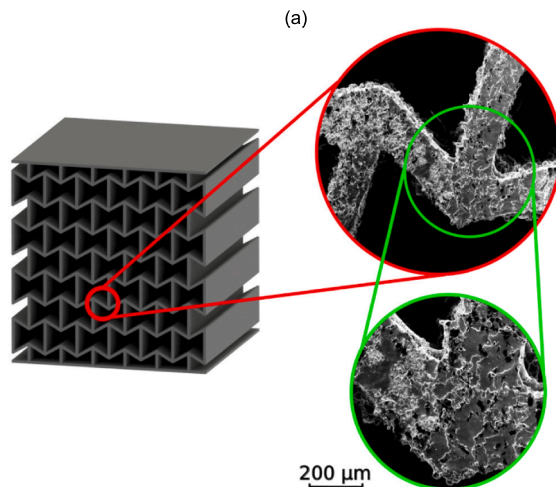


Fig. 12. Open-cell aluminum foam, PMMA bars. Stress-strain diagram recorded during the impact with an initial velocity of approximately $6.5 \text{ m} \cdot \text{s}^{-1}$ (a). Velocity profiles on both bars compared with the DIC (b).

sizes and types of the auxetic lattices were tested in the experimental campaign. Both 2D and 3D auxetic structures were investigated: a 2D re-entrant honeycomb, a 3D re-entrant honeycomb, and a 2D missing-rib structure. Here, the representative results of the 2D re-entrant honeycomb are presented as this structure is considered very versatile [7]. The structure had nominal dimensions of $12.15 \times 12.15 \times 12.58$ mm, a density $3.32 \text{ g}\cdot\text{cm}^{-3}$ and a porosity of 59% with a nominal strut thickness of 0.3 mm which was at the resolution limit of the used SLS device (AM 250, Renishaw, UK). The 2D re-entrant construct with a detailed view from the scanning electron microscopy (SEM) of the printed strut is shown in Fig. 13(a). The representative velocity histories evaluated using the strain-gauges during the impact with an initial velocity of approximately $20 \text{ m}\cdot\text{s}^{-1}$ are compared with the DIC in Fig. 13(b). Note that the structure reached full densification and the final stage of the experiment corresponded to the elastic collision, where the velocities of the individual bars converged and the bars finally separated due to the reflected elastic waves. The wave separation technique was able to reliably separate the waves until the random speckle pattern mounted on the transmission bar disappeared from the images and the DIC tracking was no longer possible.

3.3.1. Dynamic crushing at different strain-rates

Special attention was paid to the analysis of the crushing behavior of the 2D re-entrant auxetic constructs. The specimens were subjected to impacts at two different velocities of $12 \text{ m}\cdot\text{s}^{-1}$ and $20 \text{ m}\cdot\text{s}^{-1}$. With the increasing strain-rate, the auxetic lattice exhibited a different crushing behavior. The stress value, at which the collapse of the first layer of the auxetic structure occurred, increased with the strain-rate. Furthermore, the collapse mechanism of the individual layers was different as, during the impact at the lower velocity, significant lateral movements of the layers were observed with the corresponding peaks in the loading diagram. During the impact at the higher velocity, this effect was significantly suppressed as the inertia effects and the impact velocity acted against the lateral motion. The comparison of the deformation mechanism of the 2D re-entrant honeycomb lattice at the two different impact velocities is shown in Fig. 14(a,b). More importantly, the crushing mechanism was analyzed at both faces of the specimen using the two-sided instrumentation. As many stress oscillations occurred in the post-peak plateau region, the two-sided analysis of the phenomena was important. The stress-strain diagrams for both impact velocities and both faces of the specimen are compared in Fig. 14(c). Note that the velocity measured by the DIC closely followed the strain-gauge signals in every oscillation. Furthermore, the initial collapse was observed at a higher stress for the higher impact velocity and that the oscillations in the post-peak plateau had higher amplitudes at the lower velocity.



Moreover, at the lower velocity, the stress oscillations on both faces of the specimen were approximately identical, whereas, at the higher velocity, the oscillations were delayed and/or attenuated. Also, at the lower velocity, the signals from both faces of the specimens intersected earlier than at the higher velocity showing that the behavior is related to initial wave propagation and convergence of the dynamic forces. The same structure was tested in our previous study [11,12] using an SHPB with copper pulse-shapers, a striker bar with a length of 500 mm and a similar overall length of the setup. The SHPB was used for the compression of the auxetic lattice at approximately the same impact velocity of $20 \text{ m}\cdot\text{s}^{-1}$. While it was possible to compress the construct up to the full densification with the OHPB (nominal strain > 0.5), the maximum engineering strain in the SHPB was around 0.25. Even at the lower testing velocity of approximately $12 \text{ m}\cdot\text{s}^{-1}$, the OHPB with the wave separation technique was able to reach maximum strain of 0.35-0.4. Velocity histories measured by the strain-gauges at both faces of the specimen are compared with the DIC for the impact with an initial velocity of approximately $20 \text{ m}\cdot\text{s}^{-1}$ in Fig. 14(d). Impact into the auxetic re-entrant lattice foam recorded by the high-speed camera with mapped DIC results of the longitudinal displacement and incremental strain is shown in Videos S7 and S8.

3.4. Hybrid auxetic lattices

Hybrid auxetic lattices represent a novel approach in the low-cost manufacturing of an advanced light-weight materials. In this work, the specimens were printed using a Pro Jet HD3000 3D printer (3D Systems, Rock Hill, USA) from a UV-curable polymer VisiJet EX200 with the highest resolution ($656 \times 656 \times 800$ dpi). The overall dimensions of the specimens were approximately $14 \times 14 \times 20$ mm (width, depth, height). The polymeric samples were electro-chemically coated with an $\approx 60 \mu\text{m}$ and $\approx 120 \mu\text{m}$ thick layer of nickel, respectively. The average density of the samples was: (i) $0.27 \text{ g}\cdot\text{cm}^{-3}$ for the non-coated construct, (ii) $0.469 \text{ g}\cdot\text{cm}^{-3}$ for the $60 \mu\text{m}$ coating, and (iii) $0.537 \text{ g}\cdot\text{cm}^{-3}$ for the $120 \mu\text{m}$ coating. Further information on the coating process can be found in [4]. After the coating, the polymer was taken out via pyrolysis at approximately 1000°C . The printed polymeric constructs as well as the final hybrid coated hollow-strut auxetic structures are shown in Fig. 15.

3.4.1. No coating

As the printed polymer was very brittle, the uncoated constructs disintegrated instantly after the initial impact. The disintegration captured by the high-speed camera is shown in Fig. 16(a). Nevertheless, the force measurement during the disintegration was possible with the OHPB method. The corresponding stress-strain diagrams showing the

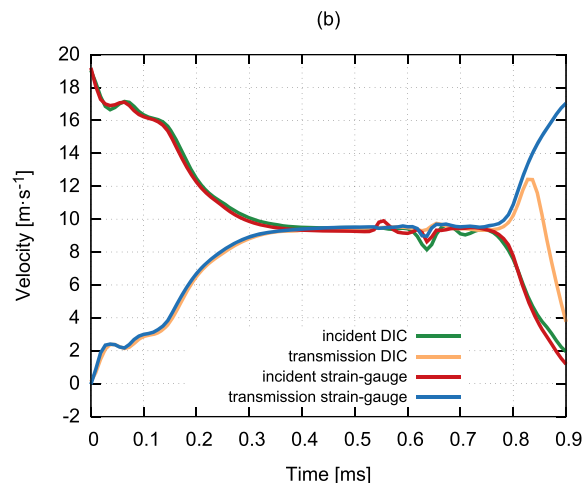


Fig. 13. The 2D re-entrant construct with an SEM detail of the printed strut (a). Velocity profiles on both bars compared with the DIC (b).

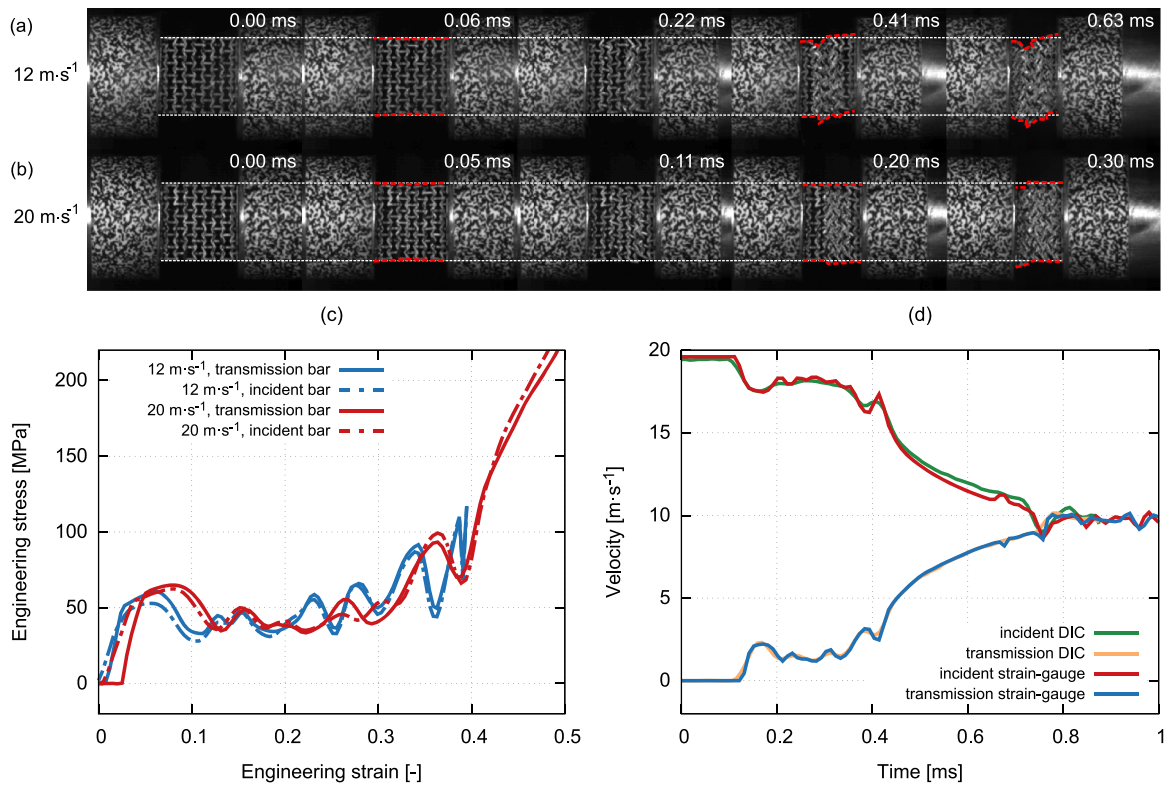


Fig. 14. Deformation mechanism of the 2D re-entrant lattice at two different impact velocities (a, b). Stress-strain diagrams at both impact velocities and both faces of the specimen (c). Velocity histories indicated by the strain-gauges at both faces of the specimen compared with the DIC for the impact with an initial velocity of approximately $20\text{m}\cdot\text{s}^{-1}$ (d).

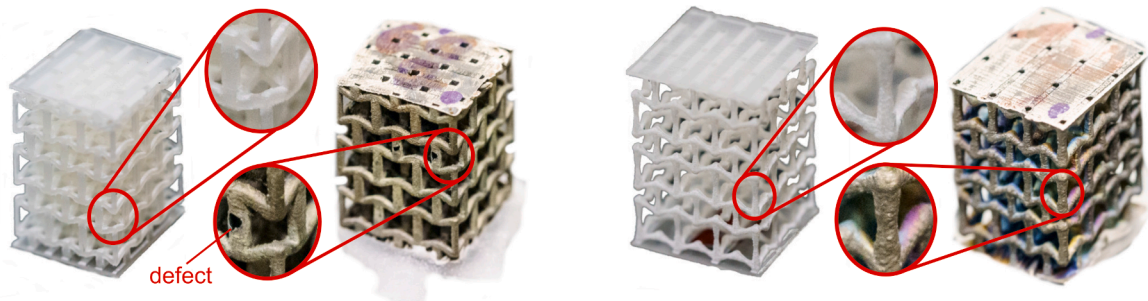


Fig. 15. The printed and coated hybrid auxetic constructs.

behavior at both faces of the disintegrating specimen are shown in Fig. 16(b). The velocity histories at both bars evaluated from the strain-gauge signals are compared with the DIC results in Fig. 16(c). Note that despite the very rapid disintegration, the short force peaks were recorded reliably and were comparable with the values from the DIC. This indicates that the wave dispersion in the PMMA bars over the short travelled distance in the OHPB was minor and the resulting force peaks were still relevant. The behavior after the disintegration when the bars hit the residuals of the specimen and underwent an elastic collision were also captured despite some discrepancy between the incident strain-gauge and the DIC, which can be identified as the wave separation in its simple form, as it cannot reliably account for the wave dispersion over long travel distances.

3.4.2. Nickel coating - $60\mu\text{m}$

The hollow-strut hybrid auxetic lattice with a coating thickness of $60\mu\text{m}$ exhibited ductile behavior. The structure deforming during the impact is shown in Fig. 17(a). Note a very profound auxetic behavior

with the struts rapidly closing into the core of the specimen. Stress-strain diagrams are presented in Fig. 17(b). The velocities evaluated from the strain-gauge signals are compared with the DIC in Fig. 17(c). Here, the perfect match of the strain-gauge velocities and the DIC is very important as the behavior of the specimen at the impacted face was different than at the opposite face. Interestingly, the incident curve was lower than the transmission curve up to the densification of the structure, where both curves converged. All the tested specimens with a coating thickness of $60\mu\text{m}$ exhibited this behavior. As the incident curve did not exhibit any stress oscillations, the phenomenon could not be simply explained by the classical convergence of the dynamic forces. As the coating process is not perfect, the coated layer had a lot of imperfections, defects and cracks (see Fig. 15) affecting the response of the samples. The distal face of the specimen was embedded in a resin for the better contact with the transmission bar face, while the impacted face was without any embedding. Also, by design, the auxetic cells were not distributed symmetrically along the length of the specimen. These factors can possibly cause some distortion and/or internal reflections of the

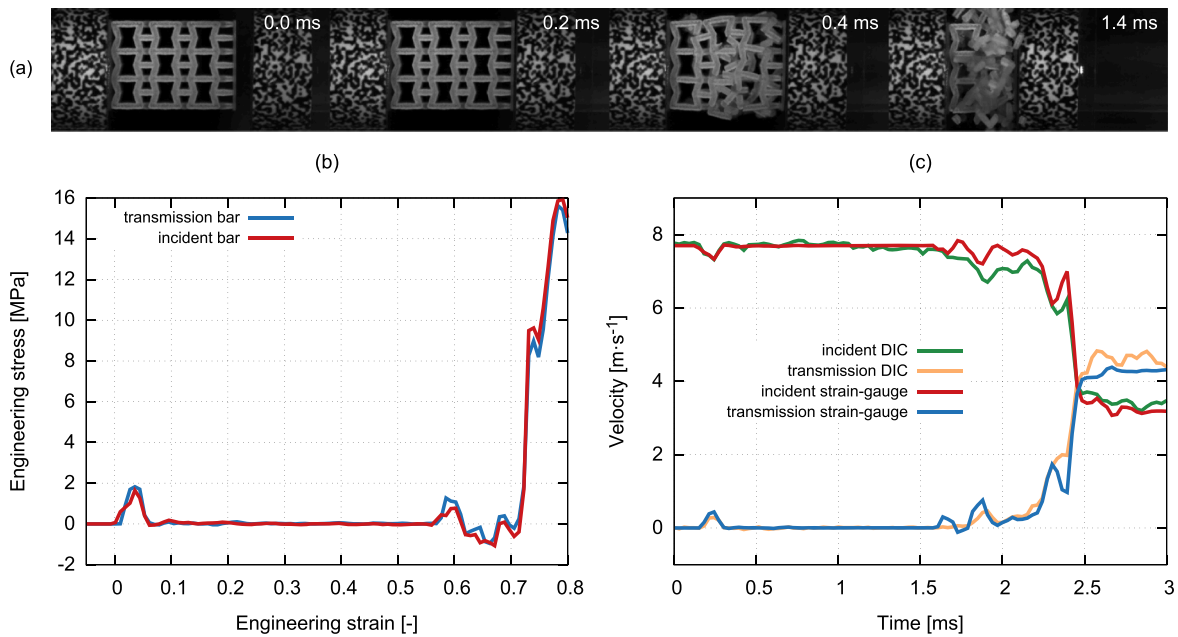


Fig. 16. The disintegration of the polymeric construct captured by the high-speed camera (a). Stress-strain diagrams showing the behavior at both faces of the disintegrating specimen (b). Velocity histories at both bars evaluated from the strain-gauge signals compared with the velocities from the DIC (c).

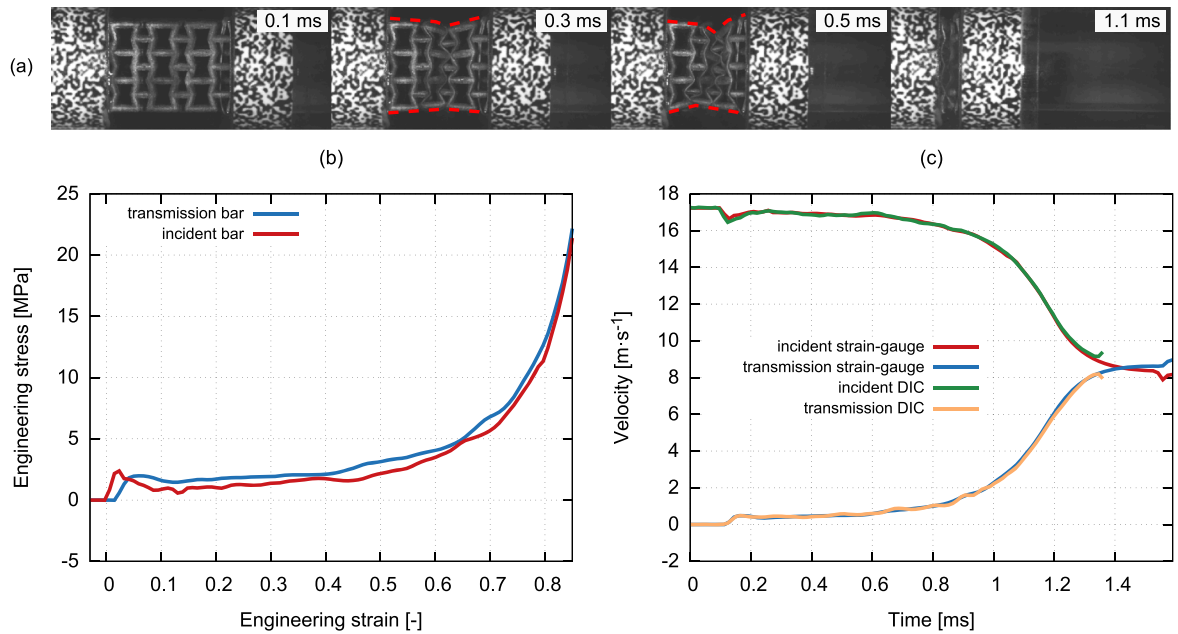


Fig. 17. The hybrid auxetic construct with a coating thickness of 60 μm deforming during the impact (a). The corresponding stress-strain diagrams (b). Velocities evaluated from the strain-gauge signals compared with the DIC (c).

strain wave in the specimen or wave transfer problems that were represented by the asymmetrical response recorded by both the strain-gauges and the DIC. Furthermore, this effect was not observed in the case of the structures with a coating thickness of 120 μm, where the dynamic forces converged quickly (see Section 3.4.3).

3.4.3. Nickel coating - 120 μm

Hybrid auxetic lattices with a coating thickness of 120 μm were tested. In this case, the behavior was very different from the constructs with a coating thickness of 60 μm. Stress-strain diagrams showing a quick convergence of the dynamic forces at the respective faces of the specimen are shown in Fig. 18(a). The velocities evaluated using the

strain-gauges and the DIC are shown in Fig. 18(b). Note that the DIC was able to track the image features and compute the velocity only for a short period of time. As these constructs exhibited a stiffer response, the speckle pattern mounted at the transmission bar quickly disappeared from the image making further tracking impossible. Impact into the hybrid auxetic lattices recorded by the high-speed camera with mapped DIC results of the displacements and incremental strains is shown in Videos S9 - S12.

4. Discussion

Several different types of cellular solids and lattices were tested using

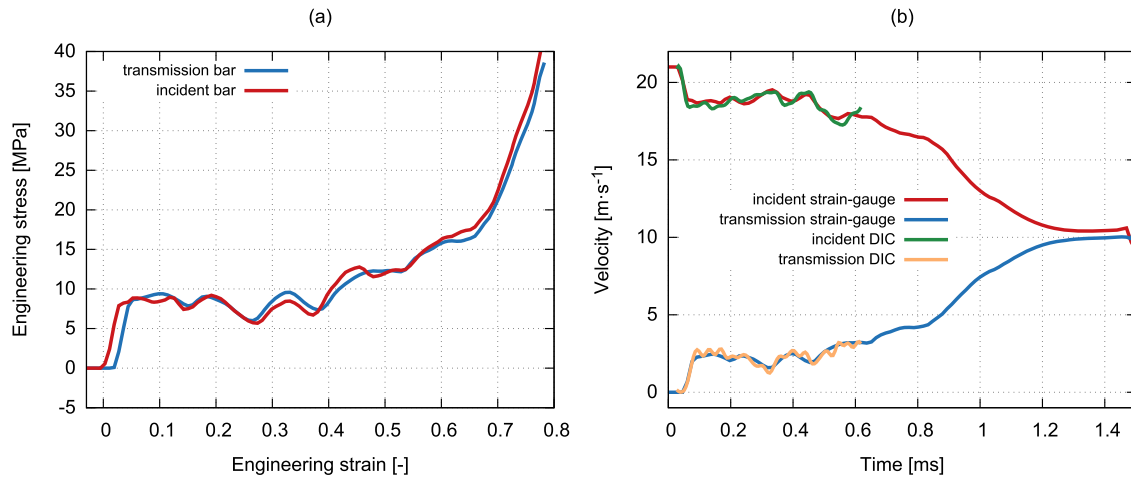


Fig. 18. The hybrid auxetic construct with a coating thickness of $120\mu\text{m}$: The corresponding stress-strain diagrams (a). Velocities evaluated from the strain-gauge signals compared with the DIC (b).

the OHPB in dynamic compression. Based on the analysis of the acquired results, the following comments, findings and remarks can be drawn:

- The DIHB experimental setup instrumented with strain-gauges mounted on both the incident and the transmission bar (the so called OHPB [67]) with the linear motion guidance system supporting the incident bar can be successfully employed for impacts with an initial velocity of at least $30\text{ m}\cdot\text{s}^{-1}$ (see representative diagrams in Fig. 19). In comparison with the similar previously published setups [62,67], the presented variant of the OHPB setup significantly extended the application envelope in terms of the maximum impact velocity (an impact velocity of $10\text{ m}\cdot\text{s}^{-1}$ is mentioned as a reasonable maximum in the arrangement published in [67]). Moreover, the linear guidance system allowed for the easy installation of the strain-gauges and wiring that is more complicated in the variant with the incident bar and strain-gauge in the barrel of the gas-gun.
- The instrumentation with the conventional strain-gauges represents a straightforward approach for the evaluation of the results which is not different from the classical Kolsky bar measurements. This approach is simple and does not require expensive instrumentation such as the PDV. However, the PDV is simultaneously a type of instrumentation suitable for the testing at higher impact velocities

[63]. Application of two strain-gauges at a single measurement point connected in a half Wheatstone bridge arrangement can compensate for the minor bending of the bars and effects of the flexural waves that can possibly occur during the testing of the specimens with a complex internal structure.

- No significant bar alignment problems were identified with the applied linear guidance system. After the careful adjustment and calibration of the experimental setup, no problems with the wave reflections from the friction clamp that attaches the incident bar to the linear guidance system occurred. The wear and tear of the polymeric linear bearings were observed particularly during impacts close to the maximum impact velocity. Thus, the bearings had to be replaced after a certain number of experiments.
- The wave separation technique based on the arrangement specific to the OHPB, where both bars have free-ends, was employed to separate the forward- and backward-propagating waves in the bars. This approach allowed the duration of the experiment to be extended several times.
- The DIC was used as a technique for the measurements of the displacements and the velocities in the vicinity of both faces of the specimen. DIC was also employed as a tool for the verification of the wave separation technique. It was shown that, under the conditions valid for the testing of low impedance cellular materials, the wave

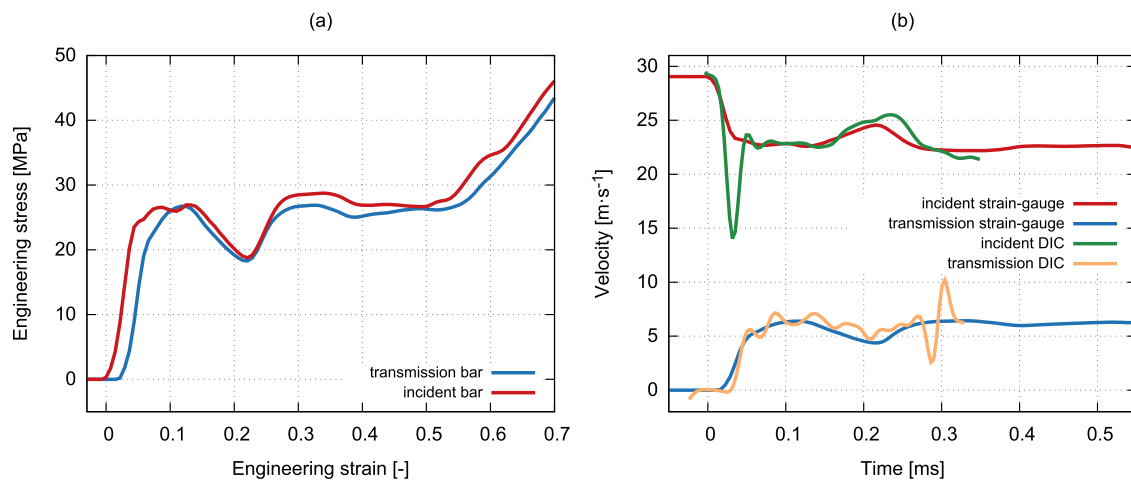


Fig. 19. The hybrid auxetic construct with a coating thickness of $120\mu\text{m}$ and rectangular struts tested at a maximum impact velocity of approximately $30\text{ m}\cdot\text{s}^{-1}$: Stress-strain diagram (a). Velocities evaluated from the strain-gauge signals compared with the DIC (b). Because of the high impact velocity, the DIC data are available only in a relatively narrow time window before the specimen moved from the area inspected by the camera.

separation technique can provide reliable decomposition of the strain pulses during the whole impact. The comparison of the velocities indicated by the DIC and strain-gauges is considered beneficial (in comparison to the displacements) as various errors can be better distinguished using the velocity measurements based on the DIC. Therefore, if successful, a more precise comparison of the measured quantities is possible.

- The DIC optimized for the sub-pixel tracking of the random speckle patterns mounted at the faces of the bars can be possibly employed as a sole technique for lower precision measurements of the velocity of the incident bar. With the known material properties of the incident bar, it would be possible to reconstruct the force present at the impact face using the wave separation approach inverse to the technique shown in the paper. The bar would have to be relatively long not to produce high frequency oscillations as, in such case, the wave reflections would be hidden in the noise and the velocity signal could not be used for the inverse separation method to calculate the actual force. The double differentiation of the DIC displacements cannot be used for the calculation of the actual acceleration (and force) as the differentiated signals are unsuitable due to significant noise. The DIC limits are particularly seen in the higher noise of the velocity signals, the high-speed camera imaging frequency and lower resolutions of the high-speed images. Nevertheless, the physical limit of the DIC for the evaluation of the velocity profiles with the employed state-of-the-art high-speed cameras lies significantly higher and was not reached in the presented method.
- The measurements with the visco-elastic bars can be significantly simplified in the OHPB under certain strict conditions. As the travel distance of the wave is short in the OHPB, the linear elastic model can be adopted instead of the frequency domain time-shifting to reconstruct the strain waves at the faces of the bars. Still, some technique that can reliably determine the dynamic material properties of the visco-elastic bars (e.g., [46]) has to be used to acquire the relevant parameters required for the linear elastic model. However, the straight-forward wave separation technique shown in the paper cannot be used for the visco-elastic bars as the distance travelled by the wave reflected from the free-end of the bar is too long and the reflected wave arrives severely attenuated and distorted.
- Both the aluminum alloy and PMMA bars were able to reliably record fine details of the crushing behavior of the cellular solids. The signals from the incident and transmission bar have comparable amplitudes and travel distance from the specimen. Therefore, problems with achieving the dynamic equilibrium typical for the SHPB are significantly reduced in this method. This can be supported by conclusions presented in [67], where, for the OHPB, the condition of the dynamic equilibrium has been achieved in a shorter time than in the conventional SHPB. In some of the presented experiments, force oscillations with an amplitude as low as 50 – 100N were reliably measured with the PMMA bars with a diameter of 20 mm.
- The method was successfully employed for the testing of several types of cellular solids, metamaterials and lattices in a high strain-rate dynamic compression. It was demonstrated that the two-sided instrumentation is a very important feature allowing for the analysis of the phenomena specific to the collapse of the individual lattice layers and the wave propagation through the specimen.
- Both closed-cell and open-cell metal foams were successfully tested using the setup, while the results are in good agreement with other papers [68,70].
- Additively manufactured auxetic lattices were tested using this method. The application of the OHPB arrangement allowed for the precise two-sided analysis of the collapse of the individual cell layers. As compared with our previous study regarding the same type of lattice tested in SHPB, the OHPB was able to compress the specimens to significantly larger strains than the SHPB with a comparable overall length at a similar strain-rate. Here, the OHPB represents an important alternative to the SHPB for testing materials at lower

strain-rates, where the SHPB would require very long striker and both bars.

- Hybrid auxetic lattices manufactured by nanocrystalline coating process of the polymeric constructs printed using a 3D printer were tested using the method. As demonstrated, it was possible to measure the uncoated polymeric constructs that underwent instant disintegration as well as the hollow strut lattices. The auxetic constructs with a coating thickness of 60 μm exhibited an unusual behavior when the incident signal was, after the settling period, in all cases lower than the transmission signal until the densification of the structure, where both signals converged. The possible causes of this phenomenon including defects in the specimens and poor or asymmetric transfer of the strain-wave from the specimen to the bar were proposed. Interestingly, this behavior was not observed in the case of the constructs with a coating thickness of 120 μm . Here, the equilibrium of the dynamic forces was achieved quickly. The DIC indicated the same trend as the strain-gauges. Furthermore, the specimens of the different materials with even lower forces at the plateau region were measured with the same setup with a symmetrical response. Thus, it is considered that the phenomenon has to be caused by the specimen or the wave transfer at the interface between the specimen and the bar. Nevertheless, the material represents a light-weight and cost-effective alternative to the still expensive additively manufactured auxetic metamaterials. It was revealed that its auxetic behavior is much more profound than in the case of the previously tested structures [11] and has the potential for further development.
- The OHPB method in the presented form has a broad potential for further improvements and development. The method is particularly beneficial for a low to medium velocity impact and penetration testing (see [Video S13](#)) of large specimens and/or specimens that are difficult to produce in large numbers, where the analysis of the wave propagation effects is important and the specimen cannot be easily launched against a well-instrumented transmission bar or anvil. The presented arrangement also allows for designs with large diameter tubular bars or with large diameter inserts.

5. Conclusions

The DIHB method with the two-sided instrumentation using conventional strain-gauges was developed and tested with different types of cellular solids, metamaterials and auxetic lattice constructs subjected to uni-axial high strain-rate compression. The method is based on the previously proposed design of the OHPB, while it significantly increases its application envelope in terms of the impact velocity as well as the experiment duration. The wave separation technique based on boundary condition at the free-end of the bar was employed to reconstruct the velocity and force histories at the faces of the specimen. DIC was used as a tool for the measurement of the particle velocities at the bars in the vicinity of the specimen. It was shown that the comparison of the velocity indicated by the DIC with the strain-gauge signals can be used for the verification of the wave separation technique. This approach is considered superior to the possible comparison of the indicated displacements as the DIC velocity is more useful to analyze sources of errors and can reveal eventual problems with the experimental setup. The method was tested at impact velocities of up to 30 $\text{m}\cdot\text{s}^{-1}$ with both linear elastic aluminum alloy bars and visco-elastic PMMA bars. The maximum velocity was constrained by the performance of the used gas-gun. It is believed that the maximum impact velocity can be further increased as no significant problems with the strain-gauges, wiring, linear guidance system or geometrical alignment of the bars during the impact at the maximum impact velocity were observed. Under certain circumstances, a simple approach using a linear elastic model can be employed for the evaluation of the experiments measured with the visco-elastic bars in the OHPB. The performance of the setup was evaluated in a series of experiments with different types of closed- and open-cell aluminum foams,

additively manufactured auxetic lattices, and hybrid nickel coated auxetic constructs subjected to dynamic uni-axial compression. The comprehensive direct impact testing methodology utilizing OHPB with two-sided instrumentation based on conventional strain-gauges and DIC was successfully employed for the high strain-rate loading of the cellular solids. The method represents an interesting, advanced, and straightforward alternative to the existing setups and is especially promising for the instrumented dynamic impact/penetration testing of large and/or expensive specimens, sandwiches or structural panels at low to medium impact velocities.

CRedit authorship contribution statement

Tomáš Fíla: Conceptualization, Methodology, Supervision, Investigation, Writing - original draft, Writing - review & editing. **Petr Koudelka:** Writing - original draft, Writing - review & editing. **Jan Falta:** Investigation, Writing - review & editing. **Petr Zlámal:** Investigation, Writing - original draft. **Václav Rada:** Investigation, Software. **Marcel Adorna:** Investigation, Data curation, Validation. **Stefan Bronder:** Resources. **Ondřej Jiroušek:** Supervision, Project administration, Funding acquisition.

Declaration of Competing Interest

The authors declare that they do not have any financial or non-financial conflict of interests

Acknowledgement

The authors acknowledge the financial support from the Operational Programme Research, Development and Education in the project INA-FYM (CZ.02.1.01/0.0/0.0/16_019/0000766) and the Czech Science Foundation (project no. 19-23675S).

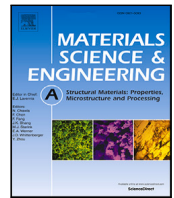
Supplementary material

Supplementary material associated with this article can be found, in the online version, at [10.1016/j.ijimpeng.2020.103767](https://doi.org/10.1016/j.ijimpeng.2020.103767)

References

- Xi H, Tang L, Luo S, Liu Y, Jiang Z, Liu Z. A numerical study of temperature effect on the penetration of aluminum foam sandwich panels under impact. *Composites Part B: Engineering* 2017;130:217–29. <https://doi.org/10.1016/j.compositesb.2017.07.044>.
- Jiroušek O, Doktor T, Kytýř D, Zlámal P, Fíla T, Koudelka P, et al. X-ray and finite element analysis of deformation response of closed-cell metal foam subjected to compressive loading. *Jun of Inst* 2013;8(02). <https://doi.org/10.1088/1748-0221/8/02/c02012>.
- Vesenjak M, Veyhl C, Fiedler T. Analysis of anisotropy and strain rate sensitivity of open-cell metal foam. *Mate Scien Engin: A* 2012;541:105–9. <https://doi.org/10.1016/j.msea.2012.02.010>.
- Jung A, Diebels S. Synthesis and mechanical properties of novel ni/pu hybrid foams: a new economic composite material for energy absorbers. *Adv Eng Mater* 2016;18(4):532–41. <https://doi.org/10.1002/adem.201500405>.
- Tancogne-Dejean T, Spierings AB, Mohr D. Additively-manufactured metallic micro-lattice materials for high specific energy absorption under static and dynamic loading. *Acta Mater* 2016;116:14–28. <https://doi.org/10.1016/j.actamat.2016.05.054>.
- Novak N, Krstulović-Opara L, Ren Z, Vesenjak M. Mechanical properties of hybrid metamaterial with auxetic chiral cellular structure and silicon filler. *Compos Struct* 2020;234:111718. <https://doi.org/10.1016/j.compstruct.2019.111718>.
- Li T, Chen Y, Hu X, Li Y, Wang L. Exploiting negative poisson's ratio to design 3D-printed composites with enhanced mechanical properties. *Mater Des* 2018;142:247–58. <https://doi.org/10.1016/j.matdes.2018.01.034>.
- Hou S, Li T, Jia Z, Wang L. Mechanical properties of sandwich composites with 3D-printed auxetic and non-auxetic lattice cores under low velocity impact. *Materials & Design* 2018;160:1305–21. <https://doi.org/10.1016/j.matdes.2018.11.002>.
- Novak N, Starčević L, Vesenjak M, Ren Z. Blast response study of the sandwich composite panels with 3D chiral auxetic core. *Compos Struct* 2019;210:167–78. <https://doi.org/10.1016/j.compstruct.2018.11.050>.
- Koudelka P, Jiroušek O, Fíla T, Doktor T. Compressive properties of auxetic structures produced with direct 3D printing. *Materiali in Tehnologije* 2016;50(3):311–7. <https://doi.org/10.17222/mit.2014.204>.
- Fíla T, Zlámal P, Jiroušek O, Falta J, Koudelka P, Kytýř D, et al. Impact testing of polymer-filled auxetics using split Hopkinson pressure bar. *Adv Eng Mater* 2017;19(10). <https://doi.org/10.1002/adem.201700076>.
- Fíla T, Koudelka P, Zlámal P, Falta J, Adorna M, Neuhäuserová M, et al. Strain dependency of poisson's ratio of SLS printed auxetic lattices subjected to quasi-static and dynamic compressive loading. *Adv Eng Mater* 2019;21(8). <https://doi.org/10.1002/adem.201900204>.
- Santosa SP, Arifurrahman F, Hafidz Izzudin M, Widagdo D, Gunawan L. Response analysis of blast impact loading of metal-foam sandwich panels. *Procedia Eng* 2017;173:495–502. <https://doi.org/10.1016/j.proeng.2016.12.073>.
- Kolsky H. An investigation of the mechanical properties of materials at very high rates of loading. *Proceedings of the Physical Society Section B* 1949;62(11):676–700. <https://doi.org/10.1088/0370-1301/62/11/302>.
- Peroni M, Solomos G, Pizzinato V. Impact behaviour testing of aluminium foam. *Int J Impact Eng* 2013;53:74–83. <https://doi.org/10.1016/j.ijimpeng.2012.07.002>.
- Peroni M, Solomos G, Babcsan N. Development of a Hopkinson bar apparatus for testing soft materials: application to a closed-cell aluminum foam. *Materials (Basel)* 2016;9(1):27. <https://doi.org/10.3390/ma9010027>.
- Deshpande V, Fleck N. High strain rate compressive behaviour of aluminium alloy foams. *Int J Impact Eng* 2000;24(3):277–98. [https://doi.org/10.1016/S0734-743X\(99\)00153-0](https://doi.org/10.1016/S0734-743X(99)00153-0).
- Han F, Cheng H, Li Z, Wang Q. The strain rate effect of an open cell aluminum foam. *Metall Mater Trans A* 2005;36(3):645–50. <https://doi.org/10.1007/s11661-005-0180-6>.
- Wang P, Xu S, Li Z, Yang J, Zhang C, Zheng H, et al. Experimental investigation on the strain-rate effect and inertia effect of closed-cell aluminum foam subjected to dynamic loading. *Materials Science and Engineering: A* 2015;620:253–61. <https://doi.org/10.1016/j.msea.2014.10.026>.
- Yang B, Tang L, Liu Y, Liu Z, Jiang Z, Fang D. Localized deformation in aluminum foam during middle speed Hopkinson bar impact tests. *Materials Science and Engineering: A* 2013;560:734–43. <https://doi.org/10.1016/j.msea.2012.10.027>.
- Islam M, Brown A, Hazell P, Kader M, Escobedo J, Saadatfar M, et al. Mechanical response and dynamic deformation mechanisms of closed-cell aluminium alloy foams under dynamic loading. *Int J Impact Eng* 2018;114:111–22. <https://doi.org/10.1016/j.ijimpeng.2017.12.012>.
- Neuhäuserová M, Koudelka P, Falta J, Adorna M, Fíla T, Zlámal P. Strain-rate and printing direction dependency of compressive behaviour of 3D printed stainless steel 316L. *Acta Polytechnica CTU Proceedings* 2019:68–72. <https://doi.org/10.14311/APP.2019.25.0068>.
- Nishi M, Tanaka S, Vesenjak M, Ren Z, Hokamoto K. Experimental and computational analysis of the uni-directional porous (unipore) copper mechanical response at high-velocity impact. *Int J Impact Eng* 2020;136:103409. <https://doi.org/10.1016/j.ijimpeng.2019.103409>.
- Novak N, Vesenjak M, Tanaka S, Hokamoto K, Ren Z. Compressive behaviour of chiral auxetic cellular structures at different strain rates. *Int J Impact Eng* 2020;141:103566. <https://doi.org/10.1016/j.ijimpeng.2020.103566>.
- Wang L, Ding Y, Yang L. Experimental investigation on dynamic constitutive behavior of aluminum foams by new inverse methods from wave propagation measurements. *Int J Impact Eng* 2013;62:48–59. <https://doi.org/10.1016/j.ijimpeng.2013.06.002>.
- Adorna M, Zlámal P, Fíla T, Falta J, Felten M, Fries M, et al. Testing of hybrid nickel-polyurethane foams at high strain-rates using hopkinson bar and digital image correlation. *Acta Polytechnica CTU Proceedings* 2018:72–6. <https://doi.org/10.14311/APP.2018.18.0072>.
- Adorna M, Bronder S, Falta J, Zlámal P, Fíla T. Evaluation of hopkinson bar experiments using multiple digital image correlation software tools. *Acta Polytechnica CTU Proceedings* 2019:1–5. <https://doi.org/10.14311/APP.2019.25.0001>.
- Fíla T, Zlámal P, Falta J, Doktor T, Koudelka P, Kytýř D, et al. Testing of auxetic materials using hopkinson bar and digital image correlation. *EPJ Web of Conferences*. 183. EDP Sciences; 2018. <https://doi.org/10.1051/epjconf/201818302045>.
- Castro G, Nutt S, Wenchen X. Compression and low-velocity impact behavior of aluminum syntactic foam. *Materials Science and Engineering: A* 2013;578:222–9. <https://doi.org/10.1016/j.msea.2013.04.081>.
- Sudheer Kumar P, Ramachandra S, Ramamurthy U. Effect of displacement-rate on the indentation behavior of an aluminum foam. *Materials Science and Engineering: A* 2003;347(1):330–7. [https://doi.org/10.1016/S0921-5093\(02\)00608-1](https://doi.org/10.1016/S0921-5093(02)00608-1).
- Liang X, Luo H, Mu Y, Wu L, Lin H. Experimental study on stress attenuation in aluminum foam core sandwich panels in high-velocity impact. *Mater Lett* 2017;203:100–2. <https://doi.org/10.1016/j.matlet.2017.05.036>.
- Guo K, Zhu L, Li Y, Yu T, Shenoi A, Zhou Q. Experimental investigation on the dynamic behaviour of aluminum foam sandwich plate under repeated impacts. *Compos Struct* 2018;200:298–305. <https://doi.org/10.1016/j.compstruct.2018.05.148>.
- Lu G, Shen J, Hou W, Ruan D, Ong L. Dynamic indentation and penetration of aluminium foams. *Int J Mech Sci* 2008;50(5):932–43. <https://doi.org/10.1016/j.ijmeccsci.2007.09.006>.
- Mohan K, Yip TH, Idapalapati S, Chen Z. Impact response of aluminum foam core sandwich structures. *Materials Science and Engineering: A* 2011;529:94–101. <https://doi.org/10.1016/j.msea.2011.08.066>.
- Gibson L, Ashby MF. *Cellular solids: structure and properties*. Cambridge University Press; 1999. Cambridge Solid State Science Series

- [36] Ninan L, Tsai J, Sun C. Use of split Hopkinson pressure bar for testing off-axis composites. *Int J Impact Eng* 2001;25(3):291–313. [https://doi.org/10.1016/S0734-743X\(00\)00039-7](https://doi.org/10.1016/S0734-743X(00)00039-7).
- [37] Song B, Chen W. Loading and unloading split Hopkinson pressure bar pulse-shaping techniques for dynamic hysteretic loops. *Exp Mech* 2004;44(6):622–7. <https://doi.org/10.1177/0014485104048911>.
- [38] Song B, Chen W. One-dimensional dynamic compressive behavior of epdm rubber. *Journal of Engineering Materials and Technology, Transactions of the ASME* 2003; 125(3):294–301. <https://doi.org/10.1115/1.1584492>.
- [39] Vecchio KS, Jiang F. Improved pulse shaping to achieve constant strain rate and stress equilibrium in split-hopkinson pressure bar testing. *Metall Mater Trans A* 2007;38 A(11):2655–65. <https://doi.org/10.1007/s11661-007-9204-8>.
- [40] Song B, Chen W. Dynamic stress equilibration in split Hopkinson pressure bar tests on soft materials. *Exp Mech* 2004;44(3):300–12. <https://doi.org/10.1177/0014485104041543>.
- [41] Jiang T, Xue P, Butt H. Pulse shaper design for dynamic testing of viscoelastic materials using polymeric SHPB. *Int J Impact Eng* 2015;79:45–52. <https://doi.org/10.1016/j.ijimpeng.2014.08.016>.
- [42] Chen W, Lu F, Zhou B. A quartz-crystal-embedded split Hopkinson pressure bar for soft materials. *Exp Mech* 2000;40(1):1–6. <https://doi.org/10.1007/BF02327540>.
- [43] Wang L, Labibes K, Azari Z, Pluvina G. Generalization of split hopkinson bar technique to use viscoelastic bars. *Int J Impact Eng* 1994;15(5):669–86. [https://doi.org/10.1016/0734-743X\(94\)90166-1](https://doi.org/10.1016/0734-743X(94)90166-1).
- [44] Zhao H, Gary G, Klepaczo JR. On the use of a viscoelastic split hopkinson pressure bar. *Int J Impact Eng* 1997;19(4):319–30. [https://doi.org/10.1016/S0734-743X\(96\)00038-3](https://doi.org/10.1016/S0734-743X(96)00038-3).
- [45] Mahfuz H, Al Mamun W, Haque A, Turner S, Mohamed H, Jeelani S. An innovative technique for measuring the high strain rate response of sandwich composites. *Compos Struct* 2000;50(3):279–85. [https://doi.org/10.1016/S0263-8223\(00\)00118-5](https://doi.org/10.1016/S0263-8223(00)00118-5).
- [46] Bacon C. An experimental method for considering dispersion and attenuation in a viscoelastic Hopkinson bar. *Exp Mech* 1998;38(4):242–9. <https://doi.org/10.1007/BF02410385>.
- [47] Bacon C. Separation of waves propagating in an elastic or viscoelastic hopkinson pressure bar with three-dimensional effects. *Int J Impact Eng* 1999;22(1):55–69. [https://doi.org/10.1016/S0734-743X\(98\)00048-7](https://doi.org/10.1016/S0734-743X(98)00048-7).
- [48] Liu Q, Subhash G. Characterization of viscoelastic properties of polymer bar using iterative deconvolution in the time domain. *Mech Mater* 2006;38(12):1105–17. <https://doi.org/10.1016/j.mechmat.2006.01.001>.
- [49] Bussac M, Collet P, Gary G, Othman R. An optimisation method for separating and rebuilding one-dimensional dispersive waves from multi-point measurements. application to elastic or viscoelastic bars. *J Mech Phys Solids* 2002;50(2):321–49. [https://doi.org/10.1016/S0022-5096\(01\)00057-6](https://doi.org/10.1016/S0022-5096(01)00057-6).
- [50] Park SW, Zhou M. Separation of elastic waves in split hopkinson bars using one-point strain measurements. *Exp Mech* 1999;39(4):287–94. <https://doi.org/10.1007/BF02329807>.
- [51] Zhao H, Gary G. A new method for the separation of waves. application to the shpb technique for an unlimited duration of measurement. *J Mech Phys Solids* 1997;45(7):1185–202. [https://doi.org/10.1016/S0022-5096\(96\)00117-2](https://doi.org/10.1016/S0022-5096(96)00117-2).
- [52] Campana F, Mancini E, Pilone D, Sasso M. Strain rate and density-dependent strength of als7 alloy foams. *Mater Sci Engin: A* 2016;651:657–67. <https://doi.org/10.1016/j.msea.2015.11.007>.
- [53] Reid S, Peng C. Dynamic uniaxial crushing of wood. *Int J Impact Eng* 1997;19(5): 531–70. [https://doi.org/10.1016/S0734-743X\(97\)00016-X](https://doi.org/10.1016/S0734-743X(97)00016-X).
- [54] Radford D, Deshpande V, Fleck N. The use of metal foam projectiles to simulate shock loading on a structure. *Int J Impact Eng* 2005;31(9):1152–71. <https://doi.org/10.1016/j.ijimpeng.2004.07.012>.
- [55] Zhao H, Elnasri I, Abdennadher S. An experimental study on the behaviour under impact loading of metallic cellular materials. *Int J Mech Sci* 2005;47(4):757–74. <https://doi.org/10.1016/j.ijmecsci.2004.12.012>.
- [56] Liu J, He S, Zhao H, Li G, Wang M. Experimental investigation on the dynamic behaviour of metal foam: from yield to densification. *Int J Impact Eng* 2018;114: 69–77. <https://doi.org/10.1016/j.ijimpeng.2017.12.016>.
- [57] Duan Y, Du B, Shi X, Hou B, Li Y. Quasi-static and dynamic compressive properties and deformation mechanisms of 3D printed polymeric cellular structures with kelvin cells. *Int J Impact Eng* 2019;132:103303. <https://doi.org/10.1016/j.ijimpeng.2019.05.017>.
- [58] Harris JA, Winter RE, McShane GJ. Impact response of additively manufactured metallic hybrid lattice materials. *Int J Impact Eng* 2017;104:177–91. <https://doi.org/10.1016/j.ijimpeng.2017.02.007>.
- [59] Lopatnikov SL, Gama BA, Jahirul Haque M, Krauthausen C, Gillespie JW, Guden M, et al. Dynamics of metal foam deformation during Taylor cylinder-Hopkinson bar impact experiment. *Compos Struct* 2003;61(1):61–71. [https://doi.org/10.1016/S0263-8223\(03\)00039-4](https://doi.org/10.1016/S0263-8223(03)00039-4).
- [60] Taylor IG. The use of flat-ended projectiles for determining dynamic yield stress i. theoretical considerations. *Proc R Soc London, Ser A* 1948;194:289–99. <https://doi.org/10.1098/rspa.1948.0081>.
- [61] Whiffin AC, Taylor IG. The use of flat-ended projectiles for determining dynamic yield stress ii. tests on various metallic materials. *Proc R Soc London, Ser A* 1948; 194:300–22. [https://doi.org/10.1016/0003-4916\(63\)90068-X](https://doi.org/10.1016/0003-4916(63)90068-X).
- [62] Hiermaier S, Meenen T. Characterization of low-impedance materials at elevated strain rates. *J Strain Anal Eng Des* 2010;45(6):401–9. <https://doi.org/10.1243/03093247JSA584>.
- [63] Lea LJ, Jardine AP. Two-wave photon doppler velocimetry measurements in direct impact Hopkinson pressure bar experiments94; 2015. <https://doi.org/10.1051/epjconf/20159401063>.
- [64] Casem D, Zellner M. Kolsky bar wave separation using a photon doppler velocimeter. *Exp Mech* 2013;53(8):1467–73. <https://doi.org/10.1007/s11340-013-9735-4>.
- [65] Cowie T, Gurnham CWA, Braithwaite CH, Lea L. Impact performance of aluminium foams in a direct impact hopkinson bar. *AIP Conf Proc* 2018;1979(1):110003. <https://doi.org/10.1063/1.5044922>.
- [66] Pang X, Du H. Investigation on dynamic penetration of closed-cell aluminium foam using in situ deceleration measurement. *Composites Part B: Engineering* 2016;100: 78–90. <https://doi.org/10.1016/j.compositesb.2016.06.040>.
- [67] Govender RA, Curry RJ. The “open” hopkinson pressure bar: towards addressing force equilibrium in specimens with non-uniform deformation. *Jun Dyna Behav of Mater* 2016;2(1):43–9. <https://doi.org/10.1007/s40870-015-0042-2>.
- [68] Dannemann KA, Lankford Jr. J. High strain rate compression of closed-cell aluminum foams. *Mater Sci Eng, A* 2000;293(1):157–64. [https://doi.org/10.1016/S0921-5093\(00\)01219-3](https://doi.org/10.1016/S0921-5093(00)01219-3).
- [69] Elnasri I, Patoatto S, Zhao H, Tsitsiris H, Hild F, Girard Y. Shock enhancement of cellular structures under impact loading: part i experiments. *J Mech Phys Solids* 2007;55(12):2652–71. <https://doi.org/10.1016/j.jmps.2007.04.005>.
- [70] Shen J, Lu G, Ruan D. Compressive behaviour of closed-cell aluminium foams at high strain rates. *Composites Part B: Engineering* 2010;41(8):678–85. <https://doi.org/10.1016/j.compositesb.2010.07.005>.
- [71] Xu S, Ruan D, Beynon J, Lu G. Experimental investigation of the dynamic behavior of aluminum foams. *Materials Science Forum* 2010;654–656:950–3. DOI:10.4028/www.scientific.net/MSF.654-656.950



Dynamic penetration of cellular solids: Experimental investigation using Hopkinson bar and computed tomography

Jan Šleichrt^{a,*}, Tomáš Fíla^a, Petr Koudelka^{a,e}, Marcel Adorna^a, Jan Falta^a, Petr Zlámal^{a,e}, Jonathan Glinz^b, Michaela Neuhäuserová^a, Tomáš Doktor^a, Anja Mauko^c, Daniel Kytýř^e, Matej Vesenjak^c, Isabel Duarte^d, Zoran Ren^c, Ondřej Jiroušek^a

^a Czech Technical University in Prague, Faculty of Transportation Sciences, Konviktská 20, 110 00 Prague, Czech Republic

^b University of Applied Sciences Upper Austria, Stelzhamerstraße 23, 4600 Wels, Austria

^c University of Maribor, Faculty of Mechanical Engineering, Smetanova ul. 17, 2000 Maribor, Slovenia

^d Centre for Mechanical Technology and Automation, Department of Mechanical Engineering, University of Aveiro, 3810-193 Aveiro, Portugal

^e Czech Academy of Sciences, Institute of Theoretical and Applied Mechanics, Prosecká 809/76, 190 00 Prague, Czech Republic

ARTICLE INFO

Keywords:

Cellular materials
Dynamic penetration
Hopkinson bar
Digital image correlation
X-ray computed micro-tomography

ABSTRACT

Light-weight cellular solids, such as aluminium foams, are promising materials for use in ballistic impact mitigation applications for their high specific deformation energy absorption capabilities. In this study, three different types of aluminium alloy based in-house fabricated cellular materials were subjected to dynamic penetration testing using an in-house experimental setup to evaluate their deformation and microstructural response. A two-sided direct impact Hopkinson bar apparatus instrumented with two high-speed cameras observing the impact area and the penetrated surface of the specimens was used. An advanced wave separation technique was employed to process the strain-gauge signals recorded during the penetration. The images captured by one of the cameras were processed using an in-house Digital Image Correlation method with sub-pixel precision, that enabled the validation of the wave separation results of the strain-gauge signals. The second camera was used to observe the penetration into the tested specimens for the correct interpretation of the measured signals with respect to the derived mechanical and the microstructural properties at the different impact velocities. A differential X-ray computed tomography of the selected specimens was performed, which allowed for an advanced pre- and post-impact volumetric analysis. The results of the performed experiments and elaborate analysis of the measured experimental data are shown in this study.

1. Introduction

Metal foams and other porous solids with a similar microstructure are materials suitable for deformation energy mitigation applications due to their low specific density and specific compressive response represented by a typical plateau of constant stress up to very high overall strains yielding their very high specific energy absorption capability [1]. Moreover, cellular materials can be beneficially used as constituents in sandwich structures and composite panels, where the cellular layers are used for the dissipation of the kinetic energy of the impacting object, while the other layers maintain the integrity of the panel [2]. However, as cellular materials often have a rather complex internal structure, with a significant amount of inhomogeneities, and their deformation mechanisms are complex, the design of the protective structures is not a straightforward task. Here, an advanced approach combining an extensive experimental investigation of the mechanical

characteristics and deformation behaviour with numerical simulations is used [3–5]. In general, the mechanical properties and deformation behaviour of cellular materials are not constant and consistent throughout the whole spectrum of the possible loading conditions and scenarios [6]. Energy absorption applications depend on dynamic loading and include dynamic impacts, dynamic indentations, penetrations, shocks or even blasts. The effects of the strain-rate sensitivity related to the inertia effects, layer collapse, strain wave propagation, shock front formation and friction have a fundamental influence on the deformation response of a material [7,8]. These effects have to be well described, understood, and taken into account during the design and optimisation phase of the protective device. As the aforementioned effects are very complex and strongly related to the specific material, it is not possible to reproduce them easily in numerical simulations using standard material models [9].

* Corresponding author.

E-mail address: sleichrt@fd.cvut.cz (J. Šleichrt).

<https://doi.org/10.1016/j.msea.2020.140096>

Received 15 April 2020; Received in revised form 31 July 2020; Accepted 11 August 2020

Available online 22 August 2020

0921-5093/© 2020 The Authors.

Published by Elsevier B.V. This is an open access article under the CC BY-NC-ND license

(<http://creativecommons.org/licenses/by-nc-nd/4.0/>).

In recent years, metal foams and other cellular materials have been investigated in a number of research studies covering the experimental, numerical and analytical characterisation of the material. Under dynamic loading conditions, various types of cellular materials have been tested experimentally using several methods. Drop-weight tests have been used for the characterisation during low velocity impacts [10]. Hopkinson bar based tests (particularly tests with the Split Hopkinson Pressure Bar - SHPB) [11–14] and Direct impact Hopkinson bar (DIHB) tests [15,16] have been carried out to investigate the material behaviour at middle to high strain-rates. Taylor anvil tests or gas-and powder-gun experiments have been performed to investigate the behaviour during high velocity impacts [17,18]. A variety of entirely numerical [19] or mixed experimental–numerical studies [20] covering the aforementioned topics have been published. The strain-rate sensitivity [21–23] and other effects related to the dynamic loading such as inertia effects [13,24], fracture and fatigue behaviour [25–27], compaction shock [28–30], wave propagation [31], and cell damage [32] have been investigated in detail. Currently, cellular materials based on artificially manufactured lattice structures [33] and metamaterials [34,35] are being extensively studied. Such studies cover topics including research of non-conventional materials like auxetics (materials with a negative Poisson's ratio) [36–38], inter-penetrating phase composites [39–42], materials based on an aluminium foam skeleton [43,44] or their constituents [45].

One of the important dynamic loading modes is penetration or dynamic indentation, where a specimen is impacted with a projectile with a cross-section smaller than the cross-section of the specimen. During the test, the projectile penetrates the specimen, while its kinetic energy is dissipated in the material. This mode of loading is fundamental for the description of crushing under the impacting object as it reliably simulates the conditions during a localised impact and can characterise the real projectile stopping capabilities of the investigated material. However, the number of published studies is lower than for other loading modes. One of the limiting factors is the complexity of the experimental procedures and particularly the instrumentation of the test. Nevertheless, studies analysing the localised impact on cellular foams [46], drop-weight based penetration testing of the aluminium foams [47–49], composite structures, sandwich panels and honeycomb panels [47,48] are available. The effects of the impactor shape and the localised effects [25,49–52] and blasts [53,54] have been investigated by several research teams. Moreover, advanced experimental techniques for penetration measurements, such as an in-situ deceleration analysis have been developed [55]. In general, the description of the deformation behaviour of metal foams under impact loading is based on elementary mechanisms such as the bending, buckling, and shearing of the cells-walls. While the cells located directly under the projectile are deformed due to the bending and buckling, the cells situated alongside the impactor are mainly deformed due to the shearing [56]. Based on the observations of the deformed specimens of the aluminium foam presented in [57], a hemispherical deformation zone caused by a flat-end impactor at velocities in the range of 3–30 ms⁻¹ is localised directly underneath the impactor. An apparent tear cracking line spreads ahead of the impactor as the deformation zone is pushed further into the foam [57].

From the published experimental results it is obvious that advanced imaging methods have to be applied for the detailed description of the deformation behaviour during penetration. Digital image correlation (DIC) has proved to be particularly suitable for the full-field analysis of the displacement and strain fields in quasi-statics [58] and even in dynamic testing [59–61]. Application of the state-of-the-art high-speed cameras with DIC has allowed for the complex analysis of the deformation behaviour of cellular [13,62], lattice structures, auxetics [63], as well as other materials [64] during medium to high-velocity loading.

Based on our experience from previous studies investigating the strain-rate sensitivity of cellular materials using the Hopkinson bar with DIC [63,65–67], a direct impact Hopkinson bar (DIHB) experimental

setup with advanced instrumentation for the low to medium velocity penetration of cellular materials has been developed. The setup was designed to overcome problems related to the penetration testing. In conventional setups, several limitations negatively affect the quality and precision of the experimental data or significantly constrain the performance reducing the application envelope of the method. Conventional drop-towers can be relatively easily applied for penetration testing [51] and instrumented with sensors such as piezo-electric load-cells. However, the range of the available impact velocities is limited by the height of the drop-weight tower. Although methods for increasing the maximum impact velocity are available (e.g., spring boosters) the drop-weight method is, in general, limited to testing with rather low impact velocities. Moreover, the common instrumentation of a drop-weight tower using a dynamic load-cell and/or accelerometer does not allow for the high precision analysis of the dynamic effects in the specimen and often produces noisy signals.

DIHB is a technique for the penetration testing of materials at medium to high strain-rates, where a rigid mass projectile directly impacts a specimen mounted on an instrumented transmission bar (or an anvil). This method is called forward direct impact Hopkinson bar (FDIHB) [68]. For velocities at which the wave propagation effects significantly influence the results, a specimen is mounted on a rigid mass projectile and launched towards a stationary instrumented transmission bar. This method is called reverse direct impact Hopkinson bar (RDIHB) [68]. Since both methods are based on the Hopkinson bar techniques and their principle relies on strain wave propagation in elastic slender bars, they produce clean and well-defined signals. However, when the penetration testing is performed on panels or larger specimens, where the wave propagation effects cannot be neglected, the RDIHB is seriously limited since the launching of a large specimen or panel against an instrumented transmission bar is challenging or even impossible. Also, the testing is single-sided in principle and a complex analysis of the panel behaviour is therefore not possible. To overcome such a problem, a method introducing the in-situ deceleration using a stand-alone accelerometer embedded in the impacting projectile [55] has been developed. This very advanced method is based on the DIHB technique and allows for a complex analysis of the behaviour during the penetration. However, the accelerometer usually produces noisy signals that have to be extensively filtered [55]. Application of a Laser Doppler Velocimetry (LDV) to produce high-quality velocity output [69] is also challenging as the sensing pattern has to be located in a relatively large distance from the front face of the projectile that is penetrating the specimen. Incorporation of the wave propagation phenomena into the evaluation procedures is thus not a trivial task.

The mechanical testing can be complemented by radiographic imaging to obtain insight into the deformation mechanism within the microstructure of the investigated specimens. Several advanced experimental methodologies for the characterisation of the mechanical response of porous solids to the loading have been developed recently [70]. Time-resolved XCT (4D XCT) experiments enable one to capture the deforming microstructure during the in-situ experiment performed in the CT scanner, either in discrete load steps [71] or continuously throughout the loading procedure (so-called on-the-fly CT [72]). The radiographical procedure can be coupled with various processing methods, where attention is focused on the digital volume correlation [73] and differential XCT [74]. Using the differential XCT, it is possible to compare the intact specimen before the start of the loading procedure (the reference state) with specimen state at arbitrary load states. This is undertaken by performing various mathematical operations on the reconstructed 3D tomographical images to suppress the common microstructural features and highlight the differences in the morphology and topology of the microstructural elements. Such a procedure has already been applied, e.g., in biomechanics to study a microcrack formation in human bones [71] and rock mechanics [75]. Although such methods are usually performed on objects subjected to loading in the quasi-static regime, it is possible to perform the XCT of

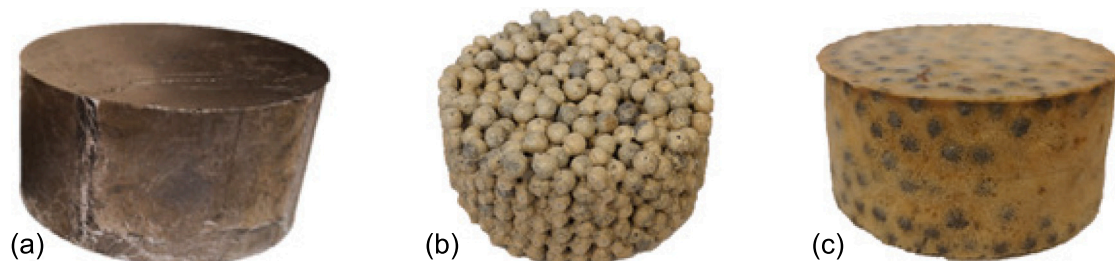


Fig. 1. The investigated specimens: (a) closed-cell aluminium foam, (b) APM, (c) hAPM.

a dynamically loaded sample by its scanning prior to the loading and after the experiment using an external scanner [76].

In this paper, we introduce a complex experimental setup for the penetration testing of cellular materials based on the Open Hopkinson Pressure Bar (OHPB) [68] method that is instrumented with strain gauges on both sides of the specimen. A wave separation technique is employed to reconstruct the strain-wave histories on the specimen boundaries. The high precision force, displacement, and velocity profiles at both sides of the specimen are calculated and analysed together with the wave propagation phenomena and dynamic forces equilibrium. The experiments are recorded using a pair of high-speed cameras to enable the DIC-based displacement and particle velocity evaluation on both sides of the specimen for verification of the strain-gauge signals together with an optical inspection of the specimen during the penetration. To correctly interpret the results derived from the optical and strain-gauge measurements, differential X-ray computed microtomography (XCT) is performed to characterise the internal structure of the samples. As a part of the high-resolution XCT procedure, the imaging of the intact specimens is used for the inspection of the internal structure of all the investigated cellular solids with respect to the representative volume element (RVE) under the impactor.

The experimental setup is used for the penetration testing of three different groups of cellular materials: (i) a closed-cell aluminium alloy foam, (ii) an Advanced Pore Morphology (APM) foam, and (iii) a hybrid APM foam (hAPM). As these cellular materials exhibit different deformation behaviours and damage mechanisms during dynamic the indentation testing, the analysis of the characteristic behaviour during low to medium velocity penetration at three different impact velocities in the range of 8–18 ms^{-1} was performed. The penetrated closed-cell metal foam and composite with medium strength matrix specimens are scanned after the impact experiments to obtain the 3D images of the loaded state for the differential analysis. The differential XCT is then employed to reveal the response of the specimens to the medium-rate impact including the localisation of the deformation around or under the impactor. Based on the complex analysis combining the mechanical, optical, and XCT data, the changes in the behaviour during the penetration together with the wave propagation characteristics and damage mechanisms were investigated and the specific trends for each type of the material were formulated.

2. Materials and methods

2.1. Tested materials

Three types of cellular metals were tested: (i) a closed-cell aluminium alloy foam, (ii) an APM foam, where aluminium spheres are coated by polyamide, and (iii) an hAPM foam, where aluminium spheres are embedded in an epoxy. A closed-cell aluminium foam with integral metal-skin over the foam core is a typical cellular material for energy absorption applications. The strain-rate sensitivity related to the closed pores and inertia has been described in several publications [12–14,21,77]. The wave propagation and shock effects in the pore cells of the metal foam have a crucial influence on the mechanical behaviour [78]. The deformation behaviour of the APM

foam, i.e., a hollow aluminium sphere composite with non-stiffening matrix, is related mainly to the response of the individual sphere particles and their connectivity, while the binding material maintains the integrity of such a multiphase material. In contrast, the influence of the matrix on the resulting deformation behaviour is significant in the hAPM composite, where the hollow spheres are embedded in a medium strength matrix. The specimens of the closed-cell aluminium foam, APM foam and hAPM foam are shown in Fig. 1.

For the production of closed-cell metal foam, a powder-compact foaming technique and a melt route process are mostly used. By the melt route process, a foaming agent or an inert gas are directly injected into a melted metal [79,80]. For the production of the samples tested in this work, the powder-compact foaming technique was implemented, where the foaming agent was mixed with a metal powder and then compacted to form a foamable precursor material [81–83]. The precursor was placed into an oven and heated to a temperature close to the melting temperature of its metallic matrix, which allows for the initiation of the foaming process and the consequent expansion of the material.

The closed-cell aluminium alloy (AlSi_7) foam samples (diameter of 60 mm; height of 30 mm) were fabricated by applying the powder-compact foaming technique [81–84]. Fig. 2(a,b) show the reconstructed 3D images of the intact closed-cell alloy foam specimen with the isosurface fitted to the cell-struts and the identified individual pores are colour-coded using their volume. The medial slice captured on the axis of symmetry shows the pore shape variation along with the height of the sample and particularly the morphology of the metal skin. It can be seen that a relatively homogeneous pore size distribution was achieved in the central part of the specimen up to approximately half of the specimen height. The pore size then increases with the distance from the axis of symmetry and towards the region near the circular face of the cylinder. The variations in the external aluminium alloy skin thickness are also apparent. On one face, the thickness of the skin is approximately 0.2 mm, however, on the other face, such a thickness can be observed only in the region near the axis of symmetry up to the radius of approximately 10 mm. In the remaining parts of the section, particularly near the vertices, very low-porosity regions were produced during the production process. By inspecting the transversal slices, similar porosity variations have also been found in the circumferential direction.

The fabrication process of the APM aluminium foam (AlSi_{10}) samples comprised a foaming and shaping step [81,85]. The fabrication and coating of the basic APM spheres were performed by Fraunhofer IFAM Bremen (Germany). In the second step, the APM specimens were manufactured within the Teflon (PTFE) moulds with a diameter of 60 mm and thickness of 30 mm. The moulds were filled with polyamide coated APM elements and placed into a 190 °C heated furnace for two hours to melt the adhesive and to bond the neighbouring APM elements together after cooling. The same manufacturing process was employed for the fabrication of the hAPM foam, which was subjected to heating at 160 °C for three hours. Fig. 2(c,d) and (e,f) shows the reconstructed 3D images of the intact APM and hAPM foam specimens. The average densities and weights of the samples are summarised in Table 1.

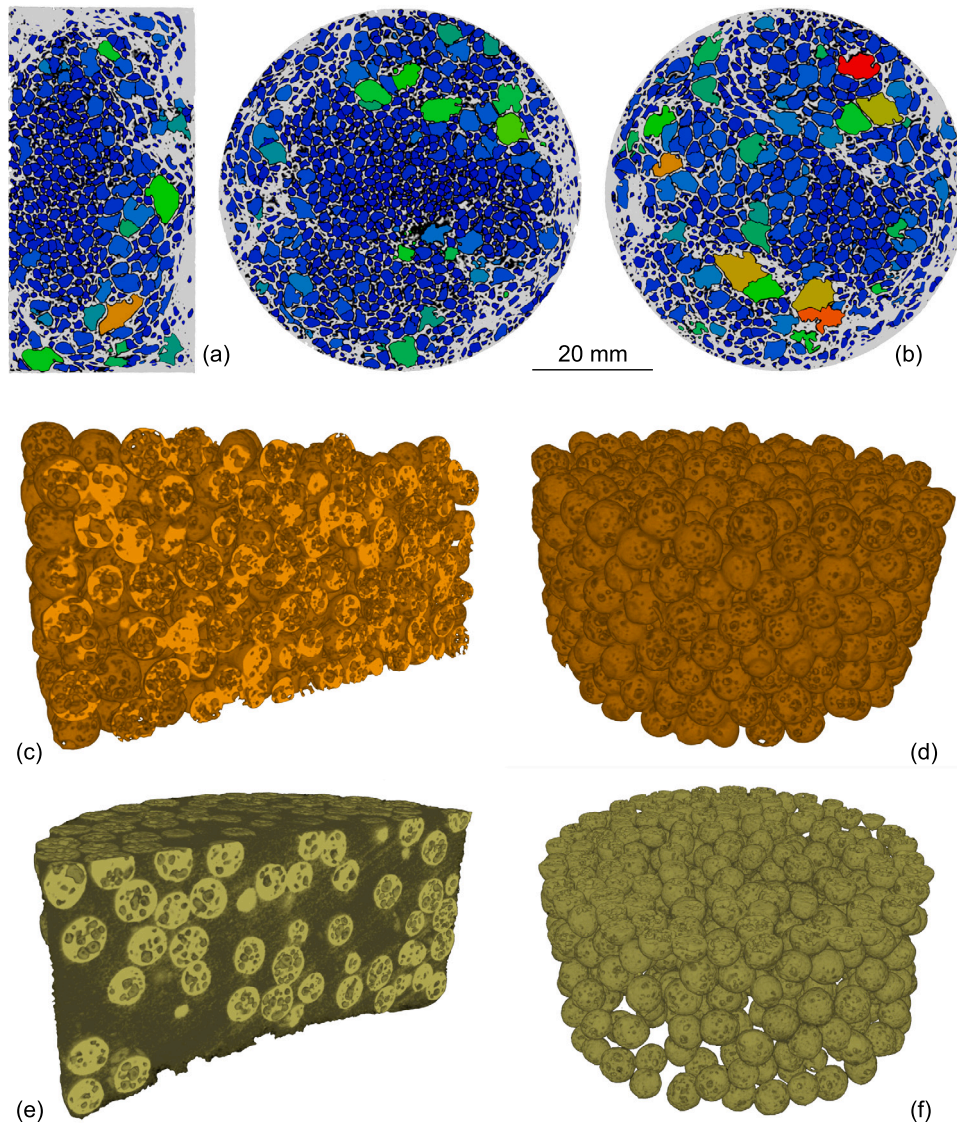


Fig. 2. XCT visualisations of the investigated materials: closed-cell foam specimen - slice in the medial plane (a), and two slices in the transversal plane (b), APM and hAPM foam specimens - perspective 3D visualisation using full intensity range (c,e), and segmentation showing only the aluminium spheres (d,f).

Table 1
The morphological properties of the specimens.

	Closed-cell aluminium foam	APM foam	hAPM foam
Density average [kgm^{-3}]	742.41 ± 47.53	597.03 ± 18.28	525.43 ± 15.40
Weight average [g]	61.73 ± 4.94	51.81 ± 1.66	44.29 ± 1.35

The segmentation of the reconstructed 3D images was used to visualise the aluminium spheres and for a general inspection of the sphere morphology as the other structural features were not apparent in the XCT. The visualisation based on the full intensity range coupled with the sectioning of the volume shows the influence of sphere coating on the resulting internal structure within the cylindrical samples (Fig. 2(d,f)). It can be seen that the APM foam exhibits a point-connectivity of spheres yielding approximately 7 spheres along with the height of the sample and 14 spheres in the radial direction. The analogous section in the 3D image of the hAPM specimen shows a significantly different microstructure, where the spheres are predominantly distributed in the region of one circular face and along the circumferential direction near the surface of the specimen. The volume around the axis of symmetry is then composed of approximately 50 %

of the epoxy matrix and 50 % of the aluminium spheres, which is an important finding influencing the interpretation of the penetration results with regard to the conclusions on the material properties. Overall, it can be observed that the requirements on the RVE dimensions, as defined by Gibson and Ashby for porous solids in [1], are fulfilled for all the samples when considering the flat-face impactor, with a diameter of 20 mm used in the experimental investigation.

2.2. Mechanical testing

The open Hopkinson Pressure Bar (OHPB) is a novel DIHB introduced in 2016 by Govender et al. [68]. The method combines the arrangements of the forward and reverse DIHB (FDIHB, RDIHB). Because the FDIHB cannot capture the phenomena related to the wave propagation and shock front at the front face of the specimen, the RDIHB has to be employed for such measurements. Using this method, the specimen is launched together with a striker towards the transmission bar, where its response is recorded. Since the method is instrumented on a single side only, additional instrumentation is required for the measurement of the displacements during the experiment (e.g., DIC or LDV) to evaluate the displacement, velocity, and force histories at both sides of the specimen.



Fig. 3. Principle of the direct impact Hopkinson bar method.

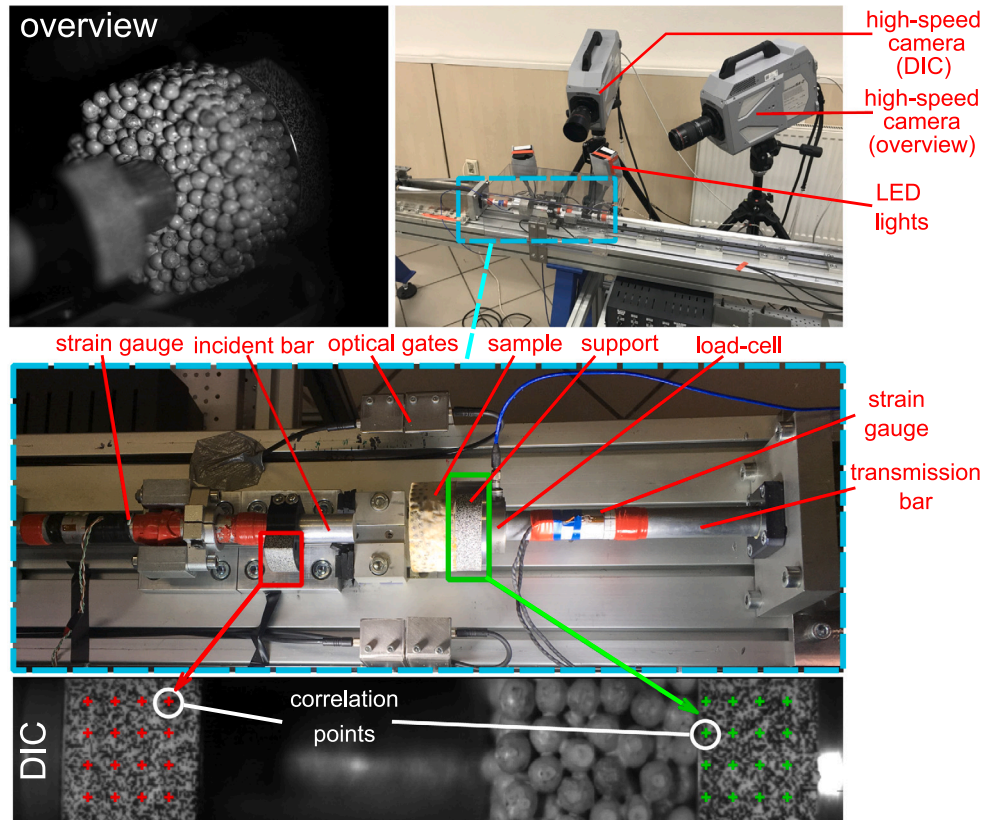


Fig. 4. The OHPB experimental setup: The high-speed cameras, their field of view and an example of the grid of correlation points established in the incident and transmission bar.

In our case, the OHPB experimental setup was modified for the penetration testing. The experiments were observed with a pair of high-speed cameras to enable the optical inspection of the experiments and the subsequent processing using DIC. As the standard experiment duration is limited to a relatively short time window (like other variants of Hopkinson bar methods) before the forward and backward propagating strain waves produce superposition at the strain-gauge, the experiment duration was prolonged by applying the wave separation technique verified using information from the DIC.

The samples were penetrated by an aluminium alloy bar at three different impact velocities to evaluate the response of the tested materials to the dynamic loading and to reveal the possible strain-rate sensitivity or inertia effects, wave propagation, and shock related changes in the deformation behaviour. The incident bar was accelerated using a single-stage gas-gun with a maximum operating pressure of 1 MPa and used as a striker that directly penetrated the samples. The tested specimens were placed on a support plate with dimensions corresponding to the sample which was firmly mounted at the end of the transmission bar, see Fig. 3.

The device consisted of aluminium bars made of a high-strength aluminium alloy (EN-AW-7075-T6) with a diameter of 20 mm. The incident bar had a length of 1600 mm. The bar was in its front part guided by a linear guideway (drylinT, Iigus, USA). A maximum impact velocity of approximately 20 ms^{-1} corresponding to the impact energy of approximately 300 J could be achieved. The transmission bar had

a length of 1600 mm. The specimen's supporting plate with a diameter of 60 mm and thickness of 40 mm was connected to the transmission bar using a bolted joint. An additional bar with a length of 1600 mm, serving as a momentum and strain-wave trap, was mounted behind the transmission bar. The residual energy of the experiment was dissipated in the momentum trap and a hydro-pneumatic damper. To measure the strain waves propagating in the setup, the incident and transmission bars were instrumented with foil strain-gauges (3/120 LY61, HBM, Germany). A pair of strain-gauges were placed at a distance of 200 mm from the specimen on both adjacent bars and connected in a Wheatstone half-bridge arrangement, so that any possible minor bending of the bars during the experiment was compensated. Moreover, the signal amplification was doubled in comparison with a single strain-gauge connected in a quarter-bridge arrangement. The strain-gauge signals were amplified using a pair of differential low-noise amplifiers (EL-LNA-2, Elsys AG, Switzerland). The signals were recorded with a high-speed digitising card (PCI-9826H, ADLINK Tech., Taiwan) at a sampling rate of 20 MHz. Photoelectric sensors (FS/FE 10-RL-PS-E4, Sensopart, Germany), serving as an optical gate, were placed in front of the tested sample perpendicularly to the incident bar trajectory and were used for the triggering and time synchronisation of the experiment. A pair of high-speed cameras (Fastcam SA-Z, Photron, Japan) were used for the optical inspection of the experiment. The first camera (further called an overview camera) served for an inspection of the specimen's front face during the impact. It was set to a recording

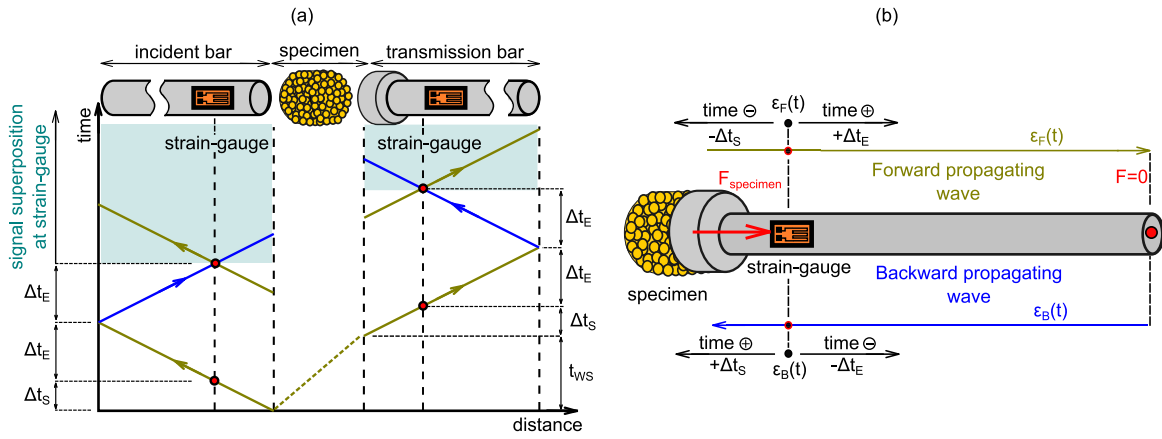


Fig. 5. The Lagrange wave propagation diagram in the OHPB experiment.

speed of 20 kfps and a resolution of 1024×1024 pixels. The second camera (further called a DIC camera) was oriented perpendicularly to the setup's longitudinal axis and observed the ends of both bars, where random speckle patterns were mounted. It was operated at a frame rate of 180 kfps and a resolution of 768×112 pixels. The images from this camera were subsequently processed using the in-house DIC tool [86] for: (i) the identification of the displacements of the individual bars, (ii) the precise calculation of the initial impact velocity, and (iii) the identification of the longitudinal strain on the surface of the penetrated specimens, when possible. Illumination of the scene was performed using a high-performance LED illumination system (Multiled QT, GS Vitec, Germany). Both cameras were synchronised with the aforementioned photoelectric sensors and with high-speed digitisers. The data acquisition and control during the experiment were performed using a custom LabView (National Instruments, USA) interface. The experimental setup is shown in Fig. 4.

2.3. Wave separation and data processing

Strain-gauge signals can be used for the evaluation of the particle velocity, the displacement and force at the boundaries of the specimen. In the standard OHPB experiment, the calculation of these quantities is based on the one-dimensional strain-wave propagation theory in elastic slender bars [68,87]. This theory is valid only over a relatively short period of time, when the recorded strain-gauge signals are not affected by the backwards-propagating strain-wave that is reflected from the free end of the bar. When the reflected strain-wave arrives at the strain-gauge location, the superposed signal is measured and it cannot be directly used for the evaluation of the mechanical results. The Lagrange diagram of wave propagation in the OHPB experiment is shown in Fig. 5. It can be seen that the strain-wave travels from the specimen's boundary through the free end, when it is reflected. The wave travel time required for the distance from the bar face to the location of the strain-gauge is denoted Δt_s . The wave travel time required for the distance from the strain-gauge location to the free end of the bar is denoted Δt_e . The wave superposition occurs when the reflected wave arrives at the location of the strain-gauge. In our case, this occurs after the time period of $2\Delta t_e$ after the wave is detected by the strain-gauge for the first time.

As the initial strain-wave always propagates from the specimen in case of OHPB, a wave separation technique can be employed to prolong the experimental time window. Methods for the wave separation in Hopkinson bar experiments have been established and can be used for elastic as well as visco-elastic bars [88–90]. The main assumption of all the methods is that the measured signal $\epsilon(t)$, the particle velocity $v(t)$, and the actual force at a certain cross-section $F(t)$ of the bar are given by [89]

$$\epsilon(t) = \epsilon_F(t) - \epsilon_B(t), \quad (1)$$

$$v(t) = c_0 [\epsilon_F(t) - \epsilon_B(t)], \quad (2)$$

$$F(t) = EA [\epsilon_F(t) + \epsilon_B(t)], \quad (3)$$

where $\epsilon_F(t)$ is the forward-propagating strain-wave, $\epsilon_B(t)$ is the backward-propagating strain-wave and c_0 is the wave propagation velocity in the bars. Normally, at least two strain-gauge locations are required on a single bar to reconstruct the forward and backward propagating waves from the measured signals using the different techniques [89]. The wave dispersion effects and attenuation have to be taken into account [88–92]. However, in case of the OHPB testing of cellular materials, some simplifications can be adopted that significantly reduce the complexity of the wave separation procedure. Here, the following conditions are met:

- The waves travel from the specimen's boundary to the free end of the bar.
- The waves are generated directly by the bar-specimen contact and the specimen has the lowest mechanical impedance in the experimental setup.
- The wavelength of the strain pulses is very long, while high frequencies are not present in the pulse as they are filtered by the plastic deformation of the specimen. Therefore, the wave attenuation and dispersion effects can be considered negligible.

By applying the time-shifting procedure shown in Fig. 5b, the forward and backward propagating waves and other respected quantities at the specimen's location can be calculated using the equations

$$\epsilon_{FS}(t - \Delta t_s) = \epsilon(t) + \epsilon_F(t - 2\Delta t_e), \quad (4)$$

$$\epsilon_{BS}(t - \Delta t_s) = -\epsilon_F(t - 2\Delta t_e + \Delta t_s), \quad (5)$$

$$v(t - \Delta t_s) = c_0 [\epsilon_{FS}(t - \Delta t_s) - \epsilon_{BS}(t - \Delta t_s)], \quad (6)$$

$$F(t - \Delta t_s) = EA [\epsilon_{FS}(t - \Delta t_s) + \epsilon_{BS}(t - \Delta t_s)]. \quad (7)$$

Since the wave dispersion effects are considered negligible in the case of the cellular materials penetration, the separated signals can be calculated using a simple time-shifting procedure that does not change the shape nor amplitude of the wave over the travelled distance. Note that at the beginning of the experiment, the strain-gauge signal $\epsilon(t)$ is never superposed. Therefore, it is possible to separate the waves using the information from the initial time window without superposition.

The wave separation technique allows for the evaluation of the experiment in a longer time window when the superposed signal is measured by the strain-gauges. The comparison of the force calculated directly from the superposed strain-gauge signal at the incident bar and the force calculated using the wave separation technique is shown in Fig. 6a. The sudden drops in the superposed signal are caused by the backwards-propagating wave. A similar comparison of the velocity calculated directly from the superposed signal and the velocity calculated using the wave separation procedure is shown in Fig. 6b.

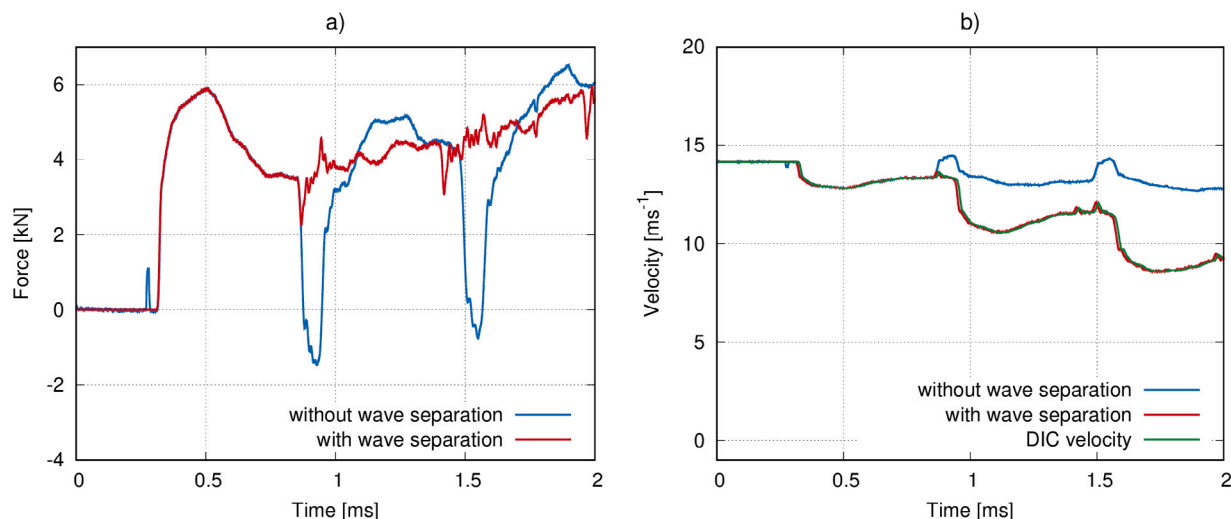


Fig. 6. (a) Incident bar force indicated by the strain-gauge calculated without the wave separation (red) and with the wave separation (blue), (b) Incident bar velocity indicated by the strain-gauge calculated without the wave separation (blue), with the wave separation (red) and compared with the velocities calculated using the DIC (green). (For interpretation of the references to colour in this figure legend, the reader is referred to the web version of this article.)

Displacement calculated from the strain-gauge can be time-shifted to the location of the random speckle pattern and compared with the DIC displacement. If a sufficient number of images with reliable tracking by DIC is available, the particle velocity can be calculated by differentiation of the DIC displacement and compared with the value evaluated based on the strain-gauge measurement.

2.4. Differential CT procedure

Using the reconstructed 3D images of the intact and impacted samples, differential tomography procedure was performed to emphasise variations within the sample microstructure and to suppress common features in the microstructure with the concentration on the region in the vicinity of the impacting bar. Due to the nature of the dynamic loading and the used experimental setup, it was not possible to perform the tomographic scanning using the in-situ methodology. Thus, the careful separation of the reconstructed volumes from the scanned stack of samples and their precise subsequent alignment was required to obtain the relevant data for the morphological analysis. For the alignment of the volumes, a 3D image registration algorithm based on a rigid transformation (i.e., the transformation considering only the translations and rotations of the sample yielding 6 degrees of freedom for the registered 3D image) with single-voxel precision was carried out in the VGStudio MAX 3.3 (Volume Graphics, Germany).

After the alignment of the volumes, two approaches for the differential tomography were used in the processing and visualization of the data. The reference 3D image of the intact specimen was subtracted from the 3D image of the impacted sample. Additionally, blended volumes were created. The blending procedure consists of the multiplication of the volume in the impacted state by a given constant followed by a sum of such a volume with the volume of the reference state. This procedure is common for 4D XCT, where such an approach can be used for, e.g., investigation of fatigue microcracks in bones (see [71]). The value of the constant for the multiplication can be obtained from an iterative procedure, where the resulting blended volume is qualitatively inspected for noise and contrast on the boundary of the region influenced by the impact to identify the optimum value. The value of the multiplier was sought in the range of $m \in \langle 2; 20 \rangle$, $m \in \mathbb{Z}$, yielding the optimal value of $m = 5$ for the closed-cell foam sample and $m = 10$ for the hAPM foam sample used in the volumetric blending of the reconstructed 3D images. After the differential tomography procedure, the generated volumes were subjected to a defect (both the closed-cell foam and the hAPM foam samples) and foam structure analysis (only

the closed-cell foam sample). Using the foam structure analysis, the pore morphology in terms of the pore-size distribution and strut-/wall-thickness analysis was extracted from the 3D images using the *Foam analysis module* of the VGStudio MAX 3.3 software together with the visualisation of the individual pores and the strut thicknesses. The foam structure analysis module was then used to identify the individual cells including their morphological properties for further analysis.

2.5. Experiments

The OHPB experimental setup was used to penetrate the specimens during a low and medium velocity impact. The specimens were mounted on a supporting plate attached to a transmission bar. During the mounting, a small amount of grease was applied on the rear face of the specimen to hold the specimen on the plate by friction. The specimens were penetrated using the flat-face incident bar projectile with a total mass of approximately 1.5 kg. A gas-gun air reservoir pressure of 200 kPa, 500 kPa, and 800 kPa was used to accelerate the incident bar to the impact velocities of approximately 8 ms^{-1} , 14 ms^{-1} and 18 ms^{-1} . The momentum trap system was not in initial contact with the bars of the experimental setup. This configuration was employed to prevent the subsequent hard impacts on the specimen after the first impact. It also prevented the unknown reflection of the wave on the rear face of the transmission bar, and, therefore, it was used for the conservation of the waves in the experimental setup and for the reconstruction of the wave propagation in the system. In our case, employing a very long transmission bar preventing the arrival of the reflected wave prior to the end of the experiment was not possible due to space limitations. When the accelerated incident bar interrupted the first optical gate in front of the specimen, the data acquisition system and both high-speed cameras were triggered. All the data were automatically uploaded to the control PC after the experiment.

3. Results

The experimental data were processed using the data processing methods described in Section 2. It was possible to evaluate the force, displacement, and velocity-time histories that were synchronised with the DIC results and with the images captured by the overview camera. The processed strain-gauge data were compared with the DIC data in terms of the indicated displacements and velocities and the output of the wave separation procedure was verified. Thus, it was possible to evaluate all the penetrations until the end of the experiment, i.e., when

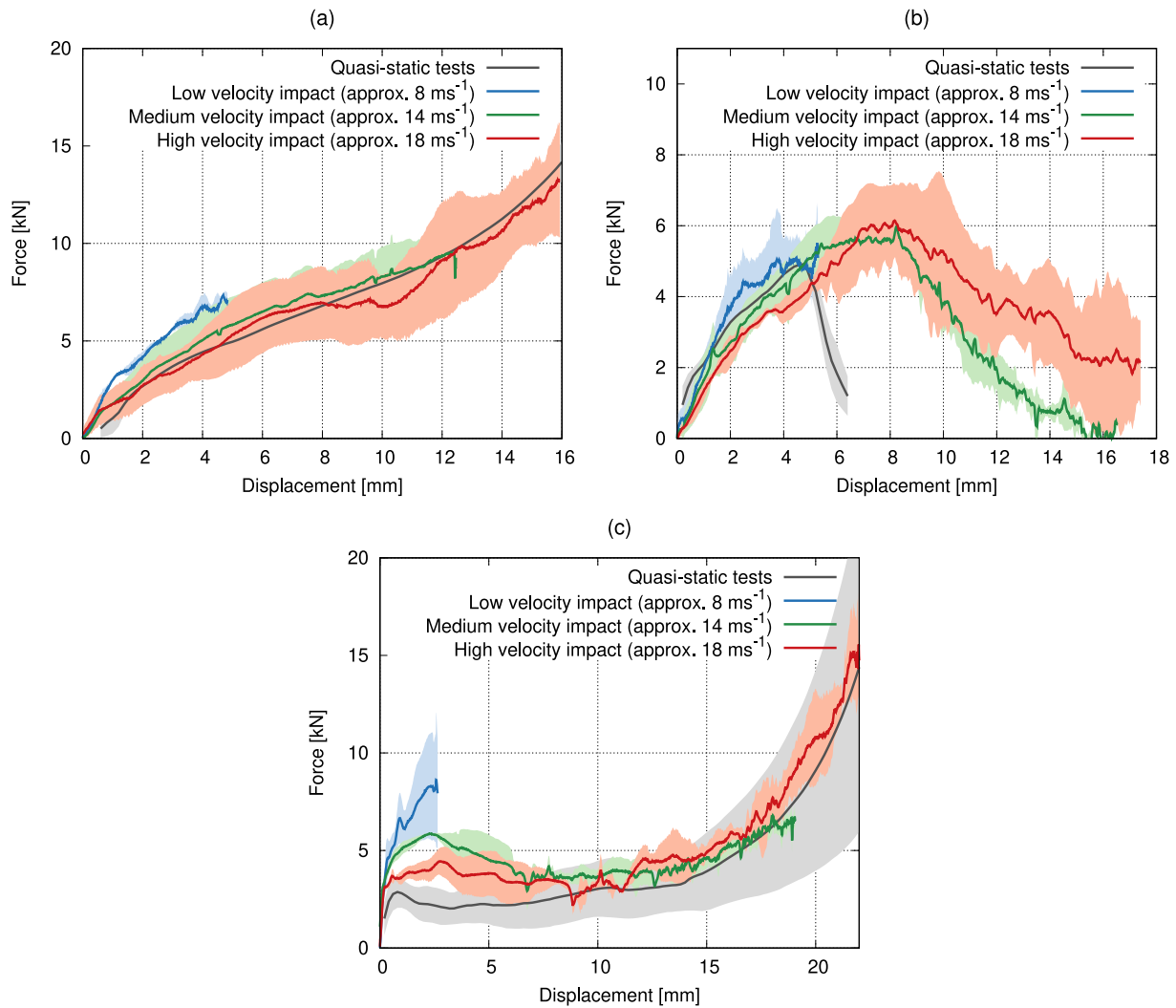


Fig. 7. The average force–displacement diagrams for the quasi-static and dynamic indentation at three impact velocities: (a) the hAPM foam, (b) the APM foam, (c) the closed-cell aluminium foam.

the impact velocity decreased to zero. As the experiments were carried out without any initial contact between the transmission bar and the momentum trap, not all the initial kinetic energy was dissipated in the specimen. A part of the initial energy of the incident bar was dissipated in the specimen, while the rest was transformed to the post-impact movement of the bars or dissipated as friction and other losses in the system. This arrangement allowed for the analysis of the effects related to the wave propagation in the specimen. In this section, the results evaluated from the strain-gauges including the force, displacement, velocity, or energy during the impact are presented and compared with the optical and DIC data. The results regarding the pre-impact as well as the post-impact analysis of the specimen's internal structure are also provided and discussed. At least three specimens were tested in quasi-static compression and dynamic penetration at each impact velocity. However, it has to be mentioned that in some experiments the measured values deviated from the average values of the set. Therefore, the exact values of the material properties had to be interpreted with caution. Still, the trends in the deformation behaviour could be observed, evaluated and discussed. From each type of tested materials, only one specimen could be processed using the XCT analysis because of its complexity, time-consuming measurements and data processing.

3.1. Force–displacement

The dependency of the piercing force on the penetration depth was evaluated. Quasi-static penetration experiments with the identical configuration of the specimen, supports, and indenter were also carried out (see Section A.1).

The corresponding average force–displacement diagrams of the hAPM foam are shown in Fig. 7a, where the monotonous hardening with the penetration depth at all the tested impact velocities can be observed. While the specimens remained compact for the low and medium impact velocity, the disintegration of the specimens occurred in the experiments with the high impact velocity. It can be seen that the piercing force decreased with the increasing impact velocity, but, in contrast to other tested materials, the standard-deviations for the individual impact velocities partially overlap.

The average force–displacement diagrams of the APM foam are shown in Fig. 7b. The APM foam exhibited a similar behaviour to the hAPM foam as a monotonous hardening with a penetration depth at all the tested impact velocities was observed. The specimens of this material always disintegrated at the medium and high impact velocity. At a low impact velocity, most of the specimens remained compact. In one case, the disintegration occurred at approximately an identical force and depth as in the quasi-static penetration tests. As in the case of the hAPM foam, the piercing force decreased with the increasing impact velocity. For this material, the effect is even less profound than in the

previous case and, again, the standard deviations for the individual impact velocities partially overlap.

Force–displacement diagrams of the closed-cell aluminium foam for the quasi-static and dynamic indentation at all the impact velocities are shown in Fig. 7c. The closed-cell aluminium foam penetrated at the low impact velocity exhibited a behaviour that is not typical for such a material as long as the piercing force increased abruptly and no plateau region was observed. Simultaneously, the penetration depth was very low and, in most of the cases, the metal skin over the porous core was not fully penetrated. During the impact at the medium velocity, the behaviour of the specimen was different. In this case, the initial increase of the piercing force is not as significant as in the low-velocity case and, after the initial penetration phase, the plateau region typical for the foam material was observed. During the high-velocity impact, the behaviour of the specimen was similar to its response on the quasi-static indentation, while the average values of the piercing force at the plateau were higher. Similarly to the hAPM foam, the piercing force decreased with the increasing impact velocity, while exhibiting stronger strain-rate dependence apparent from the standard deviations of the force–displacement diagrams.

3.2. Velocity–time

The diagrams showing the change of the actual impact velocity over time were evaluated to investigate the stopping capabilities of the individual materials are shown in Fig. 8. The average time–velocity histories for each type of material at every impact velocity are presented. The velocities were evaluated from the strain-gauges as well as from the DIC. In all the experiments, a very good agreement of the DIC indicated displacements (or velocities) with the strain-gauges data was observed.

The time–velocity histories of the hAPM foam for every impact velocity are shown in Fig. 8a, where a different velocity–time relationship can be observed. The velocity change was rather smooth and continuous. Even though the disintegration of the specimens was observed at the high impact velocity, all the specimens were able to reach zero impact velocity. The disintegration always occurred at the very end of the experiment.

The time–velocity histories of the APM foam for the impact velocities are shown in Fig. 8b. The APM foam exhibited a very different behaviour to the other materials. The stopping capability of this material was very low as the specimens disintegrated at both the medium and the high-velocity impacts and allowed the projectile to penetrate through. The decelerated velocity, prior to the disintegration, was in the order of a few metres per second (lower than 4 ms^{-1}).

The time–velocity histories of the closed-cell aluminium foam for every impact velocity are shown in Fig. 8c. The closed-cell aluminium foam was able to stop the projectile without any disintegration in all the conducted experiments. For this type of material, significant step-wise changes in the impact velocity were observed. This phenomenon was caused by the nature of the testing based on the wave propagation as a relatively long bar was used for the penetration of the specimen. The step-wise change occurred every time when the reflected wave from the free end of the bar arrived at the specimen and caused a sudden change in the velocity. This behaviour was most profound for the case of the closed-cell aluminium foam as the wave generated at the plateau region was approximately constant. Then, the backwards-propagating reflected wave had a similar amplitude with the forward-propagating wave still being generated at the plateau. At the high impact velocity, the rapid deceleration of the projectile was observed as the penetrated region was compressed to full densification. Here, the projectile was stopped even sooner than at the medium velocity.

3.3. Energy absorption

The energy absorption properties were evaluated to further investigate the stopping capabilities of the individual materials. Also, the specific energy absorption ratio defined as the energy dissipated per the unit of nominal penetrated volume was calculated. The diagram showing the energy dissipated per penetration volume for all three materials is shown in Fig. 9a.

The closed-cell foam exhibited the highest value from all the materials at the low impact velocity. For the medium velocity, its energy absorption per volume dropped by approximately 30% and again increased at the high impact velocity. This behaviour was in agreement with the presented average force–displacement diagrams. The very high energy absorption at the low velocity is related to the crushing behaviour, where the metal skin over the porous core had a significant effect on the wave propagation characteristics and resulted in the corresponding hardening. The effect is discussed in detail in the section related to the specific results of the closed-cell aluminium foam (see Section 3.5.1). The hAPM foam exhibited a monotonous increase in the energy dissipated per volume through all the impact velocities, whereas the APM foam exhibited an inverse trend. In the case of the hAPM foam, the energy dissipated per volume monotonically decreased with the impact velocity. The decrease of energy absorption of the APM foam was related to its disintegration at higher velocities. Conversely, the increase in the energy absorption of the hAPM foam was related to its monotonically increasing force–displacement response.

At a penetration depth of 3.5 mm, Fig. 9b shows a stable decrease in the energy absorption for all the materials in the initial phase of the impact. Furthermore, similar effects in the wave propagation through the specimen related to the impact velocity are visible.

A ratio between the energy dissipated in the specimen and the initial impact energy was calculated to compare the amount of energy dissipated in the material. At the low impact velocity, the ratio was almost identical for all the materials. This behaviour was related to the fact that all three materials were able to withstand the impact at such a low velocity and the residual energy was transferred into the transmission bar through the specimen. With the increasing velocity, the ratio for the APM foam rapidly decreased as it was not able to withstand the impact and disintegrated. On the other hand, the closed-cell foam, as well as the hAPM foam, exhibited similar increased values for the impact at the medium velocity since both materials were able to withstand the impact. At the high impact velocity, the hAPM material lost its ability to withstand the impact (disintegration occurred in the later phase of the impact) and exhibited lower values than the closed-cell foam that remained compact in all the experiments. The ratio of the energy dissipated in the specimen and the impact energy is shown in Fig. 9c.

Because it was not possible to perform the differential CT procedure for the APM foam as the penetration of all the specimens in this group disintegrated at the medium and high-velocity impact. The dependency of the penetration depth, where the disintegration occurred, plotted against the initial impact velocity is shown in Fig. 10a. The time, when the disintegration of the specimen started, plotted against the initial impact velocity is shown in Fig. 10b. Note that the penetration depth of the disintegration increased with the impact velocity, whereas the time of the disintegration remained approximately constant. Therefore, the inertia effects delayed the disintegration of the specimen with the increasing impact velocity and this type of material could not even withstand the lower impact energy corresponding with the medium impact velocity. The observed increase in the penetration depth did not represent an increase in the energy absorption, but it is only related to the time that is necessary to overcome the inertia and to disintegrate the specimen.

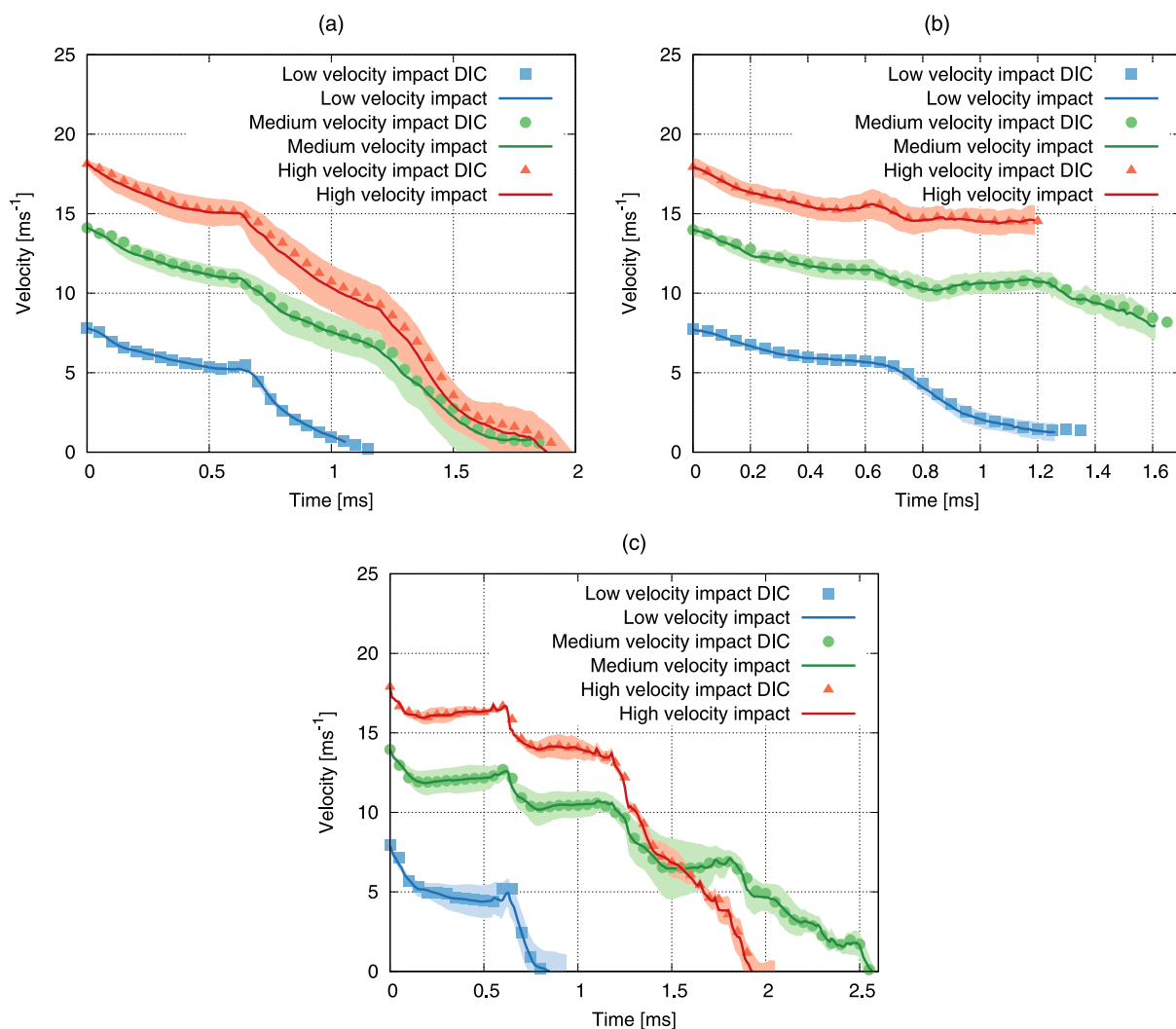


Fig. 8. The average velocity-time diagrams for the three initial impact velocities showing the velocity indicated by the strain-gauges and by the DIC: (a) the hAPM foam, (b) the APM foam, (c) the closed-cell foam.

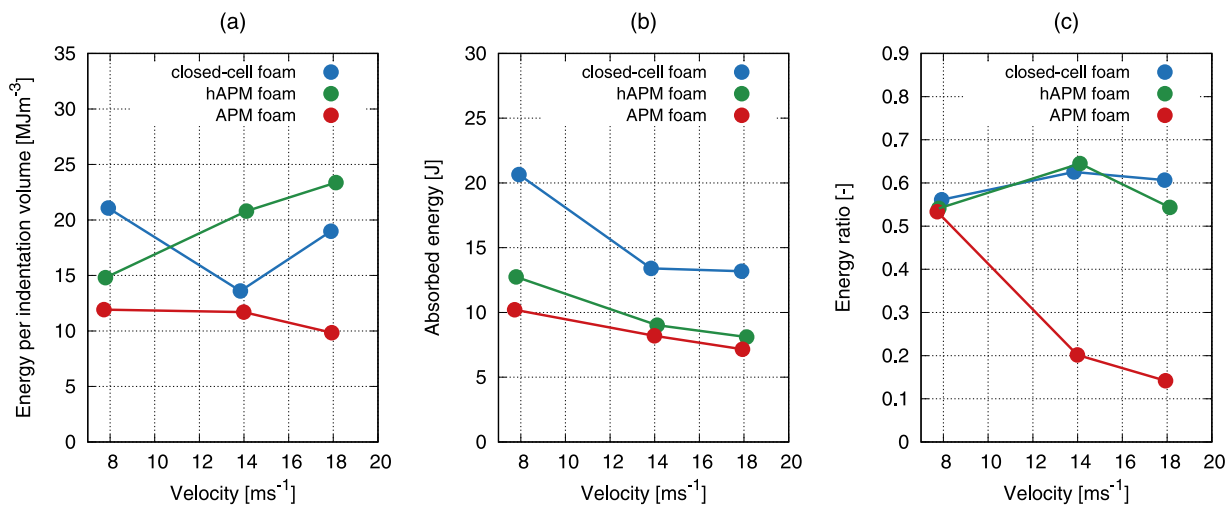


Fig. 9. (a) The diagram showing the energy dissipated per penetration volume for all three materials. (b) The diagram showing the energy dissipated per penetration volume for all three materials in the penetration depth of 3.5 mm representing the initial phase of the impact. (c) The ratio of the energy dissipated in the specimen and the initial kinetic energy of the incident bar.

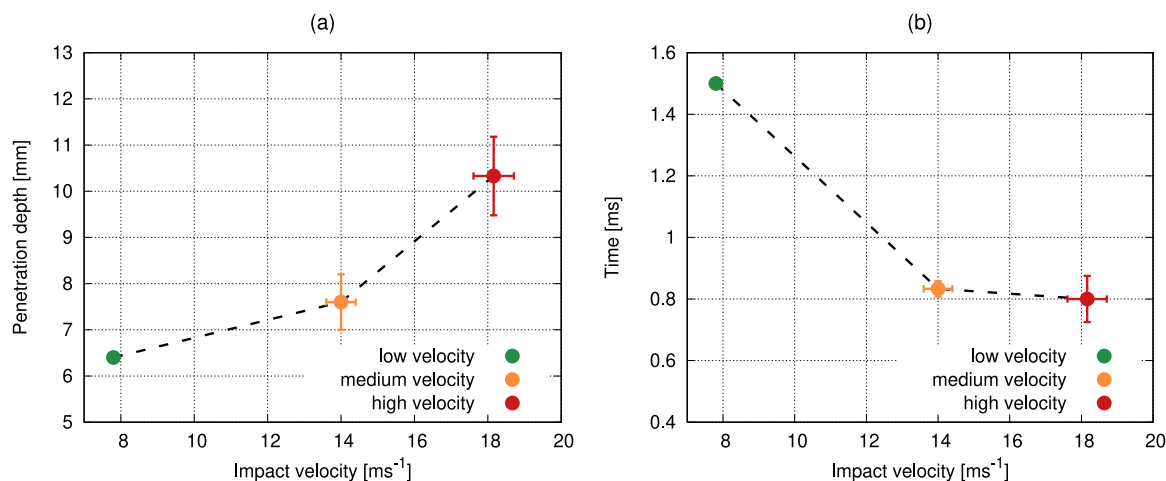


Fig. 10. (a) Penetration depth, where the disintegration of the APM foam occurred, plotted against the initial impact velocity. (b) The time, when the disintegration of the APM foam occurred, plotted against the initial impact velocity.

3.4. Wave propagation velocity and dynamic forces equilibrium

The wave propagation velocity and convergence of the dynamic forces at both faces of the specimen were analysed to investigate the possible differences that could be attributed to the wave propagation and mechanical impedance of the material. Two parameters were evaluated: (i) the wave propagation time through the specimen, (ii) the time of the specific convergence of the dynamic forces. The wave propagation time was calculated as the delay between the detection of the incident and the transmission force. This parameter represented the wave propagation time (speed of sound) in the material. The specific convergence of the dynamic forces was evaluated at the earliest time, when the transmission force was equal to the incident force. For all the materials, the wave propagation time remained similar at all the impact velocities, whereas the specific convergence of the dynamic forces occurred earlier at the medium and the high impact velocity. Thus, the equilibrium of the dynamic forces was achieved in a shorter time than in the case of the low impact velocity. As the wave propagation time remained approximately constant for all the impact velocities and was much lower than the specific convergence, the stress wave in the specimen had to be dispersed more through the volume of the specimen at the low impact velocity and more localised at the two higher velocities. The specific convergence of the dynamic forces for the closed-cell aluminium foam is shown in Fig. 11a, in Fig. 11b (for the hAPM foam), and in Fig. 11c (for the APM foam).

3.5. XCT results

3.5.1. Closed-cell foam

The differential XCT analysis of the closed-cell foam sample was performed on the basis of both the subtraction of the volumes and using the blending of the volumes due to the different characteristics of the closed-cell foam internal structure. Here, the subtraction of the loaded volume from the 3D image of the intact state can be used to isolate the porous microstructure under the final position of the impactor, as the unloaded volume subtracted from the 3D image of the impacted state allows one to evaluate the differences along the path of the impactor. Still, particularly the damaged parts of microstructure in the vicinity of the penetrating bar and around the compacted region shown in the following paragraphs remained hidden. This was caused partially due to the different intensity range of both volumes caused by the stacked imaging of the multiple samples at a time leading to a considerably low signal-to-noise ratio in the 3D images after subtraction. Fig. 12 depicts the 3D visualization of the impacted specimen, which is simply combined with the aligned volume of the intact specimen.

In Fig. 12, the penetrated volume is light-grey, the material of the intact foam prior to the mechanical testing is dark-red and the graphical elements are included for better orientation. The figure on the left shows half of the foam specimen obtained by performing a sectioning in the medial plane with the viewpoint set to capture the path of the impactor and the figure on the right is the direct view on the medial-plane section. The amber graphics represents the geometry of the penetrating bar and the cyan ellipses highlight the visible interesting features in the microstructure of the penetrated volume. Because of the microstructure constituted by the thin cell-struts from a homogeneous metal alloy, the formation of a damaged envelope caused by the deformation energy concentrated directly under the impacting bar can hardly be identified. Hence, the 2D visualizations of the slices through the reconstructed volume in the medial and transversal plane were studied, see Fig. 13(a–c) and (d,e).

Fig. 13(a–c) shows the slices in the medial plane in the intact and loaded specimen together with the slice in the blended volume. The amber graphics depicts the projection of the impacting cylinder in the medial plane, i.e., the vertical lines correspond to the edge on the circular face of the impactor, while the horizontal lines depict the diameter of the bar. No deflection of the opposite, non-impacted, circular face of the specimen was observed in the image of the impacted specimen indicating that the concurrence of the closed-cell metal foam microstructure and the integral metal skin resulted in the strain-wave propagation into the transmission bar without plastic damage to the surrounding parts of the microstructure. The image of the impacted specimen also shows how the penetrating bar damaged the porous microstructure around the circumference of the bar that led to the failure of the cell-struts and the opening of the pores in the vicinity of the bar. However, more details are revealed by analysing the blended volume (Fig. 13), where the white colour represents the air contained in the pores. The microstructure of the impacted specimen is shown in black, and the microstructure within the intact specimen is depicted in grey. The cyan line highlights the void regions formed as a result of the bar penetration into the specimen showing the extent of the open volume significantly exceeding the bar dimensions. It can be seen that the dimensions of the damaged region gradually increase with the penetration depth and continue up to 4 mm below the final penetration depth achieved in the experiment. The shape of the resulting cavity shows significant localised shear-stress induced damage leading to approximately an 11 ° deviation of the failed cell-struts region from the axis of penetration. The region of densified foam structure composed in the majority of collapsed cells then forms the deformed envelope of the microstructure having a cylindrical geometry in this case. Its boundaries can be clearly seen in the blended volume

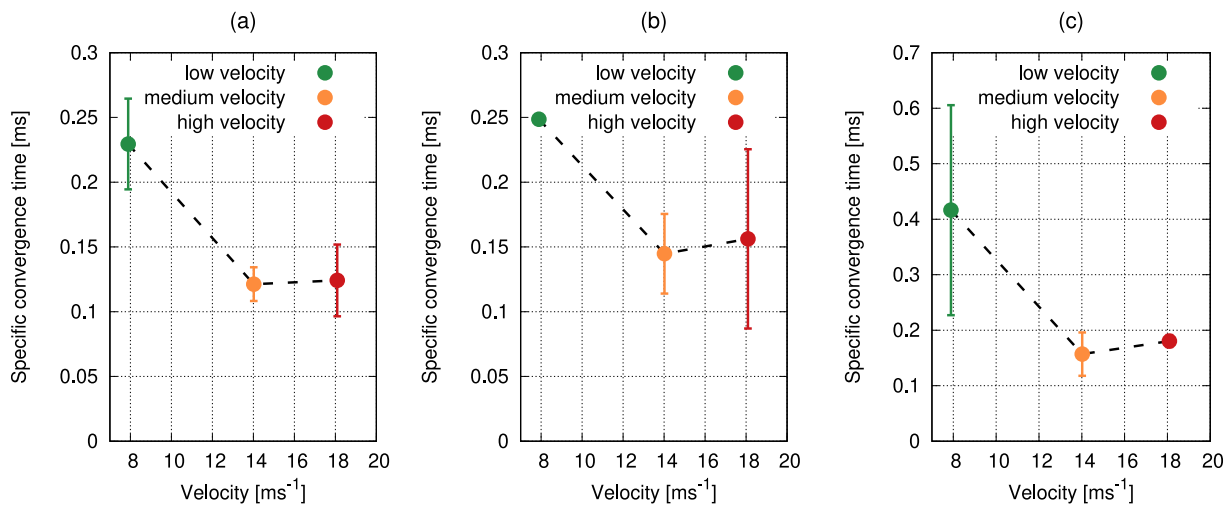


Fig. 11. Specific convergence time of the dynamic forces: (a) the closed-cell aluminium foam, (b) the hAPM foam, (c) the APM foam.

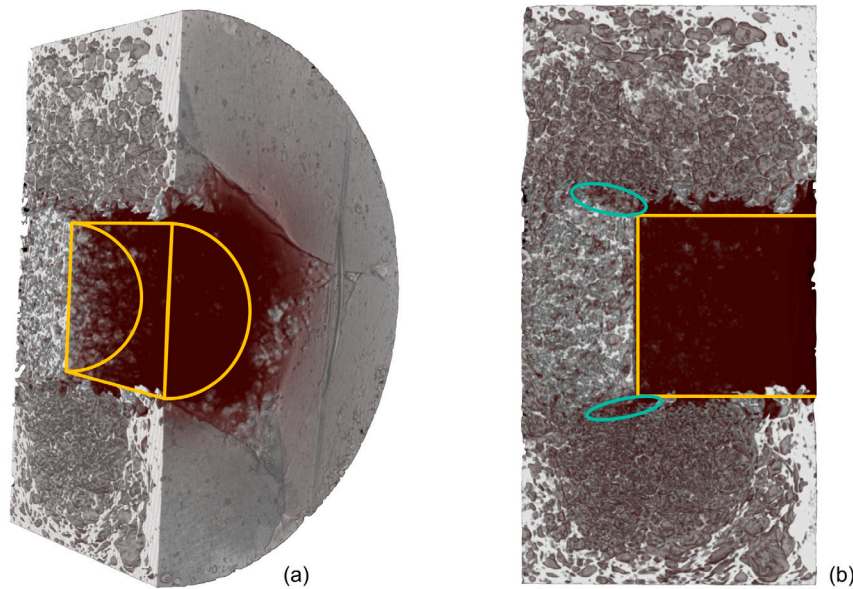


Fig. 12. Perspective 3D visualisation of penetrated closed-cell foam sample showing overlapping penetrated sample (light-grey) and the influenced volume (dark-red) - view along the penetrating bar (a) and visualization in the medial plane (b). (For interpretation of the references to colour in this figure legend, the reader is referred to the web version of this article.)

as the region with the smallest cell-volume under the impactor. The cyan graphics around the bar projection near the impacted face of the specimen show the plastic deformation of integral metal skin developed during the bar penetration resulting in a 28.4mm outer diameter of the opening. However, the conclusions made only from the analysis of the visualisation in the medial plane may be misleading due to the stochastic nature of the material microstructure. Thus, the blended volume was additionally investigated in the transversal plane as shown in Fig. 13(d,e). The left slice is located 1.3mm above and the right slice is located 0.3mm under the final position of the bar. The amber graphics depict the circumference of the impacting bar and the cyan curves highlight the void space around the impactor in the left slice and around the deformed envelope in the right slice. It can be seen that both the geometry of the void space created by the impacting bar is relatively uniform with the diameter of the circle approximating the void space boundaries of 24mm. Except for the 90° sector in the top-left direction, the dimensions of the impacting bar in the region of the accumulated material near the final penetration depth are not

exceeded by the homogeneous material and only local protrusions can be observed.

3.5.2. hAPM foam

The differential XCT analysis of the hAPM foam sample and the visualisation of the results was performed from the blended volume, because the subtraction of the reference and deformed volume resulted in a very low signal-to-noise ratio in the 3D image due to the presence of epoxy matrix in the microstructure. Unlike the closed-cell metal foam sample, where the complex microstructure composed of a high number of cells makes the interpretation difficult, the effects induced by the medium-rate dynamic impact into the hAPM foam can also be studied from the sections in the 3D reconstructed image of the loaded state as depicted in Fig. 14.

In Fig. 14, the approximate dimensions of the impacting bar in its final position after penetration are provided graphically using the amber contours. Since the visualisation is derived from the full intensity range, it is interesting to study also the possible changes in the epoxy

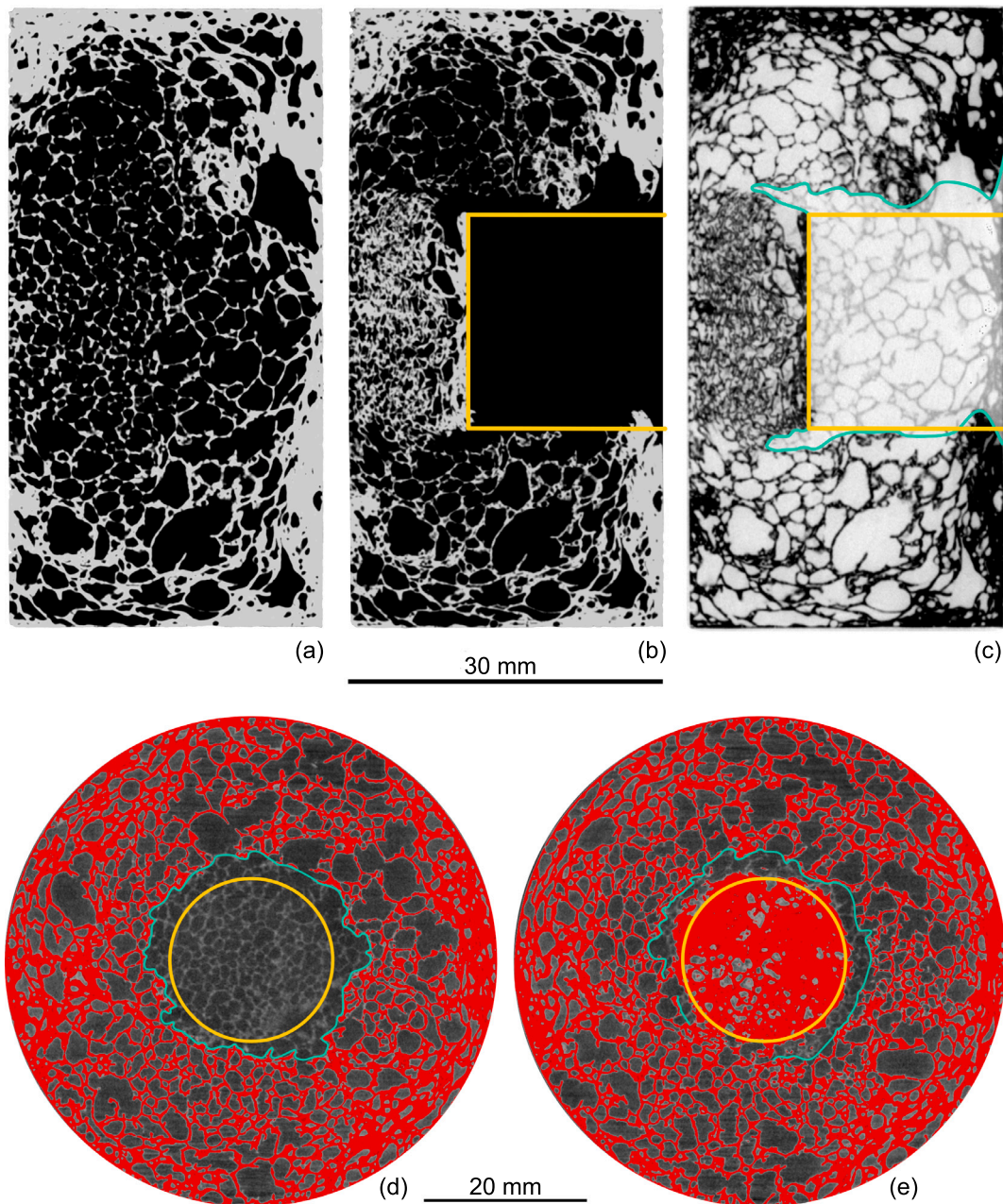


Fig. 13. 2D visualisation of the closed-cell foam sample: medial plane of the intact specimen (a), impacted specimen (b), and blended volume (c), blended volume in the transversal plane in the penetrated region (d) and under the final position of the impactor (e).

matrix. By comparing the appearance of the region directly under the impactor and in the volume around its outer edges, it can be seen that the region under the impactor exhibits a higher material density, where the extent of the region of the compacted matrix is depicted by the cyan colour. The highlighted geometry of the compacted region can be assumed to be approximately spheroid in the whole volume with the circle representing the intersection of the cylindrical impactor with the compacted region forming a spherical dome geometry. However, due to the homogeneity of the epoxy matrix, the microstructural changes in the vicinity of the impactor cannot be studied using the 3D visualisation of the reconstructed 3D images. For this reason, 2D visualisations of the slices through the reconstructed volume in the medial and transversal plane were studied, see Fig. 15(a–c) and (d,e).

The Fig. 15(a–c) shows the slices in the medial plane in the intact and loaded specimen together with the slice in the blended volume. The

amber graphics depict the projection of the impacting cylinder in the medial plane. In the visualisation of the intact specimen, an apparent 2.5 mm deflection of the right impacted face of the sample influencing the evaluation of the mechanical results is apparent aside from the aluminium sphere distribution and the voids in the epoxy matrix. In the image of the impacted specimen, the cyan graphical elements depict the identified 0.75 mm deflection of the opposite, non-impacted, circular face of the specimen. The same material density (image intensity) variations in the epoxy matrix under the final position of the impactor observed in the 3D visualisation are also apparent, although the projected geometry is closer to a wedge rather than an elliptical or circular section. Further details are revealed though when the blended volume is analysed. The blue line precisely depicts the compacted region under the impactor, which exhibits a circular shape except for the lobes near the positions corresponding to the radius of the bar. However, the shape

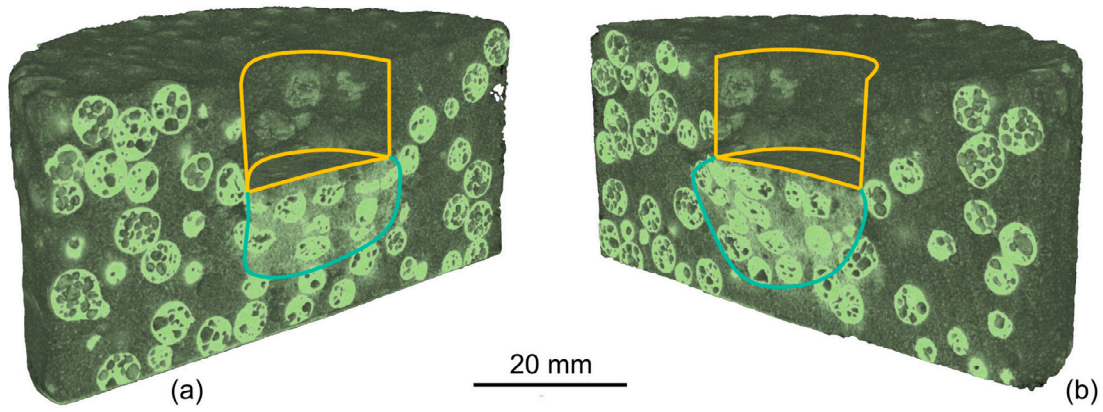


Fig. 14. Perspective 3D visualisation of the penetrated hAPM foam sample showing the medial (a) and frontal (b) plane sections through the volume of the sample.

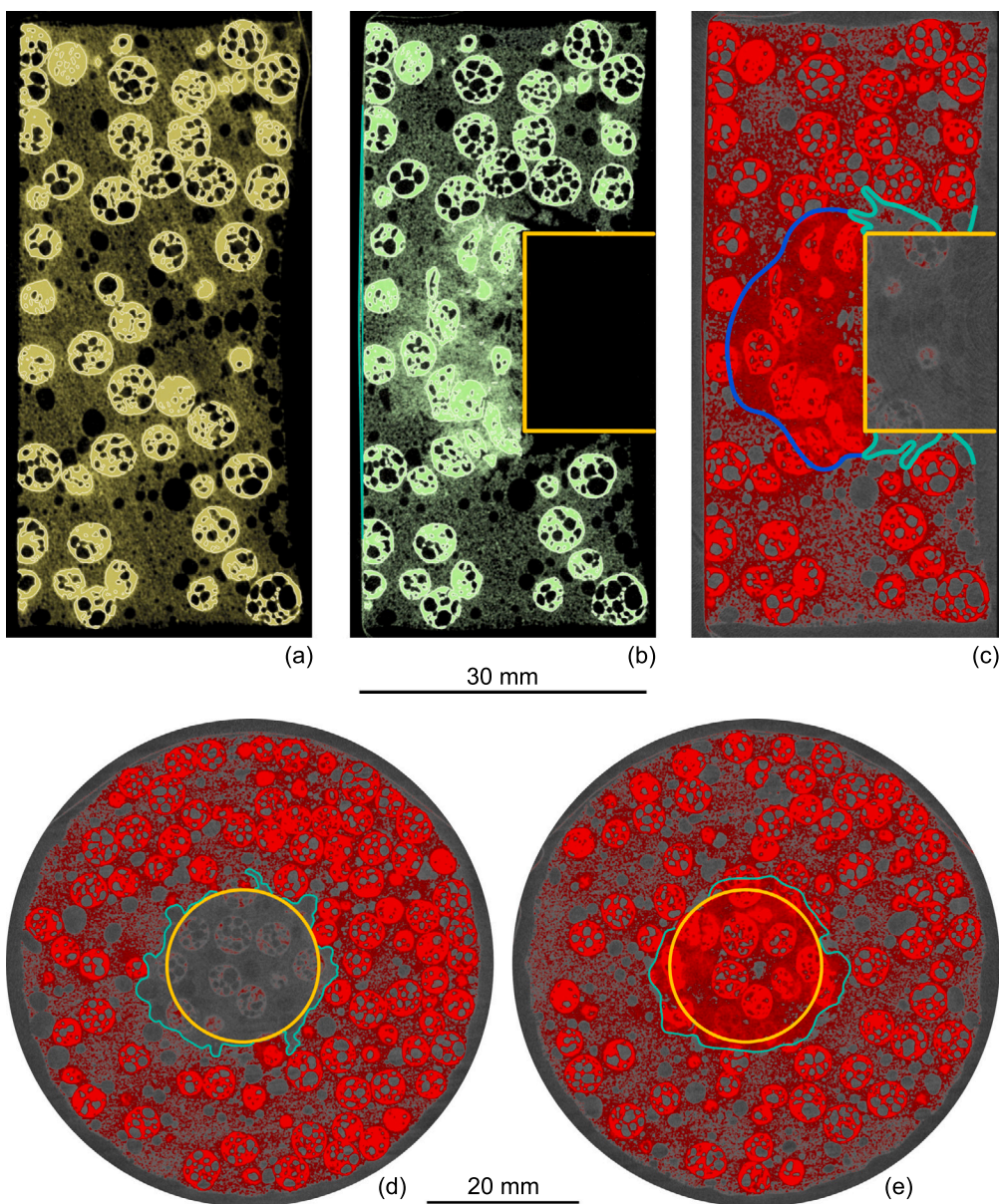


Fig. 15. 2D visualisation of the hAPM foam sample: the medial plane of the intact specimen (a), impacted specimen (b), and blended volume (c), the blended volume in the transversal plane in the penetrated region (d) and under the final position of impactor (e). (For interpretation of the references to colour in this figure legend, the reader is referred to the web version of this article.)

of the compacted region is, in this case, apparently influenced by the displaced and deformed aluminium spheres causing a more complex material response to the impact. The cyan graphics highlight, in this figure, the void regions formed as a result of the bar penetration into the specimen. The total diameter of the open volume after loading not only significantly exceeds the bar dimensions, but the shape of the cavity also shows a significant localised shear-stress induced damage of the epoxy matrix geometrically similar to the shock-wave propagation characteristics. The damage evolution is concentrated along with two apparent directions and the cavity formation, in either case, is stopped by the presence of the aluminium spheres. The two vertices of the void closer to the impacting bar reaching the depth under the final position of the impactor then undergo a smooth transition into the deformed envelope of the matrix circumventing the displaced aluminium spheres similarly to the deformed envelope region itself. Furthermore, the cyan graphics around the bar projection near the impacted face of the specimen show plastic deformation of the matrix developed during the bar penetration resulting in a plasticised area with a diameter of 25.9 mm. However, the conclusions made only from the analysis of the visualisation in the medial plane may be misleading due to the stochastic nature of the material microstructure. Thus, the blended volume was investigated in the transversal plane as shown in Fig. 15(d,e). The left slice is located 1.8 mm above and the right slice is located 2.0 mm under the final position of the bar. The amber graphics depict the circumference of the impacting bar and the cyan curves highlight the void space around the impactor in the left slice together with the extent of the deformed envelope in the right slice. It can be seen that the geometry of both the void space created by the impacting bar and the deformed envelope under its face strongly depends on the angular position of the section used to visualise the internal structure in a perpendicular direction.

4. Discussion and conclusion

The results of the OHPB based dynamic penetration tests lead to the following findings and remarks:

- A straightforward wave separation technique was employed to evaluate the forward and backward propagating waves in the setup and allowed for the investigation of the deformation behaviour over a longer time window. In all the conducted experiments, the wave separation technique provided valid and precise results for a number of wave reflections. The separation was always successful, at least, until the end of the experiment, i.e., to the point when the impact velocity decreased to zero. Using the utilised instrumentation, the wave propagation analysis during the penetration process was possible even at impact velocities close to 20 ms^{-1} . If the distance between the impact face and the strain-gauge is sufficient to form a homogeneous strain-wave, the method can be used for the instrumented testing with different types of impactors. For the incident bar used in the experiments, the inverse of the introduced wave separation method could be used to process the DIC data and roughly estimate the actual force by reconstructing the wave propagation behaviour in the bar. However, this was not possible for shorter striker bars as the individual waves in the bar could not be identified.
- The wave propagation through the specimens played a crucial role in the deformation mode of the tested cellular materials and had a significant influence on the corresponding force–displacement diagrams as well as on the energy absorption characteristics. Based on the acquired results, the wave propagation and dispersion effects are considered more important at low impact velocities. All the tested materials exhibited the longest time to specific force convergence (equal incident and transmission force) at the lowest impact velocity where the effects of wave dispersion are more pronounced, while the strain wave

propagates approximately homogeneously throughout the volume of the sample without localisation under the impactor. Some specimens of the APM foam and the hAPM foam did not reach the specific force convergence during the whole impact. The time of the specific convergence decreased for all the materials at higher impact velocities and the highest values of the specific time convergence were observed for the APM foam. The APM foam exhibited the lowest mechanical impedance related to its structure with hollow spheres embedded in the weak matrix. The significant increase in the wave convergence time was observed between the medium and high impact speed scenario, which can be attributed to the dynamic nature of the loading, where the time-to-convergence is typically proportional to the impact speed.

- All the materials exhibited a certain level of decrease in the penetration force in the initial penetration phase with an increasing impact velocity, which is a disadvantageous property in terms of the impact protection capabilities. This effect was the most pronounced in the case of the closed-cell foam and it had a crucial influence on its deformation behaviour particularly at low impact velocities. On the other hand, the effect was marginal for the APM foam and the hAPM foam as the standard deviations of the piercing force partially overlap. In general, the closed-cell metal foam exhibited deformation behaviour common to standard metal foams showing a significant plateau region (after the initial phase of the penetration), whereas the other two composite materials exhibited approximately a linear dependency of the penetration force with the penetration depth. Although the hAPM foam did not exhibit a plateau region, its energy absorption capability was comparable with the closed-cell foam despite its lower mass density, while the penetration force was only slightly higher.
- The effect of wave propagation was the most significant for the closed-cell aluminium foam, where the penetration force in the initial phase was the highest for the lowest impact velocity. This finding, not observed in the dynamic compression of the material [12,16] and even in the dynamic penetration of the similar materials without an integral skin over the foam core [46,55], was found to be connected with the damage mechanisms on the surface of the specimen and wave propagation through its volume. During the penetration at low velocity, the integral skin over the core of the specimen was penetrated smoothly (or the skin was not perforated at all), the deformation was not localised to the close vicinity of the projectile but rather spread out through the front face of the specimen and the stress wave was more dispersed through the volume of the specimen. With the increasing impact velocity, this effect was suppressed and the force–displacement relationship was closer to the standard behaviour of the closed-cell aluminium foam. The surface skin was penetrated abruptly and the wave propagation was very localised. A similar behaviour was described for the penetration of the compact as well as the sandwich panels [93]. In such a case, the transition velocity defining the change in the deformation behaviour from transient to more localized can be identified. The transition velocities for standard materials are much higher than those observed in our case. However, the values identified in the experiments were in good agreement with the energy-related change in the behaviour described in the literature [57] and with studies analysing shock and wave propagation localised behaviour [13,29]. The findings are not contrary to the studies characterising the closed-cell foams during dynamic penetration [46,55] as well as in dynamic compression [13,29,55]. After the initial penetration phase, similar effects were observed.

Therefore, in our opinion, the behaviour observed in the first part of the penetration is related to the presence of the skin over the foam. We used the data from the overview high-speed camera to investigate the surface area affected during the impact. The representative case of the specimen penetrated at the low impact

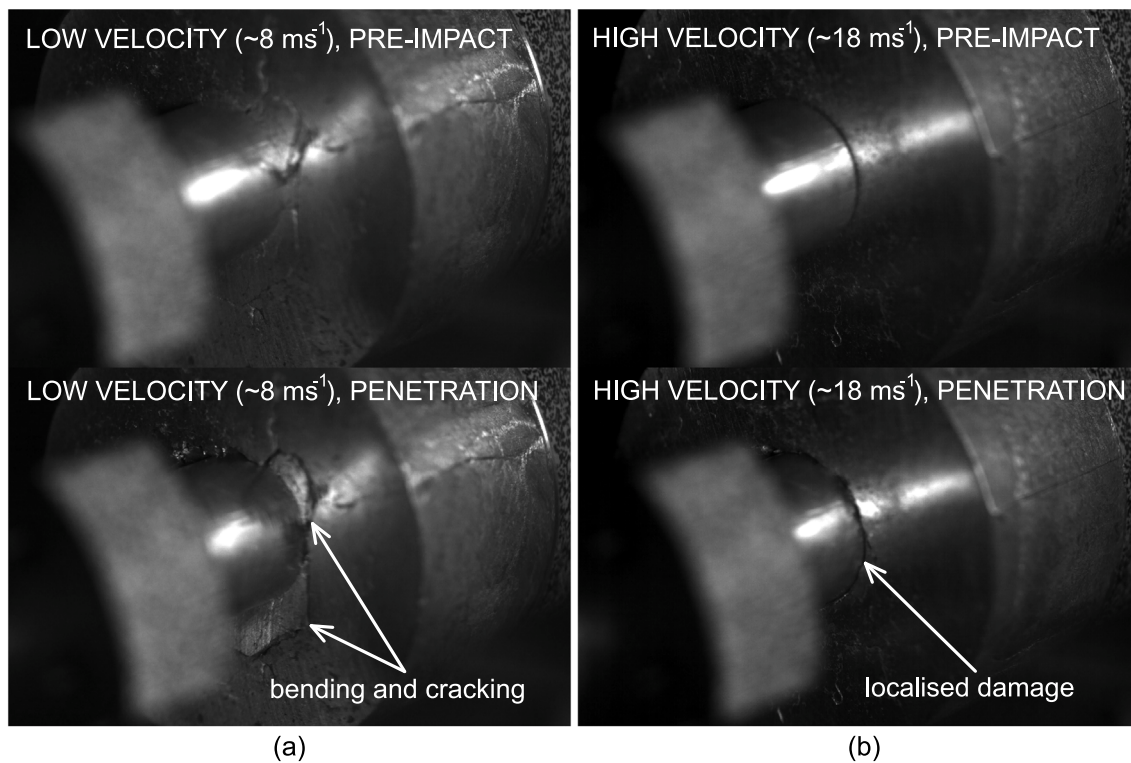


Fig. 16. The representative case of the closed-cell aluminium foam specimen penetrated at: (a) the low impact velocity compared with (b) the specimen penetrated at the high impact velocity. Note the affected area during the impact at low velocity.

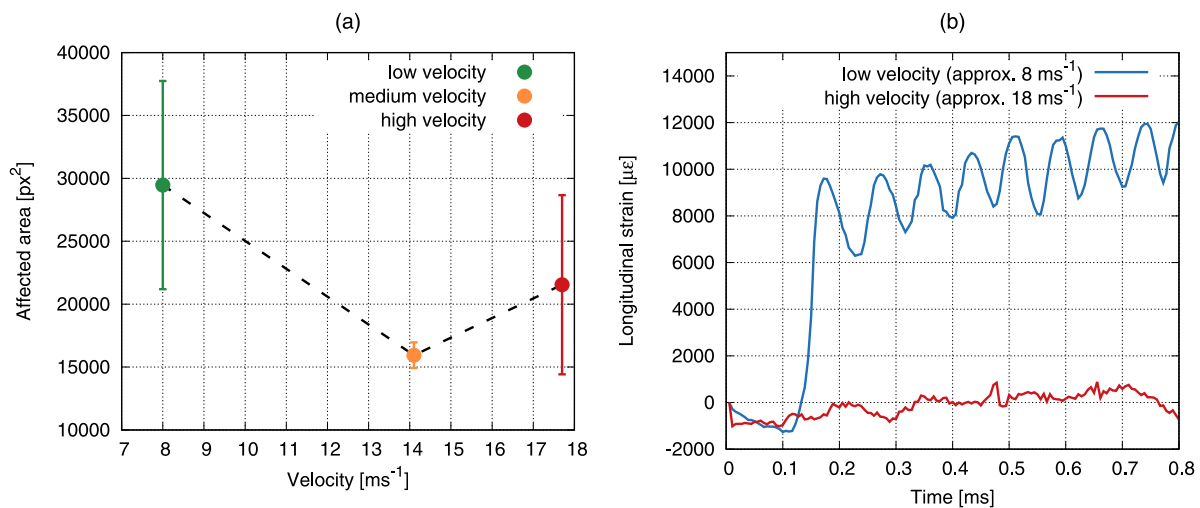


Fig. 17. (a) Size of the area at the front face of the specimen affected by the impact. (b) Longitudinal strain evaluated using the DIC on the surface of the closed-cell aluminium foam specimen at two different impact velocities.

velocity is compared with the specimen penetrated at the high impact velocity in Fig. 16. The affected area was determined as the area with the visibly changing front face of the specimen during the impact. An in-house script was developed to identify the changes on the front face of the specimen. As can be seen in Fig. 17a, the identified affected area is significantly larger for the lower impact velocity than for the other two velocities. The increased affected area at the low-velocity impact supports the conclusion that the higher strength of the closed-cell aluminium foam at the low impact velocity is related to the wave propagation and dispersion through the specimen volume while, at the higher velocities, the wave propagation is more localised under the

penetrating projectile. During most of the impacts at low velocity, the front face was not penetrated, but rather bent inwards. Furthermore, DIC was used to identify the longitudinal strain on the specimen's surface. A grid of correlation points was established on the surface of the specimen and the incremental longitudinal strain was evaluated using the calculated displacements. As can be seen in Fig. 17b, the longitudinal strain is non-zero in the case of the penetration at the low impact velocity, whereas no longitudinal strain was identified in the specimen penetrated at the high impact velocity. This finding supports the conclusion that with the increasing velocity, the penetration is more localised and concentrated under the impacting

object, whereas at the low impact velocity, the whole specimen is deformed to some extent.

- In terms of the ability of the investigated materials to perform as a protection against an object penetrating their microstructure, the closed-cell aluminium foam remained compact and was able to effectively absorb the impact energy at all the tested impact velocities. The APM foam was found to be unsuitable for penetration protection as the material exhibited a strong tendency to disintegrate at medium and high velocities. The weak matrix cannot withstand the loads and the material was predominantly damaged by the separation at the boundaries. Inertia effects also played a crucial role during the penetration of the specimens. The penetration depth at the disintegration of the APM foam increased with the impact velocity. However, the time to disintegration was approximately constant for both the medium and the high impact velocity. Therefore, the higher penetration depth at the disintegration was related to the inertia effects as a given period of time was necessary to disintegrate the specimen. The increase in load capacity of the APM foam with the impact velocity was related only to the dynamic nature of the testing as the inertia prevented its immediate disintegration, when the maximum load capacity was exceeded.
- The closed-cell foam sample and the hAPM sample were successfully subjected to the differential CT procedure for a detailed analysis of the microstructural variations resulting from the bar dynamically penetrating through the internal structure of the materials. It was possible to quantify the shape and dimensions of the cavity created by the impacting bar and the related effects resulting from strain-wave propagation through the specimen and also the characteristics of the deformed envelopes formed under the final position of the penetrator. However, it is evident that a complex XCT imaging campaign should be performed to preferably include the intact-impacted specimen pairs from all the performed penetration experiments, i.e., the quasi-static and all the dynamic impacts, to obtain thorough information on the deformation processes present during the loading procedures. Here, our initial assumption that the differential CT of the specimens subjected to the intermediate impact speed would be capable of revealing the relevant deformation mechanisms in the penetrated materials was not confirmed and particularly the tomographical analysis of low-velocity penetration would bring important advantage in the interpretation of mechanical and DIC results.
- In the closed-cell foam sample, the uniform homogeneous porosity distribution was observed only in the core region of the samples, while the integral metal skin not only caused a significant increase in the complexity of the deformation process by introducing different mechanisms of load transfer in dependence to the impact speed, but also the porosity in the majority of the sample volume was affected. The blending procedure of the intact and impacted volume provided hard evidence on the difference between the truly displaced or damaged cell-struts and the pores that were only opened by the penetrating bar. It can be also noticed that the two vertices of the void at the maximum depth of the opened cavity smoothly circumvent the densified envelope providing information about the strain wave path during the loading. The inspection of either the impacted or the blended volume shows that material is accumulated along the circular face of the impactor and around its edges, which is a combination of the metal skin itself separated from the face during the bar contact with the specimen and the cell-wall material gathered during the penetration of the bar. It can be reasonably assumed that this material accumulation is a mechanism supporting the shear failure of the individual cell-struts as the effective diameter of the impactor (i.e., the diameter of the bar is enlarged gradually by the gathered material) increases along its path.
- The deformation response of the hAPM foam sample was influenced by the non-uniform distribution of aluminium sphere particle reinforcement in the epoxy matrix, where a higher sphere density was observed near the outer edges of the specimen, outside of the penetrated region. However, the differential CT showed that the presence of the aluminium spheres in the matrix acted as a barrier shaping the propagation of the strain-wave through the specimen and that it was a factor, which can be successfully utilised to control the deformation response of such a material. In the tomographical images of the impacted volume, the observed intensity variation in the matrix under in the impactor is also independent to the displaced aluminium spheres originally distributed in the penetrated volume as only a negligible low-energy photon scatter was present in the acquired projections. Thus, it can be assumed that such a region represents the result of the kinetic energy dissipation into the impacted material resulting in the compaction of the matrix. Furthermore, it can be inferred from these results that the aluminium spheres effectively shape and resist the wave propagation in the material, while mitigating the energy by their plastic deformation in the region under the impacting bar. The boundaries of the deformed envelope under the impactor are largely hidden by the presence of plastically deformed aluminium spheres and only a rough estimation is possible from the 2D visualisations. In contrast, a 2D transverse visualisation is a useful tool for the evaluation of the void space geometry as shown by its boundaries depicted by the cyan curve in the Fig. 15d. In this visualisation orientation, the apparently larger amount of the aluminium spheres is concentrated right from the vertical axis of symmetry. The presence of the aluminium spheres and their influence on the formation of the void region can be successfully studied. When the comparing cyan highlighted regions left and right from the vertical axis of symmetry, only one continuous void was created in the region containing only the epoxy matrix without the sphere reinforcement. On the other side, three isolated regions were created and in every case, the extent of the void space was limited by the presence of the reinforcement. This supports the previous finding that the aluminium sphere reinforcement in the hAPM foam and its distribution can be used to control the transmission of the strain wave through the microstructure and influences the foam's deformation energy absorption capacity.
- Using the combination of mechanical testing, the optical inspection of the specimens, the DIC evaluation of the optical data, and the XCT analysis, it has been demonstrated that the investigated materials are more susceptible to penetration with an increase in the impact speed, which is related to the shorter wave propagation times due to the deformation and damage localised in the vicinity of the impacting object. The impactor then penetrates the microstructure to a higher depth, while the surrounding material remains intact and has no influence on the mechanical response of the samples. Owing to the epoxy matrix and the distribution of the aluminium spheres, only the hAPM foam showed an increase in the dissipated deformation energy with the high impact velocity despite the inversely proportional dependency of the absorbed energy at the depth of 3.5 mm on the impact velocity. The APM foam, composed of aluminium spheres with point-like connectivity given by the polyamide matrix, was observed to be prone to disintegration resulting from the shear stress and inertia effects induced damage to the matrix disqualifying the material in the current state from its use in the deformation energy mitigation measures. However, the confinement of the APM foam in an appropriate encasement would change the deformation characteristics considerably. In the same sense, the closed-cell foam exhibited a measurable dependence on the results of the impact velocity as a result of the influence of the metal skin. Similarly, the modification of the metal skin properties making

it functional in the stress distribution also in the higher impact velocities would significantly improve the overall performance of the closed-cell foam in the considered loading scenarios. Nevertheless, based on the high-resolution XCT and the differential CT procedures, it has been shown that the results can be used, in the case of both the closed-cell foam and hAPM foam, for the improvement of the production processes as the radiographical inspection of the internal structure pointed out problems arising from the limited control of the production process. In the case of the APM foam modified with the outer confining layer, the XCT evaluation would also be an essential tool for the inspection of its microstructure both before and after the impact loading.

Conclusion

The modified OHPB with the full two-sided instrumentation was used to penetrate the specimens at three different impact velocities ranging from 8 ms^{-1} to 18 ms^{-1} . The wave separation technique was employed to process the strain-gauge signals and to extend the useable time window of the Hopkinson bar experiment to cover the entire duration of the impact. The wave propagation phenomena, inertia effects, energy absorption and localisation of the damage were investigated in detail for all the types of the tested materials. It was found out that the time required for the convergence of the dynamic forces at both faces of the specimen was the highest for the lowest impact velocity. This effect was related to the wave propagation in the specimen as, at low impact velocities, the stress-wave was more dispersed through the volume of the specimens. With an increasing impact velocity, the damage was more localised underneath the projectile. This effect was the most profound for the closed-cell aluminium foam with an integral skin covering the foam core. During the initial phase of the penetration at low velocities, the wave propagation related effects were considered more important than the other effects such as possible strain-rate sensitivity of the material. Inertia effects also play an important role as, e.g., the APM foam disintegrated with an increasing impact velocity at higher penetration depths. However, it was identified that this behaviour was related to the inertia effects preventing the immediate disintegration of the specimen, when its loading capacity was exceeded. A differential XCT was successfully employed for a pre- and post-impact volumetric analysis of the specimens and supported the conclusions evaluated using the strain-gauge and DIC data. Altogether, the discussed effects can significantly affect the strength and deformation behaviour of the cellular materials during dynamic indentation, where the complex loading of the structure is different than during the dynamic uni-axial loading.

CRedit authorship contribution statement

Jan Šleichrt: Conceptualization, Investigation, Supervision. **Tomáš Fíla:** Conceptualization, Methodology, Writing - original draft. **Petr Koudelka:** Investigation, Writing - original draft. **Marcel Adorna:** Investigation, Visualization. **Jan Falta:** Investigation, Visualization. **Petr Zlámal:** Investigation, Visualization. **Jonathan Glinz:** Investigation. **Michaela Neuhäuserová:** Writing - original draft. **Tomáš Doktor:** Writing - review & editing. **Anja Mauko:** Resources, Writing - review & editing. **Daniel Kytýř:** Resources, Writing - review & editing. **Matej Vesenjāk:** Resources, Writing - review & editing. **Isabel Duarte:** Resources, Writing - review & editing. **Zoran Ren:** Resources, Writing - review & editing. **Ondřej Jiroušek:** Writing - review & editing.

Declaration of competing interest

The authors declare that they have no known competing financial interests or personal relationships that could have appeared to influence the work reported in this paper.

Data availability

The raw/processed data required to reproduce these findings cannot be shared at this time due to technical or time limitations.

Acknowledgements

The authors acknowledge the financial support from the Operational Programme Research, Development and Education in the project INAFYM (CZ.02.1.01/0.0/0.0/16_019/0000766), the Czech Science Foundation (project no. 19-23675S), Slovenian Research Agency (research core funding No. P2-0063) and the projects UIDB/00481/2020 and UIDP/00481/2020 - FCT - Fundação para a Ciência e a Tecnologia; and CENTRO-01-0145-FEDER-022083 - Centro Portugal Regional Operational Programme (Centro2020), under the PORTUGAL 2020 Partnership Agreement, through the European Regional Development Fund. The internal support of Ph.D. students (projects no. SGS19/123/OHK2/2T/16 and SGS20/141/OHK2/2T/16) is acknowledged as well.

Appendix A. Supplementary data

Supplementary material related to this article can be found online at <https://doi.org/10.1016/j.msea.2020.140096>. In the supplementary files, the technical detail of the SHPB setup calibration or quasi-static response of the tested materials can be found. Also, representative animations of the penetration process of each type of the material are appended.

References

- [1] Lorna J. Gibson, Michael F. Ashby, *Cellular Solids: Structure and Properties*, Cambridge University Press, 1999.
- [2] J. Zhang, Q. Qin, S. Chen, Y. Yang, Y. Ye, C. Xiang, T.J. Wang, Low-velocity impact of multilayer sandwich beams with metal foam cores: analytical, experimental, and numerical investigations, *J. Sandw. Struct. Mater.* 22 (3) (2020) 626–657.
- [3] X. Tan, B. Wang, Y. Yao, K. Yao, Y. Kang, S. Zhu, S. Chen, P. Xu, Programmable buckling-based negative stiffness metamaterial, *Mater. Lett.* 262 (2020).
- [4] P. Jiao, S.M. Nicaise, M. Azadi, J. Cortes, D.E. Lilley, W. Cha, P.K. Purohit, I. Bargatin, Tunable tensile response of honeycomb plates with nanoscale thickness: testing and modeling, *Extreme Mech. Lett.* 34 (2020).
- [5] Y. Jiang, Z. Liu, N. Matsuhisa, D. Qi, W.R. Leow, H. Yang, J. Yu, G. Chen, Y. Liu, C. Wan, Z. Liu, X. Chen, Auxetic mechanical metamaterials to enhance sensitivity of stretchable strain sensors, *Adv. Mater.* 30 (12) (2018).
- [6] J. Lankford Jr., K.A. Dannemann, Strain rate effects in porous materials, in: *Materials Research Society Symposium - Proceedings*, Vol. 521, 1998, pp. 103–108.
- [7] R. Smerd, S. Winkler, C. Salisbury, M. Worswick, D. Lloyd, M. Finn, High strain rate tensile testing of automotive aluminum alloy sheet, *Int. J. Impact Eng.* 32 (1–4) (2005) 541–560.
- [8] M. Vesenjāk, C. Veyhl, T. Fiedler, Analysis of anisotropy and strain rate sensitivity of open-cell metal foam, *Mater. Sci. Eng. A* 541 (2012) 105–109.
- [9] G. Imbalzano, P. Tran, T.D. Ngo, P.V.S. Lee, Three-dimensional modelling of auxetic sandwich panels for localised impact resistance, *J. Sandw. Struct. Mater.* 19 (3) (2017).
- [10] Yoshihiko Hangai, Naoyuki Kubota, Takao Utsunomiya, Hisanobu Kawashima, Osamu Kuwazuru, Nobuhiro Yoshikawa, Drop weight impact behavior of functionally graded aluminum foam consisting of A1050 and A6061 aluminum alloys, *Mater. Sci. Eng. A* 639 (2015) 597–603.
- [11] V.S. Deshpande, N.A. Fleck, High strain rate compressive behaviour of aluminium alloy foams, *Int. J. Impact Eng.* 24 (3) (2000) 277–298.
- [12] M. Peroni, G. Solomos, V. Pizzinato, Impact behaviour testing of aluminium foam, *Int. J. Impact Eng.* 53 (2013) 74–83, Special issue based on contributions at the 3rd International Conference on Impact Loading of Lightweight Structures.
- [13] Pengfei Wang, Songlin Xu, Zhibin Li, Jinglei Yang, Chao Zhang, Hang Zheng, Shisheng Hu, Experimental investigation on the strain-rate effect and inertia effect of closed-cell aluminum foam subjected to dynamic loading, *Mater. Sci. Eng. A* 620 (2015) 253–261.
- [14] Marco Peroni, George Solomos, Norbert Babcsan, Development of a hopkinson bar apparatus for testing soft materials: application to a closed-cell aluminum foam, *Materials* 9 (1) (2016) 27.
- [15] R.P. Merrett, G.S. Langdon, M.D. Theobald, The blast and impact loading of aluminium foam, *Mater. Des.* 44 (2013) 311–319.

- [16] Xin Pang, Hejun Du, Dynamic characteristics of aluminium foams under impact crushing, *Composites B* 112 (2017) 265–277.
- [17] Sergey L. Lopatnikov, Bazle A. Gama, Md. Jahirul Haque, Carl Krauthaus, John W. Gillespie, Mustafa Guden, Ian W. Hall, Dynamics of metal foam deformation during Taylor cylinder–Hopkinson bar impact experiment, *Compos. Struct.* 61 (1) (2003) 61–71.
- [18] Masatoshi Nishi, Shigeru Tanaka, Matej Vesenjak, Zoran Ren, Kazuyuki Hokamoto, Experimental and computational analysis of the uni-directional porous (unipore) copper mechanical response at high-velocity impact, *Int. J. Impact Eng.* 136 (2020) 103409.
- [19] R. Rajendran, A. Moorthi, S. Basu, Numerical simulation of drop weight impact behaviour of closed cell aluminium foam, *Mater. Des.* 30 (8) (2009) 2823–2830.
- [20] M. Altenajji, Z.W. Guan, W.J. Cantwell, Y. Zhao, G.K. Schleyer, Characterisation of aluminium matrix syntactic foams under drop weight impact, *Mater. Des.* 59 (2014) 296–302.
- [21] A. Paul, U. Ramamurthy, Strain rate sensitivity of a closed-cell aluminum foam, *Mater. Sci. Eng. A* 281 (1) (2000) 1–7.
- [22] G.W. Ma, Z.Q. Ye, Z.S. Shao, Modeling loading rate effect on crushing stress of metallic cellular materials, *Int. J. Impact Eng.* 36 (6) (2009) 775–782.
- [23] A. Jung, A.D. Pullen, W.G. Proud, Strain-rate effects in Ni/Al composite metal foams from quasi-static to low-velocity impact behaviour, *Composites A* 85 (2016) 1–11.
- [24] Bing Hou, H. Zhao, S. Patoffatto, J.G. Liu, Y.L. Li, Inertia effects on the progressive crushing of aluminium honeycombs under impact loading, *Int. J. Solids Struct.* 49 (19–20) (2012) 2754–2762.
- [25] Jae Ung Cho, Soon Jik Hong, Sang Kyo Lee, Chongdu Cho, Impact fracture behavior at the material of aluminum foam, *Mater. Sci. Eng. A* 539 (2012) 250–258.
- [26] Dejan Tomazincic, Branko Necemer, Matej Vesenjak, Jernej Klemenc, Low-cycle fatigue life of thin-plate auxetic cellular structures made from aluminium alloy 7075-t651, *Fatigue Fract. Eng. Mater. Struct.* 42 (5) (2019) 1022–1036.
- [27] Mehdi Taherishargh, Bálint Katona, Thomas Fiedler, Imre Norbert Orbulov, Fatigue properties of expanded perlite/aluminum syntactic foams, *J. Compos. Mater.* 51 (6) (2017) 773–781.
- [28] C.Q. Xi, Q.M. Li, Meso-scale mechanism of compaction shock propagation in cellular materials, *Int. J. Impact Eng.* 109 (2017) 321–334.
- [29] I. Elnasri, S. Patoffatto, H. Zhao, H. Tsitsiris, F. Hild, Y. Girard, Shock enhancement of cellular structures under impact loading: Part I experiments, *J. Mech. Phys. Solids* 55 (12) (2007) 2652–2671.
- [30] Sergey L. Lopatnikov, Bazle A. Gama, Md. Jahirul Haque, Carl Krauthaus, John W. Gillespie, High-velocity plate impact of metal foams, *Int. J. Impact Eng.* 30 (4) (2004) 421–445.
- [31] Zhijun Zheng, Yaodong Liu, Jilin Yu, Stephen R. Reid, Dynamic crushing of cellular materials: Continuum-based wave models for the transitional and shock modes, *Int. J. Impact Eng.* 42 (2012) 66–79.
- [32] V.P.W. Shim, K.Y. Yap, W.J. Stronge, Effects of nonhomogeneity, cell damage and strain-rate on impact crushing of a strain-softening cellular chain, *Int. J. Impact Eng.* 12 (4) (1992) 585–602.
- [33] Thomas Tancogne-Dejean, Adriaan B. Spierings, Dirk Mohr, Additively-manufactured metallic micro-lattice materials for high specific energy absorption under static and dynamic loading, *Acta Mater.* 116 (2016) 14–28.
- [34] C.P. de Jonge, H.M.A. Kolken, A.A. Zadpoor, Non-auxetic mechanical metamaterials, *Materials* 12 (4) (2019).
- [35] Nejc Novak, Matej Vesenjak, Shigeru Tanaka, Kazuyuki Hokamoto, Zoran Ren, Compressive behaviour of chiral auxetic cellular structures at different strain rates, *Int. J. Impact Eng.* 141 (2020) 103566.
- [36] T.C. Lim, A. Alderson, K.L. Alderson, Experimental studies on the impact properties of auxetic materials, *Phys. Status Solidi B* 251 (2) (2014) 307–313.
- [37] Olly Duncan, Leon Foster, Terry Senior, Andrew Alderson, Tom Allen, Quasi-static characterisation and impact testing of auxetic foam for sports safety applications, *Smart Mater. Struct.* 25 (5) (2016) 054014.
- [38] T. Fila, P. Zlamal, O. Jirousek, J. Falta, P. Koudelka, D. Kytýr, T. Doktor, J. Valach, Impact testing of polymer-filled auxetics using split Hopkinson pressure bar, *Adv. Energy Mater.* 19 (10) (2017).
- [39] Nejc Novak, Lovre Krstulovic-Opara, Zoran Ren, Matej Vesenjak, Mechanical properties of hybrid metamaterial with auxetic chiral cellular structure and silicon filler, *Compos. Struct.* 234 (2020) 111718.
- [40] Nejc Novak, Matej Vesenjak, Zoran Ren, Auxetic cellular materials – a review, *Stroj. Vestn. - J. Mech. Eng.* 62 (9) (2016) 485–493.
- [41] J. Glinz, D. Kytýr, T. Fila, J. Šleichrt, A. Schrempf, D. Furst, J. Kastner, S. Senck, In-situ compression test of artificial bone foams in controlled environment using X-ray micro-computed tomography, in: 17th Youth Symposium on Experimental Solid Mechanics, YSESM 2019, 2019, pp. 48–51.
- [42] T. Doktor, T. Fila, P. Zlamal, D. Kytýr, O. Jirousek, High strain-rate compressive testing of filling materials for inter-penetrating phase composites, in: 17th Youth Symposium on Experimental Solid Mechanics, YSESM 2019, 2019, pp. 21–24.
- [43] Isabel Duarte, Matej Vesenjak, Lovre Krstulovic-Opara, Zoran Ren, Crush performance of multifunctional hybrid foams based on an aluminium alloy open-cell foam skeleton, *Polym. Test.* 67 (2018) 246–256.
- [44] Susana C. Pinto, Paula A.A.P. Marques, Matej Vesenjak, Romeu Vicente, Luis Godinho, Lovre Krstulovic-Opara, Isabel Duarte, Characterization and physical properties of aluminium foam–polydimethylsiloxane nanocomposite hybrid structures, *Compos. Struct.* 230 (2019) 111521.
- [45] M. Neuhauserova, P. Koudelka, J. Falta, M. Adorna, T. Fila, P. Zlamal, Strain-rate and printing direction dependency of compressive behaviour of 3D printed stainless steel 316L, in: 17th Youth Symposium on Experimental Solid Mechanics, YSESM 2019, 2019, pp. 68–72.
- [46] I. Elnasri, H. Zhao, Impact perforation of aluminium cymat foam, *Int. J. Mech. Sci.* 150 (2019) 79–89.
- [47] J. Zhou, Z.W. Guan, W.J. Cantwell, The impact response of graded foam sandwich structures, *Compos. Struct.* 97 (2013) 370–377.
- [48] A.U. Ude, A.K. Ariffin, C.H. Azhari, Impact damage characteristics in reinforced woven natural silk/epoxy composite face-sheet and sandwich foam, coremat and honeycomb materials, *Int. J. Impact Eng.* 58 (2013) 31–38.
- [49] Ali Kurşun, Mehmet Şenel, Halil M. Enginsoy, Emin Bayraktar, Effect of impactor shapes on the low velocity impact damage of sandwich composite plate: Experimental study and modelling, *Composites B* 86 (2016) 143–151.
- [50] Qinghua Qin, T.J. Wang, Low-velocity impact response of fully clamped metal foam core sandwich beam incorporating local denting effect, *Compos. Struct.* 96 (2013) 346–356.
- [51] M.A. Islam, M.A. Kader, P.J. Hazell, J.P. Escobedo, A.D. Brown, M. Saadatfar, Effects of impactor shape on the deformation and energy absorption of closed cell aluminium foams under low velocity impact, *Mater. Des.* 191 (2020) 108599.
- [52] Shaoyu Hou, Tiantian Li, Zian Jia, Lifeng Wang, Mechanical properties of sandwich composites with 3D-printed auxetic and non-auxetic lattice cores under low velocity impact, *Mater. Des.* 160 (2018) 1305–1321.
- [53] Nejc Novak, Luka Starčević, Matej Vesenjak, Zoran Ren, Blast response study of the sandwich composite panels with 3D chiral auxetic core, *Compos. Struct.* 210 (2019) 167–178.
- [54] Sigit P. Santosa, Faizal Arifurrahman, Moh. Hafidz Izzudin, Djarot Widagdo, Leonardo Gunawan, Response analysis of blast impact loading of metal-foam sandwich panels, *Procedia Eng.*: *Plast. Impact Mech.* 173 (2017) 495–502.
- [55] Xin Pang, Hejun Du, Investigation on dynamic penetration of closed-cell aluminium foam using in situ deceleration measurement, *Composites B* 100 (2016) 78–90.
- [56] Bahman Taherkhani, Javad Kadkhodapour, Ali Pourkamali Anaraki, Mahmoud Saeed, Haoyun Tu, Drop impact of closed-cell aluminum foam, *J. Fail. Anal. Prev.* (2020).
- [57] S. Ramachandra, P. Sudheer Kumar, U. Ramamurthy, Impact energy absorption in an Al foam at low velocities, *Scr. Mater.* 49 (8) (2003) 741–745.
- [58] P. Koudelka, O. Jirousek, T. Fila, T. Doktor, Compressive properties of auxetic structures produced with direct 3D printing, *Mater. Tehnol.* 50 (3) (2016) 311–317.
- [59] A. Elmahdy, P. Verleysen, Challenges related to testing of composite materials at high strain rates using the split Hopkinson bar technique, in: EPJ Web of Conferences, Vol. 183, 2018.
- [60] J.T. Hammer, T.J. Liutkus, J.D. Seidt, A. Gilat, Using digital image correlation (DIC) in dynamic punch tests, *Exp. Mech.* 55 (1) (2015) 201–210.
- [61] A. Gilat, T.E. Schmidt, A.L. Walker, Full field strain measurement in compression and tensile split hopkinson bar experiments, *Exp. Mech.* 49 (2) (2009) 291–302.
- [62] D. Fang, Y. Li, H. Zhao, On the behaviour characterization of metallic cellular materials under impact loading, *Acta Mech. Sin.* 26 (6) (2010) 837–846.
- [63] T. Fila, P. Koudelka, P. Zlamal, J. Falta, M. Adorna, M. Neuhauserova, J. Luksch, O. Jirousek, Strain dependency of Poisson's ratio of SLS printed auxetic lattices subjected to quasi-static and dynamic compressive loading, *Adv. Energy Mater.* 21 (8) (2019).
- [64] A. Gilat, J.D. Seidt, Dynamic material characterization using digital image correlation, in: *Applied Mechanics and Materials*, vol. 566, 2014, pp. 3–9.
- [65] T. Fila, P. Zlamal, J. Falta, T. Doktor, P. Koudelka, D. Kytýr, M. Adorna, J. Luksch, M. Neuhauserova, J. Valach, O. Jirousek, Testing of auxetic materials using Hopkinson bar and digital image correlation, in: EPJ Web of Conferences, Vol. 183, 2018.
- [66] M. Adorna, S. Bronder, J. Falta, P. Zlamal, T. Fila, Evaluation of Hopkinson bar experiments using multiple digital image correlation software tools, in: 17th Youth Symposium on Experimental Solid Mechanics, YSESM 2019, 2019, pp. 1–5.
- [67] M. Adorna, P. Zlamal, T. Fila, J. Falta, M. Felten, M. Fries, A. Jung, Testing of hybrid nickel-polyurethane foams at high strain-rates using Hopkinson bar and digital image correlation, in: 16th Youth Symposium on Experimental Solid Mechanics, YSESM 2018, 2018, pp. 72–76.
- [68] R.A. Govender, R.J. Curry, The “open” Hopkinson pressure bar: Towards addressing force equilibrium in specimens with non-uniform deformation, *J. Dyn. Behav. Mater.* 2 (1) (2016) 43–49.
- [69] J.M. Hodgkinson, N.S. Vlachos, J.H. Whitelaw, J.G. Williams, Drop-weight impact tests with the use of laser-doppler velocimetry, *Proc. R. Soc. Lond. Ser. A: Math. Phys. Sci.* 379 (1776) (1982) 133–144.
- [70] T. Fila, I. Kumpova, P. Koudelka, P. Zlamal, D. Vavrik, O. Jirousek, A. Jung, Dual-energy X-ray micro-CT imaging of hybrid Ni/Al open-cell foam, *J. Instrum.* 11 (1) (2016).

- [71] T. Fila, P. Koudelka, I. Kumpova, M. Vopalensky, J. Šleicrt, V. Rada, P. Zlamal, J. Tarasiuk, D. Kytyr, Time-lapse micro-CT analysis of fatigue microcrack propagation in cortical bone, *J. Instrum.* 15 (03) (2020) C03031.
- [72] D. Kytyr, P. Zlamal, P. Koudelka, T. Fila, N. Krcmarova, I. Kumpova, D. Vavrik, A. Gantar, S. Novak, Deformation analysis of gellan-gum based bone scaffold using on-the-fly tomography, *Mater. Des.* 134 (2017) 400–417.
- [73] O. Jirousek, T. Doktor, D. Kytyr, P. Zlamal, T. Fila, P. Koudelka, I. Jandjsek, D. Vavrik, X-ray and finite element analysis of deformation response of closed-cell metal foam subjected to compressive loading, *J. Instrum.* 8 (02) (2013) C02012.
- [74] Roberto Cesaro, Principles and applications of differential tomography, *Nucl. Instrum. Methods Phys. Res. A* 270 (2) (1988) 572–577.
- [75] P. Koudelka, T. Fila, V. Rada, P. Zlamal, J. Šleicrt, M. Vopalensky, I. Kumpova, P. Benes, D. Vavrik, L. Vavro, M. Vavro, M. Drdacky, D. Kytyr, In-situ X-ray differential micro-tomography for investigation of water-weakening in quasi-brittle materials subjected to four-point bending, *Materials* 13 (6) (2020).
- [76] Philippe Viot, Erwan Plougonven, Dominique Bernard, Microtomography on polypropylene foam under dynamic loading: 3D analysis of bead morphology evolution, *Composites A* 39 (8) (2008) 1266–1281, Full-field Measurements in Composites Testing and Analysis.
- [77] Isabel Duarte, Matej Vesenjsek, Lovre Krstulovic-Opara, Compressive behaviour of unconstrained and constrained integral-skin closed-cell aluminium foam, *Compos. Struct.* 154 (2016) 231–238.
- [78] V.R. Feldgun, Y.S. Karinski, D.Z. Yankelevsky, A two-phase model to simulate the 1-D shock wave propagation in porous metal foam, *Int. J. Impact Eng.* 82 (2015) 113–129, *Metallic Foams under Dynamic Loading*.
- [79] M.F. Ashby, A.G. Evans, N.A. Fleck, L.J. Gibson, J.W. Hutchinson, H.N.G. Wadley (Eds.), *Metal Foams*, Butterworth-Heinemann, Burlington, 2000.
- [80] Isabel Duarte, Matej Vesenjsek, Lovre Krstulovic-Opara, Variation of quasi-static and dynamic compressive properties in single aluminium-alloy foam block, *Procedia Mater. Sci.* 4 (2014) 157–162, 8th International Conference on Porous Metals and Metallic Foams.
- [81] Joachim Baumeister, Jorg Weise, Eva Hirtz, Klaus Hohne, Jorg Hohe, Applications of aluminum hybrid foam sandwiches in battery housings for electric vehicles, *Procedia Mater. Sci.* 4 (2014) 317–321, 8th International Conference on Porous Metals and Metallic Foams.
- [82] Isabel Duarte, John Banhart, A study of aluminium foam formation–kinetics and microstructure, *Acta Mater.* 48 (9) (2000) 2349–2362.
- [83] Isabel Duarte, Matej Vesenjsek, Manuel J. Vide, Automated continuous production line of parts made of metallic foams, *Metals* 9 (5) (2019) 531.
- [84] F. Baumgartner, I. Duarte, J. Banhart, Industrialization of powder compact toaming process, *Adv. Energy Mater.* 2 (4) (2000) 168–174.
- [85] Karsten Stobener, Gerald Rausch, Aluminium foam-polymer composites: Processing and characteristics, *J. Mater. Sci.* 44 (2009) 1506–1511.
- [86] I. Jandjsek, J. Valach, D. Vavrik, Optimization and calibration of digital image correlation method, in: EAN 2010: 48th International Scientific Conference on Experimental Stress Analysis, 2010, pp. 131–136.
- [87] H. Kolsky, An investigation of the mechanical properties of materials at very high rates of loading, *Proc. Phys. Soc. Sect. B* 62 (11) (1949) 676–700.
- [88] M. Bussac, P. Collet, G. Gary, R. Othman, An optimisation method for separating and rebuilding one-dimensional dispersive waves from multi-point measurements. application to elastic or viscoelastic bars, *J. Mech. Phys. Solids* 50 (2) (2002) 321–349.
- [89] H. Zhao, G. Gary, A new method for the separation of waves. Application to the shpb technique for an unlimited duration of measurement, *J. Mech. Phys. Solids* 45 (7) (1997) 1185–1202.
- [90] C. Bacon, Separation of waves propagating in an elastic or viscoelastic Hopkinson pressure bar with three-dimensional effects, *Int. J. Impact Eng.* 22 (1) (1999) 55–69.
- [91] L. Wang, K. Labibes, Z. Azari, G. Pluinage, Generalization of split Hopkinson bar technique to use viscoelastic bars, *Int. J. Impact Eng.* 15 (5) (1994) 669–686.
- [92] Q. Liu, G. Subhash, Characterization of viscoelastic properties of polymer bar using iterative deconvolution in the time domain, *Mech. Mater.* 38 (12) (2006) 1105–1117.
- [93] Michelle S. Hoo Fatt, Dushyanth Sirivolu, A wave propagation model for the high velocity impact response of a composite sandwich panel, *Int. J. Impact Eng.* 37 (2) (2010) 117–130.